Integrative modelling of angiogenesis in the bovine corpus luteum

Sotiris A.Prokopiou, BSc.

Thesis submitted to The University of Nottingham
for the degree of Doctor of Philosophy

February 2013

Abstract

The corpus luteum (CL) is a tissue formed from the remnants of an ovulated follicle in the ovary, and it produces the progesterone needed for a healthy pregnancy. CL growth is highly dependent on a growing nutrient supply, and can be compared with the most aggressive vascular tumours. Angiogenesis, the growth of new blood vessels from existing ones, plays a key role in the growth and function of the CL. Inadequate angiogenesis has been linked to infertility in cows. The CL is composed of several vascular (e.g. endothelial cells (ECs), pericytes (PCs)), and avascular (e.g. luteal cells (LCs), immune cells) cell types, and several pro-angiogenic factors (e.g. Fibroblast Growth Factor 2, FGF2) found to be important in the angiogenic process.

The objective of this thesis is to shed light on the cellular and extracellular level determinants of angiogenesis in the bovine CL.

We begin with the relevant biological and mathematical literature in Chapter 1. In Chapter 2, an ordinary differential equation model of CL growth is introduced. We assume that the CL volume is a continuum of three cell types, ECs, LCs, and stromal cells (such as PCs). The fourth variable in the model, FGF2, enhances the EC proliferation rate. The model is able, by varying parameters such as the maximal proliferation rate of the ECs, to distinguish cases where the CL shifts from a 'normal' to a 'pathological' growth.

In Chapter 3, we present *in vitro* CL published and novel studies from Robinson's Lab. Preliminary results demonstrate interesting endothelial and pericyte behaviours regarding cell aggregation and sprout formation, which are the motivation for the next two Chapters. In these experimental studies, all the CL cell types were incorporated in the same *in vitro* culture, hence providing a closer approximation to the *in vivo* environment compared to other *in vitro* cultures which use only a single cell type (mainly ECs). However, this complicates matters in terms of distinguishing cell behaviours and factors which contribute on the overall cell dynamics. Therefore, in the Chapters 4 and 5 we use data from literature.

In Chapter 4, by using the Cellular Potts Model (CPM) framework, we focus on EC-PC interactions, and particularly on the mechanism which is responsible for the EC growth inhibition. Our model incorporates two possible mechanisms for inhibition. That is, the mechanical cell-cell contact inhibition, and the inhibition mediated from diffusive TGF-β secreted once the two cell types come in contact. Interestingly, our model results suggest that the effective range of TGF-β is a crucial determinant of the degree of EC growth inhibition.

Chapter 5, by using a CPM, is devoted to sprouting angiogenesis (the formation of new blood vessel). The dynamic interchange between stalk and tip EC phenotype is incorporated through the Notch signalling pathway, with the leading tip cell moving up macrophage-mediated VEGFA gradients in a non-uniform matrix environment. The model reproduces phenomena in sprouting angiogenesis, including sprout morphology, tip competition, and explains knockout experiments on the Notch signalling pathway.

Finally, we close with Chapter 6 where we summarise the main results from each chapter and propose model extensions for future directions.

Acknowledgements

My deepest feelings of gratitude and appreciation goes first to my supervisors: Markus Owen and Helen Byrne, for their continuous support, encouragement and their expert guidance, and Bob Robinson and George Mann for their biological insight. I am also thankful to the University of Nottingham for providing funding for this project.

I would also like to thank Nick Monk for all the fruitful discussions, his very useful guidelines and advice during the first three years of my PhD as being my internal assessor, and also, Mike Jeffrey for the very nice collaboration during my PhD studies.

I am also grateful to Yi Jiang for giving me the great opportunity to work with her at the Los Alamos National Laboratory, USA, as a summer student in 2011 during which period I developed my model in sprouting angiogenesis, and also, Luisa Iruela-Arispe for her biological insight and for providing data from mouse retina. I would also like, of course, to give thanks to James Glazier, Maciek Swat, Julio Belmonte, Abbas Shirinifard, Clayton Davis and all the other members in the CompuCell3D (CC3D) group in Indiana University, USA, for their advice and expertise in using CC3D, and for providing financial support for visiting their group in summer 2010.

I would like to thank Elena Elia, Eleni Verykouki, and Colin Worby for being such amazing friends and officemates. Special thanks to Colin for being so kind and answering my English grammatical queries.

Finally, I would like to give special thanks to my family, and to Natia, for their continued support, love, and patience throughout, without which this project would not have been possible.

Contents

List of Abbreviations

Ang	Angiopoietin
CL	Corpus luteum
CPM	Cellular Potts Model
EC	Endothelial cell
ECM	Extracellular matrix
EPC	Endothelial progenitor cells
FGF	Fibroblast growth factor
GnRH	Gonadotropin-releasing hormone
IGF	Insulin-like growth factor
MMP	Matrix metalloproteinase
mRNA	Messenger ribonucleic acid
ODE	Ordinary differential equation
PC	Pericyte
PDE	Partial differential equation
PDGF	Platelet-derived growth factor
PGF2a	Prostaglandin F2a
SMC	Smooth muscle cell
TAF	Tumour angiogenesis factor
TGF	Transforming growth factor
TIMP	Tissue inhibitor of metalloproteases
VEGF	Vascular endothelial growth factor

CHAPTER 1

Introduction

1.1 Introduction and motivation

The mammalian corpus luteum (CL) is an exceptionally dynamic ovarian tissue formed from the remnants of an ovulated follicle. It produces high amounts of the hormone progesterone which acts on the uterus to support early embryo development. A rapidly increasing supply of nutrients is required to meet these demands. As a result the growth and development of the CL is extremely rapid, and associated with a short period of intense angiogenesis. Inadequate angiogenesis has been linked to infertility in cows [146].

The CL provides a unique model system in which to study not only the cellular but also the hormonal regulation of angiogenesis. Although the CL is well studied experimentally, mathematically it has not received the attention it deserves. With angiogenesis in the CL being equalled only in the fastest growing tumours [197], more focus needs to be placed upon understanding the cellular dynamics during CL growth along with the role of angiogenesis.

The main objective of this study is to build a bridge between theoretical modelling of the CL growth and the available experimental data. Mathematical modelling of the CL growth and cell-cell interactions along with the interplay of angiogenesis may lead to an improved understanding of CL tissue growth and, therefore, reduce infertility.

In this chapter we present an overview of the relevant background biology and mathematical modelling for this study, beginning with a discussion on the bovine oestrous cycle and CL formation.

1.2 Biological background

1.2.1 The bovine oestrous cycle

Oestrous cycles give females repeated opportunities to become pregnant throughout their reproductive lifetime. The cycle is regulated by the hypothalamic-pituitary-gonadal axis, which produces hormones that dictate reproductive events. The reproductive axis is composed of the hypothalamus, pituitary, and the ovary.

The sequence of hormonal release essentially begins with the synthesis and release of gonadotropin-releasing hormone (GnRH) from the hypothalamus (a specialised portion of the brain). Its primary function is to produce GnRH in response to circulating oestrogen, or to cease GnRH production in response to progesterone (see Figure 1.1). The anterior pituitary produces the gonadotropins, follicle-stimulating hormone (FSH) and luteinizing hormone (LH), in response to GnRH and oestrogen. FSH and LH production is inhibited by progesterone. The third portion of the reproductive axis consists of the ovaries. Follicles are structures on the ovarian surface that contain the egg cells (oocytes) and produce oestrogen. Follicles range in size and maturity at different stages of the cycle, but usually only one is selected to ovulate. The corpus luteum (CL) is a tissue formed from the remnant of an ovulated follicle and is responsible for progesterone production. Both oestrogen and progesterone are produced following FSH and LH stimulation of the ovary. The uterus also contributes to reproductive control, as it produces prostaglandin F2a (PGF2a), a hormone which helps to initiate ovulation by causing the regression of the CL, which results in withdrawal of progesterone's negative feedback mechanism. Progesterone produced by the CL prevents cyclicity by acting on the anterior pituitary in a negative feedback fashion, consequently, decreasing the release of FSH and LH. Figure 1.1 illustrates the relationships between the hormones that control the oestrous cycle of the bovine female as discussed above.

Elevated concentrations of progesterone can be detected about 5 days after oestrous (ovulation). If a cow does not become pregnant, concentrations of progesterone will begin to decrease around day 17 of the oestrous cycle and this allows the cow to show oestrous again around day 21.

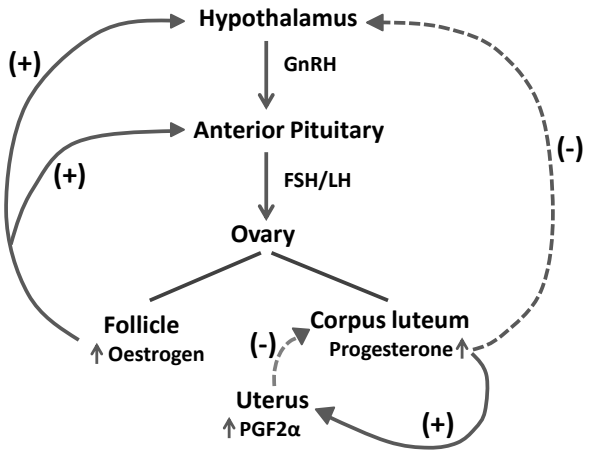

Figure 1.1: Schematic diagram showing the hypothalamic-pituitary-gonadal axis which is responsible for the control of the bovine female oestrous cycle. Key: solid curve (positive regulation); dashed curve (negative regulation).

1.2.2 The corpus luteum

De Graf was the first to record the presence of the CL in the ovaries of pregnant rabbits, and, by studying the histology of this tissue, he deduced that it was an endocrine gland (e.g. CL secretes its hormones directly into the blood). De Graf also removed the ovaries of pregnant rabbits and observed that the pregnancy was terminated. Further studies by Magnus in 1901 in ovariectomised rabbits revealed that the CL steroidal hormone progesterone played a key role in supporting gestation [170].

The CL is formed following ovulation as a result of cell proliferation in the ruptured follicle (see Figure 1.2). It develops specifically from the granulosa and theca cells of the pre-ovulatory follicle, after the LH surge. The resulting structure usually protrudes from the ovary and is yellow-brown in colour. As already noted, the CL is a tissue that secretes progesterone. In the non-pregnant cow, the function of the CL dominates the cycle from around day 5 to day 17. Alternatively, if the animal becomes pregnant, the CL is maintained for the duration of pregnancy. Progesterone has numerous physiological effects, one of the more prominent being its role in maintaining and supporting pregnancy in mammals. Without adequate levels, the developing foetus cannot be supported and pregnancy fails [167]. If there is no pregnancy, the CL regresses and allows follicular growth and ovulation to begin again. Otherwise, if implantation of a fertilised egg occurs, the levels of progesterone needed to support gestation, especially before the placenta can produce progesterone, increase exponentially. In order for the CL to meet these hormonal needs, it grows at a phenomenal rate during its early de-

velopmental stages. The rates of tissue growth and angiogenesis in the CL rival those of even the fastest growing tumours [199], although unlike tumours, the growth of the CL is a controlled physiological process. In order for this rapid growth to take place, an extensive and continuous supply of blood is needed, so a controlled physiological process known as angiogenesis (the growth of new blood vessels from existing ones) is triggered, which is described in more detail in section 1.2.4.

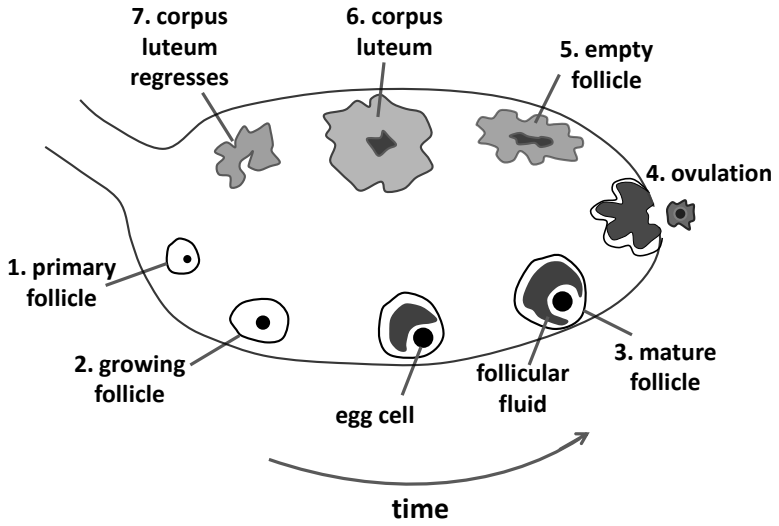

Figure 1.2: The diagram shows the formation of the corpus luteum (CL) after ovulation in the ovary. By the end of the follicular phase of the menstrual cycle, the mature follicle ruptures (ovulation), the egg cell (oocyte) is released and the ruptured follicle undergoes a transformation into the CL. Key: follicular phase (1-3); ovulation (4); luteal phase (5-7).

1.2.3 Cellular composition of the corpus luteum

The CL consists of several cell types that differ in morphological and physiological characteristics: steroidogenic (which produce hormones) small and large luteal cells, and non-steroidogenic endothelial cells (ECs), smooth muscle cells (SMCs), pericytes (PCs), fibroblasts, and immune cells. These cell types interact to maintain normal function during growth, differentiation and regression of the CL. The cellular interactions are mediated by both contact-dependent (e.g. via gap junctions [199], Notch signalling [255]) and contact-independent mechanisms (e.g. secretion of growth factors [213]).

In the remainder of this section we provide basic knowledge on the different cell types which compose the CL.

In the CL there are more non-steroidogenic cells (e.g. ECs, fibroblasts) than steroido-

genic cells (small and large luteal cells). O'Shea *et al.* in [176] have estimated that in the mid-cycle bovine CL 60-70% of cells are non-steroidogenic. Steroidogenic small luteal cells (SLCs) account for 27% and large luteal cells (LLCs) for 4% of the CL by number. Although the number of LLCs is relatively low, these large cells do comprise 40% of the total CL volume.

The vast majority of non-steroidogenic cells in the CL are ECs. The ECs express the neural cell adhesion molecule (NCAM), and it has been postulated that this molecule would mediate adhesion between ECs and LCs that also express NCAM. A functional interaction between ECs and LCs has been suggested, since ECs stimulate progesterone production by LLCs [77].

PCs are regulators of endothelial function and have been shown to produce angiogenic factors [18]. Redmer *et al.* [195] confirmed vascular endothelial growth factor (VEGF) localization to PCs/SMCs in the CL. Interestingly, during luteolysis (CL regression) ECs degenerate, but the number of SMCs and PCs remains high [197]. Therefore, it is possible that during early CL regression, PCs and SMCs may serve to regulate tissue remodeling and maintain integrity of larger blood vessels, allowing normal luteolysis to occur.

Lobel and Levey in [140] first observed immune cells, lymphocytes and macrophages, in the bovine CL, describing their presence as significant from day 14 onwards. Niswender *et al.* in [168] suggested that the immune cells are present primarily as a result of the high blood flow to the CL and that they play a passive role for most of the oestrous cycle until the time of luteolysis. The main function of the immune cells at luteolysis is thought to be destruction of the CL tissue through a variety of processes, including phagocytosis [181]. However, Adashi in [1] suggested that immune cells may have an active role in controlling the lifespan and function of the CL. There has been particular interest in tumour necrosis factor α (TNF-α), because its cytotoxic action on tumour cells has been compared with CL regression [104]. TNF-α has also been detected in the bovine CL [223].

1.2.4 Angiogenesis in the corpus luteum

In this section, we will explain why angiogenesis is an essential process underpinning CL growth and development. Angiogenesis, the process by which new capillary blood vessels sprout from pre-existing ones, is a physiological process involving the proliferation and migration of ECs, and is essential for normal tissue growth and development [116]. Because the CL grows so rapidly, and because tissue growth depends on con-

comitant vascular growth, it has long been appreciated that angiogenesis is a critical aspect of growth and function of the CL [266].

In a complex tissue, like CL, the various cell types must interact to ensure normal growth and development. Tissue growth depends upon the growth and establishment of a functional blood supply [213]; therefore, angiogenesis is one of the prominent features of the early CL. Numerous investigators have studied mechanisms associated with CL development; however, a number of important questions remain unanswered. Mechanisms that remain controversial and on which there has been recent progress include the regulation of neovascularisation and tissue remodelling during CL development [233].

Angiogenesis in the CL is a tightly regulated and highly coordinated process, which has its origins in the vasculature of the developing follicle [65]. The preovulatory follicle consists of two layers: the theca (exterior) and the granulosa (interior). These two layers are divided by the basement membrane which separates the layers. In many tissues (like tumours), hypoxia is the stimulus for the synthesis of angiogenic factors. However, in the CL angiogenesis is hormonally regulated by LH [66]. After ovulation (and breakdown of the basement membrane) the theca-derived PCs invade the granulosa-derived region (see Figure 1.3). Pericyte invasion is stimulated by growth factors produced by the granulosa cells, most likely basic fibroblast growth factor 2 (FGF2) and/or platelet derived growth factor (PDGF). The PCs then produce VEGF, which stimulates theca-derived ECs to migrate into the granulosa-derived region [66]. Extensive tissue remodelling and a period of intense angiogenesis follow over the next 2-3 days, with newly formed microvessels extending throughout the tissue. Subsequently, the PCs and ECs form the mature capillary bed.

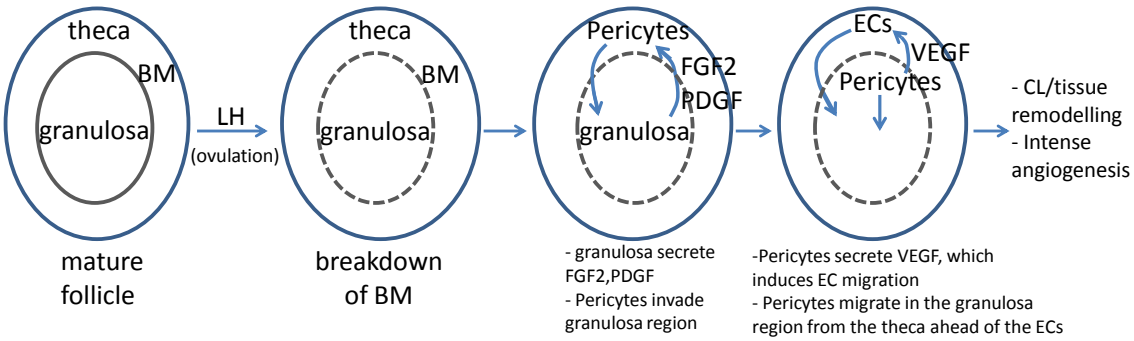

Figure 1.3: Schematic diagrams showing the evolution of the CL structure after ovulation. Key: luteinizing hormone (LH); basement membrane (BM).

1.2.5 Angiogenesis: general overview

In this section we provide a general overview of angiogenesis. The angiogenic process consists of at least three steps: (1) fragmentation of the basement membrane of the existing vessel, (2) migration of ECs from the existing vessel toward the angiogenic stimulus, and (3) proliferation of ECs [116]. Neovascularisation is completed by formation of capillary lumen and differentiation of the newly formed capillaries into arterioles and venules.

1.2.5.1 Historical overview

In the last three decades there has emerged a new field of vascular biology. Dr. John Hunter (British surgeon), in 1787, was the first who used the term 'angiogenesis' to describe blood vessels growing in reindeer antler, while in 1935, Boston pathologist Dr. Arthur Tremain Hertig described angiogenesis in the placenta of pregnant monkeys.

In the 20^{th} century, several investigators noted the tremendous vascularity of ovarian follicles and corpora lutea and recognised the importance of the ovarian vasculature in supporting growth and development of these tissues [197]. While in the 1960s, the endothelium was considered to be simply a passive container for the blood, it is now known, by the cytokines and mitogens it releases, to be an active participant in inflammation, coagulation, and repair.

Forty years ago there was little idea of how arteries and veins form in the embryo, to say nothing of the development of whole vascular networks of tubes and branches. Additionally, tumour vessels were assumed to be simple dilated host vessels. Today it is widely accepted that tumours are angiogenesis-dependent. In 1971 surgeon Judah Folkman (who is considered by many to be 'the father of angiogenesis') hypothesized that tumour growth is dependent upon angiogenesis [59]. Since then, angiogenesis itself has become a major target of tumour therapy. In 1989 Dr. Napoleone Ferrara identified and isolated the protein VEGF, a component that plays a crucial role in vessel development [57].

Numerous other promoters of angiogenesis have been identified. These factors and compounds differ in cell specificity and also in the mechanisms by which they induce new blood vessel growth. The action of many angiogenic factors can be studied *in vitro* by measuring their effect on EC migration and proliferation [40].

Angiogenesis is a complex process in which a delicate balance between promoters and inhibitors is maintained. Disturbance of this balance may result in a disrupted physio-

logical state or various pathologic conditions (see Figure 1.4).

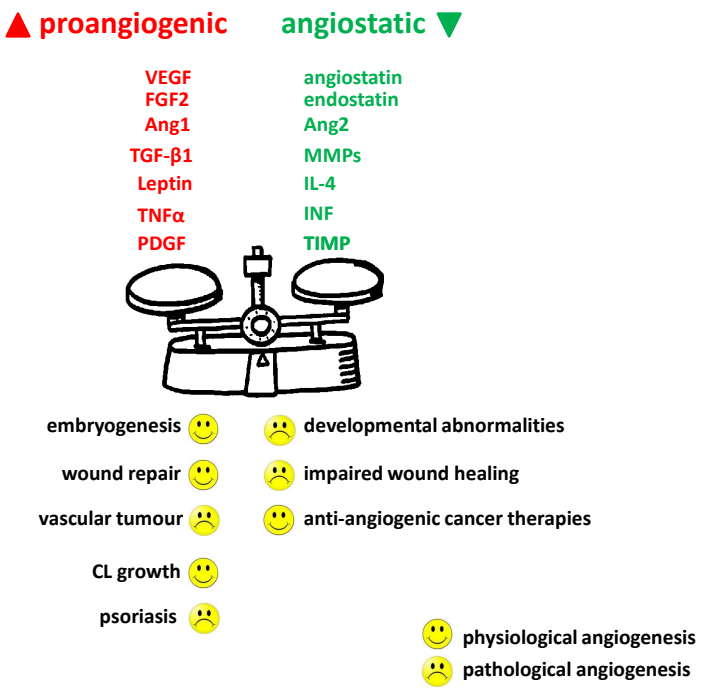

Figure 1.4: Diagram depicts how changes in the tissue balance between pro-angiogenic and anti-angiogenic (angiostatic) agents determine whether an angiogenic response is physiological (e.g. embryogenesis and CL growth) or pathological (e.g. vascular tumour), depending on the context.

1.2.5.2 Angiogenic factors

The process of angiogenesis is driven by two counteracting groups of mediators: activators and inhibitors (Figure 1.4). The activators control the different steps that lead to the formation of a new capillary, whereas the inhibitors block or markedly attenuate EC proliferation, migration, and survival, signal transduction, matrix metalloproteinase (MMPs) expression, and EC precursor development and/or recruitment.

Angiogenic factors provide the necessary 'checks and balances' required to maintain a normally quiescent yet highly responsive population of ECs by overriding signals that, if left unchecked, would lead to a relentless and destructive angiogenic response. In physiological settings, the activators and inhibitors function in a coordinated fashion to induce and sustain angiogenesis for a limited period of time, e.g. just enough to get an injured tissue sufficient nutrients to repair itself (wound repair) or in the case of the endometrium, to prepare the uterus to receive a fertilized egg. Therefore, normally the inhibitors outweigh the activators.

For angiogenesis to occur the balance must tilt in favour of the pro-angiogenic factors; this is known as the angiogenic switch. The switch may be turned on by either upregulation of angiogenic activators (inducers) or downregulation of angiogenic inhibitors.

The female reproductive organs exhibit marked periodic growth and regression, accompanied by equally striking changes in rates of blood flow. It is not surprising therefore, that they are among the few adult tissues in which angiogenesis occurs as a normal process. Ovarian follicles and corpora lutea have been shown to contain and produce angiogenic factors [196]. To better understand the complexity underlying the angiogenic response, examples of several of the better-known activators and inhibitors of angiogenesis will now be discussed in some detail, showing emphasis on their role in CL angiogenesis.

Vascular endothelial growth factors (VEGFs): Vascular endothelial growth factor (VEGF or VEGF-A) is the founding member of a family of pro-angiogenic growth actors composed of six closely related members: VEGF-A, placental growth factor (PGF), VEGF-B, VEGF-C, VEGF-D, and VEGF-E. This gene family plays a central role in regulating the growth and function of vascular and lymphatic endothelium in developing adult organisms and is a key participant in the angiogenic response that accompanies the development of malignant tumours, ocular lesions, and chronic inflammatory diseases [189].

VEGF is expressed in a wide variety of tissues, including brain, kidney, liver, and spleen, and by numerous cell types. VEGF influences many steps in the angiogenic response. It stimulates degradation of the extracellular matrix (ECM) surrounding ECs, and it promotes EC proliferation, migration, and organisation into tubular structures [189].

Oxygen tension is an important regulator of VEGF. Exposure of tissues to hypoxic conditions typically induces VEGF expression. In contrast, normoxic conditions downregulate VEGF production and promote regression of newly formed microvessels [172].

VEGF production increases in luteinizing granulosa cells of the ovulatory follicle and is stimulated by addition of human chorionic gonadotrophin (hCG) to luteinized granulosa cells in culture [66].

VEGF acts through two receptors, VEGFR-1 (Flt-1) and VEGFR-2 (KDR/Flk-1), with the first being a decoy receptor; that is, it can prevent VEGF from binding to its normal receptor (VEGFR-2). Hunigen *et al.* suggest that the CL development (associated with intense angiogenesis) is driven mainly by VEGF-A and its receptor VEGFR-2 [95].

The highest expression of VEGF-A and VEGFR-2 mRNA[1] is detected during the early developmental stages of the CL and is followed by a significant decrease during the mid- and late-developmental stages and a further decrease after regression [214]. In contrast, VEGFR-1 mRNA expression does not change during the oestrous cycle. The VEGF protein concentration in CL tissue follows the trend of mRNA expression. The VEGF protein is localised predominantly in luteal cells. The targets for VEGF are ECs where both receptors (VEGFR-1 and VEGFR-2) are found [214]. Theca-derived cells are believed to contribute on the vascularisation of the CL. For example, in the bovine CL, VEGF is predominantly localised in luteal connective tissue, and also in capillary PCs [19]. In fact, the first theca-derived cells to invade the granulosa-derived regions of the CL immediately after ovulation seem to be VEGF-containing PCs [167]. These findings suggest that theca-derived perivascular cells may direct vascularisation of the CL via production of VEGF.

Angiogenesis in the bovine CL is normally completed by day 5 of the oestrous cycle. In association with this, Tsang *et al.* found that by day 4 bovine corpora lutea were capable of producing high amounts of progesterone *in vitro* [249]. However, high expression of VEGF and its receptors after day 5 and during pregnancy had been observed [249]. This suggests a maintenance function of VEGF for the ECs of surrounding capillaries or LCs, in addition to the role of VEGF in stimulating vascular development. It has also been suggested that VEGF may be involved in stimulating follicular and luteal vascular permeability and blood flow [167].

Fibroblast growth factors (FGFs): The fibroblast growth factors (FGFs) are some of the most extensively studied pro-angiogenic substances, with FGF1 and FGF2 the best characterised. Both promote mitosis and migration of ECs [233]. Despite the fact that both are powerful angiogenic factors, FGF2 appears to be more potent in stimulating EC growth and is probably the major angiogenic factor in the CL [116]. This is supported by Robinson *et al.* [204], who found that FGF2 is up-regulated while VEGF-A remains constantly expressed during the follicular-CL transition in the cow.

FGFs signal through two receptors FGFR1 and FGFR2 [213]. FGFR1 is expressed at relatively high levels throughout the oestrous cycle. Its localisation to luteal steroidogenic cells is greatest during the mid-cycle and dramatically reduced during luteolysis. In contrast, strong staining for FGFR1 is present in ECs at all stages and is especially abundant in larger microvessels late in the oestrous cycle. Although FGFR2 in the CL

[1] messenger ribonucleic acid (mRNA): the template for protein synthesis; the form of RNA that carries information from deoxyribonucleic acid (DNA) in the nucleus to the ribosome sites of protein synthesis in the cell

is present at relatively low levels, it is localised to steroidogenic cells at all stages but is present in the vasculature (primarily the larger microvessels) only late in the oestrous cycle [197].

Platelet-derived growth factors (PDGFs): The PDGFs (PDGFA, PDGFB, PDGFC, and PDGFD) are pro-angiogenic growth factors that are expressed in a variety of tissues and produced by macrophages and ECs. PDGFs play a vital role in regulating cell growth and angiogenesis, and they exert their effects through binding and subsequent activation of two related receptors: PDGFRA and PDGFRB. PDGFs consist of either homodimers (AA, BB, CC, DD) or a heterodimer (AB) that binds two receptors simultaneously, thereby inducing a wide variety of cell responses, including proliferation, survival, and chemotaxis. PDGFs and their receptors are often expressed by neighbouring cells, suggesting a paracrine interaction. PDGF has been demonstrated to stimulate *in vitro* proliferation of theca cells from both rat [55] and pig [151], while inhibiting theca LH-induced steroid hormone synthesis [246]. In addition, the classic PDGF isoforms, PDGFA and PDGFB, were shown to contribute towards growth of preantral (without antrum - a fluid filled cavity) follicles [231].

The expression of PDGFs and receptors in the mature follicle gives rise to the question of the possible involvement of this system in the post-LH life of the follicle (the CL). It has been well established that PDGFB and PDGFRB are components of the vasculature and play an important role in angiogenesis [61, 88]. The properties of PDGFs and their receptors in inducing cell proliferation and migration suggest that signalling through these receptors may be important in the development of the CL, either by affecting migration and/or proliferation of theca cells and/or cells of the vasculature in response to the ovulatory surge of LH.

In [231], Sleer *et al.* elucidated the presence of components of the PDGF ligand-receptor system in the CL of the rat. Because of the LH-induced increase in levels of mRNA for several PDGFs and receptors, the authors suggested a role for this growth factor system during CL development. That was confirmed by the observation that inhibition of PDGF receptor signaling prior to ovulation resulted in a significant decrease in the average percentage of corpora lutea in the ovaries [231].

Angiopoietins - determinants of vessel maturation: Ang-1 and Ang-2, two members of the angiopoietin family, are of particular interest with respect to regulation of the rapidly-changing CL vasculature. Both angiopoietins bind to Tie-2 receptor which is expressed on the vascular endothelium. Ang-1 is thought to play a stabilising role:

maintaining cell-cell interactions, inhibiting apoptosis and mediating interactions between the EC and the basement membrane. In angiogenesis, Ang-1 is necessary for the maturation of newly formed vessels by recruiting PCs [66].

Ang-2 is a natural antagonist for Ang-1. It binds to the same receptor, but does not activate it, thus blocking the normal effects of Ang-1. Therefore, the ratio of Ang-2 to Ang-1 appears to play a crucial role for vascular stability. The high Ang-2/Ang-1 ratio induces vessels to become destabilised: cell-cell and cell-matrix connections are loosened and both the basement membrane and the peri-endothelial support cells become dissociated from the endothelium [187]. In such conditions, when VEGF is high, a destabilisation of blood vessels results in the formation of a new vascular network, whereas a lack of VEGF support results in a regression of blood vessels [66] (see Figure 1.5).

In [214], Schams *et al.* showed that in the early CL, Ang-1 but not Ang-2 mRNA expression changed according to the stage of the oestrous cycle. Particularly, they found that the Ang-2/Ang-1 ratio increased because of the lower expression of Ang-1 mRNA. Hence, they suggested that the Ang-Tie system is involved in the local mechanisms regulating angiogenesis in the bovine CL [214].

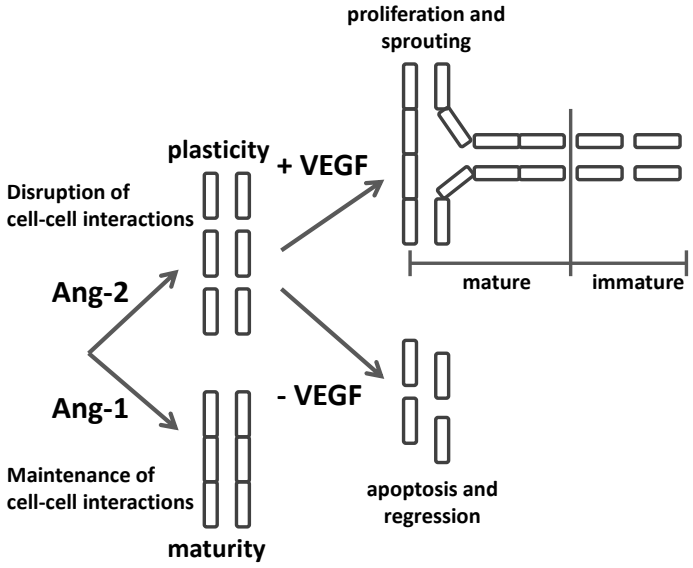

Figure 1.5: Schematic showing the regulation of EC behaviour by the angiopoietins and VEGF. An absence of Ang-2 allows Ang-1 to maintain vessels in the quiescent state (maturity); expression of Ang-2 allows either angiogenic outgrowth, or vessel regression, depending on the presence or absence of VEGF.

1.2.6 Summary

The corpus luteum (CL) plays a central role in the reproductive process because of its production of progesterone, a hormone responsible for a healthy pregnancy. The CL growth is extremely rapid and highly angiogenesis-dependent. Central to the growth and development of the CL, therefore, is vascular growth, which appears to be regulated by several angiogenic growth factors, e.g. FGF2 and VEGF. Inadequate angiogenesis has been linked to infertility in the cows. The CL is a complex tissue composed of various vascular (e.g. endothelial cells, vascular smooth muscle cells, pericytes) and non-vascular (e.g. luteal cells, fibroblasts, immune cells) cell types. Since the rates of tissue growth and angiogenesis in the CL rival those of even the fastest growing tumours, in the next section, our aim is to provide a brief review of different theoretical approaches that have been used mainly in tissue/tumour growth and angiogenesis.

We believe that mathematical modelling could lead to an improved understanding not only of angiogenic function, but also of tissue growth and development in the CL in order to alleviate infertility in cows.

1.3 Mathematical background

1.3.1 Introduction

Over the last decades, mathematical modelling has progressed to encompass a wide range of biological systems. Within the broadening sphere of mathematical biology, there has been increasing activity in the modelling of various problems related to tissue growth and angiogenesis and, in this section, we briefly provide the basic mathematical background related to these aspects.

1.3.2 Mathematical modelling of tissue growth and angiogenesis

Mathematical modelling of tissue growth and angiogenesis has been gaining momentum as a means to shed light on the biological complexity underlying normal and tumour growth, wound healing, tissue engineering, and blood vessel development. A variety of mathematical models have been developed, each focusing on different aspects of these processes. However, as stated in section 1.2 the angiogenesis-dependent growth of the CL has been compared to the tumour and, therefore, in the following we mainly focus on models inspired by tumour growth and angiogenesis.

Modelling of angiogenesis could be regarded as an attractive area for research since angiogenesis is fundamental to both the development of vasculature as well as its maintenance in the adult. Impaired angiogenesis is a feature of a wide range of clinical conditions, and predictive theoretical models of angiogenesis have a clear role in developing suitable therapeutic strategies.

Many phenomena exist on a wide range of scales and the proper modelling tool is basically dictated by the question of interest. Mathematical models may be divided broadly into two categories: continuum models at the cell density level and discrete models at the individual cell level. In particular, at the coarse-grained level (continuum models) one erases cell identity and uses continuous cell densities to describe the system. At the next finer scale (discrete models), cells within the population are modeled as discrete objects.

1.3.3 Continuum models

Continuum models focus on the dynamics of the gross tissue behaviour, including morphology, shape, and extent of vascularisation, with capillary networks being described in terms of EC densities. Microscopic details of tissue structure are averaged over short

scales to produce a description of the macroscopic-level tissue properties. At this scale, because the number of cells in the model is sufficiently large, it becomes possible and sometimes necessary to treat some or all of the cells as a single continuum. Therefore, continuum models use either systems of ordinary differential equations (ODEs) or partial differential equations (PDEs).

1.3.3.1 Ordinary differential equation (ODE) models

Some of the simplest models for tissue growth are the exponential (equation (1.3.1)), logistic (equation (1.3.2)), and Gompertz growth (equation (1.3.3))

$$\frac{dx}{dt} = kx, \tag{1.3.1}$$

$$\frac{dx}{dt} = kx(1 - \frac{x}{K}), \tag{1.3.2}$$

$$\frac{dx}{dt} = kx\ln\left(\frac{K}{x}\right), \tag{1.3.3}$$

where, $x(t)$ can be the tissue mass and K the carrying capacity (maximum tissue size). For instance, the exponential model can be relevant for the early stages of tumour growth only, whereas logistic and Gompertz model represent growth limitations (with maximal growth), due to mechanical pressure or nutrient scarcity.

The logistic model, frequently used in population dynamics, was also used in the description of tumour growth [217]. However, probably the most popular non-linear model that can be found in the literature in connection with tumour growth is the Gompertz model from Laird [125], where the Gompertz curve in [126] was fitted to experimental data.

In an attempt to design a more realistic model of tumour growth under angiogenic stimulator and inhibitor control, Hahnfeldt *et al.* in [82] proposed a two-variable model derived from the Gompertz model. The authors introduced as a variable the carrying capacity of the environment, K:

$$\begin{aligned} \frac{dx}{dt} &= kx\ln\left(\frac{K}{x}\right), \\ \frac{dK}{dt} &= -\lambda K + bS(x,K) - dI(x,K) - eKg(t). \end{aligned} \tag{1.3.4}$$

The first term of the second equation in (1.3.4) represents the spontaneous loss of functional vasculature; the second term represents the stimulatory capacity of the tumour upon the inducible vasculature (through, e.g. angiogenic factors); the third term reflects endogenous inhibition of previously generated vasculature (through, e.g. endothelial

cell death); and the last term represents inhibition of tumour vasculature due to administered inhibitors with concentration $g(t)$. This model enables to take into account the vasculature, that provides nutrients and oxygen to tumour cells, and thus to study the effects of several anti-angiogenic factors on tumour growth.

Gyllenberg *et al.* [81] and Kozusko *et al.* [120] used ODE models with two cell compartments, proliferating and quiescent, by revisiting Gompertz growth.

In addition, ODE models have been widely used to study the growth of avascular multicellular spheroids (MSS) (for example, see [24]). MSS are used in the laboratory because the reproducible manner in which they grow mimics the initial phase of *in vivo* avascular tumour growth.

Many other ODE models have been created for tissue/tumour growth, but we will briefly refer to some of those.

Kuznetsov *et al.* in [123] used an ODE model to describe the interaction between the immune system (via cytotoxic T lymphocytes) and a growing tumour. It was predicted that if the number of tumour cells injected into the mice was less than a threshold the resultant tumour growth could be controlled. However, at certain parameter values, solutions were possible that can be interpreted as tumour sneaking through, a phenomenon in which low doses of tumour cells can escape immune defenses and grow into a large tumour. They found that one of the most critical parameters was the rate at which cytotoxic cells were inactivated due to interactions with the tumour [123].

Owen and Sherratt in [179] also developed an ODE model for the early, avascular growth of a tumour, focusing on the temporal dynamics of the tumour-macrophage interaction. In particular, the authors concentrated on the inhibitory effect of macrophages due to their cytolytic activity. It was shown that although the presence of macrophages had important effects on the tumour composition, their immune response was not sufficient to prevent tumour growth. However, the extension of the model by incorporating exogenous chemical regulators admitted the possibility of tumour regression.

Although compartmental ODE modelling can contribute a lot in tracking the density of cells, tissue/tumour growth over time, in many cases spatial dependencies such as gradients arise. Obviously tissue growth *in vivo* depends on its environment. For instance, it depends on the mechanical properties of the supporting tissue, the local quantity of nutrients and oxygen, the local concentrations of pro- and anti-growth chemical factors. Therefore, incorporation of spatial dimensions is needed to meet these demands.

1.3.3.2 Partial differential equation (PDE) models

Reaction-diffusion PDEs describe the space and time evolution of the concentrations of chemical substances and of cell densities. Such equations allow to take into account the interactions of a diffusing chemical or of a population of cells with the environment.

To construct a PDE model we use the law of mass conservation to formulate generic 'conceptual' equations as given below

$$\begin{pmatrix} rate\ of \\ change\ of \\ species\ c \end{pmatrix} = \begin{pmatrix} transport\ of \\ species\ c \end{pmatrix} + \begin{pmatrix} rate\ of \\ production \\ of\ species\ c \end{pmatrix} - \begin{pmatrix} rate\ of \\ decay/uptake \\ of\ species\ c \end{pmatrix}, \tag{1.3.5}$$

describing time rates of change of substances of interest, their movement and their rates of production/decay.

A typical continuum PDE model of the type described in equation (1.3.5) (for instance, see [149]) is given by the following governing equations

$$\frac{\partial \mathbf{n}}{\partial t} = -\nabla \cdot \mathbf{J_n} + \mathbf{g}_1(n, c), \tag{1.3.6}$$

$$\frac{\partial \mathbf{c}}{\partial t} = \mathbf{D}\nabla^2 \mathbf{c} + \mathbf{g}_2(n, c), \tag{1.3.7}$$

where, $\mathbf{n}(\mathbf{x}, t)$ is comprised of the densities of all cell types involved in the process (e.g. ECs, pericytes), $\mathbf{c}(\mathbf{x}, t)$ is containing the concentrations of substances influencing cell migration and/or proliferation, $\mathbf{g}_1$, $\mathbf{g}_2$ contain the appropriate source and sink terms, and $\mathbf{D}$ is a diagonal matrix containing the diffusion coefficients of each chemical species.

The cellular fluxes ($\mathbf{J_n}$) typically include a random diffusive component and directed terms, given in the form

$$\mathbf{J_n} = J_{\text{diffusion}} + J_{\text{chemotaxis}} + J_{\text{haptotaxis}} = -D_{\mathbf{n}}\nabla \mathbf{n} + \chi_{\mathbf{c}} \mathbf{n} \nabla \mathbf{c} + \chi_h \mathbf{n} \nabla f, \tag{1.3.8}$$

where, $\chi_{\mathbf{c}}$ and χ_h is the strength of chemotaxis and haptotaxis, respectively, and f the concentration of the ECM (e.g. fibronectin). Note that chemotaxis is the directional motility of cells up a gradient of a chemoattractant, and haptotaxis is the movement up a gradient of cellular adhesion sites or substrate-bound chemoattractants.

Several PDE models in angiogenesis have been developed to study the distribution in space and time of variables such as EC density, capillary tip and branch density, and angiogenic factor concentration. Next we describe a selection of one- and two-dimensional PDE models, focusing on the model constituents and their main biological intuition.

PDE models in one space dimension

Models in one space dimension focused on tumour-induced angiogenesis and angiogenesis in wound healing include those of [6, 12, 24, 32, 174].

Particularly, in [174], Orme and Chaplain focused upon the early stage of angiogenesis wherein the ECs group together in the parent vessel to form the initial capillary sprout buds. The model postulates that the vascular ECs that form capillary tips migrate up a gradient of angiogenic factor released by a tumour. The density of new capillaries as well as the concentrations of angiogenic factors evolve according to coupled nonlinear PDEs (of the type (1.3.6)-(1.3.7)). Haptotaxis was also incorporated in the model with fibronectin being secreted by the ECs and diffusing into the surrounding area. This model was the first that addressed the question of site location (e.g. 'Does the site at which a capillary bud forms simply coincide with the site at which the VEGF concentration is highest, or is a more complex process involved?'). As was expected, by increasing the parameter γ which represents the size of the (1-D) domain, the number of EC clusters (buds) formed along the parent blood vessel increased. In addition, similar effects were obtained by varying two other parameters; ζ (the rate of matrix secretion per cells), and λ (the loss of matrix per unit matrix). These results suggested that the site(s) of bud initiation is not related only to the local distribution of VEGF in the tissue, but that is also determined by the role of haptotaxis.

In [12], Balding and McElwain developed one of the earliest mathematical models of angiogenesis (in the cornea), modelling capillary and sprout tip density in response to a diffusive tumour angiogenesis factor (TAF) governed by the equation of type (1.3.7) with constant diffusion coefficient. The model was considered in one dimension, with the TAF source situated at the one edge of the domain and a capillary at the other. The solutions exhibited a wave-like behaviour, with a wave-front of tips advancing from the parent vessel towards the TAF.

In [24], Byrne and Chaplain extended the model in [12]. The authors incorporated both random and chemotactic fluxes (see equation (1.3.8)) for the tip cell motion, whereas in [12] the authors incorporated only the chemotactic flux, by assuming that sprouts are never observed directed away from a tumour and, therefore, random motion is negligible. In [24], the authors attempted to capture the increased vessel density (or brush-border effect), by adding a second, more rapid, proliferation term, which only becomes active when TAF concentration is above a certain threshold value. That term was also incorporated in the TAF equation as a consumption term from the tip cells. The main weakness of this continuum model was its inability to distinguish between anastomosis (tip cell fusion) and tip death. This is because angiogenesis is essentially

a two-dimensional process, with tip cells sprouting in directions other than that of the propagating front.

PDE models in two space dimensions

Models of angiogenesis considered in [29, 31, 133, 171, 175], were able to account for the spatiotemporal distribution of capillary sprouts due to their two-dimensional approach. Particularly, these models studied the interactions between ECs and the ECM during angiogenesis in order to understand how cells respond to not only chemical signals via chemotaxis, but also to mechanical signals via haptotaxis. In haptotaxis, the EC population migrates up the concentration gradient of ECM, which mediates cell-cell and cell-matrix adhesion.

As an example, the model of Orme *et al.* in [175] incorporates just the role of ECs and the ECM (fibronectin), since the authors assumed the TAF concentration to be at steady state. The model examined the relative importance of various parameters, such as the chemotactic and haptotactic coefficients, the EC proliferation rate, and the diffusion coefficient on the dynamics of the angiogenic process. Without haptotaxis, the model predicted early anastomosis of the initial sprouts, and the authors used this result to suggest that haptotaxis is important for successful angiogenesis.

However, EC-ECM interactions are not only chemical (e.g. secretion of growth factors), but also mechanical since the ECs exert traction forces on the ECM fibers in order to move. These interactions were incorporated into mechano-chemical models introduced by Oster and co-workers [163, 177]. In [177], Oster *et al.* used a cell traction model which was able to reproduce morphogenetic phenomena in fowl dermis. Their aim was to show how various combinations of cell and matrix properties (e.g. cell division, traction, motility, haptotaxis, matrix elasticity) can, individually and in concert, produce equivalent patterns. For example, a decrease in cell traction was compensated by an increase in ECM density or adhesiveness, or by increased cell division, to arrive at the same spatial structure. This introduced the notion of equivalent and compensating effects in morphogenesis, and as a result, the authors suggested that many patterns are not the result of a single process, but rather emerge as the consensus of a number of interacting phenomena [177].

In [133], Levine *et al.* continued the line of investigation as in [174] (to predict the site of sprout formation), by considering the EC migration as a reinforced random walk[1] where transition probabilities are dependent on cell concentration, proteolytic enzymes

[1] Extensive reference on the concept of reinforced random walks can be found in Othmer and Stevens [178]

and fibronectin that forms the basal lamina (a layer of ECM secreted by the epithelial cells, on which the epithelium sits). Michaelis-Menten kinetics describe reactions in which EC receptors are regarded as catalysts for converting TAF into proteolytic enzyme, which in turn breaks down fibronectin and destroys the basal lamina. The model also includes secretion and uptake of fibronectin by ECs, chemotaxis to TAF and haptotaxis to lower concentrations of fibronectin. As expected, results showed that if there is enough TAF supplied to the capillary wall, the basal lamina would break down.

Mechanical forces (e.g. shear stress) on the developing capillary network are examined by other two-dimensional models [148, 162] in which the ECM is represented as a viscoelastic material interacting with the ECs. Particularly, in [162], Murray showed that if cellular traction is sufficiently high, then traction forces alone can lead to formation of networks. Additionally, it was suggested that the matrix thickness is an important factor influencing the pattern. More specifically, cells spread on a matrix whose thickness increased from one end of the dish to the other, formed polygon networks whose size increased with increasing thickness of the gelled basement membrane matrix [162].

Because the same genetic machinery regulates both angiogenesis and vasculogenesis (the process of blood vessel formation occurring by a *de novo* production of ECs) [26], a common set of mechanisms is plausible. In [147], Manoussaki extended her mechanical model of vasculogenesis to describe angiogenesis by adding long-range, chemotactic guidance cues. In her simulations, ECs migrated from an aggregate towards a chemoattractant source and cell-traction-driven migration contracted the sprout into a narrow, vessel-like cord.

Moving now from the mechano-chemical models, in [30], Chaplain presented a mathematical model based on the experimental system of the implant of a solid tumour in the cornea of a test animal. The model focused on the 'tissue response unit' which consists of ECs, a generic TAF (e.g. a cytokine such as VEGF) and a generic matrix macromolecule known to affect cell adhesion (e.g. fibronectin), where EC proliferation terms were not included. This work mainly aimed at explaining the experimentally observed fact that in the absence of EC proliferation, angiogenesis is incomplete, in the sense that the ECs fail to reach the tumour. EC migration was determined by their response to the concentrations of TAF and matrix macromolecules in the micro-environment. Therefore, EC movement consisted of a random diffusive flux, a chemotactic flux and a haptotactic flux as in equation (1.3.8). The chemotactic sensitivity was described by

$$\chi_c = \frac{\chi_0}{1 + \alpha c}. \tag{1.3.9}$$

This reflects the fact that, as the concentration $c(x, y, t)$ of TAF increases, the EC lose the ability to efficiently detect the concentration gradient, so the chemotactic sensitivity

decreases. Note that the classic chemotaxis ($\chi_c = \chi_0$: constant) is recovered in the limit $\alpha \to 0$.

In [220], Serini and co-workers also used a two-dimensional continuum model to study cell aggregation (the early stage of network formation) by ECs randomly plated on a Matrigel film. The PDE system was based on the following assumptions: the EC population can be described by a continuous distribution of density and velocity, the EC population in the early stages of its evolution (e.g. low densities) can be modelled as a fluid of non-directly interacting particles, with the ECs accelerating by gradients of chemoattractants, where the latter are released by ECs, diffuse and degrade. The hypothesis here is that the early EC aggregation is supported by chemotactic intercellular cross-talk mediated by chemoattractants. The authors suggested that the EC number and the range of activity of chemoattractant factor regulate the vascular network formation and size. Particularly, it was shown that VEGF triggered directed EC migration and that the cell number over or below an interval was not permissive for network formation. The model also predicted that the diffusivity and the half-life time of the chemoattractant determine the size of the vascular structure (e.g. with smaller diffusivity they obtained vascular networks with larger mesh).

In summary, continuum models are only meaningful when describing the average behaviour of a large number of individuals. The smaller the number of individuals in the population, the less accurate the macroscopic description becomes. This raises the question of whether a continuum description is appropriate for angiogenesis, a process controlled by the behaviour of a small number of individual cells. In contrast to these deterministic, continuum models, several different types of discrete models have been used to model the branching morphology of capillary network formation and angiogenesis.

1.3.4 Cell-based models

Continuum models provide valuable insight into the processes of angiogenesis, but they are limited in their prediction of the structure of vascular networks. To determine the procedures that describe the morphology of vascular networks cell-based models have been developed.

Each cell is treated as a discrete entity, with a set of rules which governs the actions of the cells. The cells must have some explicit set of actions which they will follow based on their current state and the states of neighbours.

Much of biological modelling use an averaged approach: a single variable represents a property of a collection of objects (populations, cells, genes, etc). Cell-based models use the reductionist view that these averaged variables should be observable or emerge from the actions and interactions of the individuals which make up the system. The objective is to describe the basic processes which control the actions of individuals, and combine them to determine the resultant macrodescriptors which give rise to higher levels of organisation.

We separate our review of cell-based models into six main groups: lattice-based models, cell-centre, cell-vertex models, cellular potts models (CPM), lattice and off-lattice multi-agent models, and particle models. We discuss the CPM in more detail since Chapters 4 and 5 are based on this framework.

1.3.4.1 Lattice-based models

The majority of cell-based models of angiogenesis simulate EC movement on a regular lattice, and in this section we provide details on some of those.

In [6], Anderson and Chaplain used a discretisation (using standard finite-difference methods) of a PDE for the EC density (n). This involves approximation of the continuous two-dimensional domain as a grid of discrete points (with a mesh size, h, between grid points), and time (t) by discrete increments of length k. That is $x = lh$, $y = mh$, $t = gk$, with $l, m, g \in \mathbb{N}^+$. The probabilities of movement of an individual EC are generated by the coefficients of the five-point finite-difference stencil in response to its local micro-environment. The discretisation of the PDE governing the migration of an EC, as given in [6], has the form:

$$n_{l,m}^{q+1} = n_{l,m}^{q} p_0 + n_{l+1,m}^{q} p_1 + n_{l-1,m}^{q} p_2 + n_{l,m+1}^{q} p_3 + n_{l,m-1}^{q} p_4, \tag{1.3.10}$$

where the subscripts specify the location on the grid and the superscripts the time steps. The probabilities $p_0, ..., p_4$ are functions of the fibronectin and TAF concentrations at the neighbouring spatial points of an individual EC. As a result, the motion of an individual cell at the sprout-tip is governed by its interactions with angiogenic factors (e.g. TAF) and matrix macromolecules (e.g. fibronectin) in its local micro-environment. Therefore, the above probabilities obviously contain contributions from diffusion, chemotaxis, and haptotaxis. The discrete model allows for branching (production of new sprouts), and anastomosis (formation of loops), and incorporates cell proliferation which additionally results in sprout extension.

In [144], Mallet and De Pillis used a hybrid (discrete-continuum) cellular automaton model to describe the interactions between a growing tumour and the immune system.

This approach incorporates both deterministic and stochastic mechanisms allowing for the consideration of individual cell behaviour and associated randomness. The model simulated chemical diffusion through deterministic PDEs and cell behaviour through a set of probabilistic rules. The spatial domain in the cellular automaton represents a two-dimensional patch of tissue supplied with nutrients by blood vessels. In the absence of the immune system, the model was able to reproduce tumours. However, introducing the immune system leads to various results depending on the choice of the T-lymphocyte (immune cells) recruitment and death parameters. Therefore, depending on the strength of T-cell recruitment and the T-cell death parameter, the tumour grew with stable and unstable oscillations and in some cases the tumour was completely destroyed. However, due to the probabilistic nature of the model it was difficult to determine exact parameter values at which the tumour becomes unstable. Additionally, simulations showed (as expected) that increasing T-cell recruitment as well as increasing the cytolytic ability of T-cells leads to greater reductions in tumour size.

In [74], Gerlee and Anderson developed a hybrid cellular automaton model which captures the growth dynamics of glycolytic tumours. The interactions between the cancer cells and the ECM were taken into account. The authors investigated the impact of the micro-environment on the growth and evolutionary dynamics of the tumour by varying the oxygen concentration and matrix density in the tissue. In particular, they focused on the emergence of the glycolytic phenotype, which is an important aspect of carcinogenesis. The results showed that environmental conditions affect both the morphology and the evolution of phenotypes in the tumour. While a low oxygen concentration destabilises the growth and leads to a branched tumour morphology, a denser matrix gives rise to a more compact tumour with less fingering. On the other hand, the combined effect of both these environmental variables leads to the emergence of the glycolytic phenotype, which is found to appear in a poorly oxygenated and dense tissue.

In [191], Qutub and Popel used a 3-D rule-based lattice model for sprouting angiogenesis. In particular, the rules concerning the tip cell activation, and migration, stalk and tip cell growth and proliferation, and persistence of sprout direction were depended on VEGF (concentration and gradients) and Delta-like 4 (Dll4; a Notch ligand [91]). The model explored the characterisation of persistence effects on vessel formation, differentiation of tip cells (from stalk cells), and stalk cell branching. The model predicts it is not until 48 hrs that branching has a significant effect on the total vessel length changes. In Dll4 haploinsufficiency (Dll4+/-; when in diploid organisms one of the two copies of a gene is mutated) the relative total vessel length changed and the number of tip cells

in 24 hrs was increased compared to the control condition (Dll4+/+).

In [41], Das *et al.* also incorporated the effect of ECM and growth factors in a 3-D lattice model to predict capillary formation. The deterministic component of the model includes the diffusion-convection-reaction equations that govern the growth factor concentrations. The model incorporates probabilities of an individual cell to transition into one of four stages: quiescence, proliferation, migration and apoptosis. The transition of each cell between states is a function of its current state, the condition of the surrounding matrix and external governing factors such as the presence or absence of flow, the growth factors present in neighbouring matrix and initial matrix stiffness. All cell-cell communication occur via the field (e.g. ECM), and direct cell-cell interactions were not considered.

In [153], McDougall *et al.* developed a hybrid model with the aim to produce the whole retinal vascular plexus (RVP) from proliferating ECs which migrate towards (poorly oxygenated) astrocytes which secrete VEGFA and fibronectin. Once a perfused vascular network has formed, astrocytes gradually downregulate VEGFA expression. The hybrid formulation allows for the tracking of individual cells (ECs, astrocytes) towards the outer retinal boundary, and visualisation of blood vessel topology. Blood perfusion is also included throughout plexus development. The resulting *in silico* RVP structures are compared with whole-mounted retinal vasculatures at various stages of development, and the agreement is found to be promising.

1.3.4.2 Cell-centre models

In cell-centre models, each cell is represented by the position (in $\mathbb{R}^2$ or $\mathbb{R}^3$) and movement of its centre.

One of the first models using a discrete framework was that of Stokes and Lauffenburger [239]. The authors proposed a stochastic model for the random motility and chemotaxis of single cells. Note that cells in this model are represented only by their centres (they do not occupy a certain area). The cell velocity was described as a persistent random walk. The resulting stochastic differential equation for cell velocity is given by

$$d\mathbf{v}_i(t) = -\beta\mathbf{v}_i(t)dt + \alpha d\mathbf{W}_i(t) + \kappa\nabla c\, sin|\tfrac{\phi_i}{2}|dt$$
$$\begin{pmatrix} change\ in \\ velocity \end{pmatrix} = \begin{pmatrix} resistance \\ to\ motion \end{pmatrix} + \begin{pmatrix} random \\ fluctuations \end{pmatrix} + \begin{pmatrix} chemotactic \\ bias \end{pmatrix}, \quad (1.3.11)$$

where, β is a 'viscosity' coefficient, $\mathbf{W}$ is the Wiener process[1] (white noise), κ is the

[1]The Wiener process is a continuous-time stochastic process, which it is often called Brownian motion

chemotactic resposiveness, c is the TAF concentration, ϕ is the angle between the direction the tip is moving and that towards the TAF source (see Figure 1.6), and subscript i denotes the i^{th} sprout [239]. The discrete framework used in the above model had

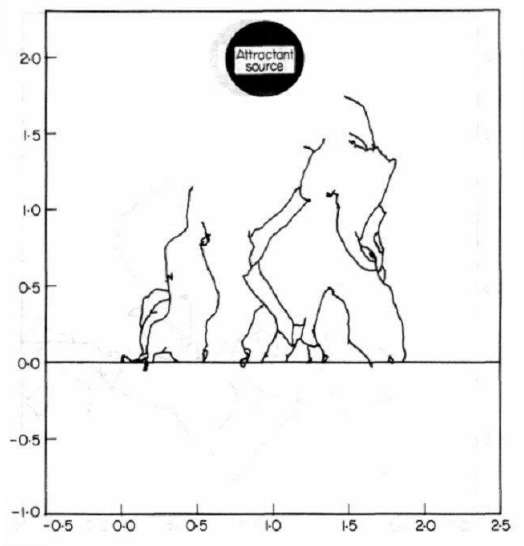

Figure 1.6: Geometry of the angiogenesis model in [239]. The primary vessel is represented by the horizontal line. The path of each capillary is determined by the trajectory of an actively migrating cell located at its tip. This tip migrates with velocity, **v** (as in equation (1.3.11)), towards the spherical source of the chemoattractant. All other cells in the sprout follow directly behind the tip cell [239].

the advantage of enabling the motion of individual ECs to be followed. Realistic capillary network structures were generated by incorporating rules for sprout branching and anastomosis. Although the model incorporated random motility and chemotaxis as mechanisms for cell migration, no account was taken of the interactions between the ECs and the ECM. The model did not include any rules to reproduce the observed increase in branching frequency at the leading edge of the network as it approached the tumour, but this would be straightforward to add.

In cell-centre models, cell movement can also be determined by a balance of forces acting on a cell. Various approaches have been developed for calculating the forces acting on a cell. These include modelling cell-cell connections with springs, and modelling the cells as deformable elastic circles/spheres.

In [54], Drasdo and Loeffler developed a cell-centre based model concerned with the buckling of a colorectal crypt. The authors developed a model for a 1-D chain of cells in 2-D space, where the cells were treated as deformable elastic circles. The force on each

cell was composed of four parts: (i) the elastic deformation force between the cells, (ii) a shear force holding the crypt in shape, (iii) a force from the stroma, and (iv) a force restricting any bending of the epithelium. The model incorporated proliferation and allowed for variation in the size of the cells through the cell cycle.

To represent the shapes of the cells (except as deformable elastic circles/spheres), a Voronoi diagram may be used (see Figure 1.7(b)). In [212], Schaller and Meyer-Hermann studied multicellular tumour spheroids by introducing a 3-D Voronoi-Delaunay hybrid model. The cell shape varied from spherical if cells were immersed in thin solution to convex polyhedral in dense tissues. The cellular interactions included direct elastic forces and cell-cell as well as cell-matrix adhesion. The spatiotemporal distribution of two nutrients, oxygen and glucose, was described by reaction-diffusion equations. The experimental growth curves were reproduced by considering the dynamics of both nutrient concentrations simultaneously.

A disadvantage of some centre-dynamics models is their reliance on Voronoi tesselation. That is, the number of vertices and the shapes of the cells do not change smoothly. Another disadvantage, is that these models can be computationally expensive, with a new Voronoi diagram needing to be constructed at each time step.

1.3.4.3 Cell-vertex models

Cell-vertex models are a type of cell-level model that view the cells as polygons. The size and shape of each cell is dictated by the movement of its vertices (see Figure 1.7(c)). In cell-vertex models the motion of the cells evolves, either through considering the balance of forces at the vertices [259] or by rearranging cells to minimise total free energy [94].

Briefly, the vertex model was first introduced by Kawasaki *et al.* in 1989 [112] for the simulation of 2-D grain (crystallites) growth. The basic idea behind this model is that the minimisation of the free energy can be achieved exclusively by the motion of the vertices. The curvature of the grain boundaries was not considered, but introduced later by Weygand [261] by the introduction of virtual vertices along the boundaries. The 2-D model of Kawasaki was extended to three dimensions from Nagai *et al.* [165].

The main advantage of cell-vertex models is that they have no need for a Delaunay triangulation or Voronoi diagram to be produced at each timestep. However, one of the main disadvantages of vertex-based models is that it is not easy to include differential cell-substrate adhesion terms for different cells, as any change in drag terms on

vertex movement would depend on all cells surrounding the vertex. Finally, as vertex-based methods contain more information than centre-based methods they can be more computationally expensive.

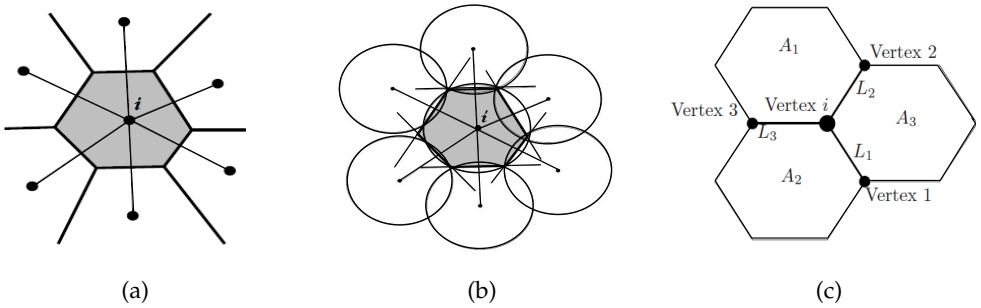

Figure 1.7: (a) Cell-centre model where the movement of cell i is determined by interactions with neighbouring cells. (b) A Voronoi diagram (shaded grey) is constructed for the polygonal shape of cell, i. (c) Cell-vertex model, where the cell shape is defined by the cell's vertices. Vertex i moves in response to size and the shapes of the surrounding cells 1,2 and 3, with areas A_1, A_2, A_3 and lengths L_1, L_2, L_3 from vertex i to vertices $1, 2, 3$ respectively.

It is important to point out that, although most of the above (cell-centre and cell-vertex) models were proposed to describe the movement of cells in sheets, cells of different types can sort out due to differing intrinsic properties, such as surface adhesivity. This led to the theory of differential adhesion and energy minimisation [237] and has been extended [78] into a Potts-type model.

1.3.4.4 Cellular Potts models

The Glazier-Graner-Hogeweg (GGH) model, also known as the Cellular Potts Model (CPM) [78], is a lattice-based approach where each cell is represented by many lattice sites, allowing physical characteristics including cell shape, surface area and volume to be modelled directly, in contrast to cellular automata [51] where each cell is represented by a single lattice site. The model configuration depends on an overall *effective energy* (or Hamiltonian) that is minimised as the systems evolves. Further details on the CPM approach are given in Chapters 4 and 5, and below we briefly present some examples of CPM applications which are related to those two Chapters.

In [155], Merks *et al.* used a CPM to demonstrate that cell elongation, in conjunction with autocrine secretion of a chemoattractant, suffices to form vascular-like morphologies and subsequent remodelling by ECs. The model results showed that reducing cell elongation below a critical cell length results in elimination of the vascular-like shapes.

Therefore, the authors concluded that an elongated cell shape is key for the spatiotemporal behaviour of the model, and they suggested that mechanism for *in vitro* vasculogenesis.

In [157], Merks *et al.* used a CPM to present the 'contact-inhibited' chemotaxis mechanism which can produce networks (without incorporating cell-autonomous elongation as in [155]) both from dispersed ECs and EC clusters without requiring long-range guidance cues. That is, ECs secrete a chemoattractant and preferentially extend pseudopods up gradients of the chemoattractant, unless contact-inhibition locally prevents chemotactic pseudopod extension. They also investigated how sprouting depends on the sensitivity of cell-ECM interaction. If that sensitivity is above a threshold the cords become thinner and longer with cords consisting of only one cell (otherwise, vascular cords are two cells wide).

In [14], Bauer *et al.* investigated the roles of EC-EC and EC-ECM interactions during the onset of angiogenesis, when the newly formed sprouts consist of only a few cells. It was the first cell-based model of tumour-induced angiogenesis to incorporate extracellular and intercellular environments, by utilising the advantages of both discrete and continuous modelling. This model incorporates ECs, ECM, as well as VEGF dynamics. At the extracellular level, a PDE describes diffusion, uptake, and half-life decay of tumour secreted VEGF. At the cellular level, a CPM is used to simulate cell migration, growth, proliferation, cellular adhesion, and ECM degradation. The extra and intercellular environments directly impact on each other. The resulting morphology of the capillary sprout is determined by several mechanisms: tip cell migration up spatial gradients of VEGF and adhesion gradients, cellular adhesion to the ECM, and competition for space. Moreover, it was shown that interplay between haptotaxis and chemotaxis can result in EC elongation, a characteristic shape for migrating cells, without needing a rule to prescribe an elongated cell shape as in [155]. Finally, the authors assumed that branch splitting resulted from ECM inhomogeneities.

In [241], Szabo *et al.* used a CPM to model the patterning processes relying on the hypothesis that multicellular patterning is the result of elongated cell-guided motility, with each cell having a measure of anisotropy (directionally dependent). Firstly, they showed that close contact with elongated cells indeed enhances and guides cell motility. Secondly, that cell density determines the interconnectedness of the structure, and it also influences the characteristic pattern size (e.g. at very low cell densities, no multicellular structures were present). The cell density was measured as volume fraction - the ratio of the area covered by cells and the overall simulation area. For example, at densities higher than 55%, the linear structures gradually disappear. At densities

under 20%, there were not enough cells to form interconnecting clusters. Additionally, the cell shape was found to be determined by the relative balance of surface tension and anisotropic bias: if anisotropic bias dominates, individual cells become extremely elongated. Note that if the cell is circular, then it is regarded as isotropic.

In [250], Turner and Sherratt used a CPM to simulate cancer cell invasion. The model incorporated the effects of cell-cell and cell-ECM adhesion (factors which are known to be very important in cell migration), as well as migration in response to haptotactic gradients created by proteolysis. The results reproduced the finger-like protrusions from the main cell mass that are observed in malignant tumours. Also consistent with biological theory and observations, the most invasive phenotype was found to be low cell-cell adhesion and high cell-ECM adhesion, combined with high proteolytic activity. The effects of including cell proliferation were also examined. Somewhat unexpectedly, the addition of cell proliferation, for certain parameter values, decreased the invasion rate. The authors suggested that this was because the increased number of cells made it more difficult for the leading cells to completely detach from the main cell mass, as happened in the case without proliferation.

In [227], Shirinifard *et al.* presented a 3-D CPM of tumour growth and tumour induced angiogenesis with simulations focused on getting more insight in differences in tumour growth with or without angiogenesis. The model was able to distinguish between several cell types: normal, hypoxic, necrotic, vascular and neo-vascular cells. If VEGF concentrations exceed a certain threshold, ECs are activated, proliferate and move towards VEGF gradients. The neo-vascular cells were contact-inhibited if the common surface area with other neo-vascular cells is above a threshold. If less, the cells grow with a rate related to the VEGF concentration, and divide if double in volume. To allow the formation of vascular networks, the model used the autocrine chemotaxis as described in [155].

1.3.4.5 Lattice and off-lattice multi-agent models

In [16], Bentley *et al.* used a 3-D multi-agent lattice model for the Notch-mediated tip cell selection in angiogenic sprout initialisation without incorporating cell migration and proliferation. Remark that the Notch signalling pathway is responsible for cell fate decisions (e.g. transition between stalk and tip cells). The model identified both VEGFA concentration and gradients, and filopodia extension as critical factors in determining the robustness of tip-stalk (checkerboard-like) patterning. It was shown that increased VEGFA levels as found in many diseases can cause the delayed response from Notch signalling and result in abnormal oscillations of tip-stalk cell fates.

In a subsequent model, Bentley *et al.* in [17] explored the system dynamics as Notch signalling is integrated with tip cell migration and fusion, but again without incorporating cell proliferation. The fusing tip cells become inhibited and neighbouring stalk cells flip fate. In pathological conditions, when VEGF is high (e.g. 10 times bigger than the normal level) it leads to sheet formation of multiple tip cells. Regarding cell-cell junction sizes on tip cell selection, results showed that if average junction size is inversely proportional to the VEGF level, then normal selection is possible, regardless of the VEGF level.

1.3.4.6 Particle models

In this section we briefly refer to a different group of models where a cell is treated as a particle or a group of particles in the absence of an underlying grid.

In [158], Milde *et al.* presented a 3-D hybrid model of sprouting angiogenesis, which considered explicitly the effect of the ECM and of the soluble as well as matrix-bound VEGF on capillary growth. Stalk cells and molecular species (VEGF, MMPs and fibronectin) are described as densities (using PDEs), whereas tip cells are represented as particles in a discrete, agent-based model. They have shown that the structure and density of the ECM has a direct effect on the morphology, expansion speed and number of branches. That is, simulation results demonstrated an increase in the number of observed branches for an increase in both the amount of distributed VEGF 'pockets' (cavities) in the numerical domain, and the level of VEGF at pocket location. In other words, the pockets of VEGF located in the ECM induced strong chemotactic cues and, therefore, the probability of sprout tips hitting a pocket was increased for a higher pocket density, leading consequently to an increase in branching.

In [166], Neuman introduced a 3-D model of interacting multicellular systems, in which the fundamental objects were not cells, but subcellular elements. The main objective was the assessment of cell shape as it emerges from cellular interactions. That was attempted by subdividing each cell into a number of subcellular elements. Both the intra and intercellular dynamics are written in terms of interactions between these elements. The dynamics of the elements are described by stochastic differential equations. The three dynamical contributions to a given element's motion are: (i) a weak stochastic component, (ii) local biomechanical interactions with other elements within the same cell, and (iii) local biomechanical interactions with elements in nearby cells.

1.3.4.7 Modelling environments

In the last decade, several groups tried to incorporate different types of models in a modelling environment, and below we present only some of the most widely used ones:

- CompuCell3D (CC3D) [78] is based on the Cellular Potts Model (CPM). The Potts model was originally developed to study ferromagentic and crystalline systems, but later it was extended to study the coarsening of foam and sorting of biological cells. CC3D is being used for studying foam morphogenesis, biofilms, cancer, as well as many other biological and physical systems. Tissue Simulation Toolkit is a two-dimensional library for the CPM which is mainly used for tissue patterning and developmental mechanisms.

- FLAME [92] is an agent-based modelling system which can be used to development applications in many areas. Some of the projects that use FLAME are: Epidermis, Sumo2 (bacteria modelling), Epitheliome. In particular, Epitheliome [256] explores the development of structure and function in epithelial tissues. It is also used in many other areas such as urothelial tissue, wound healing in skin etc. Its rule-based structure is adopted from Stekel *et al.* [238] a work on epithelial tissue, and it has been extended by including more detailed hierarchies of control (e.g. intracellular signalling pathways involved in cell-cycle control).

- Chaste [186] is a cell-based framework which supports the simulation of cell populations using cell-centre (with connectivity defined either by a Voronoi tessellation or 'overlapping spheres'), cell-vertex, or the CPM approach. Chaste has also been used in various applications such as cancer, and heart modelling, crypt formation, bacterial biofilm formation etc.

- Virtual Cell (VCell) [211] is a computational environment for modelling and simulation of cell biology. The VCell is an application that is used over the internet. Users can build models with a web-based Java interface to specify compartmental topology and geometry, molecular characteristics, and relevant interaction parameters. The VCell automatically converts the biological description into a corresponding mathematical system.

- iDynamics [129] (biofilms), VirtualLeaf [156] (plant tissue morphogenesis), CellSyS [90] (off-lattice simulation of growth and organization processes in multicellular systems in 2D and 3D).

Having provided an overview of the main types of mathematical modelling in tissue growth and angiogenesis, below we provide a summary, and in the next Chapter, our ODE model on the growth of the bovine CL will be presented.

1.3.5 Summary

A fundamental issue in modelling cell populations is that of scale. One is typically interested in systems composed of a single cell to many millions of cells (e.g. tissue, organ). At the most coarse-grained level one erases cell identity and uses continuous cell densities. At the next finer scale, cells within the population are modeled as discrete objects. The type of modelling approach (or combination thereof) that is used to simulate tissue growth or a particular aspect of angiogenesis is usually selected based on the question that the model seeks to address and the types of available data with which to construct the model.

As discussed earlier, the corpus luteum is a heterogeneous tissue and its growth is highly angiogenesis-dependent. In Chapter 2, we present an ODE model in an attempt to understand the CL growth as a continuum medium rather than working at the resolution of its individual cells.

In Chapter 4, we seek to assess the dynamics of interactions between the two main vascular cell types (endothelial cells and pericytes), and in Chapter 5, we model angiogenic sprout formation. Since both aspects (cell-cell interactions and sprouting) involve only a few cells, cell-based models are more appropriate, as attention is focused on the level of an individual cell. Particularly, the Potts framework is a good basis and appropriate for these applications since it explicitly accounts for cell shape and more importantly cell-cell adhesion.

CHAPTER 2

An ODE model for the early growth of the bovine corpus luteum

2.1 Introduction

The corpus luteum (CL) is an ovarian tissue created by follicular ovulation, and produces the progesterone needed for pregnancy. Rapid growth of the CL requires angiogenesis, the creation of new blood vessels from pre-existing ones, a process which is regulated by proteins that include fibroblast growth factor 2 (FGF2). Inadequate angiogenesis has been linked to infertility in cows.

In this Chapter we develop a time-dependent ordinary differential equation (ODE) model for the CL growth. The dependent variables represent FGF2, endothelial cells (ECs), luteal cells (LCs), and stromal cells (like pericytes (PCs)), by simply assuming that the CL volume is a continuum of the three cell types.

We assume that if the CL volume exceeds a threshold value, then cell growth is inhibited. We define the *discontinuity boundary* to be the surface at which the volume threshold is attained. This threshold separates the model into two different cases; therefore, the model is analysed as a Filippov (piecewise smooth) system.

To investigate the importance of angiogenesis on CL growth we determine how the system dynamics change as ρ_5, the maximal EC proliferation rate, is varied.

We found that a weak (low ρ_5) or strong (high ρ_5) angiogenic environment implies a 'pathological' CL growth, since the loss of CL constituents (specifically, LCs which produce progesterone) compromises pregnancy. However, for intermediate values of ρ_5, a normal CL growth (with all its cellular components being present) is maintained, which is necessary to sustain a healthy pregnancy.

2.2 Biological background

As has been described in Chapter 1, the corpus luteum (CL) is the tissue which develops from an ovarian follicle during the luteal phase of the oestrous or menstrual cycle (see Figure 1.2). The CL (mainly LCs [108]) secretes progesterone which regulates the length of the oestrous cycle and is essential for maintenance of pregnancy. Inadequate progesterone secretion is a major cause of early embryonic mortality [108]. Therefore, 'impaired angiogenesis' in the CL could result in poor embryonic development and infertility.

It is now well established that angiogenesis plays a key role in the growth and function of the CL [197, 199]. The extensive vascularisation of the CL enables it to receive one of the highest blood flows per unit tissue mass and to supply the nutrients needed for its high metabolic rate [65, 197]. The capillary network of the mature CL is so dense that most LCs are adjacent to one or more capillaries. This is perhaps not surprising, since in several mammals most (up to 85%) cells that proliferate during CL growth are ECs [198]. This enables the CL to grow at a rapid rate (0.5 g to $>$5 g in 5 days [203]) that is only surpassed by the fastest growing tumours. Such dramatic growth is essential if sufficient progesterone is to be produced to support the developing embryo [201].

Angiogenesis in the CL is controlled by a plethora of angiogenic factors, including vascular endothelial growth factor (VEGF), fibroblast growth factor 2 (FGF2) and the platelet-derived growth factor (PDGF) family. *In vitro* results suggest that all three growth factors are active regulators of CL angiogenesis [202]. These factors are thought to have complementary rather than redundant actions in CL angiogenesis, since the absence of any one signal is sufficient to cause marked alterations in endothelial network formation, and the remaining factors are unable to compensate for the loss of any other factors [202]. These studies also demonstrate that the ECs in the CL are more sensitive to FGF2 inhibition than any other growth factor. Furthermore, dynamic changes in FGF2 concentration have been observed during the follicle-luteal transition (the point before and after ovulation) in the cow, while VEGFA concentrations remained constant [202]. Hence, in this study we focus on the role played by FGF2.

Although the mechanisms responsible for the development of the CL have been studied for several decades (for review, see [96]), no mathematical models of this process have yet been developed. In the remainder of this section, we present data taken from [145, 203] to motivate the model that we have developed.

Figure 2.1(a) shows how the FGF2 concentration in the CL changes in the 12 days that follow oestrous. The surge in FGF2 that occurs during ovulation (days 1-2) [203] is fol-

lowed by a rapid decrease until FGF2 levels settle to a steady value. The rapid change in FGF2 levels during the first two days coincides with the initiation of angiogenesis in the early CL.

Figure 2.1(b) shows how the CL increases rapidly in size during the early and mid-luteal stages of the oestrous cycle [145]. In the absence of data for the LCs we anticipate that their volume is proportional to that of the CL.

Figure 2.1(c) shows how the total area of von Willebrand factor (VWF; EC marker) in CL changes over time [127], which is an indication of the changes on the EC numbers. Additionally, in Figure 2.1(d) the presence of PCs and/or smooth muscle cells is indicated by the total area of smooth-muscle actin (SMA; PC marker) in CL [127].

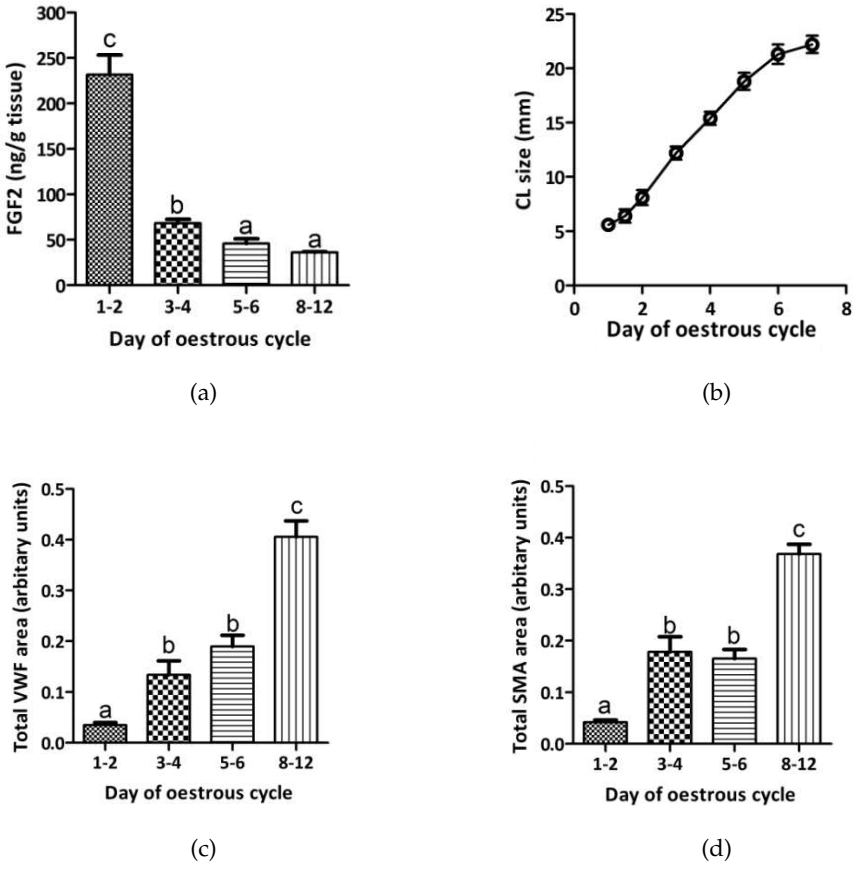

Figure 2.1: A series of plots showing the profiles of: (a) FGF2 concentration in the CL [203], (b) CL size (diameter) [145], (c) total endothelial cell area in the CL [127], and (d) total pericyte cell area during CL development (days 1 (ovulation) to 12 (mature CL)) [127]. The data are mean + S.E.M.; significant differences between groups are indicated with a<b<c; $P<0.05$. Key: the Von Willebrand Factor (VWF) and Smooth Muscle Actin (SMA) are endothelial and pericyte markers, respectively.

The main objective of this work is to develop a model that reproduces existing experimental data, and that can be used to explore the dependence of normal and pathological behaviours on parameter values.

The remainder of the Chapter is organised as follows. We present the model overview in section 2.3, the different types of steady states in section 2.4, and we proceed in section 2.5 by identifying regions of parameter space in which the steady states are physiologically realistic. We devote section 2.6 to describe how the evolution of the CL is affected by varying the 'angiogenic' parameter along with the robustness of our results to parameter values. The Chapter concludes in section 2.7 where we summarise our results.

2.3 Model overview

2.3.1 The mathematical model

In this section, we develop an ordinary differential equation (ODE) model for the time evolution of the CL in which the dependent variables represent the volumes of ECs, LCs, and all other stromal cells (such as PCs). We denote by $F(t)$ the concentration of the growth factor, FGF2, and the volumes of the ECs, LCs, and stromal cells by $E(t), L(t)$ and $R(t)$, respectively.

We postulate that CL growth is regulated by endothelial (E) and stromal cell (R) division, volumetric growth of LCs (L), and also by the FGF2 contribution as explained below.

2.3.1.1 Growth factor FGF2, F(t)

Guided by the results described in section 2.2 and following [203], we assume that ECs produce FGF2 at a constant rate, a_1, and LCs produce it at a rate which peaks during the two days that follow ovulation (see Figure 2.2).

As described in Chapter 1 (section 1.2.4), following the disassembly of the theca vasculature after ovulation, there is extensive EC proliferation and migration to the granulosa region in order to re-establish connections with other endothelial and luteal cells. The reconnection of ECs coincides with a decrease in FGF2 concentration [202]. Therefore, we hypothesize that there should be some form of feedback mechanism between ECs and LCs; that is, when ECs attach to LCs, the latter decrease their rate of FGF2 production. Hence, we assume that the rate at which individual LCs produce FGF2 is

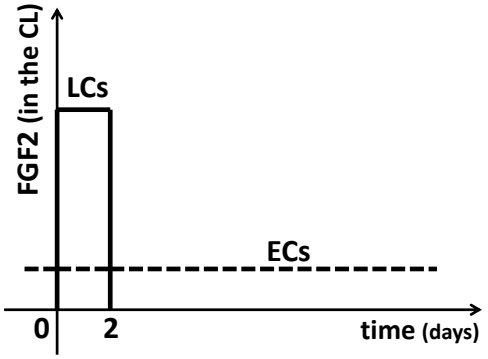

Figure 2.2: Schematic illustration of FGF2 production during CL development. Distinct localisation for ECs and LCs over time (as described in [215]), and quantification for FGF2 as described in [203], where FGF2 concentration was highest during early CL development, further suggesting that FGF2 is a key mediator of the initiation of angiogenesis [203].

a decreasing function of E/L:

$$\begin{pmatrix} rate\ at\ which\ individual \\ LCs\ produce\ FGF2 \end{pmatrix} = \frac{a_2}{R_{EL} + \frac{E}{L}}, \tag{2.3.1}$$

where the dimensionless parameter R_{EL} is the value of E/L at which FGF2 production rate (from LCs) is half-maximal. Note that the dependence on E/L becomes problematic when $L = 0$, which corresponds to some of the 'pathological' steady states later in the chapter.

Combining the above processes, we conclude that the evolution of FGF2 is given by:

$$\frac{dF}{dt} = a_1 E + \frac{a_2 L^2}{R_{EL} L + E} - d_F F, \tag{2.3.2}$$

where a_1, a_2, R_{EL} and d_F are positive constants, with d_F representing natural decay rate of FGF2.

The equations that describe the dynamics of the three cell types are of the following general form:

$$\frac{d}{dt}\begin{pmatrix} cell \\ volume \end{pmatrix} = \begin{pmatrix} rate\ of\ volume \\ increase\ due\ to \\ cell\ swelling\ or \\ proliferation \end{pmatrix} - \begin{pmatrix} rate\ of\ volume \\ loss\ due\ to \\ competition \\ for\ space \end{pmatrix}. \tag{2.3.3}$$

We postulate that the CL is contained within an elastic membrane. The ECs and stromal cells proliferate and increase in number, whereas LCs increase in volume, until eventually the CL volume ($V = E + L + R$) occupies the cavity (V^*) left by the mature

ovarian follicle after its rupture during ovulation. The surrounding membrane then becomes taut and exerts a restraining force on the cells which, if sufficiently large, leads to competition for space. We assume that this is the dominant mechanism for volume loss within the CL so that for each cell type the rate of cell death can be written as:

$$\begin{pmatrix} rate\ of \\ volume\ loss \end{pmatrix} = kCVH(V - V^*), \tag{2.3.4}$$

where, $C = E, L, R$ and k is a measure of how mechano-sensitive cells are. The equation (2.3.4) implies that all cells are equally sensitive to competition for space. H is the Heaviside step function ($H(x) = 1,\ x > 0$ and $H(x) = 0$, otherwise), which explicitly assumes no cells experience contact inhibition of growth until the CL volume threshold (V^*) is reached.

2.3.1.2 Endothelial cells, $E(t)$

The EC proliferation rate is taken to be an increasing, saturating function of FGF2. Then equation (2.3.3) supplies

$$\frac{dE}{dt} = k_E \frac{F}{F_h + F} E - kEVH(V - V^*), \tag{2.3.5}$$

where the positive parameter k_E represents the maximal rate of EC proliferation, and F_h is the FGF2 concentration at which EC proliferation is half-maximal.

2.3.1.3 Luteal cells, $L(t)$

We account for the dependence of LC swelling on nutrient levels [199] by assuming that the LC swelling rate is an increasing, saturating function of E, so that

$$\frac{dL}{dt} = k_L \frac{E}{E_{h_1} + E} L - kLVH(V - V^*). \tag{2.3.6}$$

In equation (2.3.6) the positive parameter k_L is the maximal swelling rate of the LCs, and E_{h_1} is the volume of ECs at which the swelling rate is half-maximal.

2.3.1.4 Stromal cells, $R(t)$

We assume that the evolution of all stromal cells is similar to that of the ECs and the LCs, with

$$\frac{dR}{dt} = k_R \frac{E}{E_{h_2} + E} R - kRVH(V - V^*). \tag{2.3.7}$$

In equation (2.3.7) the parameter k_R represents the maximal proliferation rate of the stromal cells, and E_{h_2} is the volume of ECs at which proliferation of the stromal cells is half-maximal.

Having presented the ODE model given in equations (2.3.2),(2.3.5)-(2.3.7), in the next section we provide the estimates for the parameter values.

2.3.2 Estimation of parameter values

The phenomenological nature of the model makes it difficult to determine many of the parameter values directly from biophysical considerations or by adapting values from the literature, and in these cases plausible estimates have been used.

Guided by estimates of the *in vitro* maximal bovine aorta EC proliferation rates of the order of 1 day(d)$^{-1}$ [137], we suppose initially that the maximal growth rate of all cell types are identical so that $k_E = k_L = k_R$, and later explore the consequences of relaxing this assumption.

Regarding the decay rate of FGF2, we fixed $d_F = 3$ d^{-1} since the half-life of FGF2 in the human body is ~ 8 hrs [15]. Concerning F_h, the FGF2 concentration at which the EC proliferation rate is half-maximal, we chose F^* (the steady level of FGF2) to be a typical late level of FGF2 (see Figure 2.1(a)), so that $F_h = F^* \simeq 50$ ng.(cm^3)$^{-1}$. We remark that in Figure 2.1(a) FGF2 has units ng/g tissue, but since the majority of tissues are water then 1 g corresponds to 1 cm^3.

A value of V^* was estimated for the maximum CL volume, where above this the cells are constrained by the outer membrane. From Figure 2.1(b), the steady value for the CL diameter is approximately 2.5 cm and, therefore, $V^* \simeq \frac{4}{3}\pi R^3 \simeq 8.2$ cm^3. In [263], Wiltbank reviewed the morphological characteristics of the main cell types of the CL in ruminants. In the mid-cycle bovine CL, small and large steroidogenic (luteal) cells constitute approximately 68% of the CL volume, the ECs approximately 13%, and therefore, the other cell types account for the remaining 19% of the total volume. Therefore, we assume that the volumes of ECs at which the swelling rate of LCs and stromal cells is half-maximal are identical. That is, $E_{h1} = E_{h2} \simeq 13\% V^* = 1.07$ cm^3.

The above statement further implies that the characteristic proportion of ECs and LCs is ECs:LCs=13:68. Therefore, an estimate for the parameter R_{EL}, the value of E/L at which FGF2 production rate (from LCs) is half-maximal was obtained. That is, $R_{EL} = 0.19$.

The methods for estimating the parameters a_1 and a_2, and the parameter k are enumerated below as methods (Ia) and (Ib), respectively.

(Ia). To estimate a_1 and a_2, we assume a steady state $\dot{F}$=0, and solve for a_1 when there are no LCs, and solve for a_2 when there are no ECs. Then, for a_1, $\dot{F} = a_1 E - d_F F$, gives $a_1 = d_F \frac{F}{E} \simeq d_F \frac{F^*}{E^*} \simeq d_F \frac{F^*}{0.13\,V^*} \simeq \frac{3*50}{1.1} \simeq 136$. For a_2, $\dot{F} = a_2 \frac{L}{R_{EL}} - d_F F$, gives $a_2 \simeq d_F R_{EL} \frac{F}{L} \simeq d_F R_{EL} \frac{F^*}{L^*} \simeq d_F R_{EL} \frac{F^*}{0.68\,V^*} = \frac{3*0.19*50}{5.6} \simeq 5.1$.

(Ib). To estimate the parameter k, the strength of the tissue constraint to the cell growth or proliferation, we assume a steady state $\dot{E}$=0 by taking the limiting case where FGF2 is sufficiently high ($F^* \gg F_h$). Therefore, $\dot{E} = 0 \Rightarrow k_E E = kEV \Rightarrow k = \frac{k_E}{V} \simeq \frac{k_E}{V^*} \simeq 0.12$.

A list of the model parameters and their units are summarised in Table 2.1. Before proceeding with our investigation of equations (2.3.2),(2.3.5)-(2.3.7), it is appropriate to nondimensionalise and, in so doing, to reduce the number of system parameters.

Table 2.1: Dimensional parameter values used in equations (2.3.2),(2.3.5)-(2.3.7).

Parameter	Value	Unit	Reference
a_1	136	ng.$(\text{cm}^3)^{-2}$.d^{-1}	estimated
a_2	5.1	ng.$(\text{cm}^3)^{-2}$.d^{-1}	estimated
k	0.12	$(\text{cm}^3)^{-1}$.d^{-1}	estimated
d_F	3	d^{-1}	[15]
k_E	1	d^{-1}	[137]
k_L	1	d^{-1}	[137]
k_R	1	d^{-1}	[137]
F_h	50	ng.$(\text{cm}^3)^{-1}$	estimated
E_{h_1}	1.1	cm^3	estimated
E_{h_2}	1.1	cm^3	estimated
V^*	8.2	cm^3	estimated
R_{EL}	0.2	-	estimated

2.3.3 Nondimensional model

We nondimensionalise equations (2.3.2),(2.3.5)-(2.3.7) by choosing $F(t)$=$F_h\hat{F}(\hat{t})$, $E(t)$=$V^*\hat{E}(\hat{t})$, $L(t)$=$V^*\hat{L}(\hat{t})$, $R(t)$=$V^*\hat{R}(\hat{t})$ and t=$\frac{\hat{t}}{kV^*}$, where, $\hat{F}$, $\hat{E}$, $\hat{L}$, $\hat{R}$ are the dimensionless dependent variables and $\hat{t}$ is the dimensionless time. By substituting for F, E, L, R and t, in (2.3.2),(2.3.5)-(2.3.7) we obtain the following dimensionless equations (hats have been dropped for notational convenience):

$$\frac{dF}{dt} = \rho_1 E + \rho_2 \frac{L^2}{\rho_3 L + E} - \rho_4 F, \tag{2.3.8}$$

$$\frac{dE}{dt} = \rho_5 \frac{F}{1+F} E - EVH(V-1), \tag{2.3.9}$$

$$\frac{dL}{dt} = \rho_6 \frac{E}{\rho_7 + E} L - LVH(V-1), \tag{2.3.10}$$

$$\frac{dR}{dt} = \rho_8 \frac{E}{\rho_9 + E} R - RVH(V-1), \tag{2.3.11}$$

where $V = E + L + R$, and the dimensionless parameters are given by:

$$\begin{aligned} &\rho_1 = \tfrac{a_1}{kF_h}, \quad \rho_2 = \tfrac{a_2}{kF_h V^*}, \quad \rho_3 = R_{EL}, \quad \rho_4 = \tfrac{d_F}{kV^*}, \quad \rho_5 = \tfrac{k_E}{kV^*}, \\ &\rho_6 = \tfrac{k_L}{kV^*}, \quad \rho_7 = \tfrac{E_{h_1}}{V^*}, \quad \rho_8 = \tfrac{k_R}{kV^*}, \text{ and } \rho_9 = \tfrac{E_{h_2}}{V^*}. \end{aligned} \tag{2.3.12}$$

The dimensionless parameter values used to generate the numerical simulations in section 2.3.5 were obtained by using equation (2.3.12) and the dimensional values from Table 2.1:

$$\begin{aligned} &\rho_1 = 23, \quad \rho_2 = 0.1, \quad \rho_3 = 0.19, \quad \rho_4 = 3, \quad \rho_5 = 1, \\ &\rho_6 = 1, \quad \rho_7 = 0.13, \quad \rho_8 = 1, \quad \rho_9 = 0.13. \end{aligned} \tag{2.3.13}$$

2.3.4 Initial conditions

As mentioned in section 2.3.2, in the mid-cycle CL, LCs comprise approximately 68% of the bovine CL volume, the ECs approximately 13%, and the other cell types account for the remaining 19% of the total volume [263].

In vivo, it can be difficult accurately to define the boundary of the CL immediately post ovulation as the CL can have a similar ultrasonographic appearance to the rest of the ovarian stroma. However, within 24 hrs the boundaries of the CL can be accurately determined and based on this we have estimated the diameter of the CL to be 8 mm on day 1, resulting in $V(t=1) \simeq \frac{4}{3}\pi R^3 = 0.27$ cm^3. We close equations (2.3.8)-(2.3.11) by imposing the following initial conditions:

$$F(0) = 4.0, \quad E(0) = 0.04, \quad L(0) = 0.18, \quad R(0) = 0.05, \tag{2.3.14}$$

with $F(0)$ estimated from Fig 2.1(a) and the value of F_h (as stated in Table 2.1) since $F(t)$=$F_h\hat{F}(\hat{t})$.

2.3.5 Typical numerical results

The Heaviside step function that appears in equations (2.3.9)-(2.3.11) introduces a discontinuity into the right-hand sides of equations (2.3.9)-(2.3.11) at $V = 1$ (the *'discontinuity boundary'* [20]), making the system *piecewise-smooth* (PWS) [20, 58].

There is a wide variety of numerical methods for solving ODEs and many of them are routinely used in established software (e.g. MATLAB), where most of these algorithms require that the ODEs are smooth. However, in PWS systems constrained motion along a discontinuity boundary is possible and requires special treatment numerically. Furthermore, from a dynamical systems of view what characterises PWS systems is that they can not only undergo standard bifurcations (e.g. Hopf bifurcations) but also *non-smooth transitions*. We solve the system given in equations (2.3.8)-(2.3.11) using Piiroinen's method [185], where the time and location of any non-smooth events are resolved as accurately as possible.

In Figure 2.3 we plot the evolution of F, E, L, R and V for a typical simulation. These results are in good qualitative agreement with the *in vivo* data presented in Figure 2.1.

In equations (2.3.9)-(2.3.11) the loss terms switch on when V increases above the threshold $V = 1$. This transition occurs at time t^* (Figure 2.3) where, in biological terms, t^* delineates the shift from the early-mid to the mid-late CL developmental stage. For $t < t^*$ and $V < 1$ the cells do not experience any growth constraints (Figure 2.3(b)). In contrast, for $t > t^*$ CL volume remains constant ($V = 1$) and the volumes of the cells evolve subject to this constraint (Figure 2.3(b)).

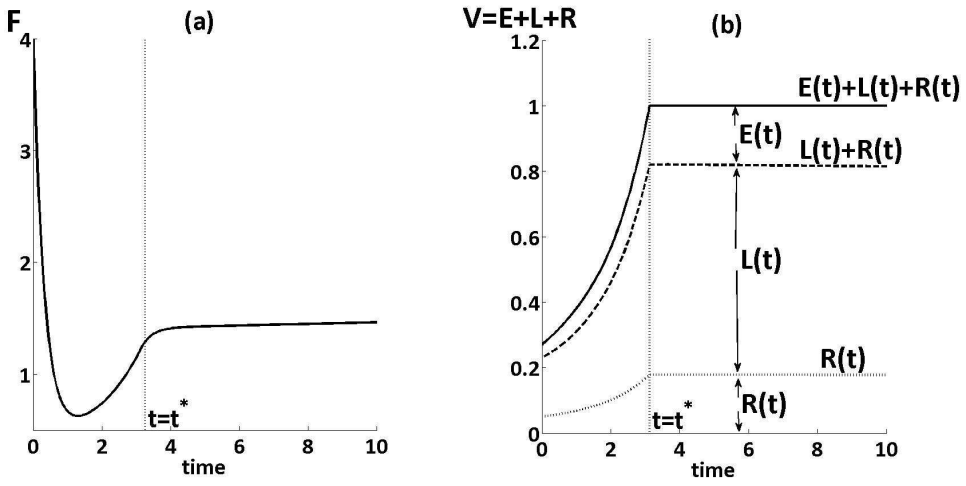

Figure 2.3: Profiles of (a) the FGF2 concentration, $F(t)$, and (b) the CL volume, $V(t) = E(t) + L(t) + R(t)$. The numerical results were obtained by solving equations (2.3.8)-(2.3.11) subject to the initial conditions (2.3.14) and the parameter values in equation (2.3.13). Note that $\rho_5 = 1$.

In Chapter 1 and also at the beginning of this Chapter we referred to the importance of angiogenesis in the CL growth and, therefore, we proceed to check the evolution of the CL under different angiogenic situations. In particular, we vary ρ_5, the maxi-

mal EC proliferation rate. Figures 2.4(a)-(b) show the evolution of E, L, R and V (as in Figure 2.3(b)) in low and high $\rho_5 = 2$, respectively. In Figure 2.4(a) (low ρ_5 - weak angiogenesis) the system evolves to an avascular steady state with $E = 0$ and, therefore, $V \simeq L + R = 1$. In Figure 2.4(b) (high ρ_5 - strong angiogenesis) both L and R diminish and $V \simeq E > 1$. Both steady states (with low or high ρ_5) are regarded as 'pathological' since at least one of the three cell types diminish and, thereby, compromise CL growth and subsequently a healthy embryo development. However, the steady state in Figure 2.3 (with intermediate value of ρ_5) is regarded as a 'healthy' situation since all of the cell types exist.

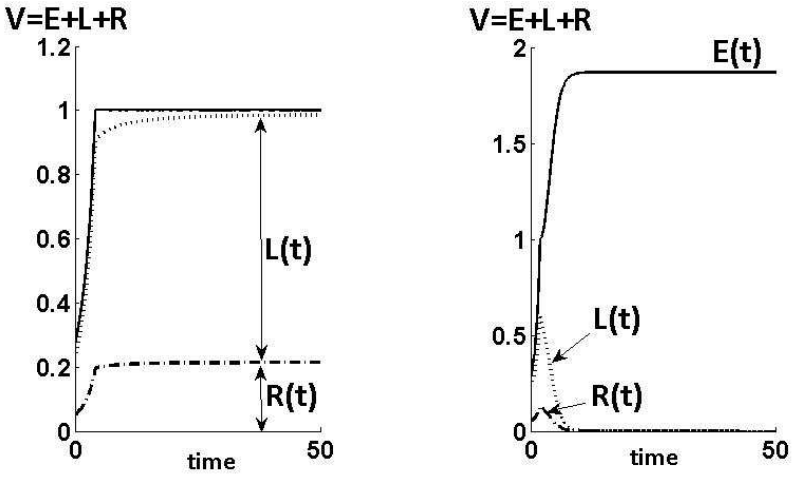

(a) $\rho_5 = 0.5; E = 0, V = 1$ (b) $\rho_5 = 2; L = R = 0, V > 1$

Figure 2.4: Profiles of the CL volume, $V(t) = E(t) + L(t) + R(t)$, with (a) low and (b) high ρ_5 (the maximal EC proliferation rate) or equivalently in low and high angiogenic environment. In (a) the system evolves to an avascular steady state ($E = 0$) with $V = 1$, whereas in (b) $L = R = 0$ and $V > 1$. The absence of any of the cell types (E, L, R) within the CL tissue may compromise a healthy embryo development and, therefore, both cases are regarded as 'pathological'.

2.3.6 A simplified model

Equations (2.3.8)-(2.3.11) define a fourth order system of ODEs, whose trajectories are difficult to visualise in phase space. Before proceeding to an analysis of the full model, we consider the case for which $L \equiv R \equiv 0$, and, $V \approx E$ so that equations (2.3.8)-(2.3.11)

reduce to the following pair of ODEs:

$$\left.\begin{aligned} FGF2: \quad & \frac{dF}{dt} = \rho_1 E - \rho_4 F, \\ CL\ volume: \quad & \frac{dE}{dt} = \rho_5 \frac{F}{1+F} E - E^2 H(E-1). \end{aligned}\right\} \tag{2.3.15}$$

The behaviour of equations (2.3.15) depends on whether $E < 1$ or $E > 1$, giving two forms of behaviour separated by the boundary $E = 1$ as explained below.

2.3.6.1 Phase plane analysis and steady states

Simple insight into the dynamics of this model can be obtained by inspecting certain nullclines. Figure 2.5 shows that the nullcline $\frac{dF}{dt} = 0$ is a line N_1 on which $E = \frac{\rho_4}{\rho_1} F$. The second nullcline $\frac{dE}{dt} = 0$ is a curve N_2 on which $E = \rho_5 \frac{F}{1+F}$ (when $E > 1$), and it consists of the coordinate axes $F = 0$ and $E = 0$ (when $E < 1$).

Interestingly, the *discontinuity boundary* $E = 1$ is shown to be attractive (see arrows in Figure 2.5) from both sides ($E < 1$ or $E > 1$). That is, the trajectories evolve onto $E = 1$, a behaviour called *sliding* [20]. We define sliding more fully in section 2.3.7.

Equations (2.3.15) admit two steady states (where $\frac{dE}{dt} = \frac{dF}{dt} = 0$): we denote by B_0 the trivial solution $(F, E) = (0, 0)$ and by B_1 the nontrivial solution $(F, E) = (\Gamma, \frac{\rho_4}{\rho_1}\Gamma)$, where $\Gamma = \frac{\rho_1 \rho_5}{\rho_4} - 1$. The state B_1 exists when $E > 1$, or equivalently

$$\rho_5 > \rho_5^* := \frac{\rho_4}{\rho_1} + 1. \tag{2.3.16}$$

Figures 2.5(a)-(b) show that when $\rho_5 \ll \rho_5^*$ or $\rho_5 < \rho_5^*$ sliding states are attracted towards a point B_{1s} at which $(F, E) = (\frac{\rho_1}{\rho_4}, 1)$, where the competing flows from $E > 1$ and $E < 1$ are equal and opposite. This point is called a *pseudo*-steady state (or *pseudo*-equilibrium [20]). As ρ_5 increases through $\rho_5 = \rho_5^*$, the steady B_{1s} approaches the point where N_1 crosses $E = 1$ at $(\frac{1}{\rho_5 - 1}, 1)$, then B_{1s} vanishes, and B_1 appears at the same point and detaches from $E = 1$ into the region $E > 1$ (Figure 2.5(c)).

2.3.6.2 Conclusions from the simplified model

In summary, for $\rho_5 > \rho_5^*$ equations (2.3.15) evolve to a steady state B_1 for which $E > 1$ (Figure 2.5(c)), while for $\rho_5 < \rho_5^*$ the system evolves to a *pseudo*-steady state which is not a zero of (2.3.15), but lies on the discontinuity boundary $E = 1$ (Figures 2.5(a)-(b)).

Biologically, high ρ_5 (high EC proliferation) implies a large CL, bigger than the wound space formed after ovulation. Smaller EC proliferation implies a minimum size of the

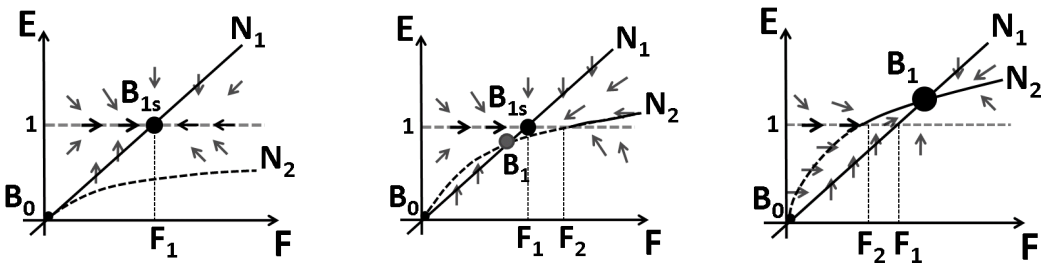

(a) $\rho_5 \ll \rho_5^*$ (b) $\rho_5 < \rho_5^*$ (c) $\rho_5 > \rho_5^*$

Figure 2.5: Phase plane schematic diagrams for the simplified model (2.3.15) for different values of ρ_5, where ρ_5^* as in equation (2.3.16). The *sliding* behaviour occurs along the discontinuity boundary $E = 1$ towards the *pseudo*-steady state, B_{1s}. Key: N_1 and N_2 are the nullclines (solid or dashed curve if they exist or not), where $E = \frac{\rho_4}{\rho_1} F$ and $E = \rho_5 \frac{F}{1+F}$, respectively. The points F_1 and F_2 lie at the intersections of N_1 and N_2 and the discontinuity boundary, $E = 1$.

CL ($V = V^*$). Similar behaviour is expected in the full model, except that the composition of the CL is unclear. In the next section we investigate the existence of steady states of the full model in more detail.

2.3.7 The full model as a Filippov system

We now express equations (2.3.8)-(2.3.11) in the form that is typically used for PWS (or Filippov) systems, namely

$$\frac{d\mathbf{x}}{dt} = \begin{cases} \mathbf{f}^+(\mathbf{x}), & \Theta(\mathbf{x}) > 0, \\ \mathbf{f}^-(\mathbf{x}), & \Theta(\mathbf{x}) < 0, \end{cases} \tag{2.3.17}$$

by letting $\mathbf{x} = (F, E, L, R) \in \mathbb{R}^4$ and defining

$$\mathbf{f}^+ := \mathbf{f}^- - (E + L + R) \cdot \begin{pmatrix} 0 \\ E \\ L \\ R \end{pmatrix}, \tag{2.3.18}$$

and

$$\mathbf{f}^- := \begin{pmatrix} \rho_1 E + \rho_2 \frac{L^2}{\rho_3 L + E} - \rho_4 F \\ \rho_5 \frac{F}{1+F} E \\ \rho_6 \frac{E}{\rho_7 + E} L \\ \rho_8 \frac{E}{\rho_9 + E} R \end{pmatrix}, \tag{2.3.19}$$

with $\Theta(\mathbf{x}) = E + L + R - 1 = V - 1$. The region of state space, $D \subset \mathbb{R}^4$, in which equations (2.3.17)-(2.3.19) govern the system dynamics, can be partitioned into two subregions, G^+ and G^- (see Figure 2.6), where

$$G^+ = \{\mathbf{x} \in \mathbb{R}^4,\ \Theta(\mathbf{x}) > 0\} \quad \text{and} \quad G^- = \{\mathbf{x} \in \mathbb{R}^4,\ \Theta(\mathbf{x}) < 0\}. \tag{2.3.20}$$

The discontinuity boundary is a smooth hypersurface, Σ, given by:

$$\Sigma = \{\mathbf{x} \in \mathbb{R}^4,\ \Theta(\mathbf{x}) = 0\}. \tag{2.3.21}$$

Σ separates trajectories for which the CL growth is constrained (G^+) from regions in which the cells that constitute the CL grow without restriction (G^-). Thus the model is a nonlinear system with an 'on-off' feedback controller specified by the CL volume (V).

Let the subscript x denote differentiation with respect to $\mathbf{x} = (F, E, L, R)$, so that $\Theta_{\mathbf{x}}(\mathbf{x}) = (0, 1, 1, 1)$ is the normal vector to Σ, and let $\langle ., . \rangle$ denote the scalar product. Then consider the quantity

$$\langle \Theta_{\mathbf{x}}(\mathbf{x}), \mathbf{f}^-(\mathbf{x}) \rangle = E\Omega, \tag{2.3.22}$$

where

$$\Omega := \frac{\rho_5 F}{1+F} + \frac{\rho_6 L}{\rho_7 + E} + \frac{\rho_8 R}{\rho_9 + E}. \tag{2.3.23}$$

The scalar product is strictly non-negative since F, E, L, R are positive or zero (in a biologically realistic situation) and $\rho_i > 0$ for all i. This means that $\mathbf{f}^-$ always points towards $\Theta = 0$, so the discontinuity boundary $V = 1$ is attractive with respect to G^- ('attractive from below', as was the case for the 2D model in section 2.3.6).

Depending on whether $\mathbf{f}^+$ points towards or away from the discontinuity boundary, two kinds of motion are now possible when $\Theta = 0$. These are known as *crossing* or *sliding*, and occur when the quantity

$$\langle \Theta_{\mathbf{x}}(\mathbf{x}), \mathbf{f}^+(\mathbf{x}) \rangle = E\Omega - 1 \tag{2.3.24}$$

is positive or negative respectively, as we now describe. If $\langle \Theta_{\mathbf{x}}(\mathbf{x}), \mathbf{f}^+(\mathbf{x}) \rangle > 0$, then the vector field $\mathbf{f}^+$ points away from Σ, implying that trajectories evolve from G^- to

G^+ by crossing Σ. Otherwise, $\mathbf{f}^+$ points towards Σ, so that the discontinuity boundary attracts trajectories from both G^+ and G^-, and solutions must slide along Σ. When sliding occurs, the CL volume remains fixed at the threshold value, $V^* = 1$. We denote the *sliding region* by $\hat{\Sigma}$ (see Figure 2.6), where

$$\hat{\Sigma} = \Big\{ \mathbf{x} \in \Sigma, \;\; 0 \leq E\Omega \leq 1 \Big\}. \tag{2.3.25}$$

Its boundaries are given by

$$\partial\Sigma^+ := \Big\{ \mathbf{x} \in \Sigma : E\Omega = 1 \Big\} \quad \text{and} \quad \partial\Sigma^- := \Big\{ \mathbf{x} \in \Sigma : E\Omega = 0 \Big\}. \tag{2.3.26}$$

On these surfaces the flow is tangent to the discontinuity boundary: at $\partial\Sigma^+$ the condition $E\Omega = 1$ means $\mathbf{f}^+(\mathbf{x})$ is tangent to Σ, while at $\partial\Sigma^-$ the condition $E\Omega = 0$ means $\mathbf{f}^-(\mathbf{x})$ is tangent to Σ.

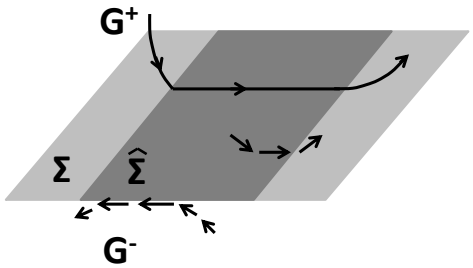

Figure 2.6: The phase space topology of a system with discontinuous vector fields (Filippov system). The discontinuity boundary, Σ, separates the phase space into two regions (G^+, G^-), and each region is governed by a different smooth vector field ($\mathbf{f}^+(\mathbf{x}), \mathbf{f}^-(\mathbf{x})$). Solutions of equations (2.3.17)-(2.3.19) attracted to the sliding region (dark grey) $\hat{\Sigma}$ follow a constrained motion on Σ.

2.3.7.1 Regular and sliding solutions

Using the above decomposition, we construct solutions of system (2.3.17) by considering separately *regular* solutions in $G^\pm$ and *sliding* solutions on Σ. Following Filippov [124], we introduce $\mathbf{g}(\mathbf{x})$, a convex combination of the two vectors $\mathbf{f}^\pm(\mathbf{x})$,

$$\mathbf{g}(\mathbf{x}) = \lambda(\mathbf{x})\mathbf{f}^+(\mathbf{x}) + (1 - \lambda(\mathbf{x}))\mathbf{f}^-(\mathbf{x}), \quad 0 \leq \lambda \leq 1, \tag{2.3.27}$$

for each nonsingular point in the sliding region, e.g. $\mathbf{x} \in \hat{\Sigma}$ such that $\langle \Theta_{\mathbf{x}}(\mathbf{x}), \mathbf{f}^-(\mathbf{x}) - \mathbf{f}^+(\mathbf{x}) \rangle \neq 0$. The function λ is defined as

$$\lambda(\mathbf{x}) = \frac{\langle \Theta_{\mathbf{x}}(\mathbf{x}), \mathbf{f}^-(\mathbf{x}) \rangle}{\langle \Theta_{\mathbf{x}}(\mathbf{x}), \mathbf{f}^-(\mathbf{x}) - \mathbf{f}^+(\mathbf{x}) \rangle} = E\Omega, \tag{2.3.28}$$

so that $\mathbf{g}(\mathbf{x})$ is everywhere tangent to $\hat{\Sigma}$. We then add the equation

$$\dot{\mathbf{x}} = \mathbf{g}(\mathbf{x}), \quad \mathbf{x} \in \hat{\Sigma}, \tag{2.3.29}$$

to the system (2.3.17), thus extending its definition to include the sliding region. Solutions of (2.3.29) are called *sliding* solutions, and $\mathbf{g}(\mathbf{x})$ is called the *sliding* vector field [20]. For (2.3.29) we have:

$$\mathbf{g}(\mathbf{x}) = \begin{pmatrix} \rho_1 E + \rho_2 \frac{L^2}{\rho_3 L + E} - \rho_4 F \\ \rho_5 \frac{F}{1+F} E - E^2 \Omega \\ \rho_6 \frac{E}{\rho_7 + E} L - EL\Omega \\ \rho_8 \frac{E}{\rho_9 + E} R - ER\Omega \end{pmatrix}. \tag{2.3.30}$$

Solutions are then defined in the following way:

Definition 5.1. A *regular orbit* is a smooth trajectory of the system (2.3.17), which does not cross the discontinuity boundary (Σ). A *sliding orbit* is a smooth trajectory of (2.3.29), that lies on the discontinuity boundary. An *orbit* will generally refer to a continuous curve $x(t)$ that is a concatenation of regular and sliding orbits.

The *crossing set* $\mathbf{x} \in \Sigma \backslash \hat{\Sigma}$ is defined as the set of all points $\mathbf{x} \in \Sigma$ for which the two vectors, $\mathbf{f}^{\pm}(\mathbf{x})$, have nontrivial transverse components to Σ. At these points a regular orbit of (2.3.17) reaching $\mathbf{x}$ from G^- concatenates with a regular orbit entering G^+ from $\mathbf{x}$. At points in the sliding set, $\mathbf{x} \in \hat{\Sigma}$, a regular orbit of (2.3.17) reaching $\mathbf{x}$ from each of G^+ and G^- concatenates with a sliding orbit inside $\hat{\Sigma}$ passing through $\mathbf{x}$. All other points on Σ belong to the sliding boundaries $\partial\Sigma^{\pm}$, and can be treated as either sliding or crossing points without ambiguity.

2.3.7.2 Different types of steady states

The different types of steady states that Filippov systems exhibit are summarised by the following definitions.

Definition 5.2. A point $\mathbf{x} \in D$ is termed an *admissible* steady state of (2.3.17) if

$$\mathbf{f}^+(\mathbf{x}) = 0 \ \text{ and } \ \Theta(\mathbf{x}) > 0, \ \text{ or } \ \mathbf{f}^-(\mathbf{x}) = 0 \ \text{ and } \ \Theta(\mathbf{x}) < 0. \tag{2.3.31}$$

Alternatively, a point $\mathbf{x} \in G^{\pm}$ is termed a *virtual* steady state of (2.3.17) if

$$\mathbf{f}^+(\mathbf{x}) = 0 \ \text{ but } \ \Theta(\mathbf{x}) < 0, \ \text{ or } \ \mathbf{f}^-(\mathbf{x}) = 0 \ \text{ but } \ \Theta(\mathbf{x}) > 0. \tag{2.3.32}$$

An admissible steady state $\mathbf{x} \in G^{\pm}$ is a steady state of the system (2.3.17), while a virtual steady state is a mathematical solution to the equations $\mathbf{f}^{\pm} = 0$ that is not a solution of (2.3.17), for example, a point $\mathbf{x} \in G^{-}$ where $\mathbf{f}^{+}(\mathbf{x}) = 0$.

Definition 5.3. A point $\mathbf{x} \in D$ is termed a *pseudo* steady state if

$$\mathbf{g}(\mathbf{x}) = 0 \ \text{ and } \ \Theta(\mathbf{x}) = 0. \tag{2.3.33}$$

As for Definition 5.2, there may exist solutions to $\mathbf{g}(\mathbf{x}) = 0$ which are invalid because $x \in \Sigma \backslash \hat{\Sigma}$. We distinguish such solutions as follows:

Definition 5.4. A *pseudo* steady state is termed *admissible* if $0< \lambda <1$ and *virtual* if $\lambda < 0$ or $\lambda > 1$, with λ as defined in (2.3.28).

For some parameter values, a steady state may lie on the discontinuity boundary. Since $\mathbf{f}^{+}$ or $\mathbf{f}^{-}$ vanishes there, we find that $\mathbf{g}$ also vanishes by (2.3.29), so that a steady state on Σ *always* coincides with a pseudo steady state. Furthermore this occurs on the sliding boundary where $\lambda = 0$ or 1. We define this as follows.

Definition 5.5. A point $\mathbf{x} \in D$ is termed a *boundary* steady state of (2.3.17) if

$$\mathbf{f}^{+}(\mathbf{x}) = 0 \ \text{ and } \ \Theta(\mathbf{x}) = 0, \quad \text{or} \quad \mathbf{f}^{-}(\mathbf{x}) = 0 \ \text{ and } \ \Theta(\mathbf{x}) = 0. \tag{2.3.34}$$

2.4 Analytical results

In this section, our aim is to present the steady states in vector fields $\mathbf{f}^{\pm}(\mathbf{x})$, which will be indicated by a superscript $\pm$, and those in the sliding vector field $\mathbf{g}(\mathbf{x})$ by a superscript s.

The steady states in the regions G^{+} and G^{-}, and in the sliding region $\hat{\Sigma}$, satisfy the following relations:

region	steady state expression	admissibility condition	
G^{+} :	$\mathbf{f}^{+}(\mathbf{x}) = \mathbf{0}$	$V \geq 1$	(2.4.1)
G^{-} :	$\mathbf{f}^{-}(\mathbf{x}) = \mathbf{0}$	$V \leq 1$	(2.4.2)
$\hat{\Sigma}$:	$\mathbf{g}(\mathbf{x}) = \mathbf{0}$	$0 \leq E\Omega \leq 1$	(2.4.3)

In addition to the admissibility condition (see Definitions 5.2 and 5.4 in section 2.3.7.2), each model variable F, E, L, R, must be positive for the steady state to be physically

realistic. Recall that $V = E + L + R$, that Ω is given by (2.3.23), and that the vector fields $\mathbf{f}^+$, $\mathbf{f}^-$ and $\mathbf{g}$ are given by (2.3.18), (2.3.19) and (2.3.30), respectively.

In the following, we list all steady states that satisfy these conditions and in section 2.5 we translate criteria for solutions to be admissible and physically realistic into constraints on the parameters ρ_i ($i = 1, ..., 9$).

2.4.1 Steady states in G^+

There are four steady states $A_i^+ = (F, E, L, R)$, $i = 1, ..., 4$ in G^+,

$$A_1^+ := E_1\,(\phi(E_1), 1, \psi(E_1), \nu(E_1) - \psi(E_1) - 1)\,, \tag{2.4.4}$$

$$A_2^+ := E_2\,(\rho_1/\rho_4, 1, 0, \eta(E_2) - 1)\,, \tag{2.4.5}$$

$$A_3^+ := E_3\,(\phi(E_3), 1, \nu(E_3) - 1, 0)\,, \tag{2.4.6}$$

$$A_4^+ := E_4\,(\rho_1/\rho_4, 1, 0, 0)\,, \tag{2.4.7}$$

$$\nu(E) := \frac{\rho_6}{\rho_7 + E},\ \ \eta(E) := \frac{\rho_8}{\rho_9 + E},\ \ \phi(E) := \frac{\rho_6}{\rho_5\rho_7 + (\rho_5 - \rho_6)E}, \tag{2.4.8}$$

$$\psi(E) := \frac{\rho_3\omega(E) + \sqrt{(\rho_3\omega(E))^2 + 4\rho_2\omega(E)}}{2\rho_2}, \tag{2.4.9}$$

$$\omega(E) := \rho_4\phi(E) - \rho_1, \tag{2.4.10}$$

$$E_1 := \frac{\rho_6\rho_9 - \rho_7\rho_8}{\rho_8 - \rho_6}, \quad E_2 = \frac{\rho_4\rho_8 - \rho_1\rho_5\rho_9}{\rho_1(\rho_5 - \rho_8)}, \quad E_4 = \rho_5 - \frac{\rho_4}{\rho_1}. \tag{2.4.11}$$

and E_3 solves the following cubic polynomial

$$\rho_2(\nu(E_3) - 1)^2 - \rho_3\omega(E_3)(\nu(E_3) - 1) - \omega(E_3) = 0. \tag{2.4.12}$$

For a physically realistic and admissible solution, we require all components of A_n^+, ($n = 1, 2, 3$ or 4) to be positive and the corresponding volume to be such that $V = E + L + R > 1$. These lead to conditions on the parameters ρ_i given in section 2.5 (see equations (2.5.1)-(2.5.10)).

Note also that all of the steady states in the vector field $\mathbf{f}^+(\mathbf{x})$ are vascular, that is, they have $E > 0$. If $\mathbf{f}^+(\mathbf{x}) = \mathbf{0}$ and $E = 0$ then the only possible steady state has $\mathbf{x} = \mathbf{0}$, and $V = 0$. This is not an admissible steady state in G^+, since $V > 1$ is required for an admissible solution.

2.4.2 Steady states in $\hat{\Sigma}$

For each steady state solution (2.4.4)-(2.4.7) in G^+, there is a similar steady state $A_i^s = (F, E, L, R)$, $i = 1, ..., 4$ in $\hat{\Sigma}$,

$$A_1^s := E_1 \left(\phi(E_1), 1, \psi(E_1), \frac{1}{E_1} - \psi(E_1) - 1 \right), \tag{2.4.13}$$

$$A_2^s := E_2 \left(\frac{\rho_1}{\rho_4}, 1, 0, \frac{1}{E_2} - 1 \right), \tag{2.4.14}$$

$$A_3^s := E_3^s \left(\phi(E_3^s), 1, \frac{1}{E_3^s} - 1, 0 \right), \tag{2.4.15}$$

$$A_4^s := \left(\frac{\rho_1}{\rho_4}, 1, 0, 0 \right). \tag{2.4.16}$$

The functions ϕ and ψ are given by (2.4.8) and (2.4.9), and the constants E_1, E_2 by (2.4.11), while E_3^s solves the following cubic polynomial

$$\rho_2 (E_3^s - 1)^2 - \rho_3 E_3^s \omega(E_3^s)(1 - E_3^s) - E_3^s \omega(E_3^s) = 0. \tag{2.4.17}$$

The admissibility conditions associated with the steady states in G^+ and $\hat{\Sigma}$ are presented in section 2.5 (see equations (2.5.11)-(2.5.16)).

2.4.3 Steady states in G^-

Any state of the form

$$A^- = \left(\frac{\rho_2}{\rho_3 \rho_4} u, 0, u, v \right), \tag{2.4.18}$$

satisfies the steady state expression (2.4.2), and is physical and admissible over the range $0 \leq v \leq 1 - u$ and $0 \leq u < 1 - v$. By varying u and v over these ranges, A^- forms a set of steady states lying in a planar surface Π^-, given by

$$\Pi^- = \left\{ (F, E, L, R) \in G^- : \; F = \frac{\rho_2}{\rho_3 \rho_4} L, \; E = 0 \right\}. \tag{2.4.19}$$

In section 2.4.4.1, a stability analysis of the plane Π^- reveals that it is not a global attractor.

2.4.4 The 5th steady state in $\hat{\Sigma}$

Where the plane Π^- intersects the discontinuity boundary $V = 1$ (see Figure 2.7), it forms a family of steady states of the sliding vector field that does not coincide with any of the steady states A_n^s above. Thus any state of the form

$$A_5^s = \left(\frac{\rho_2}{\rho_3 \rho_4} u, 0, u, 1 - u \right), \tag{2.4.20}$$

satisfies the steady state expression (2.4.3), and is physical and admissible provided that $0 \leq u \leq 1$. Note that $E = 0$ implies $E\Omega = 0$, therefore from (2.3.26) we have $A_5^s \in \partial\Sigma^-$. Thus the states A_5^s do not lie on the discontinuity boundary (Σ), but on its boundary $\partial\Sigma^-$. Since u is a variable, the set of states A_5^s belongs to a line given by

$$\Pi^s = \left\{ (F, E, L, R) \in \partial\Sigma^- : \; F = \frac{\rho_2}{\rho_3\rho_4} L, \; E = 0, \; V = 1 \right\}, \tag{2.4.21}$$

as shown in Figure 2.7. We remark that there are two limiting cases of equation (2.4.20) which we denote by $A_{5a}^s = (0, 0, 0, 1)$ and $A_{5b}^s = (\frac{\rho_2}{\rho_3\rho_4}, 0, 1, 0)$, respectively.

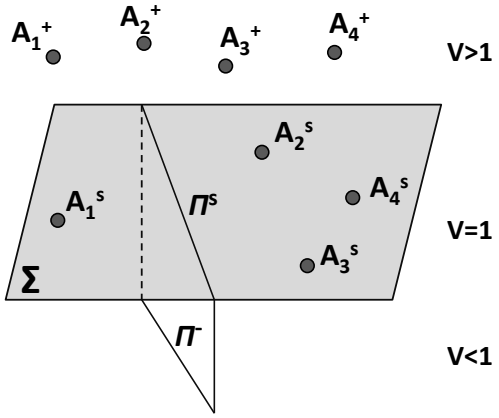

Figure 2.7: Schematic illustration showing the three-dimensional projections of four-dimensional (F, E, L, R) phase portraits. Steady states are presented for the two different regions of phase space ($V > 1$ and $V < 1$) and the discontinuity boundary, $\Sigma : V = 1$. The steady state A_5^s defines a 1-D manifold (Π^s) in the discontinuity boundary. Key: $V = E + L + R$ is the CL volume.

2.4.4.1 Stability of the plane Π^-

The stability of the plane Π^- (as defined in (2.4.19) is of some importance being a distributed object in the regions G^- and $\hat{\Sigma}$. It is also rather more simple to express, requiring the calculation of stability in only two directions orthogonal to each other and to the plane.

To determine whether Π^- is an attractor we first take coordinates $u_1 = E$, $u_2 = F - \rho^* L$, $u_3 = \rho^* F + L$, $u_4 = R$, where $\rho^* = \frac{\rho_2}{\rho_3\rho_4}$. The u_i form an orthogonal coordinate system, since $\nabla u_i \cdot \nabla u_j = 0$ for all $i \neq j \in (1, 2, 3, 4)$ with $\nabla = \left(\frac{d}{dF}, \frac{d}{dE}, \frac{d}{dL}, \frac{d}{dR} \right)$. The u_1 and u_2 coordinate axes lie perpendicular to Π^- (so Π^- is the plane $u_1 = u_2 = 0$), while u_3 and u_4 form a coordinate system over the plane Π^-.

The Jacobian of the u_1, u_2 system at $u_1 = u_2 = 0$ expresses the derivative of the flow through Π^-. Using $\dot{u}_1 = \dot{E}$ and $\dot{u}_2 = \dot{F} - \rho^* \dot{L}$, this is given by

$$J_{\Pi^-} = \begin{pmatrix} \frac{\partial \dot{u}_1}{\partial u_1} & \frac{\partial \dot{u}_1}{\partial u_2} \\ \frac{\partial \dot{u}_2}{\partial u_1} & \frac{\partial \dot{u}_2}{\partial u_2} \end{pmatrix}_{|u_1=u_2=0} = \begin{pmatrix} \frac{\rho_5 u_3 \rho^*}{u_3\rho^*+1+\rho^{*2}} & 0 \\ \rho_1 - \rho^* \frac{\rho_4}{\rho_3} - \frac{\rho_6 \rho^* u_3}{\rho_7 1+\rho^{*2}} & -\rho_4 \end{pmatrix},$$

with eigenvalues $\mu_1 = -\rho_4$ and $\mu_2 = \frac{\rho_5 u_3 \rho^*}{u_3\rho^*+1+\rho^{*2}}$. Note that $\mu_1 < 0$ since $\rho^* > 0$. Also $u_3 = \rho^* F + L > 0$ given that $F, L > 0$, and therefore $\mu_2 > 0$.

As a result, the plane Π^- is of '*saddle type*', having one stable and one unstable direction. Π^- is therefore not a global attractor.

2.5 Admissibility conditions for the steady states

The admissibility conditions for the steady states in G^+ and $\hat{\Sigma}$ as defined in section 2.4 are given below.

2.5.1 Conditions for the steady states in G^+

2.5.1.1 Conditions for A_1^+

From equation (2.4.11) we deduce that $E_1 \geq 0$ if either

$$\frac{\rho_9}{\rho_7} \leq \frac{\rho_8}{\rho_6} \leq 1 \qquad \text{or} \qquad 1 \leq \frac{\rho_8}{\rho_6} \leq \frac{\rho_9}{\rho_7}, \tag{2.5.1}$$

where, $\frac{\rho_8}{\rho_6}$ is the ratio of maximal growth rate of the stromal over luteal cells, and $\frac{\rho_9}{\rho_7}$ is the ratio of half-maximal EC value of the stromal over luteal cells. Similarly, the concentration of FGF2, $F = E_1\phi(E_1)$, is physically realistic if $\phi(E_1) \geq 0$. That is,

$$\begin{aligned} \phi(E_1) \geq 0 \quad &\Leftrightarrow \quad \rho_5\rho_7 + E_1(\rho_5 - \rho_6) \geq 0 \\ &\Leftrightarrow \quad \frac{\rho_5}{\rho_6} \geq \frac{E_1}{\rho_7 + E_1} \\ &\Leftrightarrow \quad \rho_5 \geq \rho_6 \frac{\frac{\rho_9}{\rho_7} - \frac{\rho_8}{\rho_6}}{\frac{\rho_9}{\rho_7} - 1}, \end{aligned} \tag{2.5.2}$$

which places a lower bound on ρ_5. The value of L is physically realistic if $\psi(E_1) \geq 0$ ($\Leftrightarrow \omega(E_1) \geq 0$), which implies

$$\rho_5 \leq \frac{\rho_6(\rho_4 + \rho_1 E_1)}{\rho_1(\rho_7 + E_1)}, \tag{2.5.3}$$

an upper bound to ρ_5 (since $E_1 \geq 0$).

The value of R is physically realistic if $\nu(E_1) - \psi(E_1) - 1 \geq 0$. Substituting in the expression for ψ (as in equation (2.4.9)) in terms of ω, implies

$$\rho_2 \left(\nu(E_1) - 1\right)^2 - \rho_3\omega(E_1)\left(\nu(E_1) - 1\right) \geq \omega(E_1) \geq 0. \tag{2.5.4}$$

The admissibility condition for A_1^+ is simply that the volume $V = V_1^+$ satisfies

$$V_1^+ = E_1\nu(E_1) = \frac{\rho_6\rho_9 - \rho_7\rho_8}{\rho_9 - \rho_7} \geq 1. \tag{2.5.5}$$

2.5.1.2 Conditions for A_2^+

The components of A_2^+ are non-negative if

$$E_2 = \frac{\rho_4\rho_8 - \rho_1\rho_5\rho_9}{\rho_1(\rho_5 - \rho_8)} \geq 0, \quad \text{and} \quad \eta(E_2) - 1 = \frac{\rho_8}{\rho_6}\frac{1}{\rho_9 + E_2} - 1 \geq 0. \tag{2.5.6}$$

In particular, $E_2 \geq 0$ in two cases:

$$\text{(i)}\ 1 \leq \frac{\rho_5}{\rho_8} \leq \frac{\rho_4}{\rho_1\rho_9},\ \text{or (ii)}\ \frac{\rho_4}{\rho_1\rho_9} \leq \frac{\rho_5}{\rho_8} \leq 1,$$

and $\eta(E_2) - 1 \geq 0$, iff

$$\rho_5 \geq \frac{1}{\rho_1}(\rho_4 - \rho_1\rho_9) + \rho_8.$$

The admissibility condition for A_2^+ is that the volume $V = V_2^+$ satisfies

$$V_2^+ = E_2\eta(E_2) = \frac{\rho_4\rho_8 - \rho_1\rho_9\rho_5}{\rho_4 - \rho_1\rho_9} \geq 1, \tag{2.5.7}$$

noting that $V_2^+ \geq 0$ is guaranteed by both cases (i) and (ii) above.

2.5.1.3 Conditions for A_3^+

The steady state A_3^+ is physically realistic if E_3, $\phi(E_3)$, and $(\nu(E_3) - 1)$ are positive. The solution for E_3 as a root of the cubic polynomial (2.4.12) is unilluminating so we do not present it here. We note, however, that (2.4.12) has real coefficients, hence it always has at least one real root (since complex roots appear in pairs), but the root may not be positive for all values of the parameters.

The admissibility condition can be written as

$$V_3^+ = E_3\nu(E_3) = \frac{\rho_6 E_3}{\rho_7 + E_3} \geq 1. \tag{2.5.8}$$

2.5.1.4 Conditions for A_4^+

The steady state solution A_4^+ is physically realistic if $E_4 \geq 0$, implying $\frac{\rho_5}{\rho_6} - \frac{\rho_4}{\rho_1} \geq 0$ or, as a condition on ρ_5,

$$\rho_5 \geq \frac{\rho_4}{\rho_1}. \tag{2.5.9}$$

The admissibility condition is

$$V_4^+ = \rho_5 - \frac{\rho_4}{\rho_1} \geq 1 \quad \Leftrightarrow \quad \rho_5 \geq \left(1 + \frac{\rho_4}{\rho_1}\right). \tag{2.5.10}$$

We now establish conditions under which the steady states A_n^s are physically realistic and satisfy (2.4.3).

2.5.2 Conditions for the steady states on $\hat{\Sigma}$

2.5.2.1 Conditions for A_1^s

Because the first three components of A_1^s are the same as A_1^+, the conditions (2.5.1)-(2.5.3) ensure that E_1, $\phi(E_1)$, and $\psi(E_1)$ are positive. However, the condition for R to be physically realistic becomes $\frac{1}{E_1} - \psi(E_1) - 1 \geq 0$. Substituting in the expression for ψ in terms of ω, a little manipulation gives the condition

$$\rho_2 \left(\frac{1}{E_1} - 1\right)^2 - \rho_3 \omega(E_1) \left(\frac{1}{E_1} - 1\right) \geq \omega(E_1) \geq 0. \tag{2.5.11}$$

Now consider the admissibility condition $0 \leq E_1\Omega \leq 1$. Note that $E_1\Omega$ can be obtained from the third component (L) of $g(A_1^s)$ from (2.3.30),

$$E_1\Omega = \frac{\rho_6 E_1}{\rho_7 + E_1},$$

and by substituting in E_1 from (2.4.11), after a little rearranging the admissibility condition becomes

$$0 \leq \frac{\rho_6\rho_9 - \rho_7\rho_8}{\rho_9 - \rho_7} \leq 1. \tag{2.5.12}$$

2.5.2.2 Conditions for A_2^s

Physical values of A_2^s require $E_2 \geq 0$ and $\frac{1}{E_2} - 1 \geq 0$, implying $0 \leq E_2 \leq 1$, which yields

$$0 \leq \frac{\rho_4\rho_8 - \rho_1\rho_5\rho_9}{\rho_1(\rho_5 - \rho_8)} \leq 1. \tag{2.5.13}$$

There are two cases to consider from equation (2.5.13),

(i) $\rho_8 \leq \rho_5 \leq \frac{\rho_4\rho_8}{\rho_1\rho_9}$ and $\rho_5 \geq \frac{\rho_8(\rho_4-\rho_1)}{\rho_1(1+\rho_9)}$, and

(ii) $\frac{\rho_4\rho_8}{\rho_1\rho_9} \leq \rho_5 \leq \rho_8$ and $\rho_5 \geq \frac{\rho_8(\rho_4-\rho_1)}{\rho_1(1+\rho_9)}$.

Now consider the admissibility condition $0 \leq E_2\Omega \leq 1$. Note that $E_2\Omega$ can be obtained from the fourth component (R) of $g(A_1^s)$ from (2.3.30),

$$E_2\Omega = \frac{\rho_8 E_2}{\rho_9 + E_2}.$$

Substituting in E_2 from (2.4.11), the admissibility condition becomes

$$0 \leq \frac{\rho_4\rho_8 - \rho_1\rho_5\rho_9}{\rho_4 - \rho_1\rho_9} \leq 1. \tag{2.5.14}$$

2.5.2.3 Conditions for A_3^s

For the state A_3^s to be physically realistic requires that the three quantities E_3^s, $\phi(E_3^s)$, and $\frac{1}{E_3^s} - 1$, are positive. As for A_3^+, the cubic root solution for E_3^s is unilluminating, but we note that (2.4.17) always has at least one real root which need not be positive for all values of the parameters.

The third (L) component of $g(A_3^s)$ from (2.3.30), yields

$$E_3^s\Omega = \frac{\rho_6 E_3^s}{\rho_7 + E_3^s},$$

with which the admissibility condition can be written as

$$0 \leq \frac{\rho_6 E_3^s}{\rho_7 + E_3^s} \leq 1, \tag{2.5.15}$$

in terms of the cubic root E_3^s.

2.5.2.4 Conditions for A_4^s

The condition for A_4^s to be physically realistic is simply $E_4 > 0$, which provides a lower bound to ρ_5 as in equation (2.5.9). For the admissibility condition, note that by using the second component (E) of $g(A_4^s)$, yields

$$E_4\Omega = \frac{\rho_5 F}{1+F} = \frac{\rho_1\rho_5}{\rho_1 + \rho_4}$$

and, therefore, the admissibility requires

$$0 \leq \rho_5 \leq 1 + \frac{\rho_4}{\rho_1}. \tag{2.5.16}$$

2.5.3 Summary of the admissibility conditions

The admissibility conditions for A_n^+ and A_n^s are summarised in Table 2.2. It is shown that the ranges of existence of any two steady states labelled by the same n are mutually

exclusive, except at boundaries where A_n^+ and A_n^s coalesce on the switching boundary. For example, A_3^+ and A_3^s coincide when $\nu(E_3) = 1/E_3$ (compare (2.4.6) to (2.4.15)) or, equivalently, when

$$E_3 = E_3^s = \frac{\rho_7}{\rho_6 - 1}. \tag{2.5.17}$$

Note that for $n = 3$, ρ_5^{3*} evolves by substituting E_3 from equation (2.5.17) in equation (2.4.12).

Table 2.2: Admissibility conditions for steady states

steady state	condition	in G^+	in $\hat{\Sigma}$	boundary
$n = 1$	$\frac{\rho_6\rho_9 - \rho_7\rho_8}{\rho_9 - \rho_7}$	≥ 1	≤ 1	$\rho_6 = \rho_6^* := 1 - \frac{\rho_7}{\rho_9}(1 - \rho_8)$
$n = 2$	$\frac{\rho_4\rho_8 - \rho_1\rho_5\rho_9}{\rho_4 - \rho_1\rho_9}$	≥ 1	≤ 1	$\rho_5 = \rho_5^{2*} := 1 - \frac{\rho_4}{\rho_1\rho_9}(1 - \rho_8)$
$n = 3$	$\frac{\rho_6 E_3}{\rho_7 + E_3}$	≥ 1	≤ 1	$\rho_5 = \rho_5^{3*}$ $:= \left(1 + \frac{\rho_4(\rho_6 - 1)(\rho_7 + \rho_3\mu)}{\rho_2\mu^2 + \rho_1\rho_7(\rho_7 + \rho_3\mu)}\right)$, $\mu = \rho_6 - (1 + \rho_7)$
$n = 4$	$\frac{\rho_1\rho_5}{\rho_1 + \rho_4}$	≥ 1	≤ 1	$\rho_5 = \rho_5^{4*} := 1 + \frac{\rho_4}{\rho_1}$

2.6 Sensitivity analysis

Numerical solutions of a mathematical model for particular values of the system parameters can give some understanding of the dynamics associated with the model. However, a more complete understanding relies on determining parameter values at which the qualitative behaviour of these solutions change, i.e. *bifurcations*. (For a discussion of how to define bifurcations in piecewise-smooth systems, see [20]). An important characteristic of any bifurcation is its *codimension* - this is the number of parameters that need to be varied in order for the bifurcation to occur. In this section only codimension one bifurcations are considered.

2.6.1 Steady state bifurcations at the discontinuity boundary

The composition and volume (V) of the CL vary as ρ_5, the maximal rate of EC proliferation, change for steady states $n = 2, 3, 4$ in Table 2.2. The bounds in this table are examples of a particular class of *discontinuity-induced bifurcations* known as *boundary equilibrium bifurcations* [21, 38]. As ρ_5 passes through a bifurcation value ρ_5^{j*} (where

$j = 2$, 3, or 4), a steady state A_j^+ hits the discontinuity boundary and disappears, while a sliding (pseudo) steady state A_j^s is created on the discontinuity boundary (or vice versa). Since one steady state always persists through the bifurcation, this scenario is classified as *persistence*. As an example, the persistence of A_4^s to A_4^+ as ρ_5 increases through ρ_5^{4*} is shown in Figure 2.8.

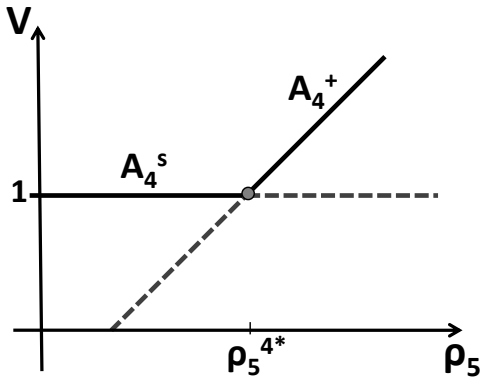

Figure 2.8: Schematic bifurcation diagram for CL volume, $V = E + L + R$, over ρ_5 (the maximal EC proliferation rate). It shows the *persistence* scenario associated with a boundary equilibrium bifurcation (BEB) occuring at $\rho_5 = \rho_5^{4*}$. For $\rho_5 < \rho_5^{4*}$, A_4^+ is a *virtual* steady state, whereas A_4^s is an *admissible pseudo* steady state. For $\rho_5 > \rho_5^{4*}$, A_4^+ is *admissible* and A_4^s is *virtual*. Thus, there is one admissible (pseudo-) steady state on either side of the bifurcation point. Key: admissible (solid lines), virtual steady state (dashed). See definitions in section 2.3.7.2.

2.6.2 Perturbation of ρ_5: the maximal EC proliferation rate

The parameter ρ_5 represents the maximal rate of EC proliferation (see equation (2.3.9)), and by varying it we can assess how the CL growth (volume), and its cellular composition (ECs, LCs, and stromal cells) is affected.

In Table 2.1 we fix $k_E = k_L = k_R$ (so that the maximum growth rate for all cell types is identical) and $E_{h1} = E_{h2}$ (so that LCs and stromal cells have the same demand for nutrients to grow), and hence $\rho_6 = \rho_8$ and $\rho_7 = \rho_9$. These parameter values lead to singular value for the steady states $A_1^{\pm}$, since the denominator of E_1 in equation (2.4.11) vanish.

To consider values of $\rho_6, \rho_7, \rho_8, \rho_9$, close to, but not at, the singular value, we take the parameters to lie on an ellipse: $\rho_8 = \rho_6(1 + r\cos\theta)$ and $\rho_9 = \rho_7(1 + r\sin\theta)$ (with radius r and $\theta \in [0, 2\pi]$) centred at the singular point S at $(\rho_8, \rho_9) = (\rho_6, \rho_7)$, and these are shown in Figure 2.9(a). In Figure 2.9(a) (inset plots), as θ varies we observe

four qualitatively different cases. In case (1), R growth rate exceeds that of L and we expect steady states with $R \neq 0$, and in (2) L and R dominance exchanges. That is, in a low nutrient (E) environment, L grow at a faster rate than R, however, as the nutrient abundance increases the growth rate of R exceeds that of L. In case (3), L growth rate exceeds that of R and we expect steady states with $L \neq 0$, and in (4) L and R dominance exchanges, where the opposite of case (2) applies.

Figure 2.9(b) shows how E varies (diagrams for F, R, L, are omitted for brevity) as θ varies, with numbers 1 to 4 representing the four cases of L-R dominance as described in Figure 2.9(a).

In biological terms, since we are interested in healthy CL development (where all four variables are non-zero), a value of $\theta := \theta^s \in (\theta^* = \frac{\pi}{4}, \theta^{**})$ is chosen, which gives a point $S^{'} = (\rho_8^*, \rho_9^*)$ on the ellipse, with $\rho_8^* > \rho_6$, $\rho_9^* > \rho_7$. For these values, the steady state $A_1^s \neq \mathbf{0}$ exists and is stable. Note that the stability of each steady state is evaluated numerically. Any case other than (2) implies a pathological CL. In particular, case (1) implies $A_{5a}^s := (0, 0, 0, 1)$, an avascular ($E = 0$) state, where only stromal cells survive and dominate the whole CL ($V = R = 1$). More importantly, there are no LCs, which implies no progesterone production to support embryo development. The case (3) yields $A_3^s := (F, E, L, 0)$. This is also regarded as a pathological condition (since $R = 0$), although embryo development might be sustained due to the presence of LCs. Choosing $\theta := \theta^{ss} = \theta^s + \pi \in (\theta^{*'} = \frac{5\pi}{4}, \theta^{**'})$ gives the symmetrical point $S^{''} = (\rho_8^{**}, \rho_9^{**})$ with $\rho_8^{**} < \rho_6$, $\rho_9^{**} < \rho_7$, which corresponds to case (4) and the system evolves either to A_{5a}^s or A_3^s.

Figure 2.10 shows the bifurcation diagram for the ECs obtained by varying ρ_5 in the case (2), corresponding to point $S^{'}$. The diagram was generated using the explicit expressions of steady states given in section 2.4 by plotting only the segments of the branches which give rise to physically realistic and admissible states (for details see section 2.5) for all four variables. Different scenarios with different steady states arise depending on the value of ρ_5. For $\rho_5 \in (\rho_5^*, \rho_5^{**})$ (intermediate levels of angiogenesis), the system can evolve to the 'healthy' state A_1^s. Outside this range, the system evolves to a pathogenic state: $A_3^s(R = 0; V = 1)$ for $\rho_5 < \rho_5^*$ (weak angiogenesis), or $A_2^s(L = 0; V = 1)$, $A_2^+(L = 0; V > 1)$, and $A_4^+(L = 0, R = 0; V > 1)$ for $\rho_5 > \rho_5^{**}$ (high angiogenesis).

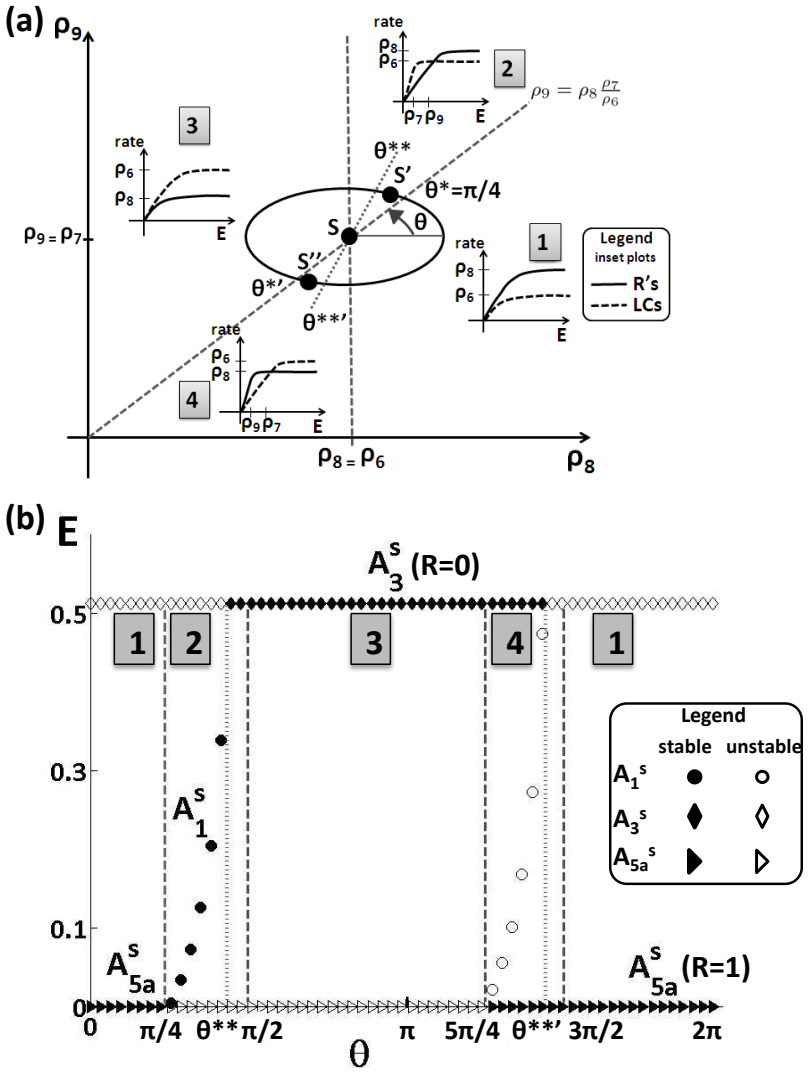

Figure 2.9: Steady state CL cellular composition depends on four qualitatively different cases regarding the growth rate of L and R. (a) In the parameter space (ρ_8, ρ_9), we consider the ellipse: $\rho_8 = \rho_6(1 + r\cos\theta)$, $\rho_9 = \rho_7(1 + r\sin\theta)$ (with $r = 0.3$ and $\theta \in [0,2\pi]$) around the singular point $S = (\rho_6, \rho_7)$ at which LCs and stromal cells have the same demand of nutrients (E) to grow. Inset plots present the four different cases. That is, how the swelling rate of L, given by $\rho_6 \frac{E}{\rho_7+E}$ (dashed curve) as in equation (2.3.10), and the proliferation rate of R, given by $\rho_8 \frac{E}{\rho_9+E}$ (solid curve) as in equation (2.3.11), change as the nutrients vary. (b) Bifurcation diagram showing how the steady state solutions for the ECs vary as the angle θ varies. For conciseness we include only the steady states that are stable for some $\theta \in [0,2\pi]$.

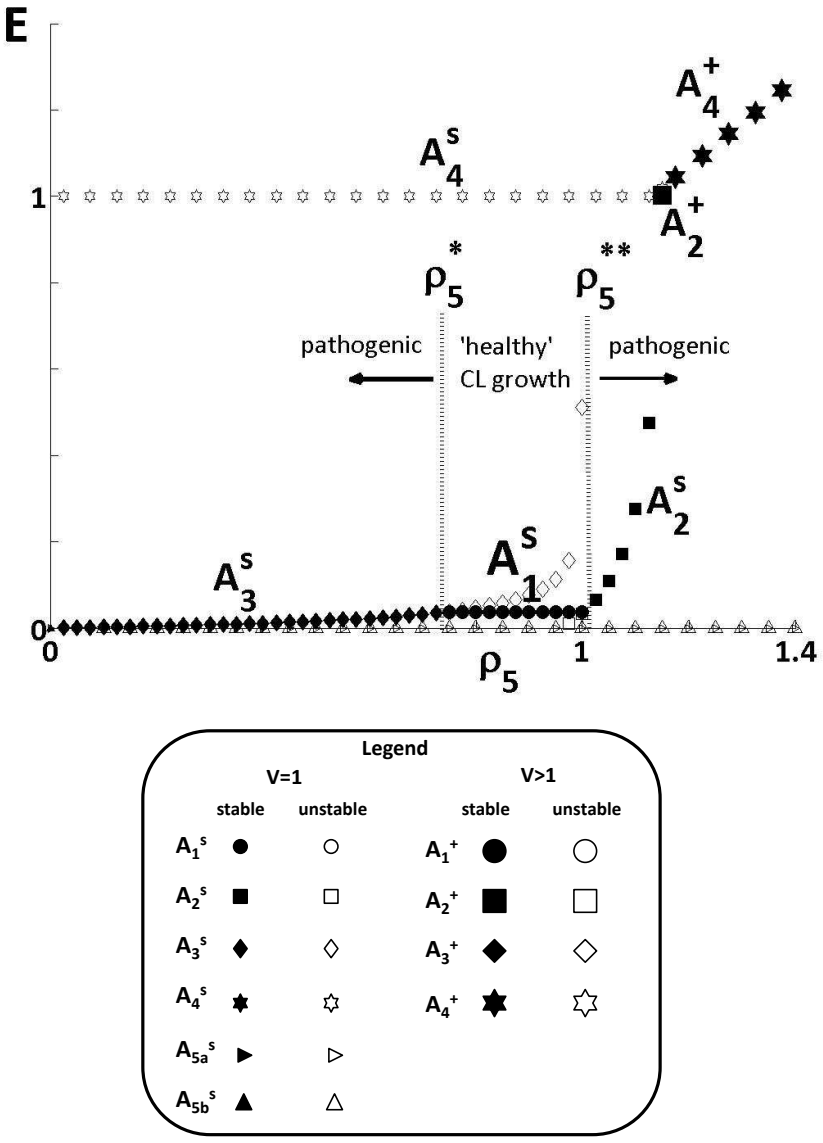

Figure 2.10: Bifurcation diagram shows how the steady state solutions for the EC volume vary as ρ_5 varies for case (2) as in Figure 2.9(a). The steady states are labelled as given in the Legend, and are further described in the text. The parameter values ρ_i $(i = 1, ..., 7)$ are specified in equation (2.3.13), $\rho_8 = \rho_8^* = 0.81$ and $\rho_9 = \rho_9^* = 0.09$ which correspond to the point S' (case (2)) in Figure 2.9(a).

2.6.3 Perturbation of other parameters

In this section our aim is to check whether the system evolves to the healthy steady state A_1^s (where none of its variables vanish) by varying parameters which are associated with a greater degree of uncertainty as estimated in section 2.3.2. In particular, parameters a_1, a_2 (rates of FGF2 production, by ECs and LCs, respectively), and k (a measure of how mechano-sensitive cells are to competition for space) were estimated in limiting cases.

In section 2.3.2, we used cases, labelled (Ia), to estimate a_1 and a_2, and (Ib) to estimate k, and in the following section we use two different cases (IIa), (IIb), for a_1, a_2, and k, respectively. Briefly, (Ia) represents the limiting case where we assume no LCs (to estimate a_1) and no ECs (to estimate a_2), while (IIa) assumes that FGF2 production from LCs after the first two days of ovulation is minimal (as shown in Figure 2.2). (Ib) assumes $F^* \gg F_h$, which implies faster EC proliferation, while (IIb) assumes $F^* = F_h$.

2.6.3.1 Cases (IIa) and (IIb) for estimating a_1, a_2 and k

The parameter values for the dimensional model in equations (2.3.2),(2.3.5)-(2.3.7) were estimated as accurately as possible. However, since there is less evidence with which to determine a_1, a_2, and k, than the other parameters, we provide here an alternative method to estimate them, as a test of robustness. These alternative methods are enumerated below as (IIa) and (IIb):

(IIa). Here we estimate a_1 and a_2 as follows. In Figure 2.2, a schematic is presented which illustrates the high FGF2 production by LCs during the first two days, while ECs are productive all over the cell cycle. Based on that, we assume that the FGF2 production from LCs after the first two days is minimal. That is, at steady state ($\dot{F} = 0$) $\frac{a_2 L}{R_{EL}+\frac{E}{L}} \to 0$, or equivalently,

$$a_1 E^* \gg \frac{a_2 L^*}{R_{EL} + \frac{E^*}{L^*}}. \tag{2.6.1}$$

In addition, at steady state,

$$\dot{F} = 0 \Leftrightarrow a_1 E^* \left(1 + \frac{1}{\gamma}\right) = d_F F^*, \tag{2.6.2}$$

where,

$$\gamma = \frac{a_1 E^*}{\frac{a_2 L^*}{R_{EL}+\frac{E^*}{L^*}}} = 0.07\frac{a_1}{a_2}, \tag{2.6.3}$$

is the ratio of FGF2 production by ECs to that by LCs. By considering this ratio to be of the order of 10 ($\gamma = 10$), equation (2.6.3) implies

$$a_1 \simeq 143\, a_2. \tag{2.6.4}$$

Equation (2.6.2) implies $a_1 = \frac{d_F F^*}{E^*(1+\frac{1}{\gamma})} \simeq 124$, and therefore, from equation (2.6.4), $a_2 \simeq 0.9$.

(IIb). Here we estimate k as follows. We assume a steady state $\dot{E} = 0$ and FGF2 steady value being smaller than for (Ib), e.g. $F^* = F_h$, and solving for k implies: $k = \frac{F}{F_h+F}\frac{k_E}{V} \sim \frac{F^*}{F_h+F^*}\frac{k_E}{V^*} \simeq \frac{1}{2}\frac{k_E}{V^*} = 0.06$.

2.6.3.2 Summary of results

The results obtained by combining cases (Ia), (IIa), (Ib), (IIb) are summarised in Table 2.3. A combination of (Ia) and (IIb) leads to a change in the steady state from $A_1^s(V = 1)$ to $A_1^+(V > 1)$. Case (IIb) gives a smaller value for k suggesting that this can lead to a non-constant CL volume. Overall, the alternative case for estimating a_1 and a_2 does not seem to lead to any change in the steady state.

Table 2.3: Table summarising how the estimates of a_1, a_2, k, and the associated stable steady state depend on the cases used for their estimation.

case	a_1	a_2	k	steady state
(Ia) & (Ib)	136	5.1	0.12	A_1^s
(Ia) & (IIb)	136	5.1	0.06	A_1^+
(IIa) & (Ib)	124	0.9	0.12	A_1^s
(IIa) & (IIb)	124	0.9	0.06	A_1^s

2.7 Discussion

In this chapter, we have developed an ODE model for the early developmental stages of the bovine corpus luteum (CL). The CL is responsible for the progesterone production needed for pregnancy. Angiogenesis, the process of new blood vessel growth from existing ones, is crucial for the CL growth. Inadequate angiogenesis has been linked to infertility in cows. Therefore, by studying the dynamic processes which regulate CL growth and development *in vivo*, our aim has been to determine how CL growth (and pregnancy in the cows) is influenced by changes in the CL vascular density.

The model describes the time evolution of four dependent variables representing the concentration of FGF2, and the volume of the endothelial (ECs), luteal (LCs) and stromal cells (R), such as pericytes (PCs), with ECs representing the vascular density in the CL. The model is based on the assumption that the CL volume (V) can be approximated by the sum of the volumes of the three cell types, and if V exceeds a threshold value, then cell growth is inhibited. The surface (Σ) at which the volume threshold is attained is called the *discontinuity boundary*, which separates the model into different cases: above, below, or on Σ. For each of those cases, the trajectories of the system emerge from a different vector field, and evolve to *real* (above or below Σ) or *pseudo* steady states (lie on Σ).

To gain some intuition about the model we firstly considered a reduced two-dimensional model for which $L \equiv R \equiv 0$ and, therefore, $V = E + L + R \approx E$. Given the importance of angiogenesis in the CL, in both the reduced and full models, the key bifurcation parameter taken to be the maximal rate of EC proliferation, ρ_5. Interesting model behaviours have been observed in the reduced model by varying ρ_5. In particular, if ρ_5 was below a threshold (see equation (2.3.16)) the CL volume remained constant ($V = 1$), *sliding* on the discontinuity boundary, $\Sigma : E = 1$, and the system evolved to a *pseudo* steady state. Sliding is a special case where trajectories starting from either vector field (above or below Σ) are constrained on Σ. However, if ρ_5 exceeded that threshold, E was able to detach from Σ into the region $E > 1$ (see Figure 2.5).

These notable cases observed in the reduced model were the motivation for further investigation into the existence of *pseudo* steady states in the full model. Therefore, in the full model, we analysed the real steady states for the two different vector fields, above and below $\Sigma : E + L + R = 1$, and the *pseudo* steady states, by exploring parameter constraints for which steady states in each region can be physically realistic (non zero) and *admissible* (see definitions in section 2.3.7.2).

As in the reduced model, the impact of varying the 'angiogenic parameter', ρ_5, was in-

vestigated in the full model, which was able to distinguish between *normal* and *pathological* cases of CL growth (see Figure 2.10). In a weak angiogenic environment (low ρ_5) two cases are distinguishable. If the growth rate of LCs exceeds that of the stromal cells, then the stromal cells are not able to survive and the LCs dominate. In that case, although progesterone production by LCs may be high, there are few blood vessels (ECs) to transport progesterone to the uterus. Alternatively, if the stromal cells are more proliferative, they dominate the CL, and progesterone production ceases (since LCs vanish). In both cases, low progesterone compromises pregnancy. In a high angiogenic environment (high ρ_5), the CL shifts from a constant to an increasing volume (steady state $A_4^+ : V > 1$) for which the CL is predicted to contain only vessels (ECs), which is biologically implausible. For intermediate values of ρ_5, a *healthy* growth of the CL (where none of its cellular components vanish) is maintained, which is necessary to sustain a healthy pregnancy.

The resulting behaviour of the (full) model was emerged using parameter values from independent data as estimated in section 2.3.2. In order to check if the system evolves to the healthy steady state we varied other parameters (except from ρ_5), which were associated with a greater degree of uncertainty. These are, a_1, a_2 (rates of FGF2 production, by ECs and LCs, respectively), and k (sensitivity of cells to competition for space). In section 2.6.3, we provided an alternative way of estimating those parameters, and results showed that the system continued to evolve to the healthy steady state.

We discuss possible extensions and improvements to the current model, later in Chapter 6. In particular, a more systematic parameter sensitivity analysis by assessing the role of all parameters if possible could be more advantageous and informative. That is, by providing information on the cases of our system which might evolve to either a pathological or a healthy CL growth.

However, we believe that the resulting model reproduces several features of CL development. That is, a transient surge in FGF2, and CL growth to a steady state volume in which the different cell types are present in proportions that are consistent with experimental observations [145, 203] and, in addition, the model can predict for normal and pathological cases of CL growth.

CHAPTER 3

In vitro corpus luteum data

In this Chapter, our intention is to motivate the work being done in Chapters 4 and 5, focusing on cell aggregation and endothelial sprout formation, respectively, by describing *in vitro* studies of the corpus luteum (CL).

Infertility and poor embryo development is a big problem in dairy cows, which is mainly caused by a deficiency in the CL ability to produce progesterone [146]. The rapid and extensive development of vascular bed is crucial for the CL to function. Motivated by this, Robinson *et al.* in [201] developed a culture system by incorporating all the CL cell types (e.g. ECs, steroidogenic cells (small and large luteal cells), fibroblasts and pericytes (PCs)) in an attempt to shed some light on the dynamics that drive angiogenesis in the CL. In this *in vitro* system EC networks were promoted by extracellular matrix (ECM) components (e.g. fibronectin). The development of EC networks *in vitro* that resembled the vasculature was stimulated by treatment with the two main angiogenic growth factors found in the CL, FGF2 and VEGFA. The system was two-dimensional, however, future work is looking to develop this novel system into three dimensions by using collagen gels.

The ECs were identified by the EC marker, von Willebrand factor (VWF), and started to form clusters ('islands') on day 2 (Figure 3.1A), then on day 5 proliferated and developed thread-like structures (Figure 3.1B). After 9 days in culture (Figure 3.1(C-D)), these structures lengthened, thickened and formed highly organised intricate networks resembling a capillary bed. Under higher magnification, they had a definite tubule-like appearance with more intense staining on the outer edge. Note that we define a cluster (or island) to be any group of cells (more than two in number and independent of type), which are in contact. Therefore, we have two main categories: the individual and the clustered cells.

Results regarding the different ECM components on the formation of endothelial net-

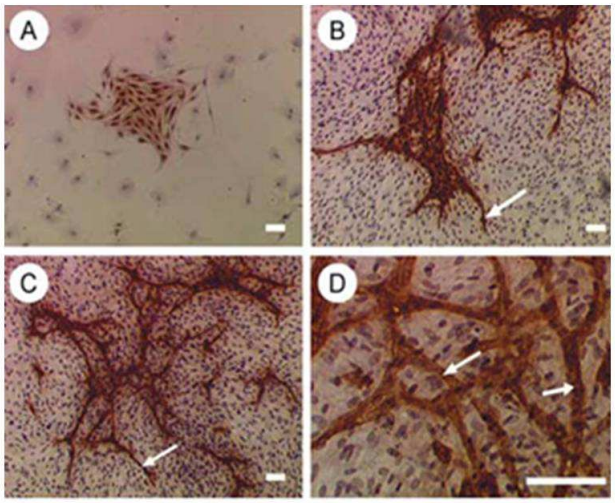

Figure 3.1: The development of endothelial tubule-like structures *in vitro* in luteal angiogenesis culture system [201]. All luteal cell types isolated from the bovine CL and ECs are immunostained using the VWF marker. (A) 2 Days: ECs form clusters, (B) 5 Days: tip cell formation (arrow), (C) 9 Days: formation of intricate networks of endothelial tubule-like structures (indicated by arrows) and are shown at higher magnification in (D). The scale bar represents 50 μm.

work suggest that collagen (Figure 3.2B) had no benefit, while fibronectin (Figure 3.2C) greatly enhanced the formation of the endothelial network.

The authors in [201] also studied the effect of FGF2 and VEGFA on the formation of endothelial networks, and below we summarise the main results:

- No FGF2 or VEGFA: endothelial tubules are formed albeit to a very limited extent (Figure 3.3A).
- FGF2 (Figure 3.3B) and VEGFA (Figure 3.3C) independently: stimulate the formation of tubules.
- FGF2 and VEGFA (Figure 3.3D) result to the greatest endothelial cell network development when they are added simultaneously.
- FGF2 rather than VEGFA increased the size of the clusters (but not their number).
- VEGFA rather than FGF2 increased the number of the clusters (but not their size).

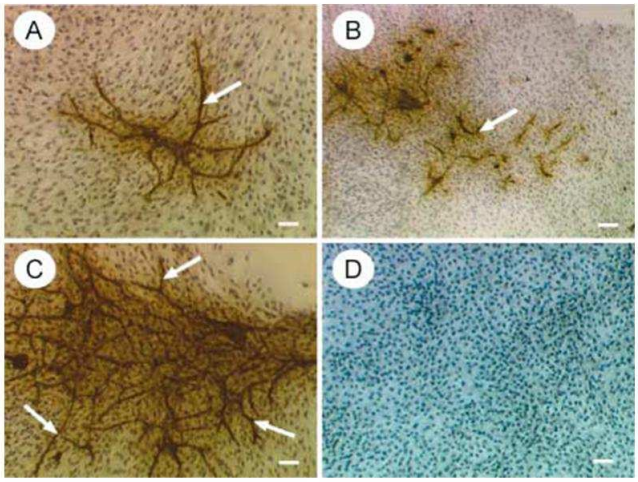

Figure 3.2: The effects of collagen and fibronectin coating on luteal angiogenesis in vitro. ECs were immunostained with VWF and representative images are shown for (A) plastic alone (control), (B) 20 μg/well collagen, (C) 10 μg/well fibronectin and (D) rabbit immunoglobulin control ($n = 3$ per treatment).

Based on the above observations, it might be suggested that FGF2 enhances cell proliferation (mitogenic), and VEGFA enhances cell aggregation (possibly via chemotaxis).

In conclusion, the successful development of endothelial cell networks *in vitro* provides a new opportunity to elucidate the physiological control of the angiogenic process in the developing CL.

Another study from Bagavandoss and Wilks in [11], characterised isolated microvascular ECs from developing rabbit CL in order to distinguish the complex physiological functions of the ECs. The isolated cells formed capillary-like tubules in collagen gel cultures. They showed that the FGF2 was mitogenic for the ECs, but several other growth factors had no effect on the EC proliferation *in vitro*. In fact, transforming growth factor-β1, TGF-β1, and tumour necrosis factor-α, TNF-α, strongly inhibited the proliferation of the ECs. Other factors (e.g. PDGF, EGF, IGF-1 etc.) were investigated but these had a more modulatory role.

In another experimental system, Stouffer and Christenson in [34] established a method for isolating a pure population of ECs from the primate (rhesus monkeys) corpora lutea by showing that both fibronectin and VEGFA stimulated EC proliferation.

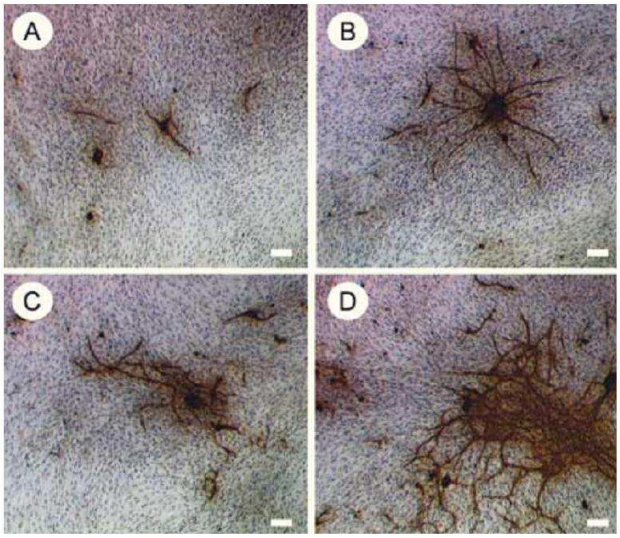

Figure 3.3: The effect of FGF2 and VEGFA on luteal angiogenesis in vitro. Representative images of the endothelial tubule development of dispersed luteal cells treated with either (A) control, (B) 1 ng/ml FGF2, (C) 1 ng/ml VEGFA or (D) 1 ng/ml FGF2 with 1 ng/ml VEGFA are shown. The endothelial cells were immunostained (brown) with VWF. The scale bar represents 50 μm.

3.1 New data acquisition

In this section we will briefly describe results from *in vitro* experiments being done in Robinson's Lab with the aim to determine the temporal changes in EC dynamics during aggregation in the formation of EC islands. Additionally, the association of ECs-PCs was investigated. In all experiments, all cell types from the bovine CL were isolated by enzymatic treatment as described in [201] and cultured for up to 9 days. Then cells were fixed every day and immunostained for VWF or SMA or dual stained. Images of the EC and PC pattern were acquired using *Leica* light microscope (under a 10x objective lens) connected to a digital camera. For each time point (days 1, 2 and 3) a single coverslip per experiment was analysed. Numbers of aggregated ECs and PCs were recorded using Image Pro-Plus 5.0 (Media Cybernetics, Wokingham, UK). This was repeated for as many fields of view as possible in order to cover the whole well (in vitro domain). Experiments were performed by R.S. Robinson and K.J. Woad, and image analysis/quantification that follows by S.A. Prokopiou. Although Image Pro-Plus provides an automated way to count the number of cells, I chose to count them manually (using the software), since the existence of other irrelevant cell types (not ECs nor PCs) could provide wrong and misleading results.

3.1.1 Endothelial cells

Figure 3.4 depicts representative snapshots showing the formation and progress of the EC islands over time. ECs are stained with brown colour using VWF, also indicated with red arrows. The green arrows show another cell type, likely to be PCs which surround the EC islands, and are also integrated within them (see day 3). This suggests that there is likely to be a cross-talk between ECs and PCs.

The data presented in Figure 3.5 show that both the total number of ECs and the number of EC islands decreased from day 1 to 2. Thereafter, the number of ECs increases from day 2 to 3; however, the number of clusters remains constant. These together imply that whole EC islands failed to establish themselves in culture or underwent cell death. Then, in those islands that survive, there was proliferation of the ECs.

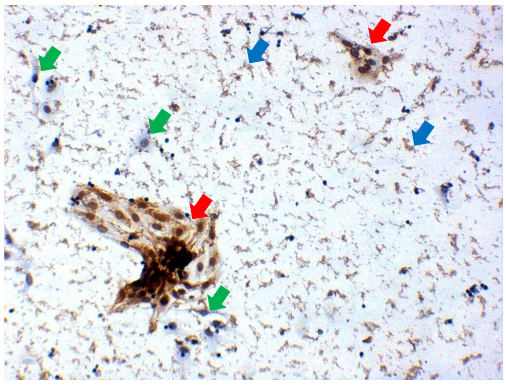

(a) day 1

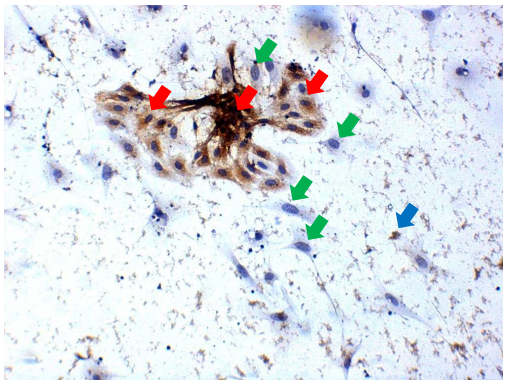

(b) day 2

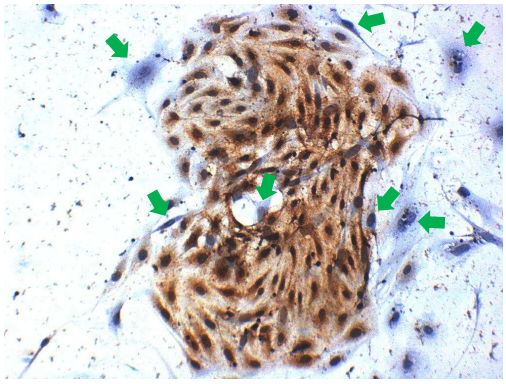

(c) day 3

Figure 3.4: The time course for the development of EC 'islands' *in vitro*. All cell types from a recently ovulated bovine CL were dispersed and then grown on fibronectin in specialised EC medium. The ECs were immunostained by VWF immunocytochemistry (brown; also marked with red arrows). A different cell type (indicated by green arrows) was observed to surround the EC islands as well as integrating within them (see green arrow on day 3). These cells are possibly pericytes (PCs). Blue arrows point to other cell types from the CL (e.g. fibroblasts, immune cells).

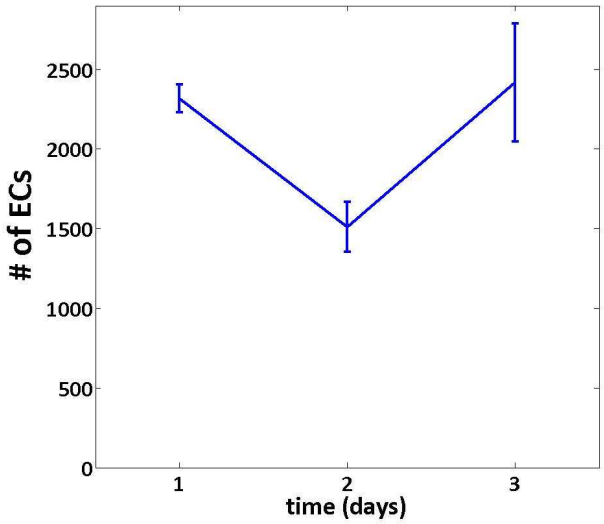

(a)

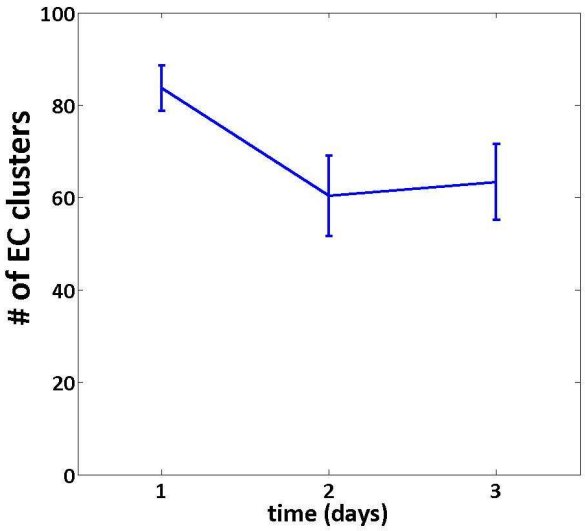

(b)

Figure 3.5: (a) Total number of ECs, and (b) total number of EC clusters on days 1,2,3. The data are mean ± S.E.M. from 3 individual experiments.

3.1.2 Pericytes

In [202], Robinson *et al.* noted that PCs proliferate intensively *in vitro* by forming a dense network after 3 days of culturing (see Figure 3.6(a), and Figure 3.6(b)-(c) in higher magnification).

At early time points (e.g. 3 hrs), SMA positive cells (PCs) tended to have a uniform appearance (flat, broad cells) and these were distributed across the whole well (Figure 3.6(b)). By day 1, PCs were associated with EC islands (red dotted line in Figure 3.6(c)). They were localised to the outer edge of the EC islands as well as forming an integral component of the islands. These PCs had a broad, flat cell appearance but some of them had developed slender projections which formed multiple connections with other PCs, ECs and/or other unidentified cell types.

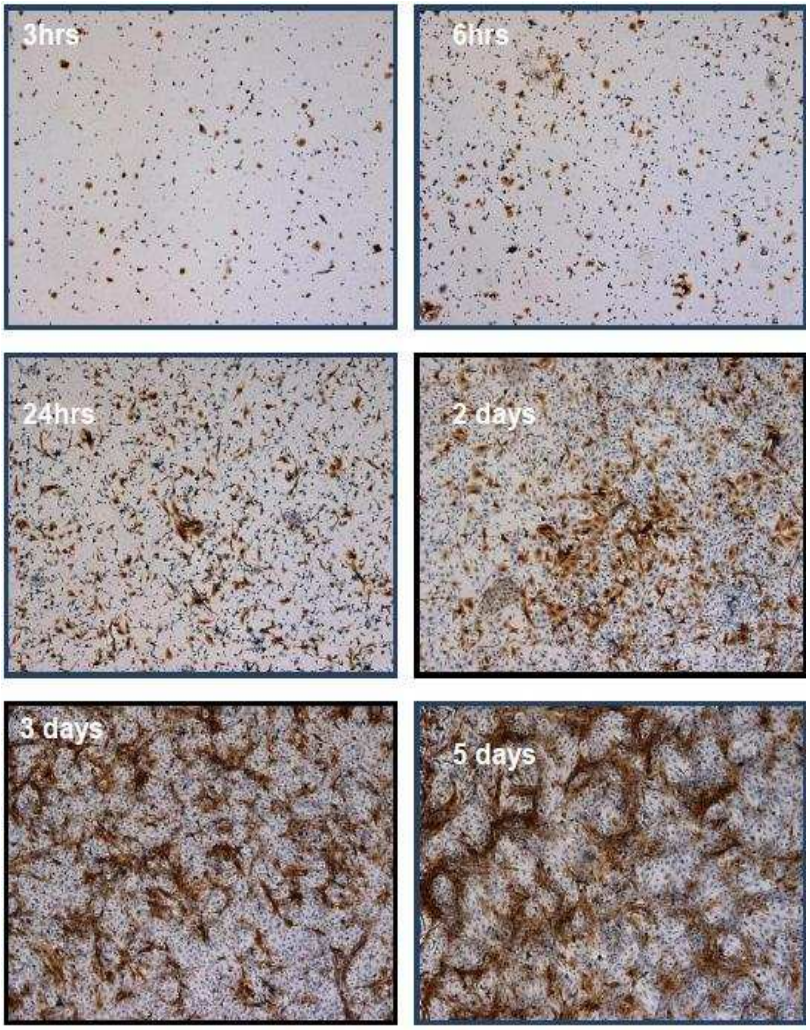

(a)

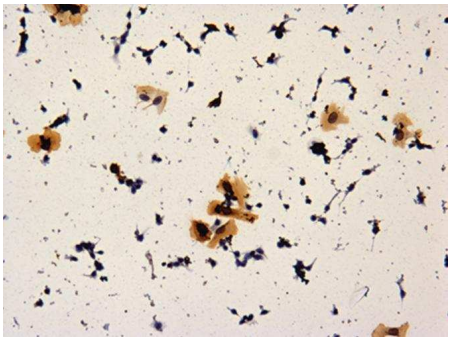

(b) 3 hrs

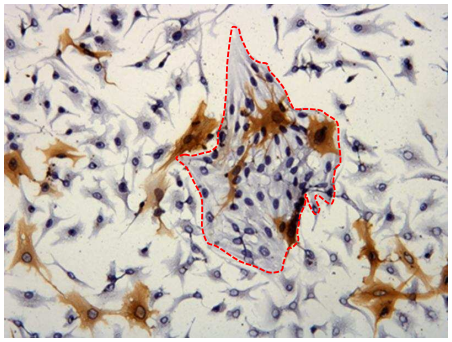

(c) 24 hrs

Figure 3.6: All cell types from a recently ovulated bovine CL were dispersed and then grown on fibronectin. PCs are immunostained using SMA marker (brown). (a) Time course of PC growth from 3 hrs to 5 days in culture showing the intense PC proliferation. (b)-(c) Higher magnification of 3 and 24 hrs showing that a number of individual PCs were observed ar 3 hrs in culture (b), and in (c) PCs had taken on a more elongated shape with the ability of being associated with EC clusters (red dotted line).

3.1.3 Endothelial cells & pericytes (dual localisation)

Intrigued by the experimental snapshots on ECs, and PCs in Figures 3.4 and 3.6, respectively, regarding the possible cross-talk between EC 'islands' and the other cell type (which assumed to be PCs) we performed dual localisation with VWF and SMA for ECs and PCs, respectively. Indeed, Figure 3.7 depicts representative snapshots showing EC 'islands' in brown colour (and red arrows) being surrounded and integrated with PCs shown in purple colour (and green arrows).

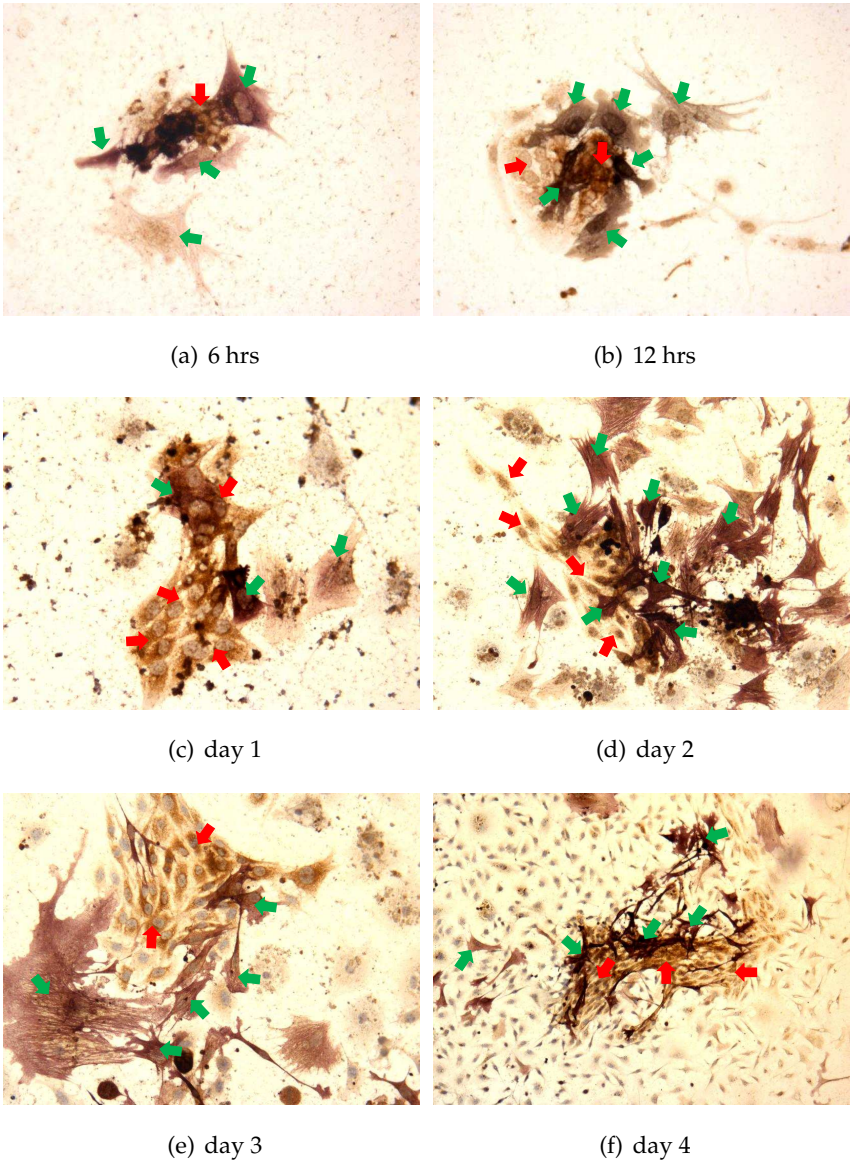

(a) 6 hrs (b) 12 hrs

(c) day 1 (d) day 2

(e) day 3 (f) day 4

Figure 3.7: All cell types from a recently ovulated bovine CL were dispersed and then grown on fibronectin in specialised EC medium. ECs are immunostained using VWF marker (brown; and red arrows) and PCs with SMA marker (dark brown/purple; and green arrows).

Figure 3.8 presents results on number of ECs and PCs, and number of EC and PC clusters from one experiment only. The pattern of EC growth is different compared to Figure 3.5. In particular, in this current experiment there was no decline of the number of ECs, and the number of EC clusters. The exact reason for this is unknown, but it's likely to be due to different ability of ECs to establish in culture (e.g. lower viability of ECs). From this experiment, what is clear is that there is a large increase (∼5 fold) of the number of PCs, and the number of PC clusters over the time course.

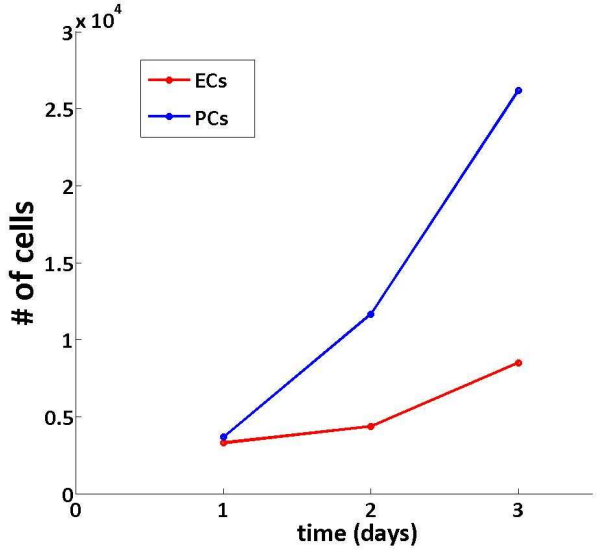

(a)

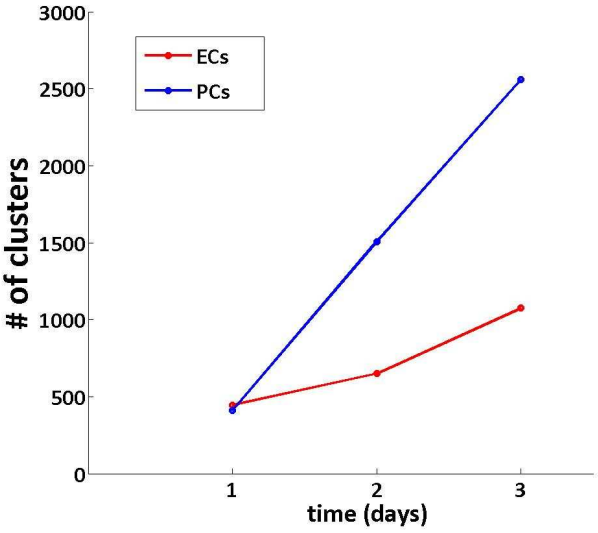

(b)

Figure 3.8: (a) Total number of ECs and PCs, and (b) total number of EC and PC clusters in days 1,2,3 from a single experiment.

3.2 Discussion

In this Chapter we have shown for the first time that not all the EC clusters were able to establish in culture, but once established they manage to grow rapidly. Preliminary results have shown some exciting observations regarding the associations between PCs and the EC clusters, namely, that the PCs form an integral part of them (see Figure 3.7), and the number of PCs increase dramatically (see Figure 3.8).

To the best of our knowledge, there are no reports of EC clusters being lost during multi-cell type culture systems. The exact mechanisms by which the EC clusters are not able to survive are unknown. However, one possible explanation is that the survival ability of ECs might have been reduced due to the numerous processing steps (e.g. enzymatic dispersion, centrifugation) involved from tissue to culture. Additionally, ECs appear to be more sensitive to changes in their environment [personal communication with R.S. Robinson]. An alternative explanation is that some apoptotic ECs within a cluster adversely affected the other ECs leading to the loss of that cluster. Futhermore, immune cells (e.g. macrophages) are stimulated by these apoptotic ECs and migrate to the cluster and digest it as a whole. Note that macrophages are found in abundance during the early CL growth stages [226]. Indeed, we observed apoptotic looking ECs within our cultures.

The large increase in number of PCs has previously been reported [202] (see Figure 3.6), but the current study has extended this to quantify this increase. Regarding the PC recruitment to the EC clusters, the secretion of angiogenic factors (e.g. FGF2, VEGFA, PDGF) are the main candidates for this EC-derived event. It was also noted that the PCs have multiple phenotypes (e.g. myofibroblasts, fibroblasts, smooth muscle cells), which is likely to represent the different roles during the angiogenic process.

The *in vitro* work from Robinson *et al.* [201] by using all of the CL cell types in the same experimental system provides a closer approximation to the *in vivo* environment compared to other *in vitro* experiments where only a single cell type (ECs) is used. However, having all cell types together make it more difficult to distinguish the effect of one cell type to the other which is the main focus of Chapter 4 with regard to EC-PC interactions and, particularly, how PCs affect endothelial proliferation. In addition to this, given that cell staining techniques (immunocytochemistry) are not efficient at early time points (e.g. 6hrs, 12 hrs), we are not able to clearly distinguish the different cell types between them. Therefore, quantitative work proved to be difficult, or otherwise it could provide misleading results. For these reasons, in Chapter 4, we are using results from EC-PC co-culture systems, mainly from Orlidge and D'Amore [173].

CHAPTER 4

Endothelial-Pericyte interactions in angiogenesis

4.1 Introduction

The corpus luteum (CL) is an excellent model to study angiogenesis. Intense neovascular processes begin after ovulation, accompanying and sustaining the development of the CL. During CL development more than 50% of its proliferating cells are of vascular origin (e.g. endothelial cells (ECs), pericytes (PCs)). PCs, the cells that surround capillary ECs may play key roles in blood vessel formation, maturation and maintenance. Interestingly, *in vitro* CL studies presented in Chapter 3 reveal possible cross-talk between PCs and EC clusters (see Figure 3.7).

Control of cell proliferation is a fundamental aspect of tissue physiology central to morphogenesis, wound healing, and cancer. Notably, PCs have been proposed to play a key role in regulating EC proliferation. By using mixed EC-PC co-cultures, Orlidge and D'Amore [173] observed that (growth-arrested) PCs had an anti-proliferative effect on ECs, and it has been proposed that transforming growth factor-β1 (TGF-β1) is a crucial factor for this result.

Motivated by results in Chapter 3 and the experimental study [173], we developed an *in silico* EC-PC co-culture system, using the Cellular Potts Model (CPM) framework. Our aim is to gain insight into the role of PCs on the EC growth, by focusing on cluster formation, the first step in the *in vitro* angiogenic process (see Figure 3.1). Our model allows for heterocellular interactions between ECs and PCs (along with interactions between cells of the same type) in order to assess the PC-derived suppression mechanism to EC growth.

To understand the reported empirical findings in the low density and sparse EC-PC

populations in [173], we expand the widely used CPM to incorporate active cell motility in order to allow for cell-cell interactions. In doing this, we are able to assess the effect of speed and directional persistence time of cell movement on cell clustering and contact inhibition. ECs, in contrast to the growth-arrested PCs, are able to proliferate based on a phase cell cycle model. Mechanical contact between cells and TGF-β1 secreted from both ECs and PCs at their contact area can adversely affect the progress of the phase model. Simulation results are analysed and compared with experimental results in [173] wherever possible. Our model provides further support that the effective range of TGF-β1 is of great importance to EC growth inhibition.

The remainder of this Chapter is organised as follows. Section 4.2 provides the biological background on the two main vascular cell types (ECs and PCs). We present the model overview in section 4.3, and the basic steps of the *in silico* model development in section 4.4. Section 4.5 is devoted to the numerical results, and section 4.6 provides some model alternatives. The Chapter concludes in section 4.7 where we summarise our results.

4.2 Biological background

In this section, we present current knowledge on the *in vivo* role of ECs and PCs, the cross-talk between them, and also, their *in vitro* behaviour.

4.2.1 Endothelial cells and pericytes *in vivo*

ECs form a single layer that lines the entire vascular system. This thin monolayer regulates the exchange of nutrients and waste products between the blood stream and the surrounding tissues. However, it takes two cell types to make blood vessels; ECs and PCs. While the ECs are the better characterised of the two, PCs are now coming into focus as important regulators of angiogenesis and blood vessel function.

PCs have an intermediate phenotype between vascular smooth muscle cells (vSMCs) and fibroblasts and seem to have the capacity to differentiate also in the latter direction. The following list summarises briefly their most important functional properties: their key role in regulation of different cellular processes in the vasculature, including endothelial proliferation and differentiation ([8, 89],[2]), the stabilisation and control of permeability of blood vessels under physiological and pathophysiological conditions [254, 264], their participation in vasculogenesis and angiogenesis [18, 111, 194], and their involvement in the regulation of contractility and tone of vascular smooth muscle

and hence participation in organ blood flow regulation [110, 122].

PCs and vSMCs reside at the interface between the endothelium and the surrounding tissue and are as such ideally positioned to take an active part in the angiogenic process [70]. The PC coverage of the endothelial surface is only partial, and varies extensively between the capillary beds of different tissues [230]. The reason coverage is as low as 10% in some tissues and as high as 50% in other tissues is not known, but likely reflects specific functional features of the microvessels in different organs. The highest PC density has been described for neural tissues and is stated to be almost in parity with ECs in brain and retina. For comparison, the PC to EC ratio is stated to be 1:100 in striated muscle [192]. In addition, the distribution of PCs in the vessel wall is not random. They are more prevalent at capillary branching points, although this is not obligatory. Typically, the part of a vessel engaged in the transport of gases and/or nutrients is free of PC coverage [70].

Despite the several functions of PCs relevant to angiogenesis proposed above, our understanding of PCs is still limited compared to that of the ECs. For a deeper understanding of angiogenesis, it is important to shed light on the mechanisms controlling EC-PC communication.

Vascular formation involves a complex interplay of signals from ECs, PCs/vSMCs, and non-vascular cells required for proper vessel assembly and function. These interactions are both temporally and spatially regulated. The exact mechanism(s) by which ECs recruit PCs or vSMCs during vessel formation is unknown. Potential regulators include soluble factors that act in an autocrine and/or paracrine manner, as well as homotypic (EC-EC, PC-PC) and heterotypic (EC-PC) cell contacts [88]. ECs are a source of diffusible factors which can impact PCs in terms of PC-precursor maturation, proliferation and migration [88].

Accumulated evidence shows that plateled-derived growth factor-B (PDGF-B) plays a critical role in the recruitment of PCs to newly formed vessels. During angiogenesis PDGF-B is expressed by the sprouting endothelium and platelet-derived growth factor receptor-β (PDGFR-β) is expressed by the PC/vSMCs progenitors [85, 138] suggesting a paracrine mode of interaction between the two cell types (see Figure 4.1). Therefore, an endothelial PDGF-B signal controls PC recruitment to angiogenic vessels. It is likely that the amount of PDGF-B available determines the number of PCs recruited [252]. It is of particular interest that only a subset of the ECs express PDGF-B in the angiogenic situation [85]. That is, PDGF-B expression is mainly seen in the cells situated at the tip of the sprouts.

In this way, Minakawa *et al.* [159] developed a chemotactic assay and showed that PCs

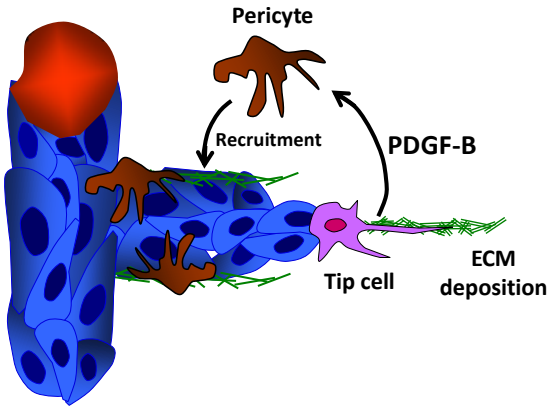

Figure 4.1: Schematic diagram showing the PDGF-B/PDGFR-β interactions with PDGF-B synthesised and secreted by the migratory endothelial tip cells. Endothelial-derived PDGF-B acts to recruit pericytes, which express the PDGFR-β, that then migrate and proliferate along newly formed blood vessels.

are chemotactically attracted to capillary-like structures (CLSs). One feasible reason for the observed association of PCs with CLSs could be the release of chemotactic products secreted by ECs in CLS formation.

ECs have been reported to synthesize FGF2 and its release from the cell cytoplasm may occur during cell injury or death [164]. FGF2 is angiogenic, as well as mitogenic [40] and chemotactic [208] for vSMCs. Thus, although its mechanism of release remains unclear, it is also a candidate for involvement in vSMC or PC recruitment by EC.

PCs may well play a leading role in angiogenesis. In the CL, the PCs are the first vascular cells to invade the granulosa folds of the ruptured follicle (during ovulation) [5]. This supports the view that PCs are pioneers in CL angiogenesis due to their ability to secrete ECM, which allows EC migration. This opposes the common view that PC recruitment lags behind that of ECs in the angiogenic process.

4.2.2 Endothelial cells and pericytes *in vitro*

The *in vitro* formation of capillary-like tubes by ECs is a powerful method to screen for various factors that promote or inhibit angiogenesis. However, isolation and culture of microvascular ECs from a solid tissue (e.g. CL) remains a hard task.

4.2.2.1 Isolated endothelial cells *in vitro*

ECs have been the target of *in vitro* studies with the aim to answer several fundamental biological questions regarding the cellular architecture of tubes and how, for instance, clusters of ECs can give branches and, therefore, network formation. However, the process of EC self-organisation *in vitro* to form vascular-like patterns is a complex biological process, involving a large set of interacting elements. Angiogenic cells undergo specific structural alterations regarding cell shape, cellular projections and cell surface modifications, indicating changes in intercellular interactivity.

In 1973, Gimbrone *et al.* [76] and Jaffe *et al.* [102] were the first who managed to successfully grow vascular ECs from human umbilical vein endothelial cells (HUVECs) *in vitro*. Subsequently, numerous *in vitro* systems of angiogenesis have been proposed (for a review, see Auerbach *et al.* [9]) with the aim to approximate as closely as possible the *in vivo* situation. Since new blood vessels are comprised of vascular ECs, *in vitro* models of angiogenesis mainly focused on cultured ECs. In most models, a two-dimensional arrangement of ECs is explored [183, 247, 248], whereas models with more cell types are scarce and we will refer to some of them in section 4.2.2.3.

4.2.2.2 Isolated pericytes *in vitro*

Interesting information regarding the possible functions of PCs has been derived by studying homogenous cultures of PCs [47, 50, 87, 143]. Cultured PCs appear as large, spreading, stellate cells with highly irregular edges. They display numerous long filamentous processes and are characterised by prominent intracellular fibers of actin. Their morphology differentiates them from ECs ('cobblestone-like' morphology [109, 193]), fibroblasts (long, spindle-shaped, with extended filopodia), and smooth muscle cells ('hill and valley' growth). It should also be noted that their growth is not contact-inhibited [192] and, after reaching confluence, PCs start forming multilayers.

A major problem in PC research, recognised by Zimmermann already in 1923 and still valid, is the general lack of unequivocal PC markers. The strong degree of uncertainty experienced in attempts to grow PCs *in vitro* is caused mainly by their occasionally claimed pluripotency (differentiate into either vSMC or fibroblast).

Several markers have been used to identify PCs, including smooth muscle α-actin (SMA), desmin, NG-2, PDGFR-β, aminopeptidase A and N, RGS5, and XlacZ4. However, none of these markers is absolutely specific for PCs, and none of them recognises all PCs; their expression varies between organs and developmental stages [8]. As a result, the heterogeneous morphology and marker expression make identification of PCs

a challenge.

Since PCs exist in close association with microvascular ECs *in vivo*, their physiologic functions are best examined in the context of their interactions with microvascular endothelium. However, there have been a limited number of *in vitro* co-culture (EC-PC) studies, which are discussed in the following section.

4.2.2.3 *In vitro* co-cultures of ECs and PCs

PCs have been proposed to play a significant role in regulating EC proliferation. Tissues with the greatest number of associated PCs such as the brain and retina were found to have the lowest microvascular EC turnover rate [234]. Studies on diabetic retinopathy also support the suggestion that PCs inhibit EC growth; prior to the rapid neovascularisation characteristic of this disease, there occurs a selective loss of PCs associated with the retinal capillaries [234].

Orlidge and D'Amore [173] developed an *in vitro* co-culture system to mimic the interactions between ECs (isolated from bovine adrenal cortex) and PCs/vSMCs (from bovine retinas). They found that an activated form of TGF-β1 produced by these co-cultures *totally* inhibited the growth of ECs (see Figure 4.2). TGF-β1 is a cytokine which can be found in a latent form on the plasma membranes of ECs and PCs and is activated once the two cell types come into contact [173].

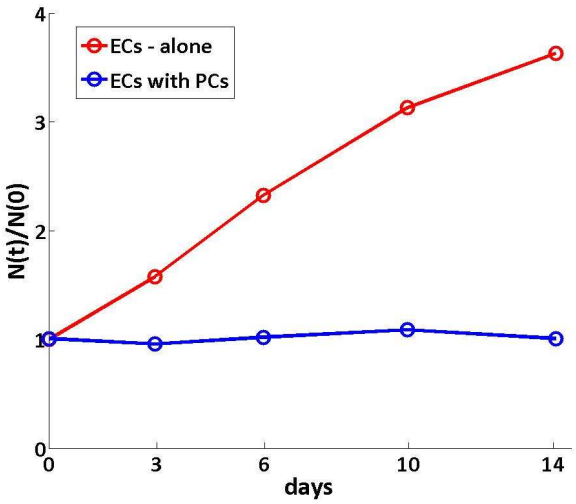

Figure 4.2: The effect of PCs on EC proliferation is depicted by comparing the normalised number ($N(t)/N(0)$) of ECs grown alone to the one of ECs in co-culture with PCs over time. Data redrawn from [173].

Yamagishi *et al.* [264] also studied interactions between retinal PCs and HUVECs. Close

contact of the two cell types was found to *partially* inhibit growth of HUVECs, whereas substitution of PCs with fibroblasts gave no inhibition.

Sato and Rifkin [209] confirmed that in a co-culture of bovine aortic ECs with bovine PCs or SMCs the latent form of TGF-β1 was activated resulting in the inhibition of EC movement.

Kondo *et al.* [118] showed that in co-culture with retinal PCs, the proliferation of retinal capillary ECs was significantly inhibited. However, no such inhibition was observed in a co-culture where contact between the two cell types was not allowed. Those results led to the hypothesis that the concentration of soluble growth factors emerged from PCs is important for the suppression of EC growth. Results in a later report from the same investigator [119] provided the first evidence that conditioned medium from the cultivation of PCs alone can inhibit retinal neovascularisation, further suggesting that the soluble growth factor is TGF-β1. The latter result is in contrast with the aforementioned experiments [173, 209, 264] which suggest that inhibition of EC growth is a result of TGF-β1 activated only when ECs and PCs come into contact.

Having provided the necessary biological background on endothelial and pericyte interactions, in the next section we present our model overview.

4.3 Model overview

4.3.1 Contact-inhibition of cell proliferation rate

An increasing number of agents has been shown to either positively or negatively influence the growth of vascular ECs. Best known among the stimulators of EC growth are acidic and basic FGF (aFGF; bFGF or FGF2) [39]. *In vitro*, it has been shown that ECs produce FGF2 [190, 218], and that endogenous FGF2 modulates EC proliferation and migration [208]. FGF2 is also expressed by other cultured cell types including fibroblasts, SMCs, and glial cells [53]. In addition, Lee *et al.* [131] found that the distribution of bovine pulmonary artery ECs (BPAE) division times showed a shift to shorter division times in the presence of FGF2, indicating the mitogenic effects of FGF2 on the growth of BPAE.

FGF2 has a dual action. Firstly, chemotaxis enhances EC clustering (and also strengthens EC-EC aggregation), the initial stage of angiogenesis on which our model focuses, and secondly, FGF2 promotes EC proliferation.

As we described earlier (see Figure 4.1), PC recruitment is mainly controlled through the PDGF-B/PDGFR-β signalling pathway. However, FGF2 could also serve to main-

tain PC recruitment to EC clusters and, thereby, enhance PC proliferation [88]. Other growth factors which have been shown to be mitogenic for PCs include heparin-binding epidermal growth factor and endothelin [88].

Despite the biological knowledge on the possible interactions between ECs and PCs as described above, a biologically meaningful mathematical model is required to be validated against biological measurements. Therefore, according to the available experimental data on co-culture systems described earlier in section 4.2.2.3, we decided to model the experimental design adopted by Orlidge and D'Amore [173]. In that experimental system, ECs were co-cultured with growth-arrested PCs in order to assess the negative effect of PCs on EC proliferation.

Therefore, our model is mainly based on the following assumptions which arise from the above study [173]:

1. ECs and PCs are randomly seeded in a 1:1 ratio.
2. PCs are growth-arrested, and only ECs are able to divide.
3. There is no FGF2 secreted by the cells or externally added in the domain.
4. TGF-β1 is secreted by both ECs and PCs at their common contact area.
5. TGF-β1 inhibits the EC growth.

Figure 4.3(a) shows a network diagram with all possible EC-PC interactions, while Figure 4.3(b) depicts the subset of interactions which we consider here as developed by [173].

4.3.2 The Cellular Potts Model (CPM) approach

Cell-based computer simulations can be an effective tool to check biological hypotheses and mechanisms. In our model, cell shape and cell-cell contacts play an important role in cell communication. Therefore, to understand the basic mechanisms of interactions between ECs and PCs, we adopted a two-dimensional Cellular Potts Model (CPM) approach [78] where both variables can be explicitly represented. The CPM is a discrete lattice model initially developed by Glazier and Graner to study the cell sorting behaviour that had been observed experimentally in *Hydra* aggregates [78], and it is based on an energy minimization principle. The CPM has already been used to model a multitude of biological phenomena including fruiting body formation of Dictyostelium [105], avascular tumour growth [106], cancer invasion [250] and vasculogenesis [155].

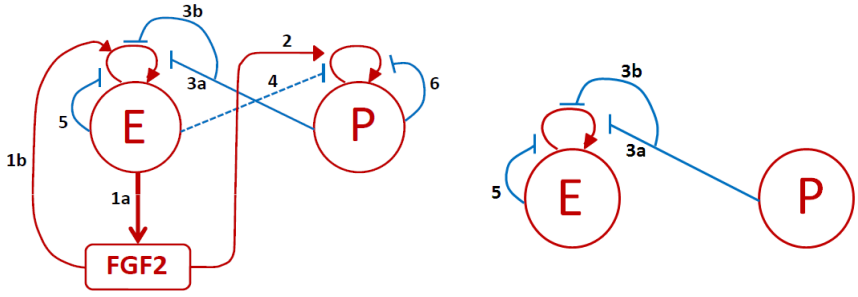

(a) (b)

Figure 4.3: Network diagrams present the EC-PC autocrine and paracrine interactions explained with the given numbers on the arrows as known from literature (a), and as developed by [173] (b). (1a) ECs secrete FGF2, which enhances the proliferation rate of ECs (1b), and PCs (2). PCs may inhibit EC growth by contact (3a), and by diffusive TGF-β1 (3b), which is activated once ECs and PCs come in contact. There is also some evidence that ECs might suppress PCs proliferation (4) but in lesser extent [173]. Note that (3a,b) and (4) is the heterotypic (EC-PC), whereas (5) and (6) is the homotypic (EC-EC and PC-PC, respectively) contact inhibition.

In the CPM, each cell which is placed on a square numerical grid (in $2D$) consists of multiple lattice sites (pixels). Every single pixel in an individual cell is given the same identity number, $\sigma = 1, ..., N$ (also called 'spin' in the original Potts model), where N is the total number of cells. In order to identify different cell types, cells are given a second identity, $\tau = 1, ..., k$, where k is the number of the different cell types. The substrate (medium, e.g. extracellular matrix) is normally represented as a generalised cell with $\tau = 0$. The energy of a configuration of identities is determined by summing the interaction energies (J) between pairs of neighbouring lattice sites. Therefore, J describes the relative strength of cell-cell adhesion that occurs via e.g. transmembrane cadherin proteins.

A description of all cell interactions are given through an effective energy function or Hamiltonian (H),

$$H = \sum_{(\vec{x},\vec{x'})} J_{\tau(\sigma(\vec{x})),\tau(\sigma(\vec{x'}))} \left(1 - \delta_{\sigma(\vec{x}),\sigma(\vec{x'})}\right) + H', \tag{4.3.1}$$

where $\tau(\sigma)$ represents the type of the cell occupying a grid space σ, which in our model can only be either an EC or a PC. The Kronecker delta function is $\delta_{x,y} = 1$, if $x = y; 0$, if $x \neq y$, and the term $(1 - \delta_{\sigma(\vec{x}),\sigma(\vec{x'})})$ ensures that adhesive energy only accrues at cell surfaces (see Figure 4.4). H' can be any constraint on the cell behaviour (e.g. chemotaxis [210],

haptotaxis [250], cell elongation [155]).

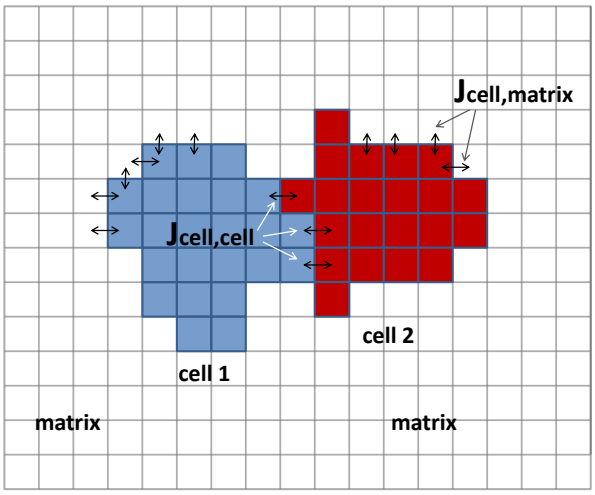

Figure 4.4: Adhesion energies (J) at cell-cell and cell-matrix interfaces as implemented at the CPM framework.

To mimic cytoskeletally driven, active surface fluctuations, a lattice site $\vec{x}$ and a neighbouring target $\vec{x'}$ is repeatedly and randomly selected, and we calculate how the effective energy would change if the initial site displaced the target. If the energy decreases H ($\Delta H = H_{new} - H_{old} < 0$), the change is allowed to occur. However, if H would increase ($\Delta H > 0$), the change will be accepted with Boltzmann probability, $p = \exp(-\Delta H/T)$. T is the 'temperature' (like thermal fluctuations in statistical physics [22]) of the system, which influences the likelihood of energetically unfavourable events taking place: the higher T, the more out-of-equilibrium the system will be. Biologically, T indicates the amplitude of cell membrane fluctuations (and not active cell movement), which is characterised by polarised membrane extension and retraction. On a lattice with M sites, M site copy attempts represent our basic unit of time, one Monte Carlo Step (MCS).

4.3.2.1 Cell area constraint

The energy in (4.3.1) is minimised by typically incorporating a constraint on the cell area,

$$H'_{area} = \lambda_A \sum_{\sigma>0} (\alpha_\sigma - A_\sigma)^2 , \tag{4.3.2}$$

with α_σ being the current area of a cell. The cells are constrained to have an area close to a fixed target area, A_σ, so that they do not grow or shrink. The factor, λ_A, is the strength of the cell area constraint which corresponds to the elasticity of the cell membrane. The growth constraint, H'_{area}, delivers a penalty to the total energy for any deviation from the target area and summation goes for all cells with the exception of the medium ($\sigma > 0$).

4.3.2.2 Modelling of cell random motion

Mombach and Glazier in [161] claimed that the thermodynamic approach (regarding T: 'temperature') used in the CPM approach [78] is an appropriate way of modelling the random component of cell movement, as experimental evidence indicates that individual cells in a cell mass exhibit Brownian motion in the absence of chemical or adhesion gradients [161].

However, in order to achieve (random) motility of the cells in a more realistic way (rather than only fluctuations of the cell membrane), we include an extra reduction in energy for motion

$$H'_{motility} = r(cos\theta(t), sin\theta(t)) \cdot (\vec{x}_{CM} - \vec{x'}_{CM}), \tag{4.3.3}$$

with r representing the cell speed from its centre of mass ($\vec{x}_{CM}$), and $\theta(t) \in [0, 2\pi]$ the rotation angle which updates every t_{per} (the persistence time). The t_{per} refers to the average duration of locomotion in one direction before a random change of direction.

Active cell motility using the CPM framework was also attempted in some other modelling studies. In modelling collective endothelial cell motion (where cells can be both motile and adhere to one another), Szabo *et al.* in [242] incorporated active cell motility in an attempt to understand streaming behaviours in high density cultures. The authors modelled active cell motility by first assigning a cell polarity vector $\vec{p}_i$ to each cell i and then increase the probability of the motility steps that advance the cell centre in the direction parallel to $\vec{p}_i$ as

$$w(\vec{x} \to \vec{x'}) = m \sum_i \Delta\vec{X}_i(\vec{x} \to \vec{x'}) \frac{\vec{p}_i}{|\vec{p}_i|}, \tag{4.3.4}$$

where m sets the magnitude of the bias, and $\Delta\vec{X}_i$ represents the displacement of the centre $\vec{x}$ of cell i. The cell polarity vector was an attempt to represent the localisation and magnitude of the biochemical changes characterising the leading edge of a migratory cell. Cell polarity vectors are updated by assuming a spontaneous decay k and a positive feedback from cell displacements as

$$\Delta\vec{p}_i = -k\vec{p}_i + \Delta\vec{X}_i. \tag{4.3.5}$$

A characteristic memory length (persistence time) k' of the polarisation vector is defined as $k' = 1/k$.

In another recent work, Szabo *et al.* in [243] studied the cell invasion from an aggregate into a surrounding ECM. The authors modelled active cell motility according to their previous work [242]. By exploring the interplay between haptotaxis, matrix degradation and active cell movement, the model showed that the cells are able to both invade the ECM and follow the ECM tracks, and also that ECM can increase motion persistence.

4.3.2.3 Modelling the EC cell cycle: contact-inhibition

Instead of explicitly modelling the cell cycle of the ECs by considering all the intermediate stages as in [251], we use a simple phase model as in [180] in which $\phi^j \in [0,1]$ represents the phase of the cycle of EC j, with

$$\frac{d\phi^j_{EC}}{dt} = \frac{1}{1+a_4P^j}\frac{1}{1+a_5TGF\beta1}a_1, \tag{4.3.6}$$

and the reset condition that when $\phi^j_{EC} = 1$ it is reset to zero (so that $\phi^j_{EC} = 0$ represents the start of the cell cycle, and $\phi^j_{EC} = 1$ its completion). In equation (4.3.6) the right hand side specifies the speed of progress through the cycle. The constant rate, a_1, specifies the speed of the phase in the presence of no additional factors. In section 4.4, we discuss further on the value of a_1.

The growth of vascular cells *in vitro* is characterised by cell-cell interactions, where neighbouring cells touch one another. If during this growth process an EC becomes surrounded by other cells, it will stop growing [130]. Therefore, only a fraction of cells will continue to grow and divide. As we mentioned earlier, Orlidge and D'Amore [173] found that PCs co-cultured with ECs adversely affect the EC growth as a result of the TGF-β1 being activated when the two cell types come into contact.

By considering the above statements and findings, we model EC growth inhibition by assuming that the proliferation rate of ECs is inversely proportional to the *ContactArea*

(P^j) with its neighbours. P^j is the ratio between (cell j)-neighbour (of either type) common perimeter and the total perimeter of cell j,

$$P^j = \frac{\sum_{(\vec{x},\vec{x'})} \left(1 - \delta_{\sigma(\vec{x}),\sigma(\vec{x'})}\right) \left(1 - \delta_{\sigma(\vec{x}),0}\right) \delta_{\sigma(\vec{x}),j}}{\sum_{(\vec{x},\vec{x'})} \left(1 - \delta_{\sigma(\vec{x}),\sigma(\vec{x'})}\right) \delta_{\sigma(\vec{x}),j}}, \tag{4.3.7}$$

with $\sum_{(\vec{x},\vec{x'})}$ summing over all pairs of adjacent sites in the lattice. $TGF\beta1$ in equation (4.3.6) is the concentration of the growth factor secreted at the common perimeter, and the constants a_4, a_5 are the strengths of contact inhibition by mechanical contact, and the diffusive TGF-β1, which is described by the following PDE

$$\frac{\partial TGB\beta1}{\partial t} = D\nabla^2 TGF\beta1 + s - \delta TGF\beta1, \tag{4.3.8}$$

with D being the diffusion constant, and s, δ represent the secretion and decay rate, respectively. Table 4.1 summarises the behaviours of ECs and PCs as implemented in our model based on the experimental system of Orlidge and D'Amore [173].

Overall, in reality not all cells in a cluster are exposed to the same amount of inhibition [115], which is implied from equation (4.3.6); that is, the cells at the centre of a cluster experience more contact and, therefore, their mitotic phase is delayed compared to the cells located at the perimeter of a cluster and the individual cells.

Taking further the mitosis into account, division in our model applies in the middle of and perpendicular to the longest cell axis. After mitosis, both daughter cells inherit half of their mother's target area. This assumption is in agreement with *in vitro* experiments which have shown that the positioning of microtubule asters is such that the cell will divide perpendicular to the longest axis [93]. However, Drasdo *et al.* in [68] assumed that the orientation of cell division is determined by the direction of the total force exerted on the dividing cell by all its neighbours.

Table 4.1: Rules for the various cell types based on the experimental system of Orlidge and D'Amore [173].

Cell behaviour	Endothelial cells	Pericytes
growth	X	X
mitosis	✓ (see equation (4.3.6))	X
secrete TGF-β1	only when in contact with pericytes	only when in contact with endothelial cells

4.4 Methods

This section outlines the basic steps of the *in silico* model development along with the experimental systems [40, 130, 173] used for validation. Our simulations use the open-source simulation environment CompuCell3D (CC3D) and Python scripts specifically developed by the author.

4.4.1 Model setup

4.4.1.1 Cell density

In co-cultures with direct contact, Orlidge and D'Amore [173] plated the growth-arrested PCs at a density of 20,000 cells per 16-mm well. After overnight attachment equal numbers of capillary ECs were added into the wells.

Therefore, 40,000 cells (EC:PC=1:1) in total were plated in an Area$\simeq \pi R^2 \simeq 2\text{x}10^8 \mu m^2$. If each cell is about 100 μm^2 [263], that means the initial area coverage was $\sim$2%. Since the numerical domain in the *in silico* model is 200x200 pixels^2 and each pixel is $2\mu m$ (see section 4.4.2), that implies $N = 32$ *in silico* cells (ECs and PCs).

4.4.1.2 Initial conditions

To simulate the cell interactions, 32 cells (both ECs and PCs) occupy randomly chosen positions within the grid. At this point we should make clear that since ECs and PCs are randomly distributed in our *in silico* domain, heterogeneities in the spatial distribution of seed cells may affect the observed cell proliferation rates. In order to avoid any biased allocation of the two cell types, each simulation starts with a different initial condition (seeding positions of the cells). Figure 4.5 shows a representative initial condition, with ECs and PCs being in a ratio of EC:PC=1:1 as in [173].

Note that by using the existing plugins in CC3D to generate the initial conditions, different seed numbers produce different sequences of random numbers with the ratio of EC:PC=1:1 not being exact. Since perturbation experiments in [173] with different cell ratios showed to greatly impact the EC growth, we chose to generate random locations of the cells in the numerical domain by using our scripts in MATLAB software package in order to keep the ratio exact.

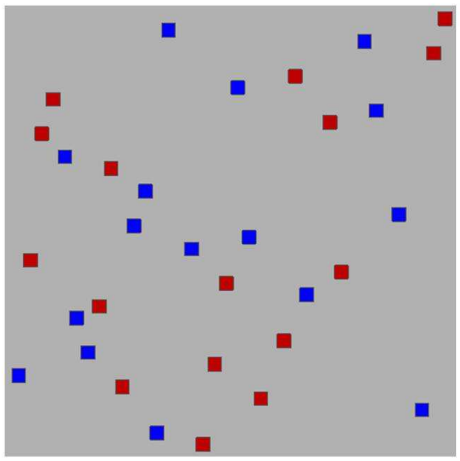

Figure 4.5: A representative initial configuration of the simulation, with ECs (red) and PCs (blue) randomly distributed in the numerical domain in a ratio EC:PC=1:1.

4.4.2 Space & time conversions

The target area of each cell is 25 pixel^2. The ECs *in vitro* have approximately 10 μm diameter and 100 μm^2 area [263]. This sets the space conversion as: 1 pixel = 2 μm. Thus, each cell in the *in silico* model represents 1 cell in reality. We ran our simulations on a 200x200 CPM lattice with periodic boundary conditions.

Based on experimental data [130], the speed of ECs without the existence of any additional growth factor was $\sim 0.4 - 0.5\, \mu m/min$. By considering the persistence time ($\sim$ 30min) in [130], we set the temporal conversion as 1 MCS $\simeq$ 1 min so that cells can move for several MCS before changing direction, a value similar to the one used in other CPM studies [155, 227, 242].

4.4.3 The initial phase $\phi(0)$ and the *quiescent* period (t_q)

In the experimental system [130], the authors found that the period between inoculation (seeding of cells) and the first division varied widely among the ECs of a population. Some divided between 12 and 18 hrs after inoculation, others required more than 24 hrs. The wide variability of the first division time complicates the choice of the initial conditions for our simulations. Therefore, for the first division of the cells, the cell phase counters in equation (4.3.6) are loaded with a random number ($\phi(0)$: 'initial' phase) such that $\phi(0) \in (0, 1)$. If this is not done, the model will underestimate the time interval required for the first division of each cell and will over-predict the cell

population in the initial stages of proliferation [130]. Note that $\phi(0)$ can be close to 1 since some cells before being dissociated from a tissue, might be close to division, and $\phi(t)$ is reset to zero when $\phi(t) = 1$.

Another important issue regarding the choice of the initial conditions in our simulations is about the *quiescent* period (t_q: the time from the initial *in vitro* cell seeding up to several hrs), during which cells adhere to the tissue culture surface, spread, and then start migrating. In terms of implementation, the phase counter for each cell starts to progress after ∼4 hrs [154]. That is, $\phi(0)$ for each cell remains fixed for the first 4 hrs.

4.4.4 Parameters

The default parameter values used for our simulations are summarised in Table 4.2, unless otherwise stated. Below we provide a discussion on how some of those were estimated.

4.4.4.1 Doubling time of ECs: estimation of parameters a_1

The constant rate a_1 as in equation (4.3.6) was estimated using data from D'Amore and Smith [40]. In that experimental system, ECs and PCs were cultured independently in varied concentrations of different growth factors (e.g. FGF2) in order to investigate the contribution of each growth factor on the cells' proliferation rate. Below we explain how we estimated these rates for the ECs.

Initially, 10,000 ECs were seeded and in the absence of FGF2 (FGF2=0 ng/ml) the cell number tripled in approximately 3 days. Therefore, by considering $t_q \sim 4$ hrs, the basic EC cycle time is ∼36 hrs=2160 MCS, so $a_1 = \frac{1}{2160}$ MCS^{-1} = 0.00046 MCS^{-1}.

4.4.4.2 Cell-cell adhesion: contact energies (J)

Contact communication is known to result in the initiation of different developmental fates [80]. The differential adhesion hypothesis (DAH), advanced in the 1960s from Steinberg [236], proposed that cell sorting dynamics arise from tissue surface tensions that in turn arise from differences in intercellular adhesiveness, which served as a basis for quantitative approaches on cell adhesion [161].

In the CPM, interactions between neighbouring pixels have an effective energy (J), which characterises the strength of cell-cell and cell-matrix adhesion. Larger J means more energy is associated with the interface between two cells, which is less energetically favorable, corresponding to weaker adhesivity.

Our simulations used up to 3 generalised cell types: medium, ECs, and PCs. The contact energies among them are shown in Table 4.2. Note that $J_{EC,PC} < J_{EC,EC} \ll J_{PC,PC}$ implies that: 1) the heterotypic (EC-PC) contacts are stronger than the homotypic (EC-EC, PC-PC) ones, and that 2) ECs adhere more strongly between them (create zipper-like structures along their borders through adherent junctions [45]) compared to the loose contacts between PCs as shown in Figure 4.6.

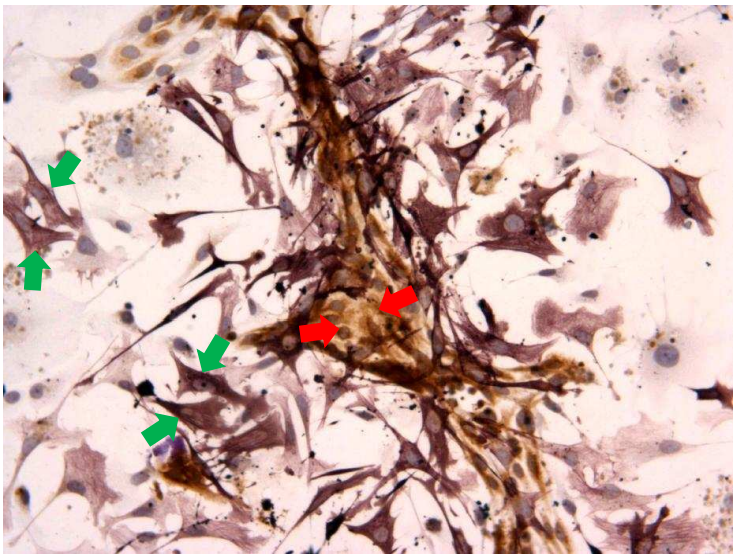

Figure 4.6: Snapshot from EC-PC co-culture system [Courtesy of Dr. R.S. Robinson], showing the loose contacts between PCs (green arrows) compared to the strong ones between ECs (red arrows). Key: ECs (brown); PCs (dark purple).

It is worthy to mention that although it shows to be of great importance, there is very limited experimental work on the evaluation of the strength of cell-cell adhesion (either homotypic or heterotypic).

4.4.4.3 TGF-β1: diffusion, secretion and decay

TGF-β1 is a key regulator of cell growth and differentiation. It exists in a latent (inactive) form, and is activated once cells (e.g. ECs, PCs, macrophages) come into contact [173].

In our model, TGF-β1 is activated at the contact area between ECs and PCs, and is secreted by both cell types. We used the same diffusion parameters as proposed by Merks *et al.* in [155, 157] (see Table 4.2). We used these values to obtain steep gradients by assuming that the diffusion of TGF-β1 is a local event and mainly affects the ECs in close proximity, since its diffusion length ($L = \sqrt{\frac{D}{\delta}} = 30\mu m \sim 3$ cell length) is short.

Table 4.2: Default parameter settings for simulations

Parameter	Description	CPM value	Dim/nal value	Reference
Cell features:				
(for ECs and PCs)				
A	cell target area	25 pixels^2	100 μm^2	[263]
λ_A	resistance to changes in size	10	/	/
T	cell-membrane fluctuations	10	/	/
Adhesion:				
(contact energies)				
J_{EE}	EC-EC	15	/	/
J_{PP}	PC-PC	100	/	/
J_{EP}	EC-PC	5	/	/
J_{cM}	cell-medium	20	/	/
TGF-β1:				
D	diffusion constant	1.5 pixels^2/MCS	10^{-13} m^2/s	[155, 157]
s	secretion rate	0.006 nM/MCs	10^{-4} nM/s	[155, 157]
δ	decay constant	0.006 1/MCS	10^{-4} 1/s	[155, 157]

4.5 Results

Having provided the basic biological background and our model overview based on the experimental system of Orlidge and D'Amore [173], our aim is to proceed with the following systematic approach: we start with single cell experiments in different motility scenarios (low, intermediate, high speed and persistence time). Then we proceed with pure EC populations (without PCs) to assess cluster formation, with and without mitosis, in the different motility scenarios. Finally, we present results from simulations with both ECs and PCs in order to investigate the mechanisms for the total inhibition of the EC growth.

4.5.1 Single cell experiments

In this section, in the absence of any external influence (e.g. FGF2), we present results from single cell experiments with the aim to estimate the motility parameters: r (speed of motility) and t_{per} (directional persistence time), as presented in equation(4.3.3).

By considering the sparse cell populations in [173], we expect that the properties of random cell motility (r and t_{per}) may significantly affect the likelihood of cells making contacts, which can lead to cell cycle delay.

Mathematically, a random walk is a series of steps, where each step is taken in a completely random direction from the one before. This kind of path was famously analysed by Albert Einstein in a study of Brownian motion and he showed that the mean square of the distance (*msd*) travelled by a particle following a random walk is given by

$$msd(t) = \langle \Delta_i(t)^2 \rangle = \langle (\vec{x}_i(t) - \vec{x}_i(0))^2 \rangle, \tag{4.5.1}$$

where, $\vec{x}_i$ denotes the centre of cell i and $\vec{x}_i(t) - \vec{x}_i(0)$ is the (vector) distance travelled by the cell over some time interval of length t. The squared magnitude of this vector is averaged (as indicated by the angle brackets) over many such time intervals.

If the cell encountered no other cells, travelling ballistically, then the distance it travelled would be proportional to the time interval - distance equals velocity times time - and the *msd* would increase quadratically with t. In denser phases, quadratic behaviour holds only for a very short time interval, of the order of the mean collision time. Beyond this time the motion is better described as a random walk, for which the *msd* increases only linearly with time ($msd \sim t$). The rate of growth of the *msd* depends on how often the cell suffers collisions. At higher density, it will take longer to diffuse a given distance, as other cells continually impede its progress.

The limiting slope of $msd(t)$, considered for time intervals sufficiently long for it to be in the linear regime, is related to the self-diffusion constant D,

$$\lim_{t\to\infty} \frac{d\langle \Delta_i(t)^2 \rangle}{\Delta t} = 2nD \tag{4.5.2}$$

where, n is the dimension of the space.

In Figure 4.7, results from simulation studies are shown, exploring the movement of a single cell under various conditions ($r = 10, 30, 90$ and $t_{per} = 10, 30, 90$ min). In the left-hand column, cell positions (the centre of mass is calculated to determine the (x, y) coordinate values) are plotted for 50 simulations. The central column shows the corresponding displacement (d(t)=$\sqrt{\vec{x}_{CM}(t+\Delta t) - \vec{x}_{CM}(0)}$, with $\Delta t = 1$ min) for each simulation in 24 hrs with the red thick line representing the average displacement of all simulations. The bottom plot summarises the averages for each of the scenarios. The right-hand column shows the instantaneous speed ($S = \vec{x}_{CM}(t+\Delta t) - \vec{x}_{CM}(t)$) of a cell for a single experiment. In the experimental system of Lee *et al.* [131], persistent random walks were performed by bovine pulmonary artery ECs (without FGF2) with $t_{per} \sim 30$ min and $S \sim 0.4 - 0.5\, \mu m/min$. Therefore, by fixing $t_{per} = 30$ min, we found that $r \simeq 30$ is to be the value which gives the right estimation for speed.

In addition, since equation (4.5.2) implies $\langle \Delta_i(t) \rangle \sim 2\sqrt{Dt}$ (for $n = 2$), we approximated the diffusion of the random walk (for $r = 30$ and $t_{per} = 30$ min) to be $D = 0.625\, \mu m^2/min$, which is consistent with various estimates (see supplementary material in [180]). Figure 4.7 also reveals that speed depends only upon r and not on t_{per}.

In modelling collective endothelial cell motion, Szabo *et al.* in [242] used $t_{per} = 1$ hr, and in [243] Szabo *et al.* in a study of cell invasion in an ECM environment used $t_{per} \sim 2$ hrs for unconstrained motion and ∼10 hrs in a constrained ECM environment. In [135], amoebae showed a persistence time ∼10 min beyond which they started to lose their direction. Experimental studies from Stokes and Lauffenburger [239] on the locomotion of microvessel ECs and fibroblasts have shown that these cells execute persistent random walks in culture with calculated speed values in the range 0.1-1 $\mu m/min$ and t_{per} in 0.1-5 hrs. In [258], Ware *et al.* studied the effect of epidermal growth factor (EGF) treatment across a range of human matrix substratum (Amgel) levels on fibroblast migration speed and persistence time. Findings revealed that, in the absence of EGF, cell migration speed and directional persistence are relatively independent of Amgel level. The net effect of EGF is to increase the frequency of changes in the cell direction. However, the mean persistence time with or without the effect of EGF was ∼30 min. Taking the above measurements into consideration, we may deduce that speed and persistence time of cell motion depend on the type of cells and the experimental sys-

tem. As we mentioned above, with regard to our model, in the absence of any specific data on EC motility in [173] we use $t_{per} = 30$ min as described by Lee *et al.* [131], since their model shares important similarities with ours (e.g. sparse EC population cultured without any additional growth factors).

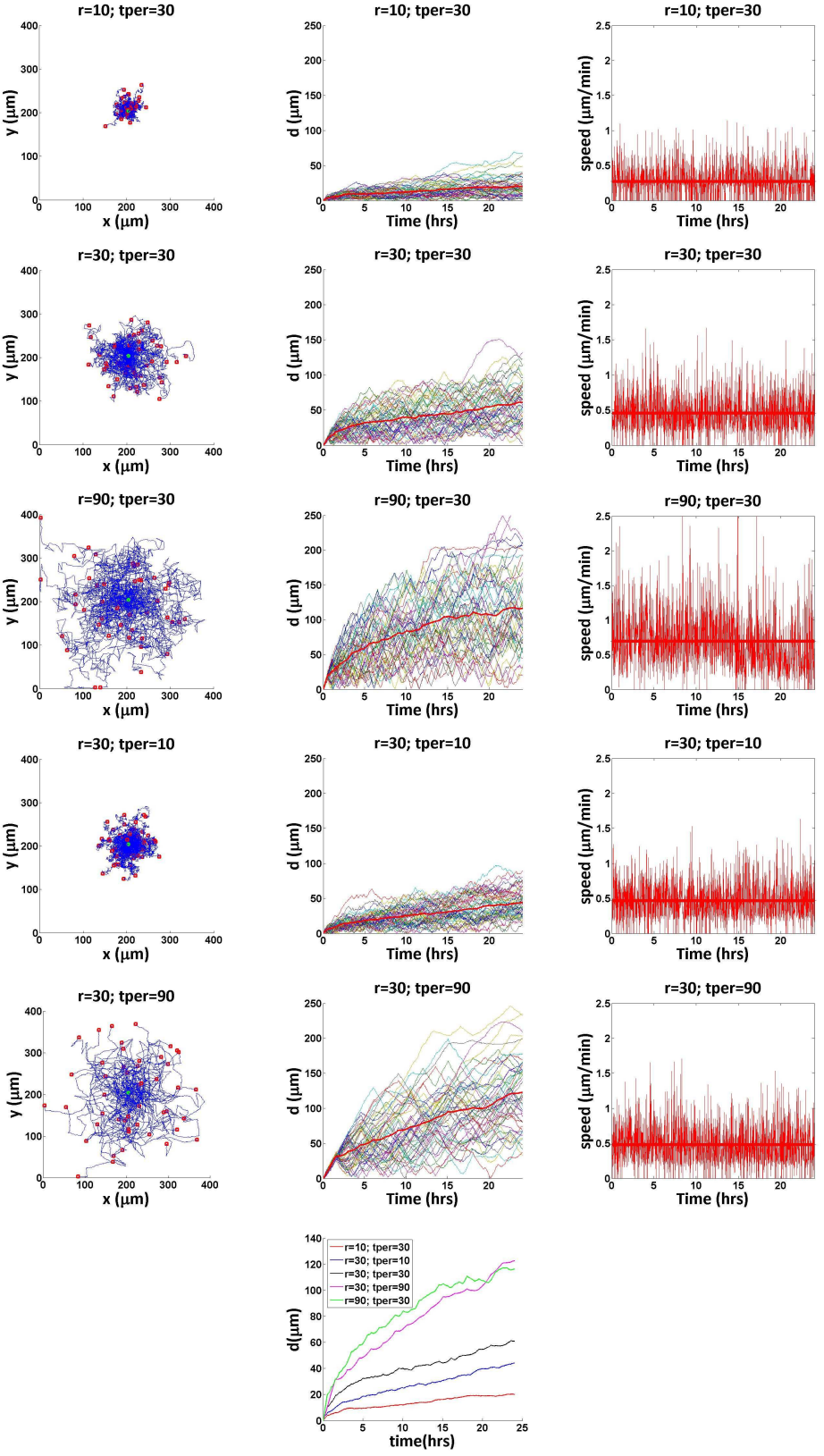

Figure 4.7: Motion statistics from single cell experiments under various conditions ($r = 10, 30, 90$ and $t_{per} = 10, 30, 90$ min) over 24 hrs. The three columns represent (left to right) cell positions, displacement (d), instantaneous speed.

4.5.2 Simulations with only ECs

Having assessed the role of migration speed (r) and directional persistence time (t_{per}) with single cell experiments, in this section, our aim is to investigate the effects of those on pure EC populations (without PCs) first, and how they affect cell aggregation (cluster formation) and, therefore, contact inhibition.

4.5.2.1 Effects of migration speed (r) and persistence time (t_{per}) on cluster formation and contact inhibition

Cell aggregation could be governed by multiple factors, such as secreted molecules attracting the cells toward each other (chemotaxis), by changes in the adhesive properties of cells (cell-cell adhesion), cell proliferation (consecutive divisions of non-migrating cells), random cell motility, haptokinetic motility (cell-matrix adhesion), and also cell density.

Figure 4.8 shows results from simulations with only ECs without mitosis. Plots in the first row show that in a low speed ($r = 10$; red line) environment, regardless of the persistence time, the numbers of both individual (I) and clustered (C) ECs remain approximately constant over 1.5 days. (Note that we define a cluster to be any group of cells (more than two in number and independent of type), which are in contact.) That implies little to no clustering, since cells are not able in such a case to move long distances and contact other cells. On the other hand, in higher speeds ($r = 30, 90$; blue, black curves) the likelihood of cell-cell collision increases. However, when $r = 90$ the number of individual and clustered cells exhibit a 'noisy' behaviour (see last two plots in the first row) which implies 'impaired' (not stable) clustering. The latter relies on the fact that in high speed scenarios, two cells which collide during their movement are more likely to detach from each other and return back to individual. This is in contrast to lower speed scenarios, where cells remain clustered once they contact other cells (stable clustering). Bar charts in the last three rows confirm results from above; that is, when $r = 30$ and $t_{per} = 30, 90$, the number of individual cells (categorised as cluster size=1) decreases compared to the other cases, suggesting that medium motility ($r = 30$) enhances clustering.

Figure 4.9 shows results from simulations with only ECs with mitosis. Remark that $t_q \sim 4$ hrs represents the *quiescent* period (see section 4.4.3), the time required from cells to establish in culture before start moving, dividing etc. Therefore, for each motility scenario we ran the model for $t = 4$ hrs and $t = 3$ days in order to assess clustering before and after cell division. Results from the last three rows show that all the motility

scenarios exhibit similar (clustering) results up to 4 hrs (before division). Similarly, no obvious differences are observed at later time points (3 days), among results from low motility scenarios ($r = 10; t_{per} = 10, 30, 90$). However, in medium motility ($r = 30$) by increasing t_{per} we notice that the number of small clusters (cluster size=2) decreases while the number of bigger clusters (cluster size=4) increases. This is a consequence of the ability of cells to move for a longer time before they change direction, and that increases the likelihood of making contact with other cells. In the high speed scenario ($r = 90$) increased t_{per} results in less clustering; that is, the number of individual cells increases, while the number of bigger clusters drops. In addition, note that if $r = 90$ and persistence time is either medium or high ($t_{per} = 30, 90$), the number of individual cells in 3 days is greater than the one in 4 hrs. That results from the interchange of cells from clustered to individual, and vice versa, as was described in Figure 4.8. Plots in the first row (Figure 4.9) support the aforementioned results. In particular, if $r = 90$, the number of individual cells, regardless of t_{per}, does not reach zero as opposed to low and intermediate cell speeds ($r = 10, 30$). Furthermore, the individual cells increase as t_{per} becomes larger; in fact, note that if $t_{per} = 30, 90$ the number of individual cells (I) overtakes the number of clustered cells (C).

In biological terms, increased cell speed implies more active and rapid membrane extensions. Concurrently, there are increased chances for the cell to change direction and, thus, its persistence time should decrease [258].

Having provided results on EC aggregation from different motility scenarios, a first attempt of our model is to estimate parameter values in equation (4.3.6) such that model assumptions summarised in section 4.3.1 allow one to reproduce quantitative results (see Figure 4.2) presented by Orlidge and D'Amore [173].

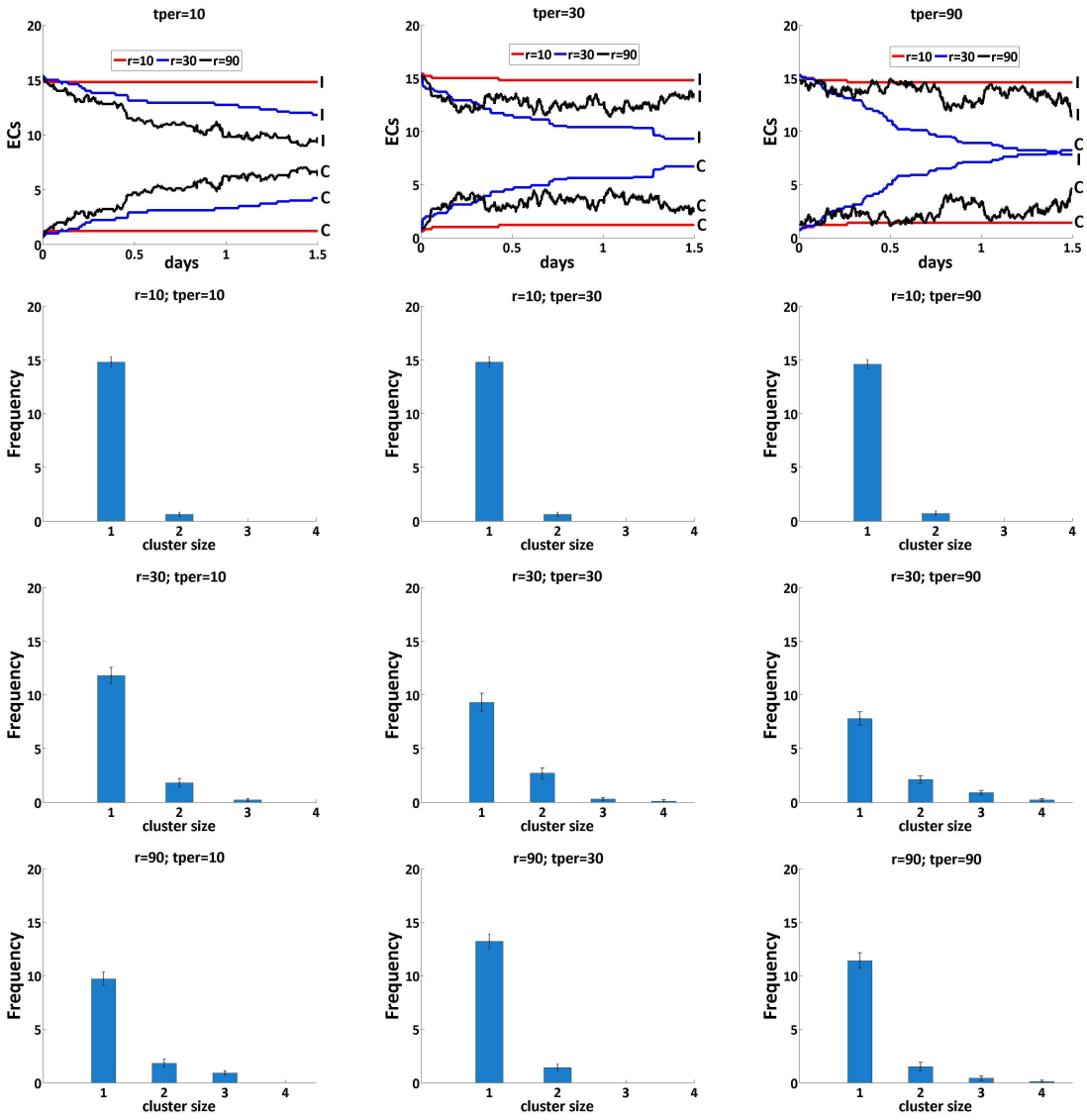

Figure 4.8: Simulation results with only ECs (N=16 cells) without mitosis for the different motility scenarios for cell speed ($r = 10, 30, 90$) and persistence time ($t_{per} = 10, 30, 90$ min). First row of plots present the number of ECs over time. Key: individual cells (I); clustered cells (C). Each curve represents the mean of 10 simulations for 36 hrs. The plots below present the number of clusters over size. Error bars show the mean of simulations $\pm$ S.E.M.

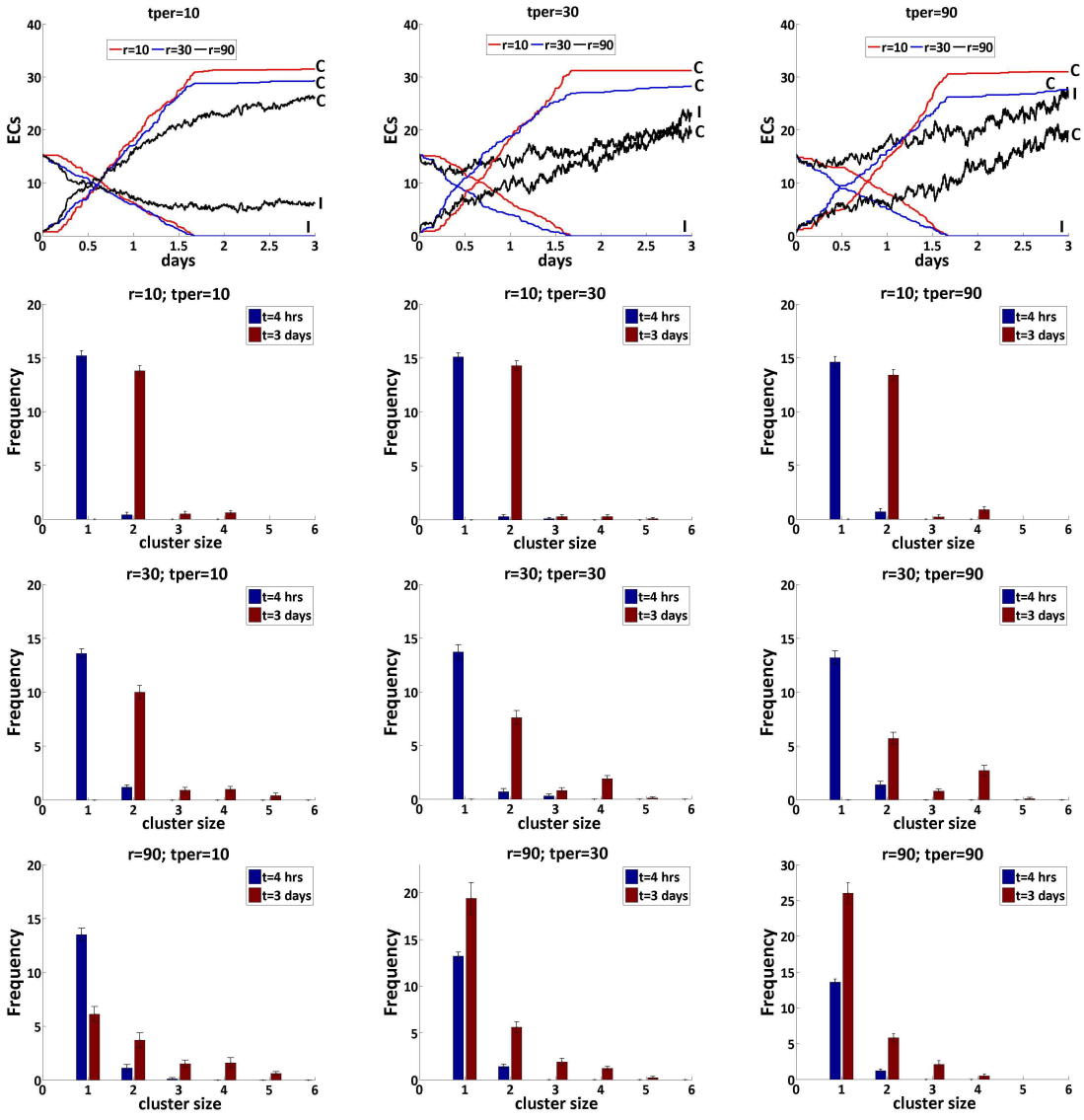

Figure 4.9: Simulation results with only ECs (N(0)=16 cells) with mitosis for the different motility scenarios for cell speed ($r = 10, 30, 90$) and persistence time ($t_{per} = 10, 30, 90$ min). First row of plots present the number of ECs over time. Key: individual cells (I); clustered cells (C). Each curve represents the mean of 10 simulations. The plots below present the number of clusters over size for both $t = 4$ hrs (blue bar) and $t = 3$ days (red bar). Error bars show the mean of simulations $\pm$ S.E.M.

4.5.2.2 Estimation of parameter a_4: strength of contact inhibition

In this section, our aim is to estimate parameter a_4, the strength of the mechanical contact inhibition, in the absence of any other effects (e.g. TGF-β1). Therefore, we ran simulations with ECs only (for the moment, excluding PCs) by retaining the same cell density in the *in silico* domain as in the experimental system of Orlidge and D'Amore [173]. In the absence of PCs there is no activated TGF-β1 and, therefore, the equation (4.3.6) is reduced to

$$\frac{d\phi_{EC}^{j}}{dt} = \frac{1}{1 + a_4\, P^j} a_1. \tag{4.5.3}$$

Several scenarios of motility were tested in section 4.5.1. Due to the lack of data on cell motility from the *in vitro* experiments in [173], we postulate that cells therein exhibited medium motility, since they were not affected from any external signals (e.g. addition of growth factors). Therefore, results that follow were executed in a medium motility ($r = 30$) and persistence time ($t_{per} = 30$) environment, unless otherwise specified. Figure 4.10 presents the normalised number of ECs (N(t)/N(0)) over time showing the value of parameter a_4 which is closer to the data points. The sparse cell density results in a step-like endothelial growth for the first ~6 days, however, in the following section we show that the growth becomes more linear by increasing the number of cells in the *in silico* domain.

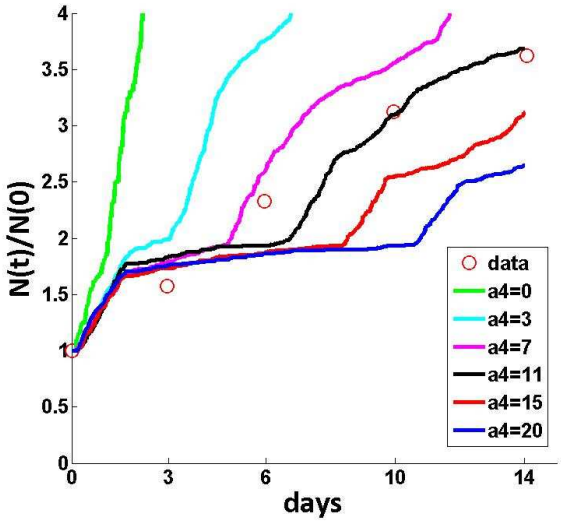

Figure 4.10: Normalised number of ECs (N(t)/N(0)=16) over time by varying a_4, the strength of contact inhibition. Each curve represents the mean of 10 simulations. The estimated value of $a_4 \sim 11$ is closer to the experimental data from Orlidge and D'Amore [173] (represented by '$\circ$'), where ECs were cultured alone (without PCs). For the rest of the simulations a_4 is taken to be $a_4 = 11$, unless otherwise specified.

4.5.2.3 Vary initial cell density

By considering the step-like EC growth for the first ∼6 days as shown in Figure 4.10, in this section, our aim is to assess the impact of the initial cell density on the EC growth.

Figure 4.11 depicts theoretical predictions for two different endothelial seeding densities (without FGF2). It is shown that if we increase the EC density (N=32 ECs), cell growth becomes substantially linear. This is a consequence of the increased cell collisions and the more intensive contact inhibition in a higher-density population. On the other hand, cells in a lower-density population (N=16 ECs) are more synchronised; that is, the first division times of the majority of cells (mainly individual) are similar which results in the step-like EC growth.

Regarding the EC density, Szabo *et al.* [241] in a multicellular sprouting model mentioned that cell density determined the interconnectedness of the network structure, and also influenced the characteristic pattern size. In particular, by measuring density as the ratio of the area covered by cells and the overall simulation area, at densities higher than 55%, the linear structures gradually disappeared, whereas at densities under 20%, there were not enough cells to form interconnecting clusters.

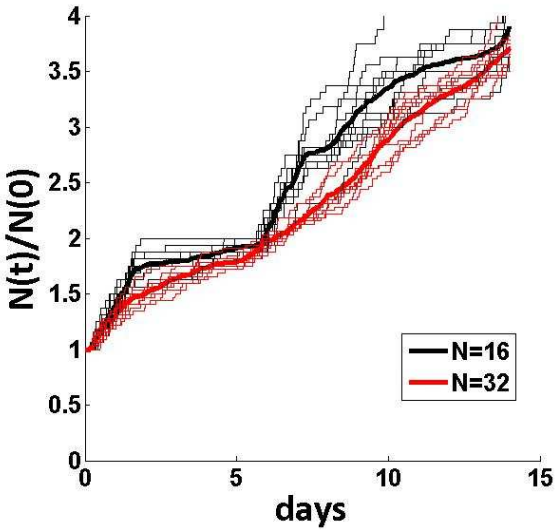

Figure 4.11: Normalised number of ECs (N(t)/N(0)) over time by varying the seeding number of ECs (N=16, 32). In a low-density population, we observe a step-like EC growth. However, in a higher-density population, the growth becomes more linear. Each group of curves with different colour presents simulations from different cell density with the thick curves being the mean of each group of 10 simulations.

4.5.2.4 Vary initial cell density & cell motility

Results in the previous section highlighted the importance of the initial cell density on the EC growth. As cell density increases, contact inhibition starts to dominate and restricts the migration of individual cells. More cells are in contact with others and, therefore, they become less proliferative. Note that in cancer cells the mechanism of contact inhibition is usually disrupted, resulting in uncontrolled cell movement and sustained cell proliferation [245]. Furthermore, Lee *et al.* [130] using a cellular automaton model for the proliferation of migrating ECs showed that the seeding (initial) cell density, the cell speed, and the spatial distribution of the cells are crucial parameters in determining the temporal evolution of cell proliferation rates.

Motivated by the cell behaviour in [245] and findings in [130], in this section, our aim is to assess the concurrent variation of cell density and cell motility on the EC growth.

Figure 4.12 shows simulation results from three different cell densities (N=16, 32, 96) and cell speeds ($r = 10, 30, 90$), while keeping persistence time constant ($t_{per} = 30$). It is clear that in a low cell density (N=16) and high motility ($r = 90$) environment the proliferation increases. This is a result of the reduced cell collisions (in small N), and also the detachment of cells from clusters resulting in more individual (and more proliferative) cells (in large r).

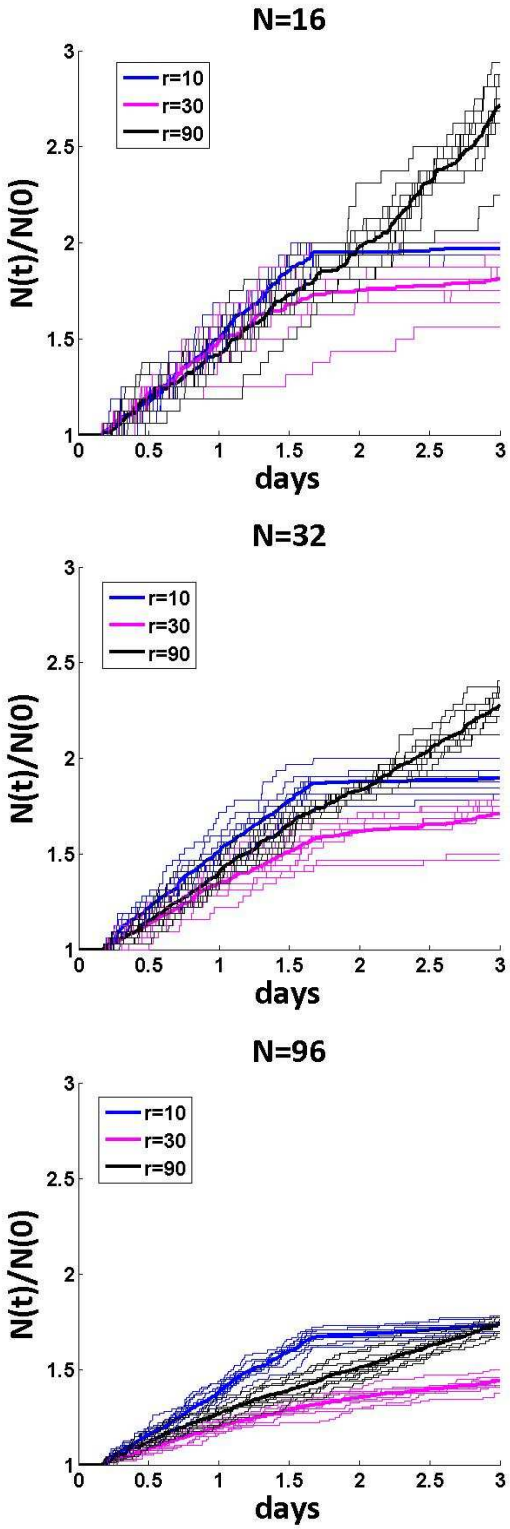

Figure 4.12: Normalised number of ECs (N(t)/N(0)) over time by varying the seeding number of ECs (N(0)) along with the cell speed (r). Each group of curves with different colour presents simulations from different cell density and cell speed with the thick curves being the mean of each group of 10 simulations.

4.5.3 Simulations with both ECs and PCs

The main goal of this study is to shed light on the pericyte-mediated inhibition mechanism on the EC growth. Therefore, in this section we extend our *in silico* model by incorporating the second vascular cell type, the PCs.

Briefly, as mentioned in section 4.2.2.3, Kondo *et al.* in [119] suggest that the presence of PCs is not necessary (rather than conditioned medium (CM) from PCs) to suppress the EC growth. The latter appears to be in contrast to the results of Orlidge and D'Amore [173], and Sato and Rifkin [209], who reported that CM from cultivation of PCs or SMCs alone showed no significant impact on the EC growth. Results from [119] also suggest that the most abundant anti-angiogenic growth factor in the CM was found to be soluble TGF-β1, whereas results from [173, 209] suggest that TGF-β1 is secreted once the ECs and PCs come into contact.

Motivated mainly by the experimental system of Orlidge and D'Amore [173], and also by the above findings of EC-PC co-culture systems [119, 209], we ran simulations by incorporating both cell types (N(0)=32 ECs and PCs in a 1:1 ratio as in [173]).

Figure 4.14 shows results on cluster formation over the different motility scenarios ($r = 10, 30, 90$ and $t_{per} = 10, 30, 90$ min). Mitosis was not considered in an attempt to assess which scenario(s) is more likely to result in a total inhibition of the EC growth. If cell speed is low ($r = 10$; see plots in first row), it might be suggested that it would not be possible to result in total inhibition since the number of endothelial individual cells (cluster size=1) is considerably higher than the other cases ($r = 30, 90$). Therefore, the motility scenarios with increased cell speed (and persistence time) are more plausible candidates for total inhibition of the EC growth, since cell collisions are more frequent. However, remark that results in section 4.5.2 showed that high cell speed ($r = 90$) yields an increased number of individual cells, which eventually leads to higher cell proliferation. Overall, we suggest that medium cell speed ($r = 30$) is more likely to result in total inhibition of the EC growth.

Furthermore, having estimated parameter a_4 as described earlier in section 4.5.2, we aim next to estimate parameter a_5, the strength of contact inhibition from the diffusive TGF-β1 (being secreted when the two cell types make contact with each other) as described in equation (4.3.6). Results in Figure 4.15 reveal that even large values of a_5 are not able to totally suppress EC growth, which could suggest that a different parameter/factor should be responsible for the total inhibition.

Simulation results in Figure 4.16 support the last suggestion. It is shown that by increasing the diffusion length $\left(L = \sqrt{\frac{D}{\delta}}\right)$ of the TGF-β1 (by decreasing the decay rate

δ) it may lead to total inhibition of the EC growth.

In summary, our model suggests that medium cell speed (and persistence time) along with an increased diffusion length of TGF-β1 might suffice to totally inhibit the EC growth in an EC-PC co-culture system. In the aforementioned experimental systems [119, 173, 209], there was no reference on the effective range of the anti-angiogenic growth factor, and further experimental work might prove that.

Experimental images with ECs and PCs in the co-culture system of Orlidge and D'Amore [173] (see a representative in Figure 4.13) show protrusions of PCs making long-distance contacts with ECs. Notably, diffusive TGF-β1 in our model might represent the role of PC projections, and in the future, it would be interesting to check if long projections (filopodia) could replace the role of the TGF-β1.

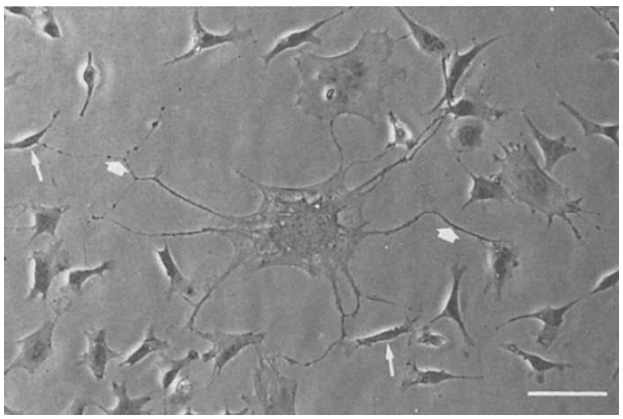

Figure 4.13: Phase-contrast micrograph in [173] depicting the morphology of ECs directly co-cultured with PCs. ECs and PCs at a 10:1 ratio, illustrating a centrally located PC extending many processes (short arrows) that contact multiple ECs (long arrows). Bar: 10 μm.

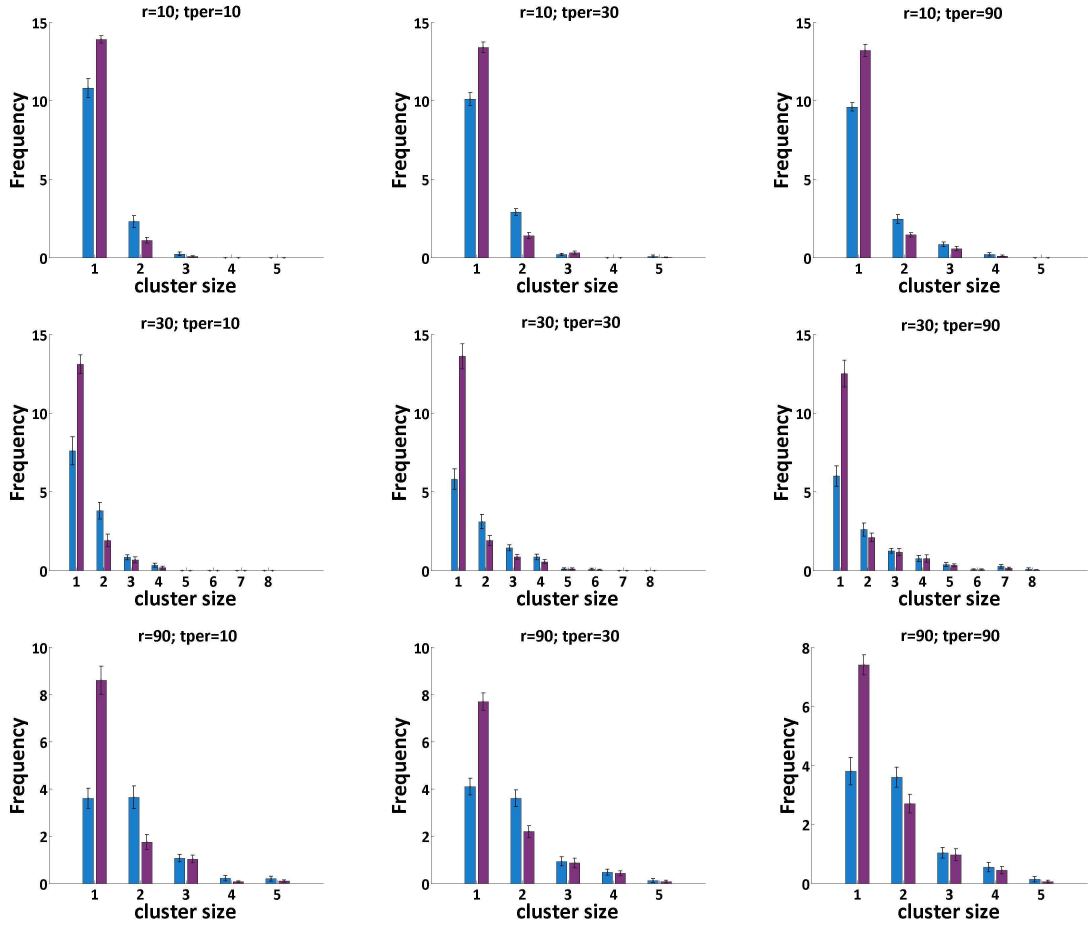

Figure 4.14: Simulation results with both ECs and PCs (N(0)=32 cells; EC:PC=1:1) in 36 hrs present the number of clusters over size. The different motility scenarios for cell speed ($r = 10, 30, 90$) and persistence time ($t_{per} = 10, 30, 90$ min) were tested without mitosis. Key: ECs (left bars); PCs (right bars). Contact energies: $J_{EP} = 5 < J_{EE} = 15 \ll J_{PP} = 100$. Error bars show the mean of 10 simulations $\pm$ S.E.M.

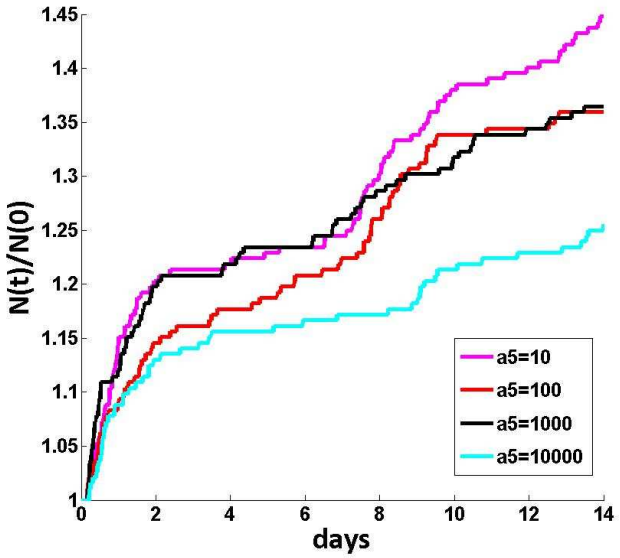

Figure 4.15: Normalised number of ECs (N(t)/N(0)=16) co-cultured with growth-arrested PCs in a 1:1 ratio over time. We vary a_5, the strength of contact inhibition by the diffusive TGF-β1. Each curve represents the mean of 10 simulations.

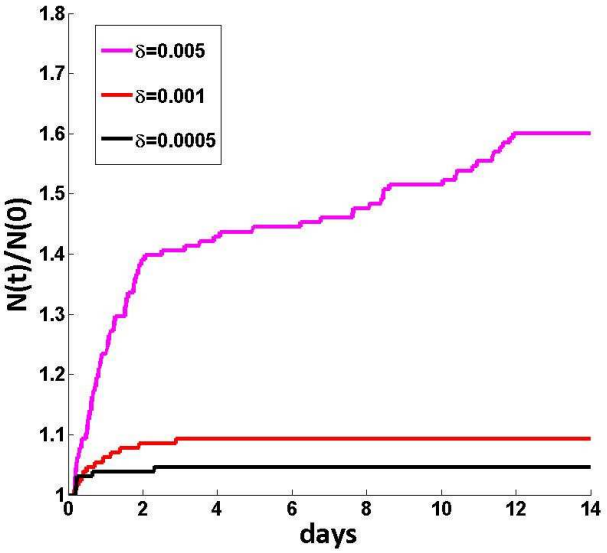

Figure 4.16: Normalised number of ECs (N(t)/N(0)) co-cultured with growth-arrested PCs in a 1:1 ratio over time. We vary δ, the decay rate of TGF-β1 ($\delta = 0.005, 0.001, 0.0005 \simeq 3.5, 8, 11$ cell length). Each curve represents the mean of 10 simulations.

4.5.4 Cell ratio studies

In Orlidge and D'Amore [173], to assess the influence of the ratio of ECs to PCs on the modulation of EC growth, direct co-cultures were established for 10 days at EC:PC ratios of 1:1, 2:1, 5:1, 10:1, and 20:1. In particular, the number of ECs was kept constant (20,000 cells/well), while the number of PCs was varied. All other experimental conditions remained unchanged. In terms of implementation in our model, the exact ratios for the aforementioned ratios are 16:16, 16:8, 16:3, 16:2, 16:1, respectively.

Figure 4.17 (right column) shows cell ratio results from [173]. In particular, comparable inhibition of EC growth was observed at all ratios by day 3 and was constant up to day 10 in co-culture for the ratios up to and including 10:1. However, when ECs were co-cultured with PCs at a 20:1 ratio, the inhibition of EC growth was similar to other ratios at day 3, but steadily diminished over the remainder of the time course.

Figure 4.17 (left column) shows results from our *in silico* model with the different EC:PC ratios. It is shown that our simulation results for ratios 1:1 and 2:1 are in qualitative agreement with the experimental results in [173]. However, for the rest of the ratios our model predicts EC growth in the first two days, whereas the experimental results show no EC growth until day 3. The exact mechanism for that is unknown, but one possible explanation could be that the long PC-protrusions (see Figure 4.13) might be able to suppress multiple ECs being in close proximity.

It is important to note that decreased PC to EC ratios have been observed in several diseases (e.g. multiple sclerosis [35], brain tumour [268], diabetic retinopathy [83]). Overall, our model results showed that, indeed, a decreased PC to EC ratio is important to disrupt the total inhibition of the EC growth.

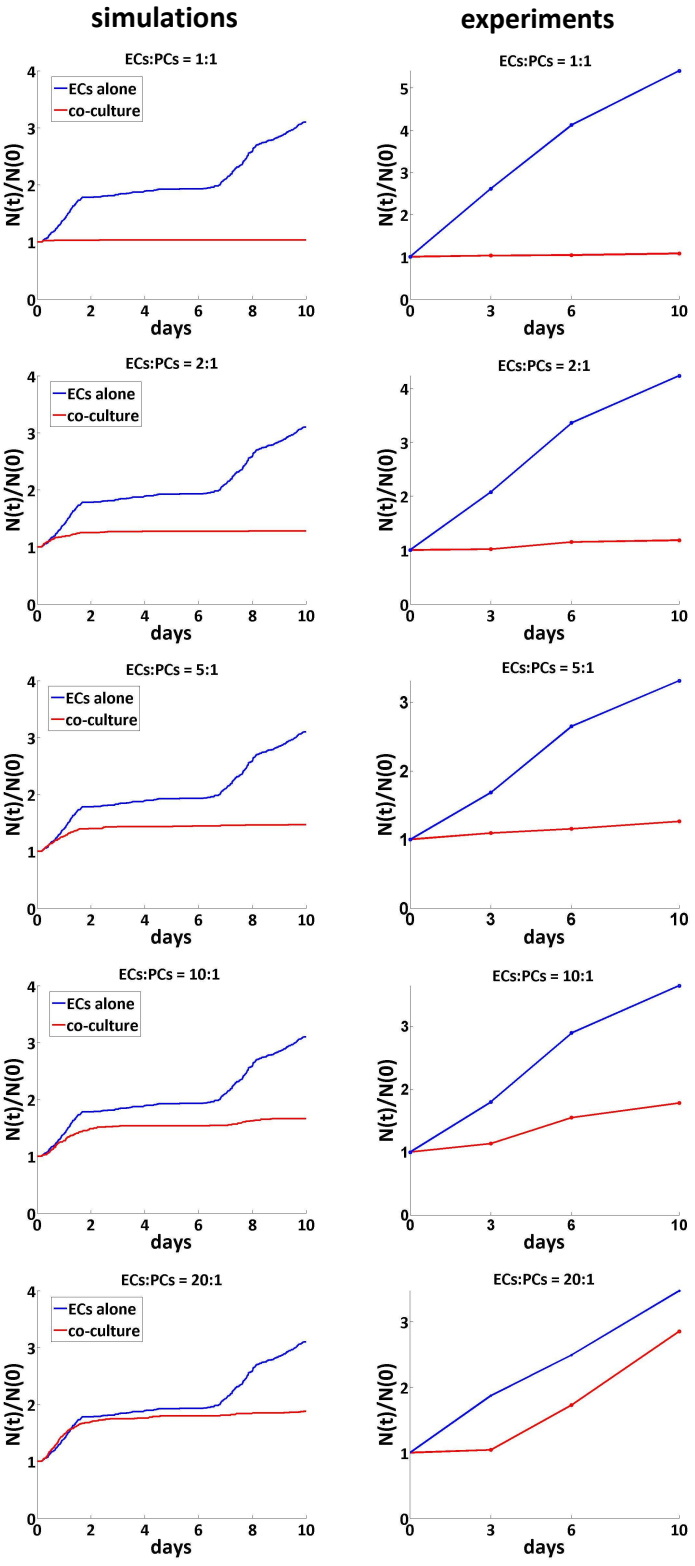

Figure 4.17: Cell ratio studies for ECs:PCs. Left column: Results from our *in silico* model. Right column: Results from Orlidge and D'Amore [173]. Note that for the simulations the exact ratios for 1:1, 2:1, 5:1, 10:1, 20:1 are 16:16, 16:8, 16:3, 16:2, 16:1, respectively. Each curve represents the mean of 10 simulations. Parameter values used: $a_4 = 11$, $a_5 = 1000$, $\delta = 0.0005$, $r = 30$, $tper = 30$.

4.5.5 Sensitivity analysis

The parameters used in our model (summarised in Table 4.2) were selected so as to fit data from the experimental system in [173]. However, a sensitivity analysis on some of those parameters is performed in order to assess any possible variability in clustering and inhibition of the EC growth.

4.5.5.1 Contact energies:

Contact energies, homotypic (EC-EC, PC-PC) and heterotypic (EC-PC), may play a crucial role in clustering and, therefore, contact inhibition. As we mentioned in section 4.4, in our simulations, unless otherwise stated, we chose $J_{EC,PC} = 5 < J_{EC,EC} = 15 \ll J_{PC,PC} = 100$ by assuming that heterotypic contacts are stronger than homotypic. As a consequence of the large $J_{PC,PC}$, PCs exist more commonly as individuals rather than clustered with other PCs and, thereby, more motile in order to search the domain and make contacts with ECs.

Due to the lack of any experimental (quantitative) data on contact energies (forces), we aim next to investigate results from different scenarios regarding the homotypic and heterotypic affinity, in the following way:

1. $J_{EC,PC} = 5 < J_{EC,EC} = 15$ and vary $J_{PC,PC}$,
2. $J_{EC,EC} = J_{PC,PC} = 5$ and vary $J_{EC,PC}$.

In particular, we are interested in the case where heterotypic are stronger than the homotypic contacts (case (1)), and the inverse via case (2). Figures 4.18 and 4.19 depict results for the two cases. It is shown that, in terms of clustering, there is not any obvious difference between the two. Regarding the effect of contact inhibition on the EC growth it would be more informative to assess the effect of these cases on the EC growth (N(t)/N(0)), as shown in Figure 4.20. In particular, case (1) (see Figure 4.20 (a)) results in total inhibition regardless of the affinity between PCs ($J_{PC,PC}$). On the other hand, in case (2) (see Figure 4.20 (b)) large $J_{EC,PC}$ results in increased EC growth, since the low affinity between ECs and PCs yields less secretion of TGF-β1 and, therefore, less inhibition.

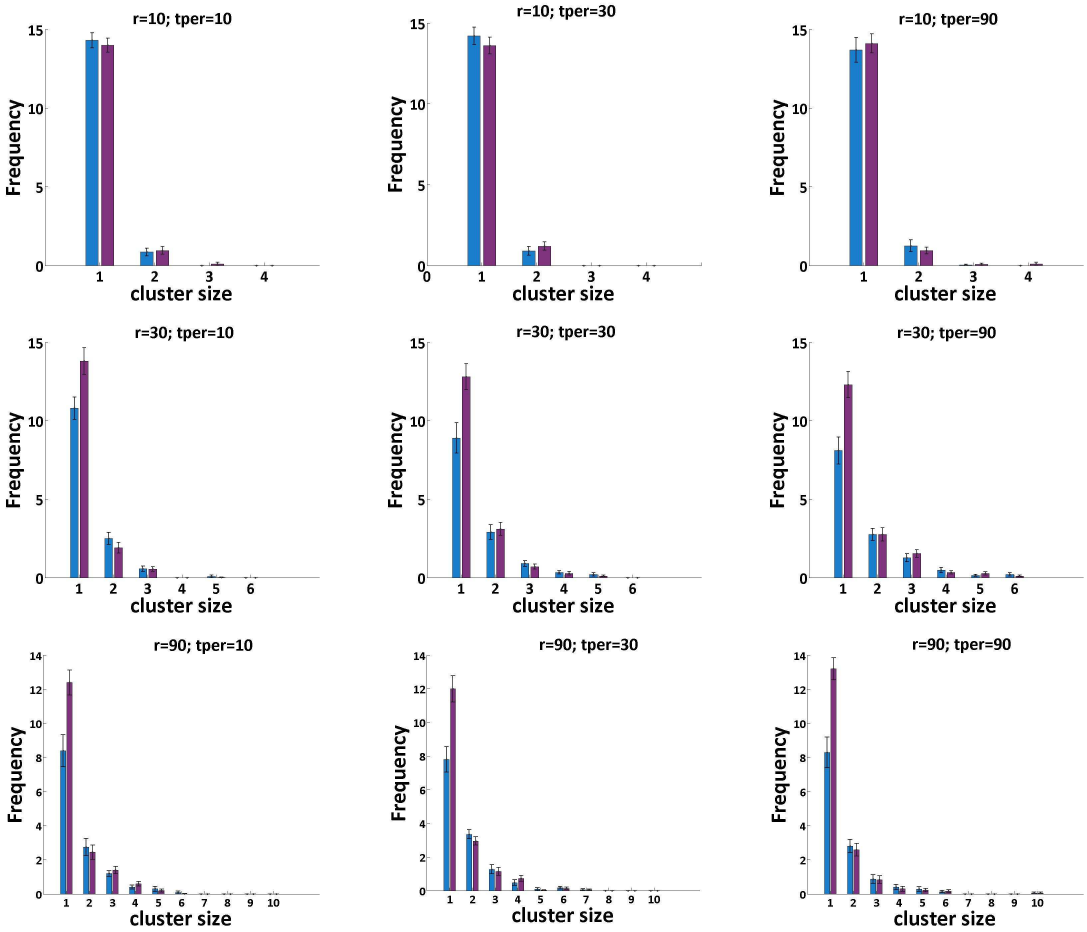

Figure 4.18: Simulation results with both ECs and PCs (N=32 cells; EC:PC=1:1) present the number of clusters over size in 36 hrs. The different motility scenarios for cell speed ($r = 10, 30, 90$) and persistence time ($t_{per} = 10, 30, 90$ min) were tested without mitosis when heterotypic contact energies are stronger than homotypic (e.g. $J_{EP} = 5 < J_{EE} = J_{PP} = 15$). Key: ECs (left bars); PCs (right bars). Error bars show the mean of 10 simulations $\pm$ S.E.M.

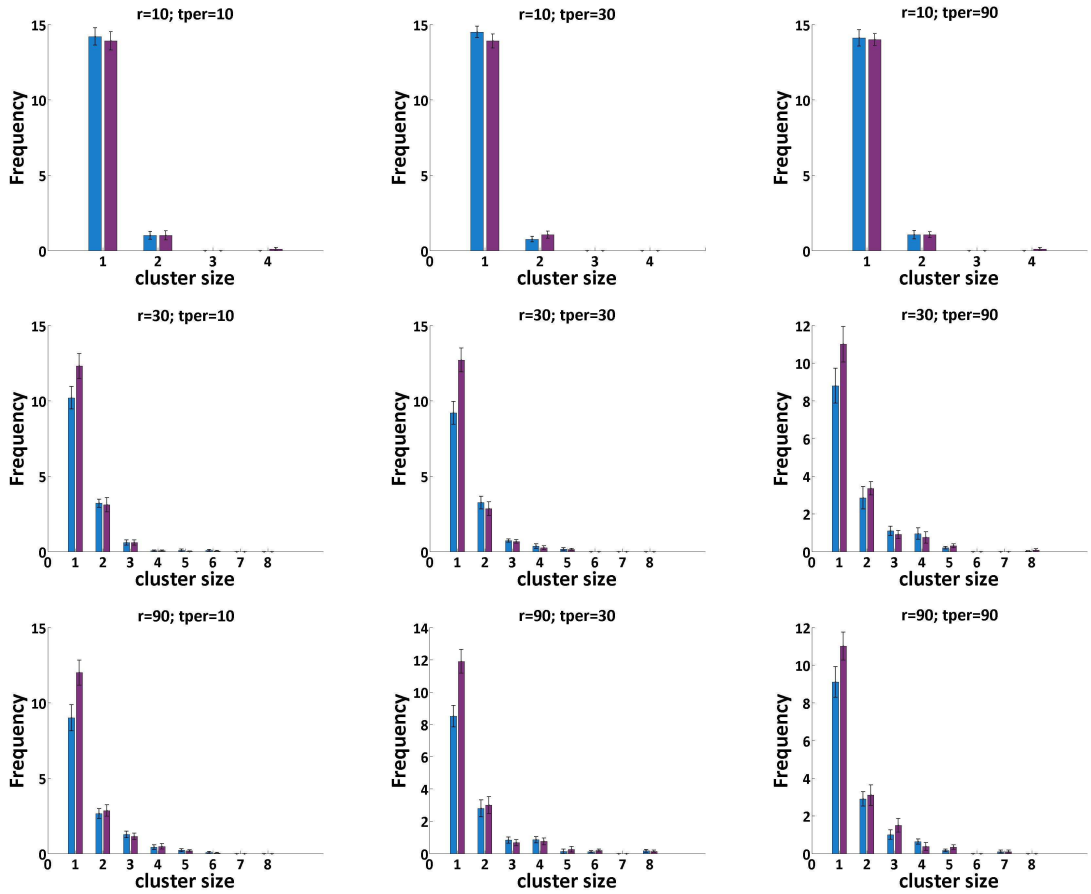

Figure 4.19: Simulation results with both ECs and PCs (N=32 cells; EC:PC=1:1) present the number of clusters over size in 36 hrs. The different motility scenarios for cell speed ($r = 10, 30, 90$) and persistence time ($t_{per} = 10, 30, 90$ min) were tested without mitosis when homotypic contact energies are stronger than heterotypic (e.g. $J_{EC,EC} = J_{PC,PC} = 5 < J_{EC,PC} = 15$). Key: ECs (left bars); PCs (right bars). Error bars show the mean of 10 simulations $\pm$ S.E.M.

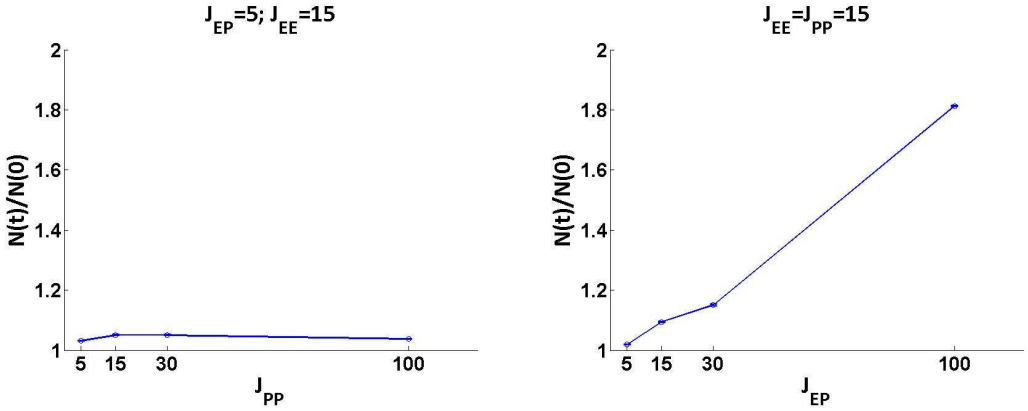

(a) (b)

Figure 4.20: Normalised number of ECs (N(t)/N(0)) co-cultured with growth-arrested PCs in a 1:1 ratio by varying contact energies, (a) J_{PP}, and (b) J_{EP}. Each point represents the mean of 10 simulations for 3 days. The data are mean $\pm$ S.E.M.

4.6 The role of FGF2 and model variants

4.6.1 The role of FGF2

As mentioned in section 4.3, our model assumptions are mainly based on the experimental system of Orlidge and D'Amore [173]. In [173], all cultures were grown in media containing 10% calf serum without any additional growth factors.

It is a fact that the variability in the purity of growth factor preparations and differing cell culture conditions make comparison among the results difficult. Therefore, D'Amore and Smith in [40] developed homogeneous mono-cultures of several cell types (including ECs and PCs) by adding external growth factors (e.g. FGF2) in order to test their effect on cell proliferation.

By considering the mitogenic action of FGF2 and the model set up in [40] the network diagram in Figure 4.3(b) can change to the one in Figure 4.21. Therefore, we extend our model by assuming that ECs proliferate at a rate which depends on the concentration of the FGF2 according to a Michaelis-Menten form and, therefore, equation (4.3.6) changes to

$$\frac{d\phi^j_{EC}}{dt} = \frac{1}{1+a_4P^j}\frac{1}{1+a_5TGF\beta 1}\left(a_1 + a_2\frac{FGF2}{a_3+FGF2}\right). \tag{4.6.1}$$

The right hand side of equation (4.6.1) specifies the speed of progress through the cycle

as a function of FGF2. The new constant, a_2, is the maximum rate which could be retrieved in high FGF2 concentrations, while a_3 is the FGF2 concentration at which a_2 is half maximal.

Furthermore, in [40], ECs were cultured for 3 days in different external FGF2 concentrations and the EC number was half maximum when FGF2 was ∼1 ng/ml (see Figure 4.22; data). Therefore, the parameter a_3 was chosen to be $a_3 = 1$ ng/ml. Regarding a_2 and the FGF2 contribution to the EC proliferation rate, the addition of FGF2 (>4 ng/ml) [40] increased the number of ECs from 10,000 to 120,000 in 3 days. Therefore, the EC cycle time decreases from ∼36 hrs (as it was in [173]) to ∼20 hrs=1200 MCS, which implies $a_1 + a_2 = \frac{1}{1200} = 0.00083 \Rightarrow a_2 = 0.00037$ MCS^{-1}.

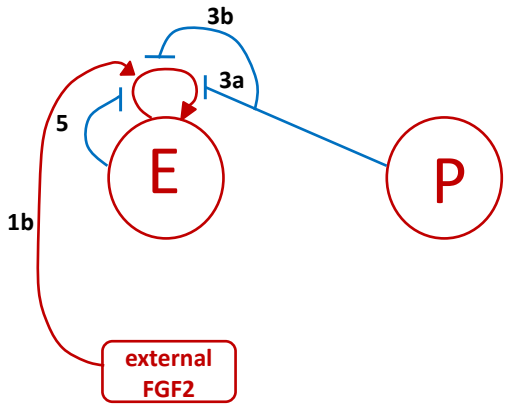

Figure 4.21: Network diagram presents the EC-PC autocrine and paracrine interactions explained with the given numbers on the arrows as in Figure 4.3. Note that in (1b) the FGF2 is not secreted from the ECs (as in Figure 4.3), but is added externally (uniformly distributed in the domain) as in [40].

Notably, the set up of the two experimental systems [40, 173] was the same except from the initial cell density (half cell density in [40]). For that reason, in this section we ran the model with N(0)=8 ECs (instead of N(0)=16 ECs as in section 4.5.2).

Numerical results using equation (4.6.1) are depicted in Figure 4.22 showing the normalised number of ECs (N(t)/N(0)) over uniform FGF2 concentration. It is shown that in medium motility ($r = 30$), even by decreasing the strength of contact inhibition ($a_4 = 11, 7, 3$), our model is not able to fit the data from D'Amore and Smith [40]. Motivated by the results in Figures 4.8 and 4.9 (EC clustering without and with mitosis, respectively), where we observed that increased motility ($r = 90$) can increase cell pro-

liferation, interestingly, by increasing cell motility ($r = 90$) and a_2, the model was able to fit the data sufficiently well (see Figure 4.22; magenta curve).

In summary, we may conclude that in sparse cell populations increased cell speed can relieve contact inhibition and, therefore, increase cell proliferation.

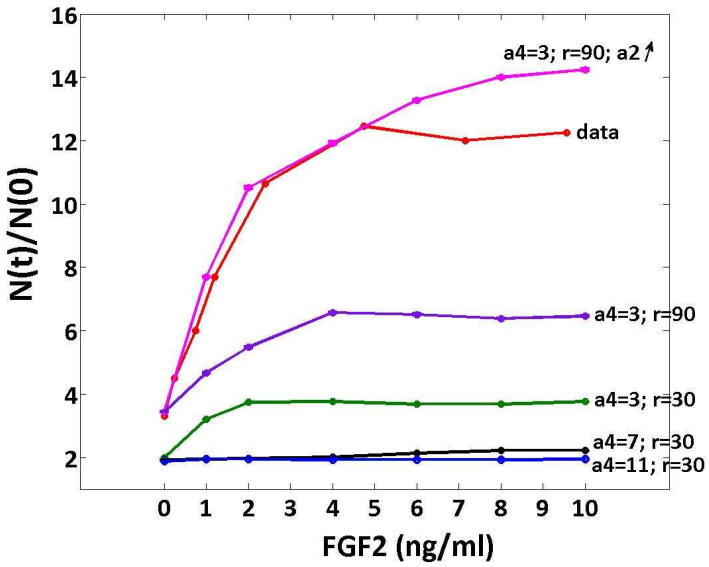

Figure 4.22: Normalised number of ECs (N(t)/N(0)) over uniform concentration of FGF2 in 3 days, by varying a_2, a_4, and cell motility (r). The case represented by the magenta curve can give a good fit to the data redrawn from [40]. Note that N(0)=8 ECs in order to be consistent with the initial density in [40]. Parameters: a_2 is kept constant ($a_2 = 0.00037$ as estimated in section 4.4.4.1) for all cases, with the exception of the case represented by the magenta curve in which $a_2 = 0.00085$.

4.6.2 Model variants

In this section we present two model alternatives by which the EC population can triple in about 3 days as in D'Amore and Smith [40] (as shown in Figure 4.22; data). Firstly, we consider a stronger affinity of ECs to the medium (ECM) and, secondly, a lower affinity between the daughter cells for a certain period of time.

4.6.2.1 Strong affinity between ECs and the medium

ECs have been noted to prefer coatings with some matrix component [192], whereas PCs, unlike ECs, generally grow at similar rates regardless of the substrates [192]. Therefore, the affinity between ECs and the medium ($J_{EC,Medium}$) is another important factor which could impact EC cycle, and it would probably be reasonable to consider a strong affinity between ECs and the medium. Figure 4.23 shows results for the morphology (clustering) and the quantified contact inhibition when $J_{EC,Medium} = 10 < J_{EC,EC} = 15$ compared to the default model in which parameters used are as shown in Table 4.2 ($J_{EC,EC} = 15 < J_{EC,Medium} = 20$). Figure 4.23(d) shows that smaller $J_{EC,Medium}$ results in considerably increased cell proliferation compared to the default model, and notably, the EC population can triple in approximately 3 days.

4.6.2.2 Low affinity between daughter cells

Lee *et al.* in [131] studied the *in vitro* EC locomotion and observed that immediately after a cell division, the daughter cells moved away from each other. The distance between daughter cells was about 20 μm.

Motivated by this finding, we extend our model by allowing daughter cells to represent a different cell type for a certain period of time ($t_{daughter}$) after detachment (with $J_{daughter,daughter} = 100$). Subsequently, they convert back into their initial type (EC). Since daughter cells remain as individual cells (due to their low affinity), they are in turn more motile and not contact inhibited. Therefore, the EC population is able to triple in approximately 3 days if $t_{daughter}$ is sufficiently large (see Figure 4.23 (d)), which is comparable with the case in section 4.6.2.1.

Overall, both model alternatives as presented above can fit the experimental data from D'Amore and Smith [40] (Figure 4.23 (d)). However, it is worthy to note that results in Figure 4.23 (e) show that the the case in section 4.6.2.1 can result in slightly increased area coverage of the domain compared to the case in section 4.6.2.2, because in the former case cells are more well spread in the medium.

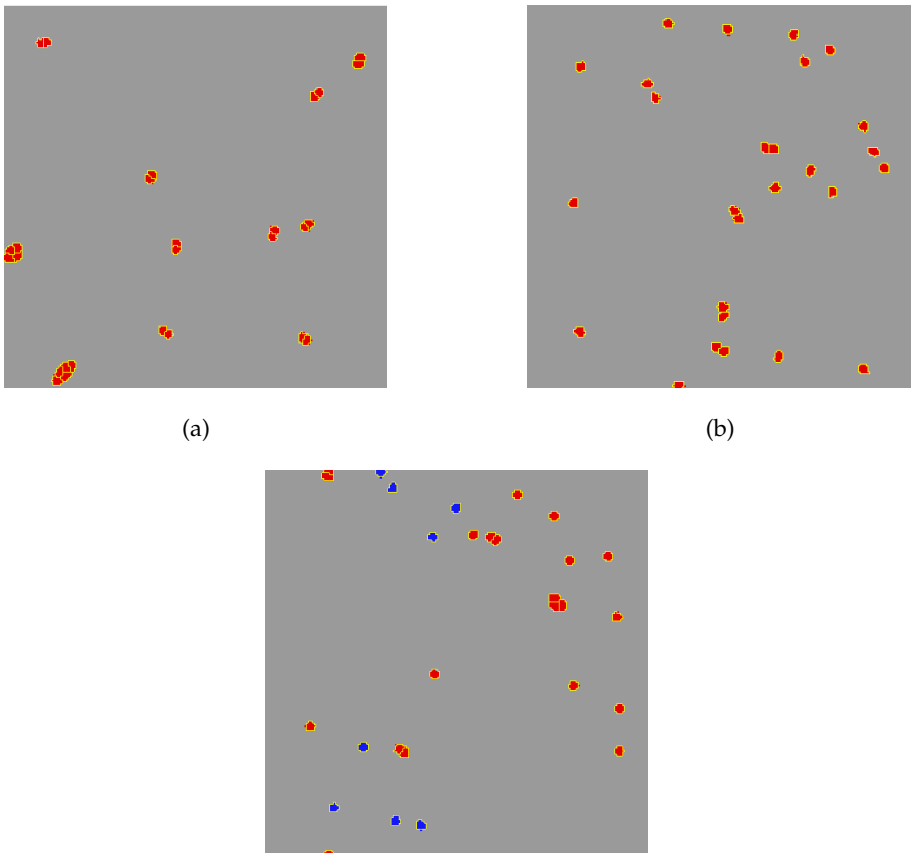

(a) (b)

(c)

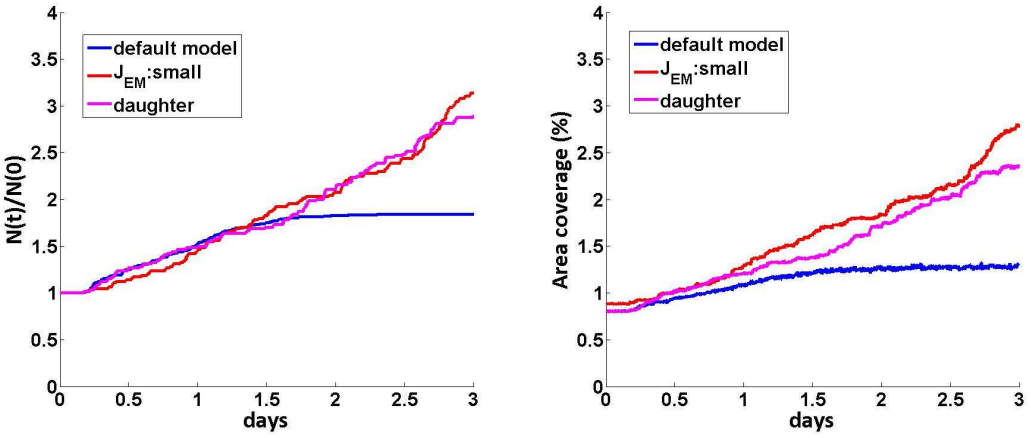

(d) (e)

Figure 4.23: Cluster formation in 3 days for (a) the default model (parameters used as in Table 4.2), (b) strong affinity between ECs and the medium (section 4.6.2.1), with $J_{EC,Medium} = 10 < J_{EC,EC} = 15$, and (c) low affinity between daughter cells (section 4.6.2.2), with $t_{daughter} = 1300$ MCS. Key: ECs (red); EC daughter cells (blue). (d) Normalised number of ECs (N(t)/N(0)), and (e) area coverage (%) for the different cases (a)-(c). Note that in the default model, N(0)=16 ECs (as in [173]), and in the other two cases, N(0)=8 ECs (as in [40]).

4.7 Discussion

In this chapter, we have developed a 2-D Cellular Potts Model (CPM) with the aim to understand the dynamics of interactions between two of the main vascular cell types, the endothelial cells (ECs) and pericytes (PCs). In particular, we focused on the main mechanisms responsible for the total inhibition of the EC growth in an EC-PC co-culture system.

Vascular formation involves a complex interplay of signals from ECs, PCs, and non-vascular cells required for proper vessel assembly and function. These interactions are both temporally and spatially regulated. PCs play an important role in vascular stability and are integral to injury responses.

The process of EC-PC interaction is a result of cell-cell adhesion, cell division, and cell migration, that involves a complex interplay among different interaction and control mechanisms on the cellular (and subcellular) level. To gain insight into this well-orchestrated interplay, *in vitro* EC-PC co-culture studies have been performed [40, 119, 173, 209], which revealed the pericyte-mediated suppression of the EC growth.

Our model assumptions and validation were mainly based on the experimental system of Orlidge and D'Amore [173]. The authors suggest that the inhibition of the EC growth depends on the co-existence and contact of the two cell types. In particular, a latent form of the anti-angiogenic growth factor TGF-β1 is activated only when ECs and PCs contact each other. However, the last assumption is in contrast to observations from the experimental system of Kondo *et al.* [119]. The latter suggests that inhibition of the EC growth in pure EC cultures is also possible in medium conditioned by soluble TGF-β1 rather than by actual contact between the two cell types. In our model, we allowed TGF-β1 to be secreted from both cell types at their contact area and diffuse in the domain.

Motivated by the sparse cell population in [173], we incorporated actual cell motility in the CPM framework (and not only the membrane fluctuations). This allowed cells to move randomly in the domain and make contacts with other cells. We determined two foundational parameters of motility, speed (r) and persistence time (t_{per}), in order to gain a better insight into the role of cell motility on cell aggregation and, therefore, contact inhibition. When cells collide with each other with high speed they might detach depending on their predefined direction. On the other hand, cells may not leave each other and adhere tightly together if they have about the same direction.

Another advance of our model is that the proliferation of the ECs was implemented via a phase cell cycle model. Once ECs become mature enough they divide and begin to

form small clusters. Note that the PCs in [173] were growth-arrested, which was also the case in our model.

Overall, cells in our model can proliferate, migrate, and aggregate with other cells. When clusters become big enough they may enlarge even more by merging with adjacent clusters. Aggregation could also be governed by several other factors, such as secreted molecules attracting the cells toward each other or by changes in the adhesive properties of cells. Growth factors might also increase the speed of the cells [131, 243], and extracellular matrix (ECM) may enhance the persistence of cell motion [243]. In the current study, cells divide and migrate randomly without the effect of any external factor (e.g. FGF2, ECM). However, this would be an interesting extension to address in future work.

In vitro experimental data from corpus luteum presented in Chapter 3, suggest that cell or whole cluster death is an important factor which could impact the overall cell population. However, in our model cell death mechanisms were not considered, since results in [173] have not shown any indication on that.

All the aforementioned mechanisms (e.g. motility, division) incorporated in the *in silico* model collectively act together to give the macroscopic result (clustering). Most of the model parameters were estimated from the experimental studies [40, 131, 173] and simulated results resembled efficiently the experimental data in [173]. That was achieved by following a systematic approach. That is, we started with single cell experiments, and by fixing t_{per} from [131], we estimated cell speed (r) as in [131]. Then by using pure EC populations we estimated a_4, the contact inhibition parameter, which fits the growth data in [173]. Cluster formation with and without mitosis was also assessed in three different motility scenarios (low, medium, and high motility). Simulation results in sections 4.5.1 and 4.5.2 showed that motility plays a critical role on cell aggregation. Particularly, in the first scenario (low motility), cells are not able to make contacts with neighbours, unless they are initially attached or in close proximity with other cells. On the other hand, medium and high motility scenarios can enhance cell collisions. However, in high motility clustered cells may separate from each other and return back to their individual (and more motile) stage. Individual cells are not contact inhibited and, therefore, this could eventually result in increased cell proliferation. By considering the above findings, we may suggest that medium motility is able to enhance clustering and, thereby, increase contact inhibition.

Having assessed cell clustering in pure EC populations, we extended our model by incorporating equal number of growth-arrested PCs and ECs in order to investigate the mechanism(s) responsible for the total EC growth. Interestingly, our model results

showed that increasing the diffusion length of the TGF-β1 may result in total inhibition of the EC growth.

Furthermore, cell ratio (EC:PC) studies in [173] showed that the total inhibition is possible up to and including a ratio of EC:PC=10:1. However, a ratio of 20:1 results in total inhibition through the first 3 days of co-culture, followed by resumed EC growth. These observations suggest that the ability of the PCs to contact multiple ECs may allow for a constant degree of EC inhibition in the presence of increasing numbers of ECs. Decreased PC to EC ratios have been observed following multiple sclerosis [35], brain tumour [268], diabetic retinopathy [83], aging [64], and in a variety of angiopathies [244]. However, increased PC coverage may also be an indicator of vascular dysfunction. Simulation results from our model with different cell ratios showed that, indeed, a decreased PC to EC ratio is important to disrupt the total inhibition of the EC growth.

Cell-cell adhesion is crucial in cluster formation and, therefore, contact inhibition. For this reason, sensitivity analysis in contact energies followed in our study in order to assess the effect of the homotypic (EC-EC, PC-PC) and heterotypic (EC-PC) affinity on the inhibition of the EC growth. Most importantly, simulation results revealed that if heterotypic are stronger than the homotypic contacts, then by varying the homotypic contacts between PCs, no considerable change is observed on the EC growth.

As we mentioned previously, our model assumptions were mainly based on the experimental system in [173], in which cells were cultured without any additional growth factor. However, D'Amore and Smith [40], in an experimental system with the same set up as [173] (except from the initial cell density, which was half in [40]) assessed the effect of FGF2 on the EC growth. Therefore, we extended our model by incorporating uniform FGF2 concentration in the whole domain. Results showed that higher cell speed (relieving cells from contact inhibition) was the key factor to allow for the best fit to the increased EC growth in [40]. Two alternative ways (without FGF2) were also presented in which we were able to match the EC growth in [40]. Namely, allowing strong affinity between ECs and the medium or lower affinity between the daughter cells for a certain period of time. From the above results, it becomes clear that contact energies may play a crucial role in cell proliferation.

The CPM framework has been proved very efficient to describe in detail all the processes governing the growth of contact-inhibited cells. Despite the power of cellular automata model (e.g. [130]) using thousands of seeding cells and describing efficiently important cell behaviours (e.g. division, migration), it is not possible to assess the change of cell shape, one of the main advantages of the CPM, and also the contact area which is perhaps the only way to test the effect of contact inhibition.

In conclusion, we believe that our model has the potential to become a predictive tool since most of its parameters can be fitted from experimental data. A unique feature of this model is the incorporation of a second vascular cell type, such as pericytes. We found that the cell-specific parameters, and in particular the contact energies, the speed of cells (and persistence time) along with the diffusion length of the TGF-β1 have a significant impact on the inhibition of the EC growth and, therefore, we suggest *in vitro* experiments to test our model predictions. However, different limitations of the model could be noticed and these are discussed in Chapter 6. Overall, it seems probable that the relationship between ECs and PCs *in vitro* will be the subject of future studies. Further understanding of the pericyte behaviour may lead to better insights into the angiogenic processes, and also, to novel targeted therapies for vascular diseases.

CHAPTER 5

Sprout formation in angiogenesis

5.1 Introduction

Vascular cell types (e.g. endothelial cells (ECs) and pericytes (PCs)) have the ability to self-organise geometrically into vascular networks. In Chapter 4, we assessed the EC-PC cluster formation initiated from randomly dispersed cells, which is the first step in the *in vitro* angiogenic process (see Figure 3.1). In this Chapter, we build on this work, concentrating on the role of two EC phenotypes (the stalk and tip cells) in endothelial sprout formation.

In angiogenesis, new blood vessels headed by a migrating tip cell sprout from pre-existing vessels in response to signals. This is known to be regulated by two signalling pathways concurrently, vascular endothelial growth factor (VEGF) and Notch. VEGF upregulates Delta-like 4 (Dll4; a Notch ligand) [142] in stalk cells of a nearby blood vessel. The Notch signalling is responsible for cell fate decisions. In particular, for the interchange from the stalk to the tip EC phenotype leading to checkerboard ('salt and pepper') patterns along the vessel. Stalk cells selected to become tip cells are the ones with higher levels of Dll4.

Novel retinal angiogenesis data from embryonic mouse [Courtesy of Dr. Luisa Iruela-Arispe] suggest that VEGFA might be secreted by macrophages (immune cells) located in close proximity to tip cells. Motivated by existing experimental observations, *in vitro* CL data on spout and network formation (see Figure 3.1), and novel results from Arispe's Lab, we developed a cell-based, multi-scale mathematical model based on the cellular potts framework. Our aim is to investigate the sprout evolution initiated from a parent blood vessel by integrating the two signalling pathways. The model incorporates three level descriptions: 1) macrophage-mediated VEGFA activates Notch signalling in a nearby blood vessel, 2) tip and stalk EC phenotypes positioned along

the sprout ('salt and pepper' pattern) are dynamically interchangeable depending on their Dll4 level, and 3) sprout morphology and polarisation depend on chemotaxis (cells move up VEGFA gradients) and the alignment of the extracellular matrix (ECM) fibers. The model reproduces phenomena in sprouting angiogenesis, including sprout morphology, tip competition, and explains and predicts perturbation experiments on Notch signalling pathway.

5.2 Biological background

5.2.1 Angiogenesis

Angiogenesis, the formation of blood vessels from a pre-existing vasculature, is a process whereby capillary sprouts are formed in response to externally supplied angiogenic stimuli. The new sprouts provide tissues and organs with oxygen and nutrients, and remove the metabolic waste. Angiogenesis takes place in physiological situations, such as embryonic development, wound healing and reproduction (e.g. corpus luteum development [197]). The healthy body controls angiogenesis through an intricate balance between pro- and anti-angiogenic factors [28]. Over the years, numerous growth factors and chemokines have been shown to influence the process. This balance, though, is sometimes disrupted and angiogenesis also appears in many pathologies, like diabetes [150], rheumatoid arthritis [117], cardiovascular ischemic complications [25], proliferative retinopathy [63], and cancer [27]. In either case, however, the well-ordered sequence of events characterising angiogenesis is the same involving several sequential steps.

5.2.1.1 *In vitro* and *in vivo* models in angiogenesis

Numerous *in vivo* models for studying angiogenesis have been developed, including the mouse retina (for review, see [69]) and hindbrain model [73], the corneal pocket assay [114], the chick chorioallantoic membrane assay [3, 60]. The zebrafish is used as a model for vertebrate development in many research fields, including vascular biology, since blood vessel development in zebrafish follows a spatiotemporally conserved pattern [101].

In addition, a number of *in vitro* assays have been developed (discussed in Chapter 4; for review, see [9]), which have provided important insights into the cellular mechanisms of angiogenesis.

5.2.1.2 Sprouting angiogenesis

Sprouting angiogenesis is initiated by (e.g. hypoxic) tissues or cells (e.g. macrophages [56], astrocytes [260]) which demand the formation of new blood vessels and, therefore, they secrete a number of chemicals (Figure 5.1). These are collectively known as tumour angiogenic factors (e.g. vascular endothelial growth factor, VEGF) [59], which bound to EC receptors of the nearest blood vessel. Subsequently, the extracellular matrix (ECM) and basement membrane, surrounding the ECs, are degraded locally by activated proteases (e.g. matrix metalloproteinases, MMPs).

How individual ECs adopt specific phenotypes and how they coordinate their behaviour during sprouting (?)

Several experimental studies have revealed the heterogeneity of a growing vascular sprout. It is composed of a tip cell at the leading front, followed by stalk cells. The latter cells comprise the body of the sprout and are responsible for the elongation of the new vascular branch (Figure 5.1). They also establish junctions with neighbouring cells and produce basement membrane components to ensure the integrity of the sprout [184]. Adding to the cellular heterogeneity of a vessel, recent work by Carmeliet and colleagues describe phalanx cells as the more quiescent type of ECs [152], whereas the tip and stalk cell phenotypes characterise the 'activated endothelium' [75].

Where, when and how the activated endothelium transits to quiescence is poorly understood. The distinct tip and stalk EC phenotypes display different gene expression profiles, suggesting that their specification is determined genetically [46]. However, a single unique gene or protein that can be used reliably and unambiguously as a molecular marker for tip cells has not been identified.

A key pathway, though, regulating the specification of tip and stalk cells is the Notch signalling pathway which is described next. This finding concurrently emerged from several groups using three distinct experimental models of angiogenesis including solid tumour in mice [169, 200], postnatal mouse retinas [86, 142, 240], and zebrafish embryos [132, 229]. Our model is mainly based on retina angiogenesis, with the main angiogenic developmental stages described in Figure 5.2.

5.2.2 Notch signalling

Notch signalling is the canonical signalling pathway between neighbouring cells. It plays an important role in fine-grained patterning processes such as the formation of checkerboard-like differentiation patterns and sharp boundaries between developing

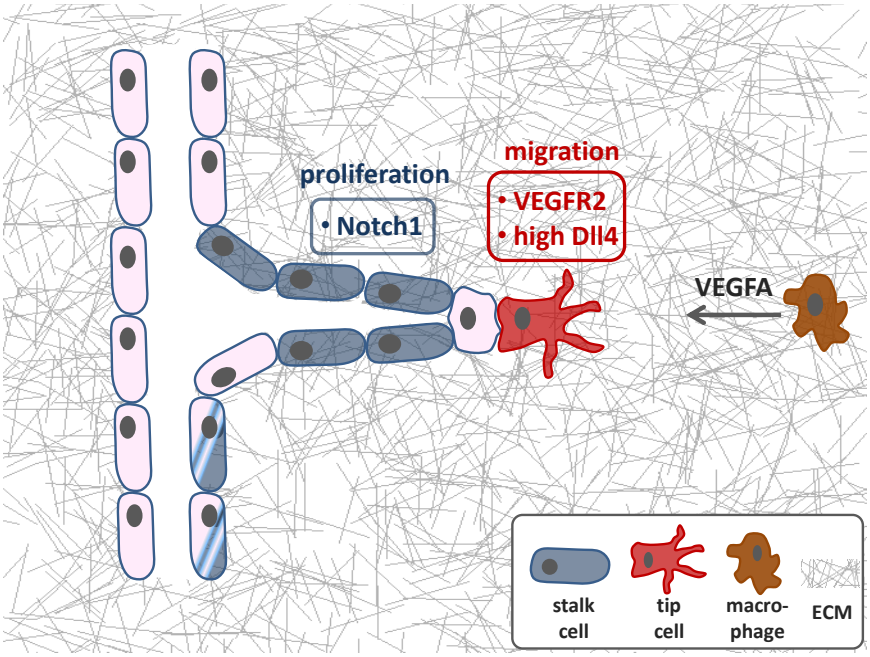

Figure 5.1: Schematic of processes involved in a growing vascular sprout. A growing sprout is mainly composed of tip (red) and stalk (blue) cells, where each EC phenotype responds differently to a VEGF source (macrophage (brown)). As guidance posts, macrophages act as 'bridge cells' to assist tip cells and provide precision in preparation for the fusion of these specialised ECs [56].

tissues [224].

Notch signalling is mediated by the interaction between Notch receptors (Notch 1, Notch 2, Notch 3, and Notch 4) and Delta/Serrate/LAG-2 (DSL) ligands [23]. Upon interaction between a Notch receptor in one cell and a DSL ligand in a neighbouring cell, the Notch intracellular domain (NICD) is cleaved, translocates to the nucleus and co-activates downstream transcriptional targets.

Notch has a role in various processes such as lateral-inhibition [224], synchronising cells during somitogenesis [48], asymmetric cell division [13, 205], and neuronal plasticity [4, 136]. In this study, we are mostly interested in the lateral-inhibition mechanism, which is responsible for the interchange between stalk and tip EC phenotype [86].

5.2.2.1 Lateral-inhibition

One of the classical Notch-dependent patterning processes is lateral-inhibition, which is a general mechanism for the formation of alternating, checkerboard-like, differentia-

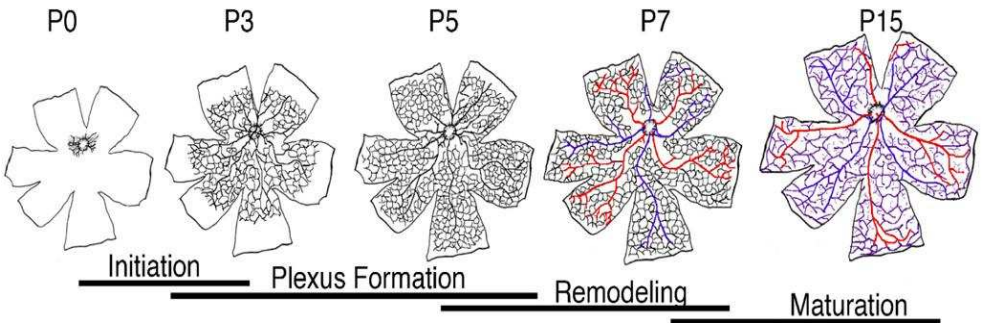

Figure 5.2: Vascular morphogenesis in the mouse retina [91]. The schemes depict the developmental stages of the mouse retinal vasculature during the first 15 post-natal days (P). Initiation of the primary vascular network begins at P0 when vessels sprout from the optic nerve head, and begin extending and fusing to form a capillary plexus [52]. The more mature vessels near the optic nerve head begin to remodel after P3 and develop into an alternating radial pattern of arteries and veins, connected by capillary beds. As the edge of the plexus reaches the perimeter of the retina (P7 and 8), vascular sprouts grow downward and form a secondary vascular plexus. By P15, the primary and secondary networks have matured and an intermediate plexus develops between the two established vascular layers [52].

tion patterns.

Lateral-inhibition, mediated by Delta-Notch (D-N) signalling, is used throughout development to limit the number of initially equivalent cells that adopt a particular fate. It is one of the most studied developmental patterning processes. The concept of lateral-inhibition was initially proposed by Wigglesworth [262] who noticed that new bristles in the developing kissing bug emerged at positions, which are the most distant from existing bristles.

Examples of lateral-inhibition include the anchor cell/ventral uterine precursor cell differentiation in Caenorhabditis elegans [222], bristle patterning in flies [84], neurogenesis in flies and vertebrates [7, 221], and inner ear patterning in vertebrates [79].

Notch signalling is also commonly used for defining boundaries between developing tissues, for example the formation of wing veins [97] and margin boundaries [43] in the developing fly and the rhombomere boundaries in vertebrate hindbrain [33].

5.2.3 Dynamic lateral-inhibition in sprouting angiogenesis: shuffling between stalk and tip cells

Sprout formation requires the coordinated behaviour of all EC phenotypes. The tip cell located at the leading edge of the growing vessel senses the environment for angiogenic factors through the presence of filopodia. In contrast, the stalk cells situated behind the tip cells are highly proliferative cells and allow the vessel to elongate towards angiogenic stimuli.

Endothelial tip cells are induced and guided by an extracellular gradient of VEGFA (and/or VEGFC [75]). ECs express three different VEGF receptors (VEGFR). The activity of VEGFR2 (Flk-1) regulates most of the EC responses to VEGFA, including induction of tip cell filopodia and EC migration, proliferation, survival, and vascular permeability.

What determines which cell eventually becomes a tip cell?

Recent *in vivo* and *in vitro* studies from Gerhard *et al.* in [103] on retina sprout angiogenesis revealed that ECs dynamically compete with each other for the tip cell position. In particular, it was shown that VEGFR2 levels between two cells affect which of the cells will become a tip cell, in a competitive manner. The authors suggested that the balance between VEGFR2 and VEGFR1 (Flt-1) expression in individual ECs affects their potential to become tip cells during sprouting angiogenesis. That is, cells with higher VEGFR2 levels stand a better chance to take and maintain the leading position.

The tip cell is dynamically challenged and replaced by migrating cells from the stalk region. This dynamic competition between ECs for a tip or stalk phenotype depends on the integration of the VEGFA-Dll4-Notch1 signalling pathway, the main focus of the current work, which is discussed next.

5.2.4 VEGFA-Dll4-Notch1 signalling pathway

One of the hallmark achievements in the field in recent years has been the identification of the D-N pathway as the instructive regulator of tip versus stalk cell fate [98]. Both the receptor (Notch1) and ligand (Dll4) are cell bound and thus act only through cell-cell contact.

The VEGFA-VEGFR2 signalling was shown to upregulate expression of Dll4 in tip cells [142], allowing Dll4 to activate Notch1 in the adjacent stalk cells, causing suppression of the tip cell phenotype. Hence, ECs exposed to the highest VEGFA concentration are most likely to become tip cells. This coordinated regulation ensures the selection of a

single cell as the leader (e.g. tip), while the adjacent cells become followers (stalk cells).

To form new blood vessels, the endothelial tip cells of two existing vessels come together by the process of anastomosis. But how do they find each other?

Previous studies have mainly focused on understanding how tip cells initiate vessel sprouting; so nearly nothing is known about how these cells fuse with neighbouring sprouts to form a perfused vessel. Macrophages, phagocytic cells of the immune system, seem to provide a bridge and mediate their union [27]. Figure 5.3(a) shows macrophages (being collocated with VEGFA), which probably act as coordinators for the angiogenic network formation.

5.2.5 Macrophages: their role in anastomosis

Recently, Fantin and co-workers in [56] reported that, precisely when tip cells are about to fuse, a process referred to as anastomosis, tissue-resident macrophages are located in the vicinity of vessel branches. Further, the absence of macrophages or blockade of their function impairs vessel fusion. The latter highlights the growing evidence for a link between macrophages and angiogenesis.

It should be noted that there are two types of macrophages. As their name (Greek for 'big eater') reflects, they can inhibit angiogenesis by initiating a cell-death program in ECs and engulfing the dying cells [141]. The macrophages that carry out these processes are of the type termed M1 [228]. Another type of macrophage, called M2, promotes angiogenesis by releasing pro-angiogenic factors such as VEGFA [98] and VEGFC [75] and, thereby, induces tip-cell formation [4,5]. The macrophages that Fantin and colleagues describe are of type M2, and this is also the type that we are referring to in our model.

5.2.6 The role of ECM in sprouting angiogenesis: haptotaxis

The ECM is a mesh-like network (see Figure 5.3(b)) with the main components being proteoglycans, fibrous proteins such as collagen and elastin and adhesive proteins like laminin and fibronectin.

The ECM has many roles in angiogenesis. It is essential for EC migration, proliferation and survival, since it provides structural support and chemical cues for cell adhesion and motility [99]. ECM components like collagen I and fibrin are capable of supporting chemotactic migration [63]. The density and spatial distribution of ECM proteins such as fibronectin and collagen can affect the speed and direction of cell migration [49].

Furthermore, ECs are able to secrete and degrade ECM components.

ECs activated by VEGFA first degrade the basement membrane of the parent vessel and then migrate into the ECM towards the VEGFA source (e.g. macrophage). The

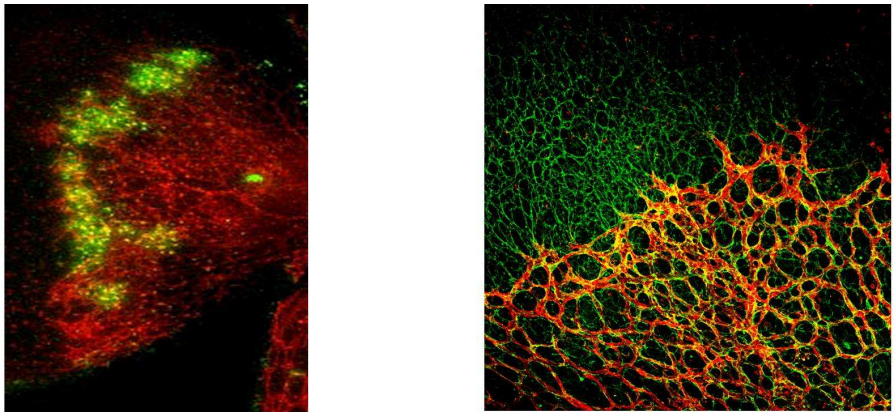

(a) (b)

Figure 5.3: (a) VEGFA (green) identified by using a soluble Flt-1 probe in retinas at P7, possibly shows the location of macrophages just behind the tip cells [Courtesy of Dr. Luisa Iruela-Arispe], (b) Sprouting vasculature (red) is shown to align over fibronectin network (green) in retinas at P7 [Courtesy of Dr. Luisa Iruela-Arispe].

local degradation (e.g. via MMPs) and deposition of matrix proteins by ECs and the heterogeneity of the ECM can all create local gradients of ECM components which can drive EC migration, a process called haptotaxis. In vitro experiments have shown that collagen [219] and fibronectin [232] gradients can guide EC migration. Note that in this study we consider haptotaxis, however, ECM production and degradation are not being considered.

5.2.7 Elongation & Cell-cell adhesion

A crucial characteristic of sprout formation is (stalk and tip) cell elongation. To elongate the stalk region, stalk cells must also divide, maintain contact with the leading tip cell, and form a lumen [44]. However, the mechanisms of how trailing cells remain in contact with the leading front remain mostly unexplored. For instance, VE-cadherin which clusters at EC interfaces is important to maintain cell-cell contacts, as its absence induces random non-directional migration of disconnected cells [253]. However, it is also known that the junctional molecule VE-cadherin shifts the EC response to VEGFA from proliferation and migration to survival and quiescence [257]. Therefore, the strength of adhesion between ECs plays a critical role to the sprout formation.

The junctions between ECs during sprouting are known to be highly contorted, irregular and indeed dynamic as cells stretch and move [17]. Cell-cell adhesions inhibit cell migration and need to be broken down to allow cells to migrate. VEGFA can break endothelial cell-cell contacts by disrupting the VE-cadherin/beta-catenin complex at adherens junctions [128]. In addition, the adhesion molecule VE-cadherin regulates fusion between ECs of vessel branches. Intriguingly, low levels of VE-cadherin are also expressed in macrophages, raising the question of whether this molecule promotes the 'zipping' of tip cells with macrophage bridge cells.

Having provided the necessary biological background, we proceed to summarise some relevant mathematical models.

5.3 Mathematical models in sprouting angiogenesis

Angiogenesis modelling is a useful tool for understanding the interplay between the factors that affect it and for the design of experiments of a predictive nature. In Chapter 1 we discussed in detail a number of mathematical model systems for studying aspects of angiogenesis. In Table 5.1 we summarise those that have delivered key insights as models for angiogenic sprouting, and in the next section we present our model.

The aim of the current work is to expand our understanding of sprout evolution through the VEGFA-Dll4-Notch1 signalling pathway along with the dynamic competition between stalk and tip cells for the tip cell position. We incorporate all of the mechanisms in Table 5.1, and in doing so, we improve upon other sprouting angiogenesis models, which used only some of these.

Table 5.1: Main mechanisms incorporated in sprouting angiogenesis models

Model/Mechanism	Type of model	ECM	Mitosis	VEGF	stalk/tip phenotype	Delta/ Notch	D/N blockade
Bauer *et al.* [14]	2-D cellular potts model	non-uniform (ECM fibers)	✓	✓ secreted from source	X	X	X
Milde *et al.* [158]	3-D particle model (stalk cell density, particle representation of the tip cell)	non-uniform (ECM fibers, ECM proteolysis)	✓	✓ bound- & soluble-VEGF isoforms	✓ (one leading tip cell)	X	X
Bentley *et al.* [16]	3-D (multi-agent) lattice model	X	X	✓ static gradients	✓ ('salt-pepper' pattern)	✓	✓
Bentley *et al.* [17]	3-D (multi-agent) lattice model	X	X	✓ static gradients	✓ ('salt-pepper' pattern)	✓	X
Qutub *et al.* [191]	3-D lattice model	uniform (collagen concentration)	✓	✓ static gradients	✓ (one leading tip cell)	✓	✓
Das *et al.* [41]	3-D lattice model	uniform (collagen concentration, ECM proteolysis)	✓	✓ bound- & soluble-VEGF isoforms	X	X	X
McDougall *et al.* [153]	2-D hybrid discrete-continuum model	uniform (fibronectin concentration secreted by astrocytes, ECM proteolysis)	✓	✓ secreted by astrocytes	✓ (one leading tip cell)	X	X

5.4 Model overview

Our multi-scale model consists of three levels. At the cellular level, a discrete lattice Cellular Potts Model (CPM) considers cell growth, proliferation, elongation, and inter-cellular adhesion. At the extracellular level, a parabolic partial differential equation (PDE) describes secretion and diffusion of a chemical concentration (VEGFA) secreted by the macrophage. At the subcellular level, an ordinary differential equation (ODE) model is used to model the D-N activity in each cell coupled with the contribution of VEGFA from the extracellular level. The three levels are closely integrated and their interplay is depicted in Figure 5.4.

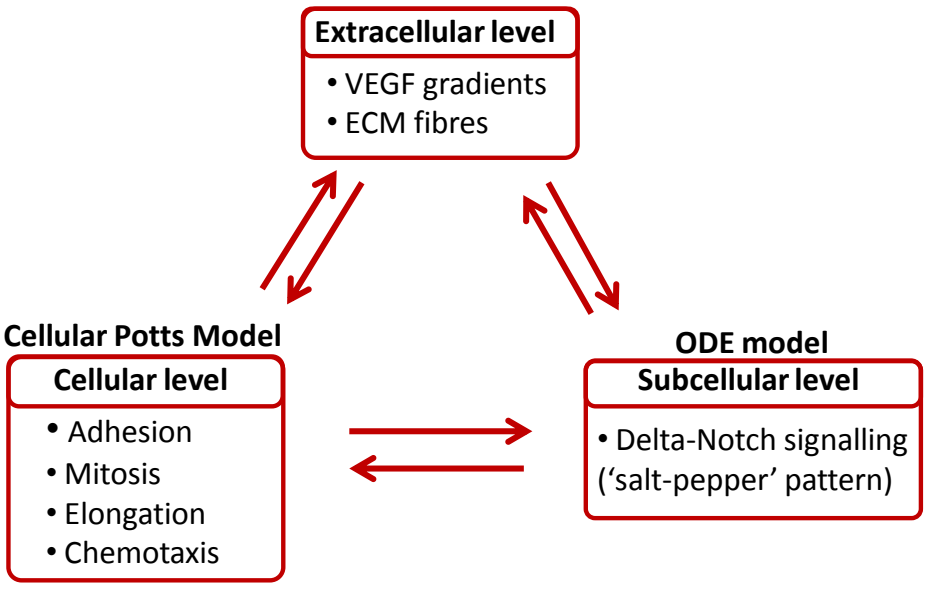

Figure 5.4: Flow chart of the multi-scale model, showing how the micro- and macro-scales interact with each other.

5.4.1 Cellular level: CPM

The cellular model is based on the CPM [78] framework as described in Chapter 4, and the cell interactions are characterised through a total energy (or Hamiltonian, H):

$$H = \sum_{(\vec{x},\vec{x}')} J_{\tau(\sigma(\vec{x})),\tau(\sigma(\vec{x}'))} \left(1 - \delta_{\sigma(\vec{x}),\sigma(\vec{x}')}\right) + \lambda_{area} \sum_{\sigma>0} (a_\sigma - A_\sigma)^2 + H', \tag{5.4.1}$$

where, J are the contact energies, a_σ the cell area, A_σ the target cell area, and H' can be any constraint on the cell behaviour. There are three cell types in our model, the

macrophage, and the two EC phenotypes (stalk and tip cells). In Table 5.2 we summarise the different behaviours of the stalk and tip cells, which are discussed in detail in the following sections. For each model ingredient we discuss the biology, previous approaches, and our approach. Note that in Table 5.2 we define target length as a function of area, which might not be consistent in terms of the units of the two measures. However, in terms of implementation, we only consider the numerical value of the two and not their units.

Table 5.2: Stalk and tip cell behaviours

	Behaviour	**Stalk cells**	**Tip cells**
1.	chemotaxis	weak	strong
2.	growth	if adjacent to tip cells	X
3.	mitosis	if cell area$(a) > 2a(0)$ and cell cycle time >17 hrs	X
4.	elongation	target length = $a/2$ (if adjacent to tip cells)	target length = $a/2$
5.	switch phenotype	become tip if Delta>threshold	become stalk if Delta<threshold

5.4.1.1 Mitosis

It is well accepted that in the absence of EC proliferation, angiogenesis is incomplete. That is, the ECs fail to reach their target (e.g. the tumour [6]). Sprouting is possible without proliferation of cells only up to a limited extension length. Proliferation is necessary to sustain sprouting for a longer period and to grow a large enough sprout that can reach its target [71].

After the tip cell activation from VEGFA, initially, small sprouts are formed by aggregation and migration of ECs that are recruited from the parent vessel. The sprout will further extend when some of the ECs in the sprout begin to divide [10, 62]. Tip cells rarely proliferate [72], although division of the leading cell of intersegmental vessel (ISV) sprouts in zebrafish has been observed [229]. By contrast, stalk cells are strongly proliferative, and thus, support sustained elongation of the growing sprout [72]. However, experimental observations indicate that stalk cell proliferation does not push the tip cell forward, but rather that the tip cells themselves interact with the surrounding

substrate to pull the growing sprout further in the direction of the growth [184].

In [158], Milde *et al.*, to account for the cell cycle, assumed that a capillary branches when its tip cell divides into two daughter cells. After the branching event, there is a threshold time span before which a tip cell cannot proliferate or branch.

In [17], Bentley *et al.* excluded cell growth and division in their study by claiming focus on the early stages of sprouting: migration, fusion and lateral-inhibition, and by also declaring that cell division is not necessary for initial sprouting and fusion in early plexus formation [10].

Location of cell division on the sprout

Although the general idea is that proliferation occurs behind the tip cell, there is no clear view about the exact location of EC mitosis during angiogenesis. Experiments have shown that proliferation can occur some distance behind the sprout tip [182], at the base of a new sprout [113], and even at the tip of the sprout [207]. In addition, other studies suggest that proliferation might occur when the connection between adjacent cells has been disrupted [10].

Since experimental models have reported conflicting results regarding the precise region of proliferating cells during angiogenesis [113], Bauer *et al.* [14] tested different proliferating regions (namely, only at the tip, immediately behind the tip, three cell lengths behind the tip, and at the base of the sprout) with no marked differences in sprout morphology. However, numerical results in [14] indicated that as the proliferation region moves further away from the migrating tip, the average rate of sprout extension towards the VEGF source increases.

In Qutub and Popel [191], the model assumption that tip cells may also proliferate (although with a lower probability than stalk cells) has an impact on the total vessel growth. In the same model, cell elongation had also a significant effect on the total vessel extension, since tip cell elongation was the stimulus for cell proliferation and migration; without it, the cell may migrate to an extent, but was not able to proliferate until stimulated.

Role of VEGF in cell proliferation

In experimental studies, Gerhardt *et al.* [72] in a study of retinal angiogenesis, and Geudens and Gerhardt [75] in a review on blood vessel formation, demonstrated that VEGF independently regulates tip cell migration (via VEGF gradients) and proliferation of stalk cells (via VEGF concentration). In a review on vascular-specific growth factors, Yancopoulos *et al.* [265] noted that VEGF does promote vascular EC prolifera-

tion, and must work in concert with other factors.

In *in silico* studies, Qutub and Popel [191] considered VEGF concentration on stalk cell proliferation, and Dll4 levels on tip cell proliferation, in a probabilistic way.

Mitosis in our model based on cell cycle time

In our cell level model, we postulate that only stalk cells adjacent to tip cells proliferate. In an attempt to avoid any predefined or probabilistic rules (as in [191]), each cell carries a clock defined as

$$\frac{d\phi}{dt} = a_1, \tag{5.4.2}$$

which progresses only when the cell is a stalk cell that is adjacent to a tip cell, and a_1 was chosen to be the time conversion between real time and MCS. That is, $a_1 = 0.01$ hrs/MCS (e.g. 1 MCS = 0.01 hrs). A stalk cell can divide if two conditions apply: 1) its clock (ϕ) reaches the cell cycle duration (17 hrs as evaluated in section 5.5, which is very close to the one (18 hrs) used in [14, 30]), and 2) its cell area doubles, which grows with a rate $\mu = \frac{2a(0)-a(0)}{\text{cell cycle}} = \frac{25}{1700} = 0.0147$ pixels/MCS. Note that $\phi(0) \in [0, 17]$, and when $\phi(t) = 17$ it is reset to zero.

Cell division is simply reassigning half of the area to a new cell id (daughter cell), and the daughter cells inherit all the properties of their parent.

As we mentioned above, VEGF might influence endothelial proliferation, however, we simply postulate that the proliferation rate is independent from any external (growth) factors, which could be considered as a future extension to our model.

5.4.1.2 Elongation

To elongate the stalk region, stalk cells must divide, but cell elongation also seems to be important. Although the shape of stalk and tip cells is not clearly defined, tip cells are more elongated and retain a more spindle shape (due to filopodia) during sprout evolution. As can be observed from experimental images in [75], stalk cells which are in close contact with tip cells also appeared to be elongated. We suppose that this is an attempt from stalk cells to retain the integrity of the sprout. That is, if only tip cells are the ones which are able to elongate it is likely that the head tip cell will eventually detach from the following stalk cell presumably as a result of the chemotactic strength.

Therefore, in our model, the elongation of the tip cells and only those stalk cells which are adjacent with tip cells can be incorporated in the model by including an extra reduction in the energy equation (5.4.1). That is,

$$H'_{length} = \lambda_{length} \sum \left(l_\sigma - L_\sigma(t)\right), \tag{5.4.3}$$

where, l_σ is the length of cell σ along its longest axis, $L_{\sigma(t)}$ its target length, and λ_{length} the strength of the length constraint. Note that we do not assign a constant target length as in [155], but instead, a dynamic constraint to the cell length

$$L_\sigma(t) = a_\sigma(t)/2, \tag{5.4.4}$$

where, $a_\sigma(t)$ is the current cell area at each MCS. One of the main reasons for implementing tip and stalk cell elongation in the way as described above is to prevent cells from elongating before tip cell activation. In addition, by dividing cell area by 2, and by also considering that cells double in size before they divide, it allows the cells to have a cell length in a range (from $a_\sigma(0)/2$ to $a_\sigma(0)$), which is in agreement with experimental measurements [75].

5.4.2 Extracellular microenvironment

5.4.2.1 VEGFA: concentration and local gradients

VEGF is one of the main growth factors involved in angiogenesis. Experimental studies have predicted that the absolute VEGF concentration and the VEGF gradient play separate roles in new blood vessel formation, in a microenvironment-dependent way.

Cells interact with their microenvironment, which is characterised by local concentration of macrophage-mediated VEGFA, described by the following equation:

$$\frac{\partial VEGFA}{\partial t} = D_V \nabla^2 VEGFA + s - \delta VEGFA, \tag{5.4.5}$$

where, VEGFA concentration diffuses in the domain (with zero flux boundary conditions) with D_V being the diffusion coefficient, s is the secretion rate and δ the linear decay. Chemotaxis can be incorporated by including an additional reduction in the total energy (equation (5.4.1)) for extensions and retractions towards higher concentrations of VEGFA (as described in [210])

$$H'_{chem} = \lambda_{chem} \left(VEGFA(\vec{x}) - VEGFA(\vec{x}') \right), \tag{5.4.6}$$

where, $\vec{x}'$ is the neighbour into which site $\vec{x}$ copies its id (σ), and λ_{chem} is the strength of the chemotactic response up VEGF gradients.

In the *in silico* studies [16, 17, 191], VEGFA gradient and local VEGFA concentrations were constant inputs. However, in our model VEGFA is dynamic, and as we will see in the next section, its concentration leads to up-regulation of Delta [139], whereas local gradients guide tip cell migration and, thereby, sprout polarisation.

High VEGF concentrations (pathological conditions)
In Bentley *et al.* [17], high VEGF concentrations led to sheet formation of multiple tip cells. This is due to all cells attempting to become tip cells. This emergent sheet-like sprouting morphology is consistent with observations of developing mouse retinas in conditions of excessive VEGF concentrations [72].

In Qutub and Popel [191], the model predicted little effect of VEGF concentration on overall vessel growth within the range of 1-25 ng/ml. At 50 ng/ml VEGF, the average increase in vessel length looks noticeably higher compared to 25 ng/ml VEGF. However, the degree of variation in vessel length changes is very high at this concentration, and in some instances, vessel length change could be similar to those at lower concentrations.

There are also a number of other factors that influence VEGF gradients and a cell's response to them. ECs themselves may secrete VEGF as they form a sprout. This autocrine behaviour of ECs (which is probably valid in the *in vitro* rather than the *in vivo* case) was modelled previously by Serini *et al.* [220], and Merks *et al.* in [155, 157]. In addition, cells such as pericytes, endothelial cell precursors, smooth muscle cells, and astrocytes in retina [260] may influence VEGF levels by secretion. ECM heterogeneity and the presence of different VEGF isoforms (soluble and matrix-bounded as modelled by Milde *et al.* in [158]) and heparin binding groups on cells could also alter the response to VEGF gradients.

5.4.2.2 ECM: haptotaxis

ECM is another important factor in the extracellular environment that cells interact with and affects their behaviour. As mentioned in section 5.2.6, haptotaxis is the directional migration of cells up ECM gradients or the the sensitivity of cells to absolute concentrations of ECM components. The latter can be incorporated in the model with the following energy minimization equation

$$H'_{hapt} = \lambda_{ECM} \left(m(\vec{x}) - m(\vec{x}') \right), \tag{5.4.7}$$

where, $m(\vec{x})$ is the ECM concentration at site $\vec{x}$, and λ_{ECM} is the strength of the preferential attachment to ECM. Therefore, depending on the thickness of the ECM fibers, cells will have more affinity to increase or decrease their surface resulting in increased or decreased spreading, respectively. Further details regarding the ECM implementation within the CPM framework are provided in section 5.5.

Experimental studies showed that aligned fibers in the ECM can guide cell migration, and these guiding structures can in turn be remodelled by EC tip cells [134]. Differences

in ECM rigidity or stiffness can also direct migration. In addition, tip cells must break through the basement membrane, proteolytically degrade and invade into the ECM in order to form a new capillary [134]. However, note that remodelling of ECM by ECs, stiffness of ECM, and ECM degradation are not considered in our model.

The effect of ECM in the sprout formation has been published previously by Bauer *et al.* [14], and Milde *et al.* [158], who explicitly incorporated the role of the ECM. Briefly, in [14], the authors assumed that branch splitting resulted from ECM inhomogeneities, and in [158], the authors showed that the structure and density of the ECM has a direct effect on the morphology, expansion speed and number of branches.

5.4.3 Subcellular level: modelling lateral-inhibition

At the subcellular level, the tip cell activation is regulated via the D-N pathway, which is stimulated by the macrophage-mediated VEGFA. The contact lateral-inhibition effect for the exchange of the EC (stalk-tip) phenotype is implemented using a modification of a well established mathematical framework that has been proposed by Collier [37]. The model is defined by a set of coupled ODEs, which describe the dynamical processes of Delta and Notch activation and inhibition in contacting cells. Motivated by Lobov *et al.* [142], where the authors acknowledged the dynamical regulation of Delta expression by VEGFA in the retinal vasculature, we extend Collier's non-dimensional model by incorporating the contribution of the VEGF (as defined in equation (5.4.5)) in the following model,

$$
\begin{aligned}
Delta: \qquad & \frac{dD_j}{dt} = v\left(\alpha \frac{VEGF}{VEGF_h + VEGF}\frac{1}{1+bN_j^2} - D_j\right), \\
Notch: \qquad & \frac{dN_j}{dt} = \frac{\bar{D_j}^2}{a+\bar{D_j}^2} - N_j, \\
trans-Delta: \qquad & \bar{D}_j = \textstyle\sum_i \dfrac{D_i P_{ij}}{P_j},
\end{aligned}
\tag{5.4.8}
$$

where, D_j, N_j, are the levels of Delta and Notch activity in cell j, respectively. At this point, it should be noted that Delta ligands and Notch receptors are assumed to be uniformly distributed on the cell membranes. $VEGF_h$ is the sensitivity of Delta to VEGF or otherwise is the VEGF level at which α, the maximum Delta production rate, is half. For the trans-Delta, the sum is taken over the immediate (contacting) neighbours i of cell j, P_j is the perimeter of cell j, and P_{ij} is the common area of cell j with its neighbour

cells i, which is defined as

$$P_{ij} = \sum_{(\vec{x},\vec{x'})} \left(1 - \delta_{\sigma(\vec{x}),\sigma(\vec{x'})}\right) \left(1 - \delta_{\sigma(\vec{x'}),0}\right) \delta_{\sigma(\vec{x}),i}, \tag{5.4.9}$$

with $\sum_{(\vec{x},\vec{x'})}$ summing over all pairs of adjacent sites in the lattice.

Equations (5.4.8) describe (i) the activation of Notch production within each cell as a function of the levels of (trans-) Delta expressed by neighbouring cells, (ii) the inhibition of Delta expression by Notch, and (iii) the total (trans-) Delta signal ($\bar{D}_j$) received by cell j. The novelty in our model compared to Collier *et al.* [37] is (iv) the activation of Delta production by extra-cellular VEGF secreted from the macrophage. In the absence of VEGF signalling, there is no up-regulation of Delta and, therefore, no tip cell activation. In addition, regarding the VEGFA, we assume an even distribution of VEGFA molecules and that the molecules are in sufficient abundance that stochastic effects can be neglected.

The model of Collier *et al.* [37], and our model presented in equations (5.4.8) incorporate the implicit assumption that all interactions are non-delayed. However, in reality the basic production mechanisms that regulate target genes (e.g. Hes [100]) expression of Notch signalling are associated with time delays and this might be considered for future work.

In the following we present mathematical analysis on perturbations of the homogeneous steady state of equations (5.4.8), and parameter ranges in which the 'salt and pepper' pattern is maintained. In section 5.5 we provide the model set up, and in section 5.6 we present results on sprout formation.

5.4.3.1 Analysis of perturbations of the homogeneous steady state

In this section we consider the non-dimensional model as given in equations (5.4.8), which can be rewritten in the following simplified form

$$\begin{aligned} \frac{dD_j}{dt} &= v\left(\alpha h(V) g(N_j) - D_j\right) , \\ \frac{dN_j}{dt} &= f(\bar{D}_j) - N_j , \end{aligned} \tag{5.4.10}$$

where, $h(V) = \dfrac{VEGF}{VEGF_h + VEGF}$, $g(N_j) = \dfrac{1}{1 + bN_j^2}$, $f(\bar{D}_j) = \dfrac{\bar{D}_j{}^2}{a + \bar{D}_j{}^2}$, and $\bar{D}_j = \sum_i \dfrac{D_i P_{ij}}{P_j}$. Note that f, g are continuously differentiable, with f monotonic increasing

and g monotonic decreasing. Under these conditions there exists exactly one homogeneous steady state (HSS), $(D_j^*, N_j^*) = (\alpha h(V) g(N_j^*), f(\bar{D}_j^*)) = \left(\alpha h(V) g(N_j^*), f\left(\frac{D_j^*}{\sigma}\right)\right)$, where $\sigma = 1$, if squares/hexagons; $\sigma = 2$, if strings. The analysis in this section applies to a specific set up in which VEGF is uniform and constant, and that the cells are arranged into precise configurations (i.e. strings, squares, hexagons). The HSS is defined as the steady state in which all cells have identical levels of Delta and Notch, and we wish to determine the patterns that emerge from perturbations about this steady state. Therefore, we assume that $D_j = D_j^* + \tilde{D}_j$, $N_j = N_j^* + \tilde{N}_j$ for $\tilde{D}_j \ll D^*$, $\tilde{N}_j \ll N^*$, and by also making the following ansatz

$$\tilde{D}(\mathbf{x}, t) = \hat{D}(t) \exp^{ik\mathbf{x}}, \tag{5.4.11}$$

which allows us to remove the spatial dependency $\mathbf{x}$ of D, we get

$$\bar{\tilde{D}} = \tilde{D}\frac{K}{\sigma}, \tag{5.4.12}$$

where $K(k)$, the 'nearest neighbour contributions', is defined as

$$K(k) = \begin{cases} cos(k) & (\text{string}), K \in [-1, 1], \\ \dfrac{cos(k_1) + cos(k_2)}{2} & (\text{squares}), K \in [-1, 1], \\ \dfrac{cos(k_1) + |cos(k_2)| + cos(k_1 + k_2)}{3} & (\text{hexagons}), K \in [-1/2, 1], \end{cases} \tag{5.4.13}$$

with k being the wavenumber (or wave-vector, $k = (k_1, k_2)$ in two space dimensions).

The system (5.4.10) can be linearised about the HSS to give

$$\begin{aligned} \frac{d\tilde{D}}{dt} &= v\left(\alpha h(V) g'(N^*)\tilde{N} - \tilde{D}\right), \\ \frac{d\tilde{N}}{dt} &= f'(\tfrac{D^*}{\sigma})\tilde{D}\frac{K}{\sigma} - \tilde{N}, \end{aligned} \tag{5.4.14}$$

where $F = f'(\frac{D^*}{\sigma}) = \frac{2a\frac{D^*}{\sigma}}{(a+(\frac{D^*}{\sigma})^2)^2} > 0$, $G = g'(N^*) = -\frac{2bN^*}{(1+bN^{*2})^2} < 0$, and $'$ denotes differentiation. The linearised system (5.4.14) gives the following Jacobian matrix

$$J(K) = \begin{pmatrix} -v & v\alpha h(V) G \\ F\dfrac{K}{\sigma} & -1 \end{pmatrix}. \tag{5.4.15}$$

We note that the trace, $tr(J(K)) = -v - 1$, is always negative since $v > 0$, and

$$det(J(K)) = v\left(1 - \alpha h(V) F G \frac{K}{\sigma}\right). \tag{5.4.16}$$

From stability analysis we know that if $tr(J) < 0$ and $det(J) > 0$ then we have a stable HSS. As a model for lateral-inhibition, we are most interested in the case where the HSS is stable to homogeneous ($k = 0$), and unstable to heterogeneous ($k \neq 0$) perturbations. That is when $det(J(1)) > 0$, and $det(J(K)) < 0$ for some $K \in [-1, 1)$ or $[-1/2, 1)$.

Remark that G is always negative and, therefore, we exclude the cases when $K > 0$ (for which $det(J) > 0$). In strings/squares we consider the case where $K = -1$, and for hexagons where $K = -1/2$ (when the $\Re(\lambda)$ is maximal, with λ the eigenvalue of $J(K)$; for instance, see Figure 5.5 for strings/squares) and, therefore, if

$$\begin{aligned}
&\text{strings:} \quad det(J(-1)) < 0 \Leftrightarrow \Phi^{'}\left(\frac{K}{\sigma}\right) = \Phi^{'}\left(\frac{-1}{2}\right) = \alpha h(V) FG < -2, \\
&\text{squares:} \quad det(J(-1)) < 0 \Leftrightarrow \Phi^{''}\left(\frac{K}{\sigma}\right) = \Phi^{''}\left(\frac{-1}{1}\right) = \alpha h(V) FG < -1, \\
&\text{hexagons:} \quad det(J(-1/2)) < 0 \Leftrightarrow \Phi^{''}\left(\frac{K}{\sigma}\right) = \Phi^{''}\left(\frac{-1/2}{1}\right) = \alpha h(V) FG < -2.
\end{aligned} \tag{5.4.17}$$

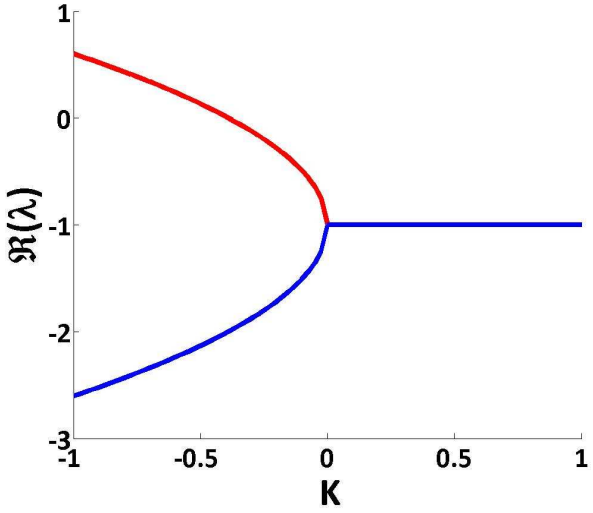

Figure 5.5: The $\Re(\lambda_{1,2})$ of the eigenvalues $\lambda_{1,2}$ (denoted with different colour), evaluated from the Jacobian as in (5.4.15), is maximal when $K = -1$ (for strings/squares as in (5.4.13)). The parameter values used in the model (5.4.10): $a = 0.01$, $b = 100$, $v = 1$, $VEGF_h = 1$, $VEGF = 1$, $\alpha = 1$.

In Figure 5.6(a)-(b) we explore for which values of α the $det(J)$ in equation (5.4.16) becomes negative. That is, (a) for strings, when $\Phi^{'} < -2$, and (b) for squares and hexagons, when $\Phi^{''} < -1, -2$, respectively. In Figure 5.6(c) we show that for $\alpha \in [0.13, 38.7]$ for strings, for $\alpha \in [0.07, 19.3]$ for squares, and for $\alpha \in [0.16, 4.5]$ for hexagons, the HSS is unstable ($det(J) < 0$) and we get the 'salt and pepper' (checkerboard) pattern, otherwise the HSS is stable ($det(J) > 0$) and no patterning is observed.

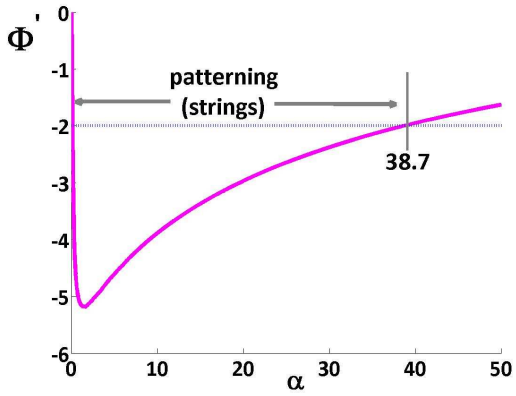

(a)

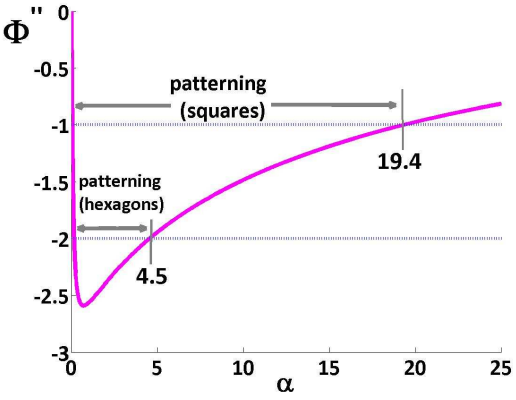

(b)

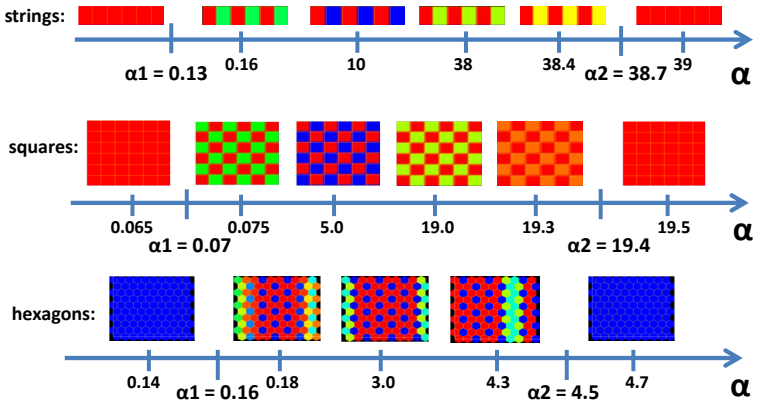

(c)

Figure 5.6: (a)-(b) $\Phi^{'}$ and $\Phi^{''}$ as in equation (5.4.17) over α (the maximum Delta production rate) showing the ranges of α for which we get the checkerboard pattern. That is, (a) for strings, when $\Phi^{'} < -2$, and (b) for squares and hexagons, when $\Phi^{''} < -1, -2$, respectively. (c) Simulation results for strings, squares, and hexagons for different values of α as in (a) and (b). The parameter values as in Figure 5.5. Colourbar: high (red) and low (blue) Delta levels at 1000 MCS.

5.5 Methods

This section outlines the basic steps of the *in silico* model development. Our simulations use the open-source simulation environment CompuCell3D (CC3D) and Python scripts specifically developed by the author.

5.5.1 Model setup

Our model is considered on a square spatial domain (size 200μm x 200μm; representing a square of corneal tissue) as depicted in Figure 5.7(a) with the parent vessel located along one side and the macrophage located at distance L=60 μm from the blood vessel. Figure 5.7(b) shows the case where the VEGF is uniform in the whole domain and macrophage is not considered.

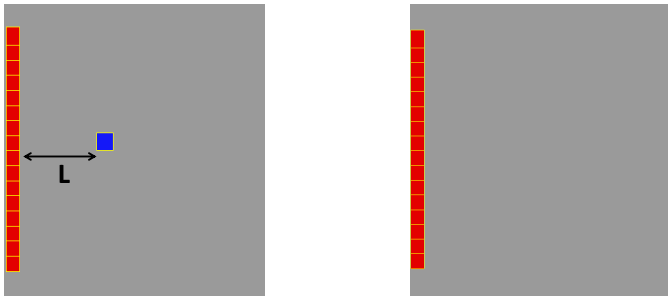

(a) (b)

Figure 5.7: Model setup on the numerical domain, (a) with, or (b) without macrophage (VEGFA source). Key: stalk cells (red); macrophage (blue).

5.5.1.1 ECM

In CC3D, the substrate (e.g. medium) is normally represented as a fixed cell covering the whole numerical domain. In order to be able to model a non-uniform structure of the ECM, we used our scripts in MATLAB software package to produce ECM fibers randomly distributed in the numerical domain as shown in Figure 5.8. We consider ECM fibers comparable to the cell size, and we assume that the ECM is rigid (fixed in space). That is, cells do not produce or degrade ECM. Each pixel in the numerical domain occupied by an ECM fiber is given a non zero (=1) value (and zero elsewhere), so that the cells can preferentially adhere to the fibers depending on the strength of ECM attachment (λ_{ECM}) as in equation (5.4.7).

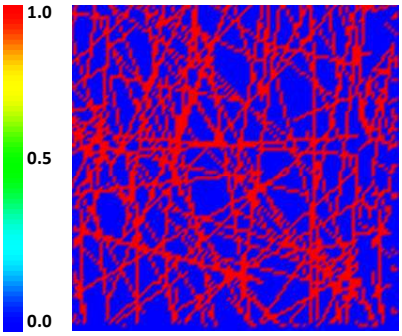

Figure 5.8: Extracellular matrix (ECM) structure as implemented in the CPM framework with the colorbar showing the ECM levels.

5.5.2 Space & time conversions

By equating the initial cell volume in the model to the real cell size (e.g. 5x5 pixels^2 = 10x10 μm^2 [263]), we can convert the lattice spacing to microns (1 pixel = 2 μm). In addition, we set the time conversion to be 1 MCS = 0.01 hrs, which is slightly different to the one (1 MCS = 0.016 hrs = 1 min) chosen in Chapter 4 in order to allow for further investigation of the stalk-tip cell exchange during sprout evolution.

5.5.3 Parameters

The default parameter values used for our simulations are summarised in Table 5.4, unless otherwise stated. Below we provide a discussion on how some of those were estimated.

5.5.3.1 Cell cycle time

Remark that in our cell level model (see section 5.4.1.1), stalk cells adjacent to tip cells can divide based on their cell cycle time (t_{cycle}). This is estimated from available data on EC numbers from retina at different post-natal time points as given in Table 5.3 [Courtesy of Luisa-Iruela Arispe]. As we mentioned (see Figure 5.2), EC sprouting from the ophthalmic vein begins around the day of birth, and a dense plexus arrives at the retinal periphery by post-natal day 7 (P7). For this reason we are interested in

sprout behaviour around P7 and, therefore, we calculate t_{cycle} as follows,

$$\begin{aligned} N_7 &= N_6 2^{24/t_{cycle}} \\ t_{cycle} &= 24 \log_2 \left(\frac{N_7}{N_6} \right) \\ t_{cycle} &\simeq 17 \text{ hrs}, \end{aligned} \tag{5.5.1}$$

where, N_j is the number of ECs in retina at day j.

Table 5.3: Number of ECs in the retina over time (post-natal days)

day	1	2	3	4	5	6	7	9	11
ECs	208	312	998	3891	10903	40934	109896	509348	1183084

5.5.3.2 VEGFA: diffusion, secretion and decay

Our simulations use parameters for VEGFA as in Table 5.4. To isolate the effects of ECM topology on sprout morphology, we assume that D is constant. This is a simplification, however, because the ECM is not homogeneous and the growth factors can be bound to and stored in the ECM.

5.5.3.3 Tip cell activation

In Qutub and Popel [191], a tip cell can be activated if VEGF concentration, [VEGF]>0.5 ng/ml. Without VEGF or with local VEGF levels below this threshold, the cells do not get activated.

However, in our model, a tip cell is activated if its Delta level is above a non-dimensional threshold value ($D^* = 0.27$). We admit that this threshold has not been evaluated from any experimental measurements, but this may be evaluated in future experiments.

5.5.3.4 Cell-cell adhesion: contact energies (J)

In all the simulation results that follow in section 5.6, we use the following set of contact energies: $J_{s,t} = 3$, $J_{s,s} = 3$, $J_{t,t} = 10$, where s, t stand for stalk and tip cell, respectively. In doing so, we assume strong adhesion between stalk and tip cells, and weaker adhesion between tip cells. Therefore, fusion of two tip cells will emerge dynamically (from the chemotactic direction and/or ECM alignment), and not from preferential adhesion between tip cells.

Table 5.4: Default parameter settings for simulations

Parameter	Description	Value	Reference
Cell features:			
A	cell target area	100 μm^2	[263]
T	cell-membrane fluctuations	10	/
λ_{area}	resistance to changes in size/area	10	/
λ_{length}	resistance to changes in length	15	/
λ_{chem}(stalk)	chemotaxis strength for stalk cells	50	/
λ_{chem}(tip)	chemotaxis strength for tip cells	200	estimated
λ_{ECM}	strength of preferential attachment to ECM	20	estimated
Adhesion:			
$J_{s,t}$	stalk-tip contact energy	3	/
$J_{s,s}$	stalk-stalk contact energy	3	/
$J_{t,t}$	tip-tip contact energy	10	/
VEGFA:			
D	diffusion constant VEGFA	10^{-11} m^2/s	[180]
s	secretion rate VEGFA	10^{-4} nM/s	[180]
δ	decay rate VEGFA	10^{-4} 1/s	[180]
D^*	Delta threshold for tip cell activation	0.27	/

5.6 Results

In this section we provide the main results from our model by considering first the influence of cell shape on D-N ('salt and pepper') patterning, and then different scenarios (see Table 5.5) regarding VEGF and ECM profiles. Cell shape, sprout width and sprout polarisation is predominantly determined by the interplay between chemotaxis, cell-cell (homotypic and heterotypic) adhesion, and the ECM environment. Figure 5.10 shows representative snapshots for each scenario at different time points, and below we provide results in greater detail.

Table 5.5: Different scenarios regarding VEGF and ECM profiles

	Scenarios
1.	homogeneous VEGF & homogeneous ECM
2.	homogeneous VEGF & heterogeneous ECM
3.	static VEGF gradients & homogeneous ECM
4.	static VEGF gradients & heterogeneous ECM
5.	heterogeneous VEGF & homogeneous ECM
6.	heterogeneous VEGF & heterogeneous ECM

5.6.1 Influence of cell shape on D-N patterning

Equation (5.4.17) shows that string ('salt and pepper') patterning occurs when $\Phi^{'} < -2$. In Figure 5.9(a) we see that this condition is satisfied for VEGF above a threshold (VEGF$>$ 0.07). In fixed cell geometries (without cell movement, fluctuations, elongation etc.) we observe no patterning for VEGF below this threshold, as expected (see Figure 5.9(b)). However, if cells are allowed to move, this condition does not necessarily hold, and we are able to generate patterning for VEGF$<$ 0.07 (see Figure 5.9(c)). This happens because if cells are not fixed, $\bar{D}_j$ as in equation (5.4.8) changes since P_{ij} (the contact areas between cell j and its neighbours) change. Note that in Figure 5.9(b), the cells at the edges of the string have larger Delta levels compared to the others, since these two cells have only one neighbour, which implies a smaller value of $\bar{D}_j$ for them, which results in increased Delta.

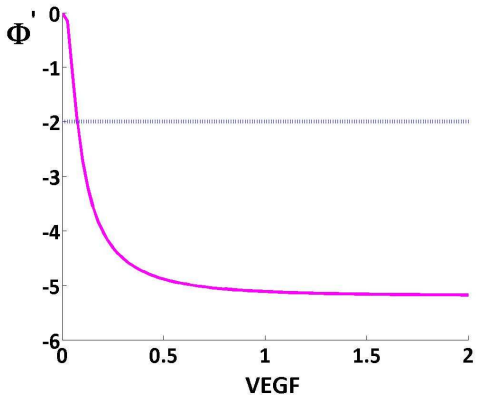

(a)

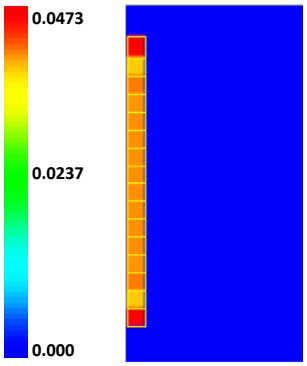

(b) fixed cells; no patterning

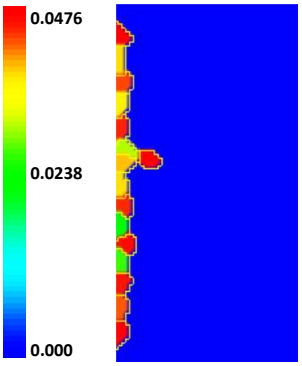

(c) not fixed cells; patterning

Figure 5.9: (a) $\Phi^{'}$ as in equation (5.4.17) over uniform VEGF, (b)-(c) Delta profile with and without fixing cell geometries, respectively, in 1000 MCS. Parameters for the model (5.4.10): VEGF= 0.05, $\alpha = 1$.

In the following, for scenarios 1 and 2 with uniform VEGF, we choose sufficiently large VEGF (= 1) so that patterning is allowed. In addition, in scenarios 1 to 6 (except from D-N patterning as in section 5.6.1) we allow for cell movement (cells are not arranged into precise configurations) and all the other cell behaviours as summarised in Table 5.2.

5.6.2 Scenarios 1 & 2

In scenarios 1 and 2, there is no VEGF gradient, which implies no sprout polarisation. Figure 5.10 shows that cell proliferation and elongation are undirected and, therefore, stalk and tip cells evenly fill the space giving a checkerboard-like pattern. This cell behaviour results in a reduced extent of EC migration (as shown later in Figure 5.11). That was also found experimentally in [72, 160], where VEGF gradient was removed

in the retina, via an increased expression of VEGFA in transgenic mouse models. In scenario 2, it can be observed that the addition of a non-uniform ECM has a weak effect. A parameter which could potentially have an effect on that is the λ_{ECM} (the preferential attachment of cells to the ECM). That is, if λ_{ECM} is large, the cells are more attractive onto the ECM fibers. However, we will see later in section 5.7 that this could adversely affect (decrease) the sprout extension.

5.6.3 Scenarios 3 & 4

In these scenarios we incorporate static VEGF gradients, which eventually lead to swollen sprout formation either with or without ECM.

Note that results in scenarios 1 to 4 approximately up to day 1 look quite similar. That is, sprouts are dominated by single elongated tip cells. However, there are distinct differences on days 2 and 3. Particularly, in scenarios 3 and 4, cell proliferation is focused on single sprouts as a result of the steep VEGF gradients.

5.6.4 Scenarios 5 & 6

Here, a fixed macrophage (VEGF source) is responsible for the VEGF gradients. The resulting morphology of the capillary sprout is determined by two main mechanisms: the macrophage-mediated VEGFA, which activates the Delta activity in each cell (according to equations (5.4.8)), and the D-N signalling pathway which yields the 'salt and pepper' pattern with tip cells migrating up VEGFA gradients.

Figure 5.10 (scenarios 5 and 6) demonstrates the model's ability to reproduce realistic capillary sprout morphologies (up to $\sim$18 hrs). Scenario 5 (with homogeneous ECM) can give a polarised sprout, but scenario 6 with heterogeneous ECM gives narrower sprouts in 12-18 hrs.

Therefore, we suggest that scenario 6 provides a close approximation to a growing vascular sprout as depicted in the schematic in Figure 5.1, and henceforth, all results shown are derived under scenario 6, unless otherwise stated. However, since the macrophage is fixed it does not allow for a longer sprout formation, because at late time points (days 2-3) we observe a mass of cells surrounding the macrophage. Therefore, in section 5.8 we extend our model by incorporating macrophage motility, a condition which can allow for longer sprout formation over 3 days.

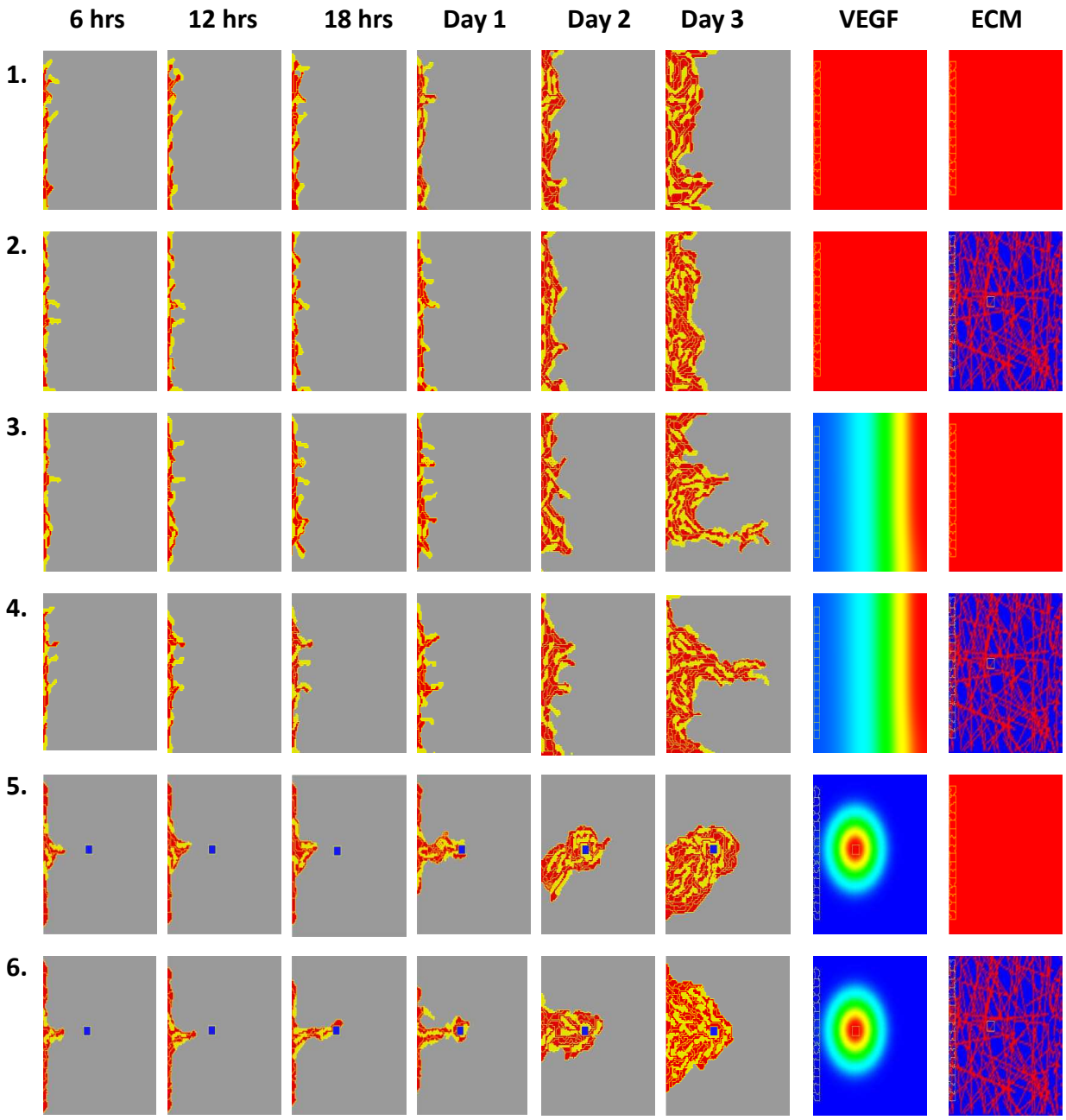

Figure 5.10: Representative snapshots at different time points (up to 3 days) from the six scenarios regarding different VEGF and ECM profiles as summarised in Table 5.5. Key: stalk cells (red), tip cells (yellow), fixed macrophage (blue).

5.6.5 Sprout length & extension speed

Sprout length is determined by measuring the distance from the parent blood vessel (located at the one side of the domain; see Figure 5.7) to the leading tip cell's centre of mass. Average sprout extension speed is then calculated as the final sprout length

over time. Figure 5.11 shows the average speed of the sprout for the six scenarios (as in Table 5.5) up to 18 hrs, the time needed from the sprout to reach the macrophage in scenario 6. Scenarios 5 and 6 are the ones with the highest speed, since cell proliferation is focused on a single sprout. The results from those two scenarios are in a good agreement with retinal experimental data [speed $\sim$3.3 $\mu m/hr$ between day 5-7; speed $\sim$4.8 $\mu m/hr$ between day 7-9] provided by Dr. Luisa-Iruela Arispe.

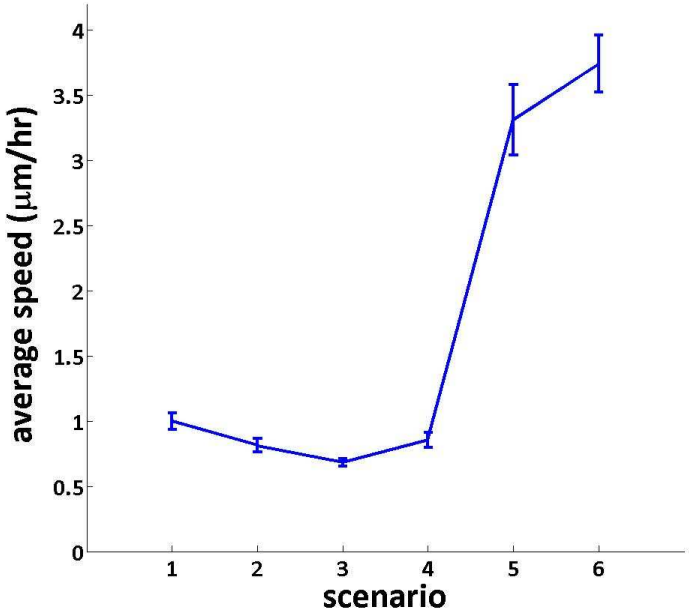

Figure 5.11: Average speed of sprout in 18 hrs for the six scenarios given in Table 5.5. Speed in scenarios 5 and 6 give a good approximation to experimental data. Results are mean $\pm$ S.E.M. from 10 simulations for each scenario.

5.6.5.1 Sprout anastomosis (fusion)

When the head tip cell of a growing sprout contacts another sprout (other head tip cell), new cell-cell junctions are established and the sprouts become connected (anastomosis, see Figure 5.12). The establishment of new contacts between tip cells is not yet fully understood. Recent descriptions of macrophage-tip cell interactions, in particular at sites where two tip cells make contact via their filopodia, raised the hypothesis that macrophages might act as 'bridge cells' that facilitate the contact and possibly stabilise nascent connections [206, 216].

It is important to note, however, that anastomosis in the complete absence of macrophages is normal, albeit less frequent [206]. Possible receptor-ligand candidates that mediate this interaction are Notch1-Dll4, Tie2-Ang2 or chemokine receptor CXCR4-stromal

cell-derived factor-1 (SDF1). Interestingly, the Notch1, Tie2 and CXCR4 receptors are expressed in macrophages [56], whereas their respective ligands Dll4, Ang2 and SDF1 are expressed in tip cells [86].

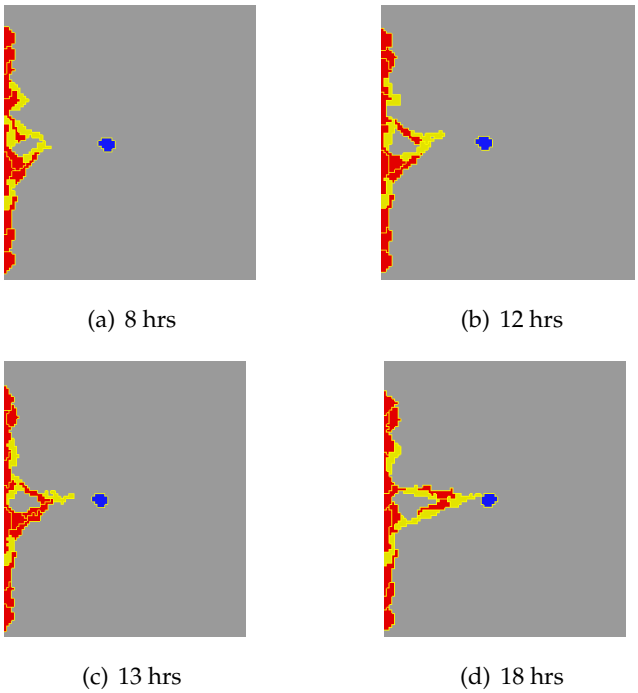

(a) 8 hrs (b) 12 hrs

(c) 13 hrs (d) 18 hrs

Figure 5.12: Representative simulation snapshots (different realisation of scenario 6 from Figure 5.10) at different time points showing the model's ability to reproduce anastomosis. (a)-(b) tip cell fusion (two adjacent tip cells), (c) one of the two tip cells becomes a stalk cell (lateral-inhibition effect from Notch signalling), and (d) the leading tip cell moves up the macrophage-mediated VEGFA gradients. Key: stalk cells (red), tip cells (yellow), macrophage (blue).

5.6.5.2 No elongation

Here we investigate the effect of cell elongation on the sprout formation in scenario 6. Figure 5.13(a) shows that if stalk cells adjacent to tip cells are not able to elongate, then the sprout splits. Similarly, Figure 5.13(b) shows that if both stalk and tip cells are not able to elongate, the same is true. Together this suggests that cell elongation is necessary for sprouting. It should be noted, however, that if cell proliferation was increased that could sometimes prevent cell detachment, but the sprout width would increase which is not desirable (results not shown in this case).

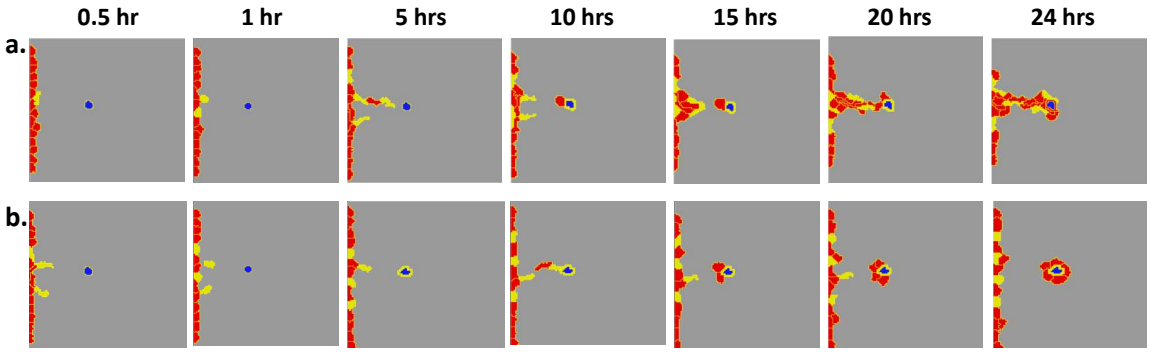

Figure 5.13: Representative simulation snapshots (derived from scenario 6) with no cell elongation, a) from the stalk cells (adjacent to tip cells), and b) from both stalk and tip cells. It can be observed that in (a) from 5 to 10 hrs a tip cell detaches from the sprout and surrounds the macrophage and, similarly, in (b) at 5 hrs the macrophage is surrounded by a tip cell. At later time points more cells follow to end up with a mass of cells around the macrophage.

5.6.6 Perturbation experiments: D-N knockouts

The VEGFA-Dll4-Notch1 signalling appears to be critical to vascular development. In this section we summarise published experimental results on VEGFA-Dll4-Notch1 signalling, and aim to address its importance in sprout growth in *in silico* knockout experiments.

5.6.6.1 *In vitro* knockout experiments of Notch signalling

The dynamic interaction between VEGF and Notch signalling was unravelled independently by several groups while studying the process of angiogenic sprouting in the postnatal mouse retina [86, 142, 240]. They all observed Dll4 expression in ECs at the leading front of the vascular plexus and found that inhibition of D-N signalling results in increased vascular density due to excessive sprouting.

Similar findings were described in the zebrafish ISV sprouting model. Inhibition of the Notch pathway induced hyperbranching of the ISVs and led to an increased number of ECs in the ISVs [132, 229]. By contrast, overexpression of the activated Notch receptor blocks sprouting of the ISVs [229].

In addition, haploinsufficiency (when in diploid organisms one of the two copies of a gene is mutated) of the Dll4 gene was embryonically lethal in many mouse strains as a result of extensive vascular defects [67, 121].

5.6.6.2 Published *in silico* knockout experiments

Below we briefly discuss results obtained from two *in silico* models which attempted to address the effects of D-N knockout experiments on vessel development.

In [191], Qutub and Popel studied the effects of VEGF protein concentrations and Dll4 haploinsufficiency (Dll4+/-) on capillary network formation. Without VEGF or with local VEGF levels less than 0.6 ng/ml, the cells in the model were not activated. Regarding the effect of haploinsufficiency of Dll4 on blood vessel sprouting, it was found that in Dll4+/- condition, the relative total vessel length and the number of tip cells in 24 hrs increased compared to control conditions. Note that the Dll4's activity (and haploinsufficiency) in [191] is ingrained in the model in a rule-based way, e.g. tip cell proliferation, the maximum number of tip cells, and the rules in branching are different in Dll4+/- and Dll4+/+ conditions.

In [16], Bentley *et al.* implemented the Dll4+/- *in silico* experiments by varying a parameter δ, which controls the expression level of Dll4 in response to VEGF (equivalent to parameter α in our model (5.4.17)). In particular, by setting δ to 1 which is equivalent to a Dll4+/- heterozygous knockout genotype (as δ was set to 2 in normal case (Dll4+/+)) showed that the model is unable to give the 'salt and pepper' pattern. The lowered inhibition level causes all cells to be classified as tip cells. The authors suggested that a Dll4+/- mutant would perform normal patterning at twice the VEGF level. However, in the following, results from our *in silico* knockout experiments suggest that the latter may not always be true.

5.6.6.3 New knockout experiments in our *in silico* model

In Figure 5.14 we present results from our *in silico* model in a Dll4+/- condition. We follow a similar approach as in [16]; that is, vary α (the maximum Delta production rate). Our parameter choice (e.g. uniform VEGF=1 (as in scenarios 1 and 2), and $\alpha = 1$) in the parameter space (α, VEGF) sets our case to be at point A (see Figure 5.14(a)). If we move from A to B, or B to C, or C to D by halving α each time (see Figures 5.14(b)-(d)), then we get patterning for all cases since we are in the white region of Figure 5.14(a), where $\Phi^{'} < -2$ as in equation (5.4.17). However, if we move from D to E, we lose patterning (high Delta in all cells). As we mentioned above, Bentley *et al.* in [16] suggested that if we double the VEGF level, patterning could be recovered. We show here an example where if we move from E to F (by doubling VEGF from 1 to 2) patterning is not recovered (see Figures 5.14(e)-(f)). Therefore, our results suggest that if $\alpha \to 0$, recovery is not necessarily possible.

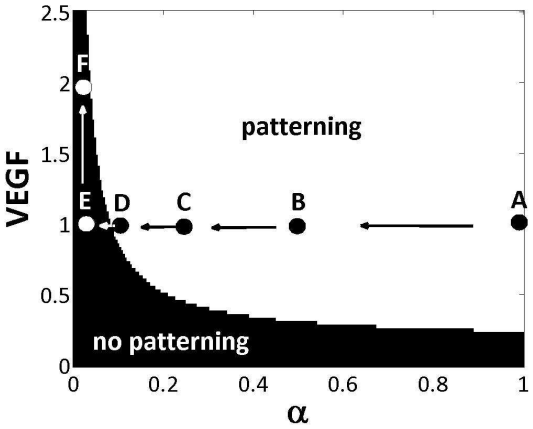

(a)

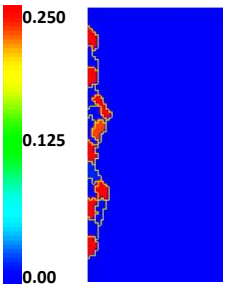

(b) $A \rightarrow B; \alpha = 0.5; VEGF = 1$

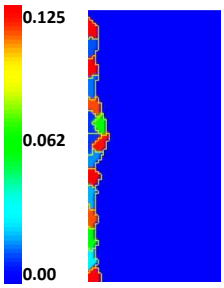

(c) $B \rightarrow C; \alpha = 0.25; VEGF = 1$

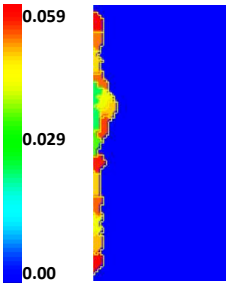

(d) $C \rightarrow D; \alpha = 0.12; VEGF = 1$

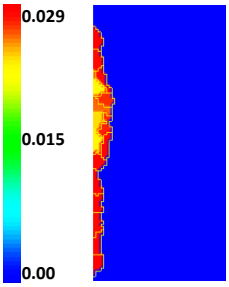

(e) $D \rightarrow E; \alpha = 0.06; VEGF = 1$

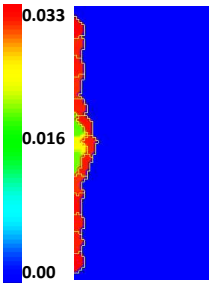

(f) $E \rightarrow F; \alpha = 0.06; VEGF = 2$

Figure 5.14: (a) VEGF over α (the maximum Delta production) shows the ranges of patterning when $\Phi^{'} < -2$ as in equation (5.4.17). See text (section 5.6.6.3) regarding the movement from point A to F. (b)-(f) Delta levels in different combinations of VEGF and α where patterning does or does not occur.

5.7 Sensitivity analysis

Dynamic rather than strictly rule-based models (e.g. [191]) are necessary for understanding the mechanisms of how sprout formation generates robust properties to cell-cell adhesion, lateral-inhibition (interchange between stalk and tip cell phenotypes), and environmental changes (e.g. chemotaxis, haptotaxis).

By considering the difficulty to get the exact parameter values either from *in vitro* or *in vivo* experiments, sensitivity analysis allows the link to the robustness of results. In our model, simulations were performed in which parameters were varied independently from their reference values presented in Table 5.4.

5.7.1 VEGF decay rate

The spatial distribution of VEGF has several influences on angiogenesis. Firstly, we varied the VEGF gradient, via the decay rate of VEGF (δ) as in equation (5.4.5).

Figure 5.15(c) shows that in normal decay rates there is directed sprouting and polarised proliferation. However, in small decay rates (Figure 5.15(a)-(b)) the sprout morphology dramatically changes. The sprout splits off resulting in a mass of cells surrounding the fixed macrophage, as a consequence of strong chemotaxis induced by steep VEGF gradients (Figure 5.15(e)). On the other hand, a large decay rate may induce shallow VEGF gradients and low VEGF levels, which in turn do not allow for tip cell activation (Figure 5.15(d)).

It is also worthy to note that by increasing the VEGF decay rate it could potentially be regarded as equivalent to an anti-VEGF therapy characterised by the administration of e.g. a VEGF aptamer, a molecule which binds to VEGF with high affinity so that the free VEGF available to ECs is reduced [267]. It is important to note though that anti-VEGF therapy depends on the day that we are referred to and, therefore, on the pericyte coverage of a sprout. Noteworthy, in retina at day 10 all vessels are fully covered by pericytes and are resistant to anti-VEGF therapy [107]. Pericytes are crucial to vessel stabilisation (maturation process). Our model does not currently incorporate pericytes, but it could be considered for future implementation. Taking the above statements and findings into account, care should be taken when suggesting any anti-angiogenic treatments at present.

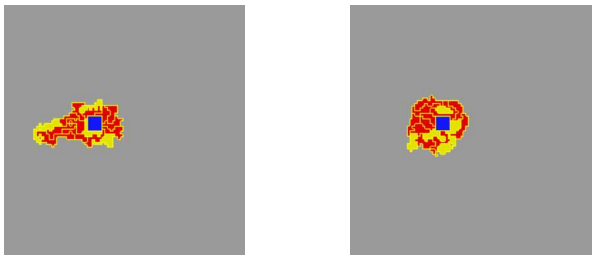

(a) $\delta = 0.0025$

(b) $\delta = 0.005$

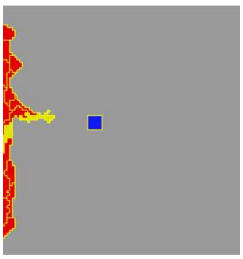

(c) $\delta = 0.01$

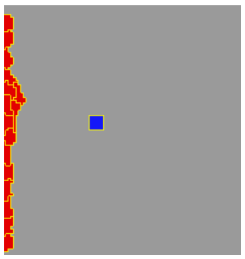

(d) $\delta = 0.02$

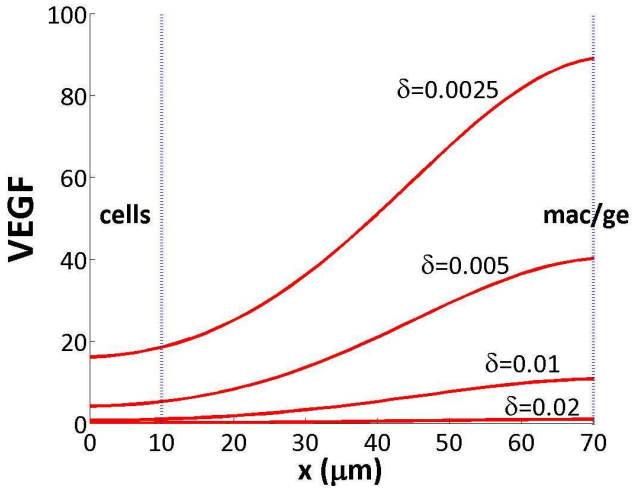

(e)

Figure 5.15: The markedly different capillary sprout morphologies (after ∼5 hrs) that result from small (a)-(b), normal (c), and large (d) VEGF decay rate δ (1/min). (e) Cross section of VEGF gradients for the four different cases of δ. Cells of the parent blood vessel are located within 0-10 μm, and the macrophage at $x = 70\mu m$. See Figure 5.7 for the model set up. Key: stalk cells (red), tip cells (yellow), macrophage (blue).

5.7.2 Strength of chemotaxis

Chemotaxis promotes migration up the macrophage-mediated VEGFA gradients, and in this section, we investigate how sprouting depends on the chemotactic strength, λ_{chem}. The value of λ_{chem} might depends on the amount of receptors for the chemoattractant expressed by the cells [225], and obviously, is hard to get values in measurable units. Therefore, a range of values was tested to find a close approximation to a growing vascular sprout, as depicted in the schematic in Figure 5.1.

In Figure 5.16 we show morphological results of sprout formation from three examples: (a) low, (b) intermediate, and (c)-(d) high λ_{chem}. Figure 5.16(a) shows that if strength of chemotaxis from tip cells is low that will eventually prevent sprouting (sprout will not reach the macrophage). However, if it is large (Figure 5.16(c)-(d)), the sprout splits off, which is comparable with low VEGF decay rate as it is shown in Figures 5.15(a)-(b). Strong chemotaxis can increase the extension speed and promote cell elongation, but the stronger the chemotaxis, the stronger the cell-cell adhesion is needed to keep cells in contact and avoid cell detachment. Therefore, a better chemotactic response is achieved at intermediate chemotactic forces (Figure 5.16(b)), where there is a balance between cell-cell adhesion and chemotactic migration.

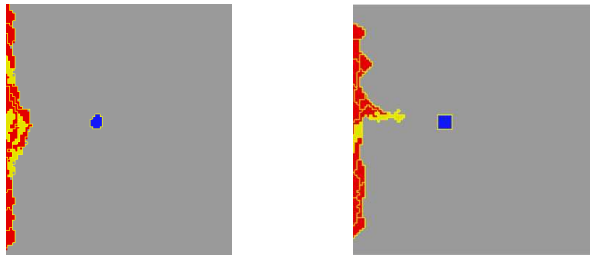

(a) $\lambda_{chem} = 10$ (b) $\lambda_{chem} = 200$

(c) $\lambda_{chem} = 500$ (d) $\lambda_{chem} = 500$

Figure 5.16: Snapshots of growing sprouts after 5 hrs (except (c) 1 hr) by varying the strength of chemotaxis (λ_{chem}) in three different cases, (a) low, (b) intermediate, and (c)-(d) high λ_{chem}.

5.7.3 Strength of preferential attachment to ECM

Next we investigate the role of haptotaxis on the speed and morphology of the sprout formation by varying the strength of preferential attachment to ECM, λ_{ECM} (see equation (5.4.7)), as shown in Figure 5.17. We found, as might be expected, that if λ_{ECM} is large (e.g. $\lambda_{ECM} = 100$) the speed decreases and the sprout is not able to reach the macrophage since cells strongly adhere to the ECM. However, intermediate values (e.g. $\lambda_{ECM} = 20$) give a good speed approximation to experimental data [speed $\sim$3.3 $\mu m/hr$ between day 5-7; speed $\sim$4.8 $\mu m/hr$ between day 7-9] provided by Dr. Luisa-Iruela Arispe. Morphological results are not shown in this case.

Our simulation results are in line with experimental results from DiMilla *et al.* in [49], where they showed that the migration behaviour of human smooth muscle cells on fibronectin and collagen IV varied with the concentration of each matrix protein. In particular, cells had maximal migration speed at small and intermediate levels of adhesiveness, since at low ECM densities, a cell cannot form strong stable adhesions to generate traction forces, and at high densities a cell cannot detach adhesions from the substrate.

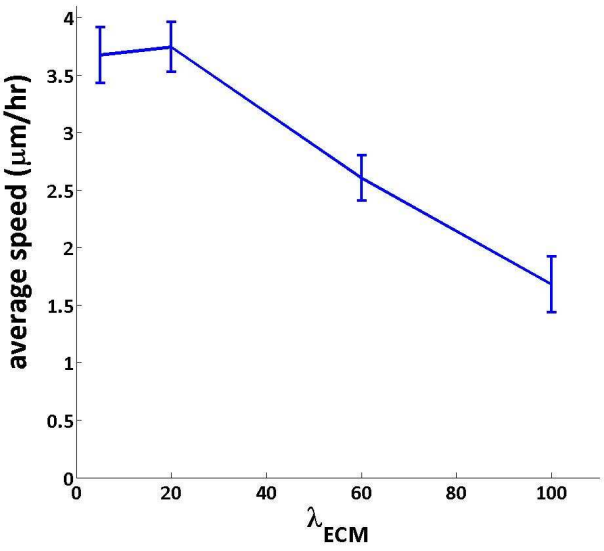

Figure 5.17: Average speed of the sprout over λ_{ECM} (strength of preferential attachment to ECM) in 18 hrs. Intermediate rather than high values of λ_{ECM} give a better speed approximation to experimental data. Results are mean $\pm$ S.E.M. from 10 simulations for each value of λ_{ECM}.

5.8 Model variants

5.8.1 Scenario 6 + Moving macrophage

As we described in section 5.6, scenario 6 provides a close approximation to a growing vascular sprout as depicted in the schematic in Figure 5.1. However, the fixed macrophage does not allow for a longer sprout formation, since a mass of cells eventually surrounds the macrophage. To tackle this problem, in this section we extend our model (in scenario 6) by allowing cell (macrophage) motility, as implemented in Chapter 4 (see equation (4.3.3)),

$$H'_{motility} = r(cos\theta(t), sin\theta(t)) \cdot (\vec{x} - \vec{x'}), \tag{5.8.1}$$

with r representing the cell speed, and θ the rotation angle. Two important questions arise at this point: first, regarding the speed of the macrophage, and second, the time point that the macrophage should start moving. A reasonable answer to start with would be to allow the macrophage to start moving from the beginning of each simulation. The speed of the macrophage must still be determined - the optimal would be to get the same speed (or at least a good approximation) for both the sprout and the macrophage. However, that would be difficult since the sprout extension speed varies at different time points depending on the steepness of the VEGF gradient.

5.8.1.1 Macrophage moves from the beginning

In this section we allow the macrophage to move from the beginning of each simulation, and with $\theta = 0$ so that it moves parallel to the x-axis and only to the right-hand side (away from the blood vessel). Since r represents the speed, it would be appropriate to assess the sprout behaviour at various values of r. In doing this, we found that for low/medium values (below 3.5 $\mu m/hr$ as in Figure 5.11), the sprout can reach the macrophage, and henceforth, the motility and direction of the macrophage depends only on the dynamics of the sprout. Reassuringly, when r lies within low/medium ranges we are able to get a sprout up to a certain time point. However, the sprout eventually splits, presumably at the point where the VEGF gradients become less steep. In Figure 5.18 we observe that after 42 hrs the detached section of the sprout continues to 'push' (chemotacting towards) the macrophage. On the other hand, if r is large (greater than 3.5 $\mu m/hr$), the sprout is no longer able to reach the macrophage, and eventually all the cells in the blood vessel become or remain as stalk. Therefore, in this case we get no sprout formation. Morphological results are not shown in this case.

Overall, we can conclude that there are two problems: the cell detachment (splitting), and finding the best match of the speeds between sprout and macrophage. In order to tackle these problems, in the next section we introduce a different scenario regarding the macrophage motility.

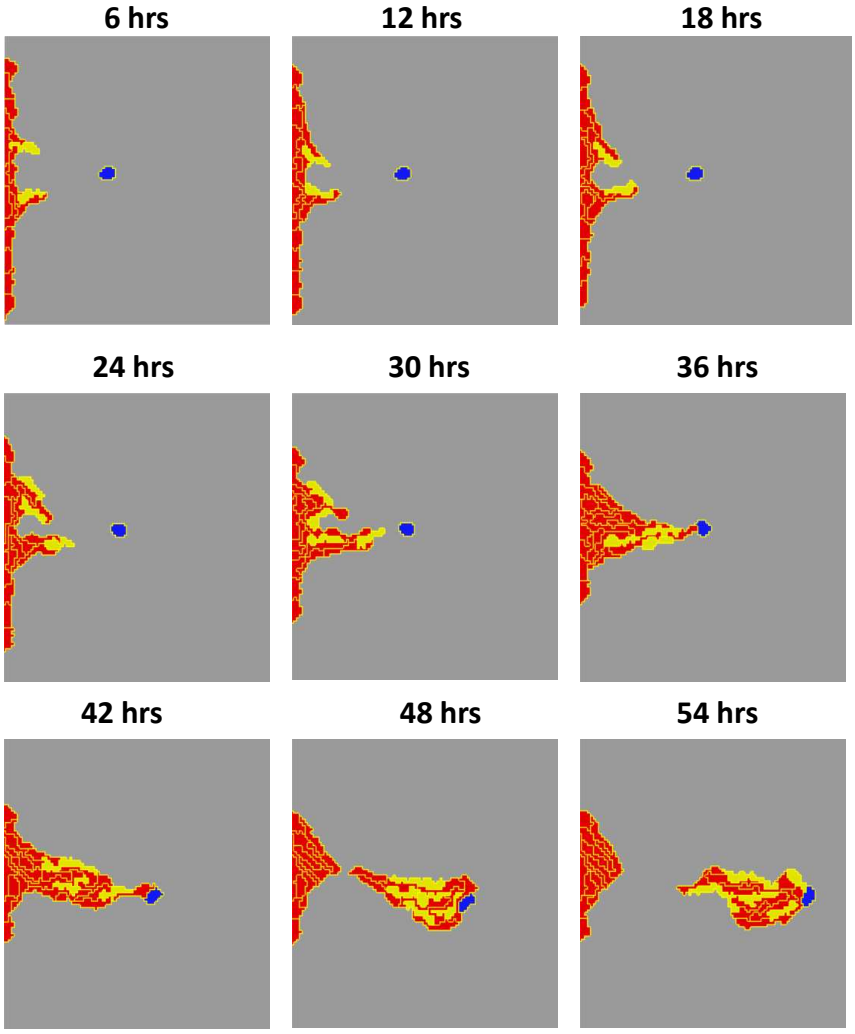

Figure 5.18: Representative snapshots showing sprout evolution at different time points with a moving macrophage at low/medium speed (as described in section 5.8.1.1). The sprout splits after 42 hrs, and the detached section of the sprout continues to 'push' the macrophage. Key: stalk cells (red), tip cells (yellow), macrophage (blue).

5.8.1.2 Macrophage moves only when in contact with the sprout

In McDougall *et al.* [153] the authors are referred to the spatio-temporal formation of the retinal vascular plexus in wild-type mice. In particular, prior to birth, astrocytes migrate from the optic nerve over the surface of the inner retina in response to a

chemotactic gradient of PDGFA. Astrocytes (which could be regarded as the equivalent to the macrophage in our model), as a respond to PDGFA, express a variety of chemotactic and haptotactic proteins, including VEGFA and fibronectin, which subsequently induce EC sprouting. Finally, the formation of blood vessels and delivery of oxygen inhibits further astrocyte activity.

Taking into consideration the (negative) feedback between the astrocytes and the blood vessels (oxygen), in this section we present an alternative way of macrophage motility. That is, the macrophage can move only when it comes in contact with the sprout (either stalk or tip cell). In doing this, the macrophage gives the appropriate amount of time to the sprout to reach it (either by elongation due to chemotaxis or cell proliferation or both). Therefore, the two speeds (sprout and macrophage) become more synchronised and, as a result, we get a straight sprout without cell detachment (see Figure 5.19). However, the problem with cell detachment reappears when we incorporate two moving macrophages, probably because cell proliferation focuses now on two sprouts instead of one (see Figure 5.20(a)). By increasing (doubling) cell proliferation rate (a_1 in equation (5.4.2)), we found that this could alleviate somehow the problem (see Figure 5.20(b)), but not always, and also other problems might arise (e.g. splitting of the parent blood vessel).

In conclusion, we suggest that the 'macrophage movement in contact idea' might provide a balance to the speeds of the sprout and the macrophage, however, the problem with the cell detachment exists in both motility scenarios, and it remains an open question for future work.

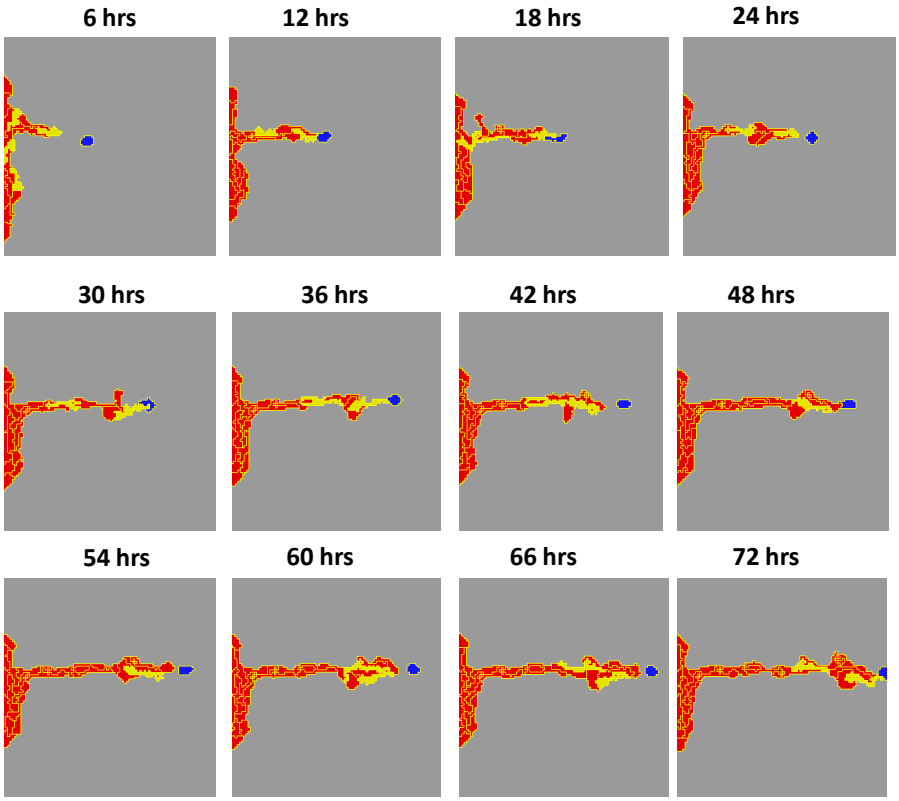

Figure 5.19: Representative snapshots showing sprout evolution at different time points (up to 3 days) with a moving macrophage (as in section 5.8.1.2) exhibiting a long sprout formation. Key: stalk cells (red), tip cells (yellow), macrophage (blue).

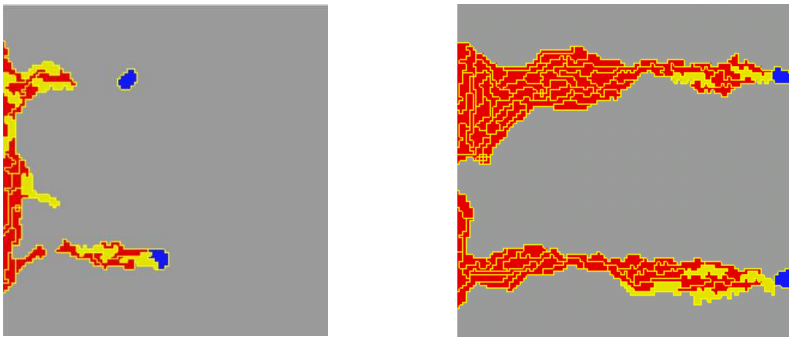

(a) (b)

Figure 5.20: Representative snapshots showing sprout evolution in (a) normal, and (b) increased stalk cell proliferation rate, by incorporating two moving macrophages as in section 5.8.1.2. The former case is more likely to result in sprout splitting.

5.8.2 Cis-inhibition: mutual inactivation of Notch and Delta

Notch signalling is often used for determining the cell fate between neighbouring cells. Delta in one cell can bind to and trans-activate Notch in a neighbouring cell. However, Delta may have a second role, inhibiting Notch activity in its own cell, a process called cis-inhibition [224] (see Figure 5.21).

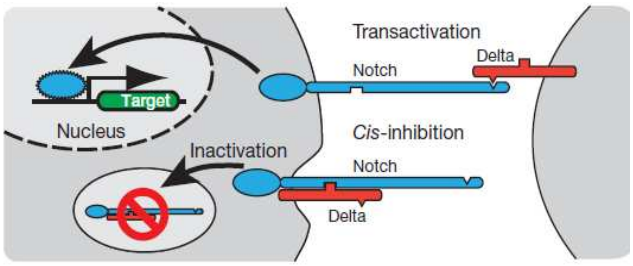

Figure 5.21: Schematic taken from [224] shows the double role of Delta in the Notch signalling pathway: transactivation (Delta from neighbouring cells) has a positive feedback on Notch, and cis-inhibition (Delta within the same cell) has a negative feedback on Notch.

Sprinzak *et al.* [235], by using a mathematical model showed that cis-inhibition could be explained if Notch and Delta in the same cell bind and mutually inactivate each other. In this case, the relative levels of Notch and Delta determine the cell's signalling state: if a cell has more Notch than Delta it becomes a 'receiver' (the cell can receive but not send). Conversely, if a cell has more Delta than Notch then it becomes a 'sender' cell (the cell can send but not receive). For strong cis-interactions the transition between these two states is extremely sharp which accounts for switch-like behaviours (e.g. sharp boundaries in wing disc in drosophila [97]).

Motivated by Sprinzak *et al.* [235], our aim is to investigate any different behaviours on sprout formation by incorporating cis-inhibition in our model (5.4.8). Therefore, we suggest the following model

$$\begin{aligned} Delta: \quad & \frac{dD_j}{dt} = v\left(\alpha \frac{VEGF}{VEGF_h + VEGF}\frac{1}{1+bN_j^2} - D_j\right), \\ Notch: \quad & \frac{dN_j}{dt} = \frac{\bar{D_j}^2}{a + \bar{D_j}^2 + \gamma D_j^2} - N_j, \\ trans-Delta: \quad & \bar{D_j} = \sum_i \frac{D_i P_{ij}}{P_j}. \end{aligned} \tag{5.8.2}$$

The difference from the model (5.4.8) is the incorporation of the cis-Delta term ($\gamma {D_j}^2$: Delta within the same cell and not from the neighbour cells) in a competitive way with

the trans-Delta (Delta received from neighbour cells), with γ being the strength of the cis-inhibition.

In the following we present mathematical analysis on perturbations of the homogeneous steady state (HSS) in model (5.8.2), and parameter ranges in which the 'salt and pepper' (checkerboard) pattern does or does not occur.

5.8.2.1 Analysis of perturbations of the homogeneous steady state in the cis-inhibition model

In this section we use the same model analysis approach as in section (5.4.3.1) by considering the non-dimensional model as given in equations (5.8.2), which can be rewritten in the following simplified form

$$\begin{aligned} \frac{dD_j}{dt} &= v\left(\alpha h(V) g(N_j) - D_j\right) \ , \\ \frac{dN_j}{dt} &= f(\bar{D}_j, D_j) - N_j \ , \end{aligned} \tag{5.8.3}$$

where $f(\bar{D}_j, D_j) = \dfrac{\bar{D_j}^2}{a + \bar{D_j}^2 + \gamma {D_j}^2}$, and $h(V)$, $g(N_j)$, and $\bar{D}_j$ as defined in the model (5.4.10). By linearising about the HSS and removing subscript j (for each cell j), the model in (5.8.3) changes to

$$\begin{aligned} \frac{d\tilde{D}}{dt} &= v\left(\alpha h(V) G \tilde{N} - \tilde{D}\right) \ , \\ \frac{d\tilde{N}}{dt} &= F_{\bar{D}}(\bar{D}, D)\tilde{D}\frac{K}{\sigma} + F_D(\bar{D}, D)\tilde{D} - \tilde{N} \ , \end{aligned} \tag{5.8.4}$$

where,

$$\begin{aligned} G &= g'(N^*), \\ F_D &= -\frac{2\gamma D \bar{D}^2}{(a + \bar{D}^2 + \gamma D^2)^2} = -\frac{2\gamma D^* (\frac{D^*}{\sigma})^2}{(a + (\frac{D^*}{\sigma})^2 + \gamma D^{*2})^2}, \\ F_{\bar{D}} &= \frac{2\bar{D}(a + \gamma D^2)}{(a + \bar{D}^2 + \gamma D^2)^2} = \frac{2(\frac{D^*}{\sigma})(a + \gamma D^{*2})}{(a + (\frac{D^*}{\sigma})^2 + \gamma D^{*2})^2}, \end{aligned}$$

with subscripts D, $\bar{D}$ denoting differentiation, K as defined in equation (5.4.13) and $\sigma = 1$, if squares/hexagons; $\sigma = 2$, if strings. The linearised system (5.8.4) gives the following Jacobian matrix

$$J(K) = \begin{pmatrix} -v & v\alpha h(V) G \\ F_{\bar{D}}\dfrac{K}{\sigma} + F_D & -1 \end{pmatrix}. \tag{5.8.5}$$

The $tr(J) = -v - 1$ remains the same as in model (5.4.10), whereas the determinant in (5.4.16) changes to

$$det(J(K)) = v\left(1 - \alpha h(V) F_{\bar{D}} G\left(\frac{K}{\sigma} - \Omega\right)\right), \tag{5.8.6}$$

where $\Omega = \dfrac{\gamma D^{*2}}{a + \gamma D^{*2}}$, and $F_D = -\dfrac{1}{\sigma}\Omega F_{\bar{D}}$. For instance, by considering the case for squares (where $K = -1; \sigma = 1$), we get

$$det(J(-1)) = v\left(1 + \alpha h(V) F_{\bar{D}} G(1 + \Omega)\right), \tag{5.8.7}$$

and, therefore, the HSS becomes unstable if

$$det(J(-1)) < 0 \Leftrightarrow \Phi = \alpha h(V) F_{\bar{D}} G(1 + \Omega) < -1. \tag{5.8.8}$$

Figure 5.22(a) shows that for small γ (e.g. $\gamma = 1$), $\Phi < -1$ for $\alpha > 0.07$. However, for large γ (e.g. $\gamma = 30$), $\Phi > -1$ always holds (for any value of α) and, therefore, we expect no 'salt and pepper' patterning. Simulation results in Figure 5.22(b) show that they are in agreement with the analytical results in Figure 5.22(a).

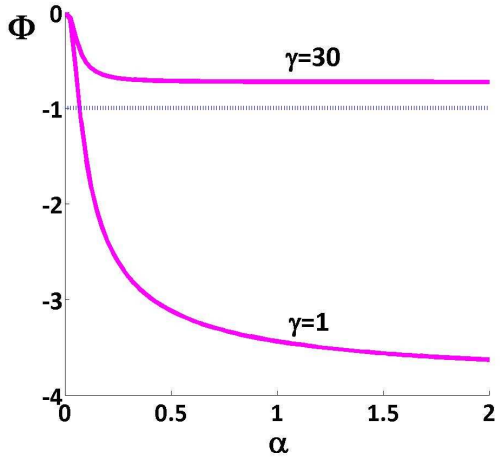

(a)

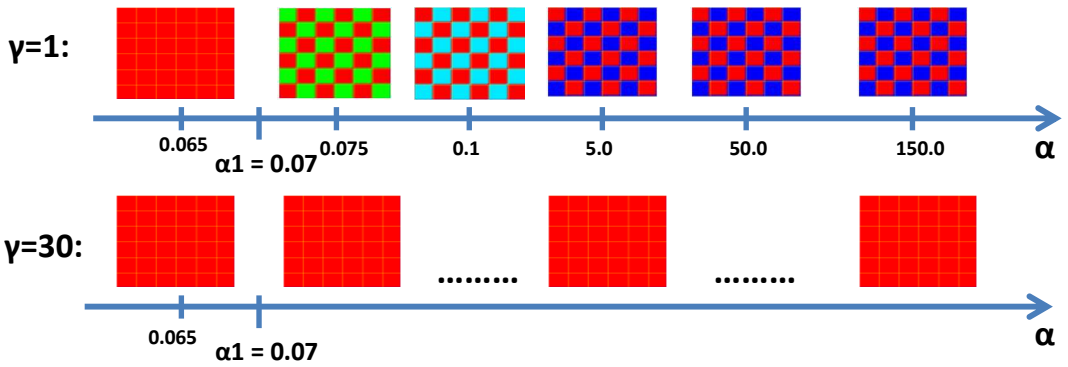

(b)

Figure 5.22: (a) $\Phi = \alpha h(V) F_{\bar{D}} G(1+\Omega)$ (as in equation (5.8.8)) over α (the maximum Delta production rate). It is shown that if the strength of cis-inhibition is low (e.g. $\gamma = 1$), $\Phi < -1$ for $\alpha > 0.07$, whereas in large γ (e.g. $\gamma = 30$), $\Phi > -1$ for any value of α. (b) Simulation results for squares for different values of α as in (a) for which we get patterning or not. The parameter values as in Figure 5.5. Colourbar: high (red) and low (blue) Delta levels at 1000 MCS.

5.8.2.2 Role of cis-inhibition on sprout formation

Figure 5.23 depicts representative snapshots of sprout evolution for different values of α (the maximum Delta production rate) and γ (the strength of cis-inhibition), prompted by results from Figure 5.22. That is, for small α we chose $\alpha = 0.05 < 0.07$ and for γ we chose $\gamma = 1$ and $\gamma = 30$. Results in Figure 5.23 show that: 1) α is small and, therefore,

there is no tip cell activation (all cells remain as stalk cells), 2) normal stalk/tip cell selection and sprouting, 3) tip cells can stay next to each other for longer before some of them convert into stalks, as a consequence of the increased α, 4) further increment of α allows tip cells to stay next to each other for even longer, which leads to sprout splitting (in approximately 5 hrs), and in 5) all cells try to become tip cells due to the strong cis-inhibition (large γ), which also causes the sprout to split.

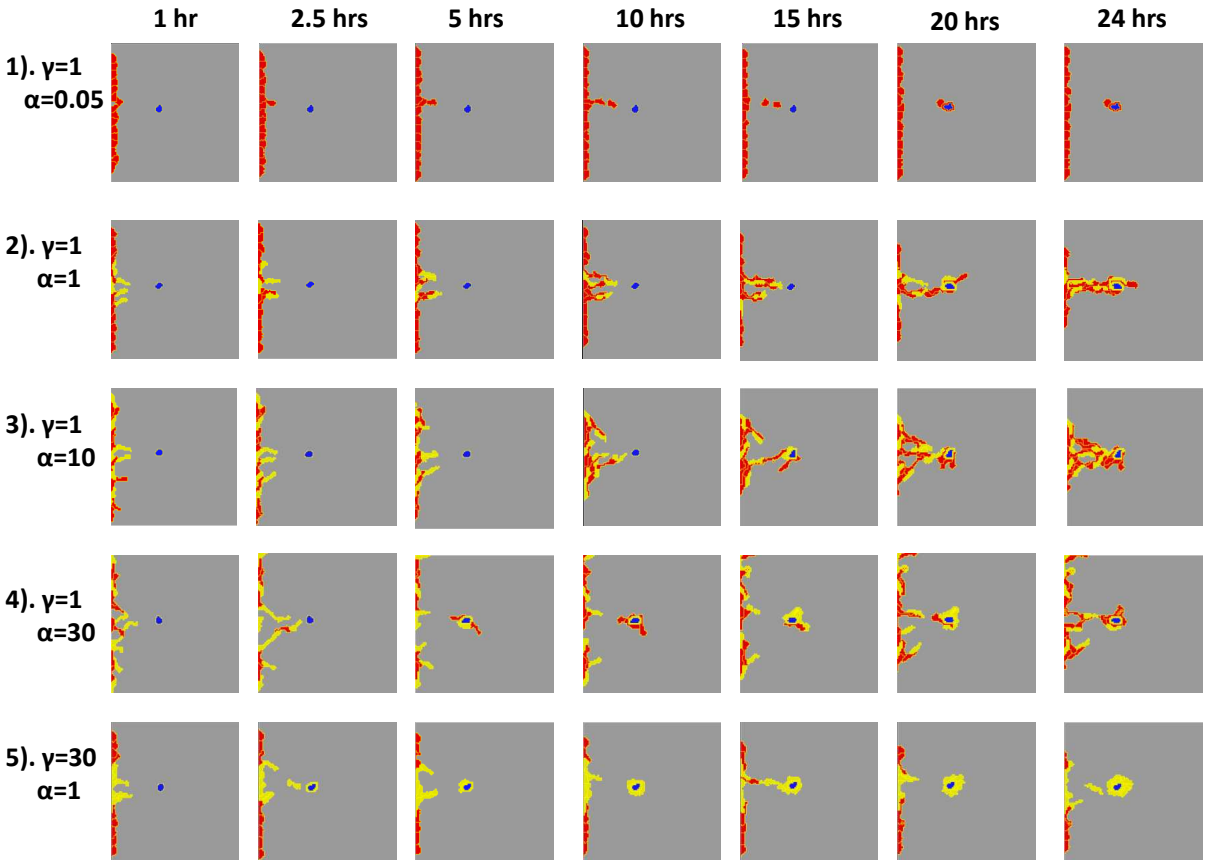

Figure 5.23: Representative snapshots showing sprout evolution at different time points by varying α (the maximum Delta production rate) and γ (the strength of cis-inhibition) in the cis-model (5.8.2) as described in section 5.8.2.2.

5.9 Discussion

In this chapter, we have developed a 2-D Cellular Potts Model (CPM) with the aim to understand the dynamic interaction between stalk and tip cells (two endothelial cell (EC) phenotypes) during sprout formation integrated via the VEGFA-Delta-Notch signalling pathway.

Sprouting angiogenesis, the initiation of microvessel growth, plays an essential role in development, reproduction (e.g. corpus luteum development; see Figure 3.1), repair, and is also a prominent feature in tumour formation as well as in a variety of diseases. It requires activation of normally quiescent ECs in pre-existing blood vessels, breakdown of existing basement membranes, migration of activated cells led by one or more endothelial tip cells and proliferation of a subset of activated ECs (stalk cells). The complex biological processes leading to sprout formation are a consequence of cell-level decisions that are based on global signals (e.g. VEGF signalling) and near-neighbour communication (e.g. Delta-Notch (D-N) signalling). Cell shape and cell-cell (homotypic and heterotypic) contacts are two significant variables in such processes (as was the case in Chapter 4) and, therefore, we chose the CPM framework for the model implementation.

In our model we assessed six different scenarios regarding homogeneous and heterogeneous VEGF and extracellular matrix (ECM) profiles on sprout morphology. In particular, two with homogeneous/uniform VEGF (no gradients), two with static VEGF gradients, and two with VEGF gradients emerged from a fixed macrophage. In each pair of scenarios we alternated between uniform and non-uniform ECM. For the non-uniform structure of the ECM, we used ECM fibers randomly distributed in the domain. In the last two scenarios, we started our simulations with a parent blood vessel located at the one side of the numerical domain and the macrophage (the VEGFA source) at some distance away from the vessel (for the model set up, see Figure 5.7). Initially, the vessel is quiescent, only composed of stalk cells, and it becomes activated once the first tip cell appears. Experimental studies have revealed a dynamic shuffling of tip and stalk cells at the leading front of growing sprouts challenging the idea of stable tip and stalk cell selection [75]. This dynamic behaviour was incorporated in our model (compared to other mathematical models using fixed cell positions) in the following way. A stalk cell may become a tip cell if its Delta level, which is upregulated from the macrophage-mediated VEGFA, exceeds a threshold value. In turn, a fine-tuned feedback loop between VEGFA and D-N signalling establishes a 'salt and pepper' distribution (checkerboard pattern) of stalk and tip cells within the activated endothelium. Cells constantly have to re-evaluate the VEGFA-Delta-Notch signalling

loop when they meet new neighbours, and the lateral-inhibition effect via the Notch signalling defines the (interchangeable) fate of the (stalk and tip) cells in the parent vessel and the new sprout. Stalk cells adjacent to tip cells may proliferate and elongate to support sprout elongation. The proliferation of stalk cells was based on the cell cycle time estimated from available retinal experimental data [Courtesy of Dr. Luisa-Iruela Arispe]. Tip cells are allowed to elongate, but not to proliferate [72]. The 'head' tip cell leads the sprout forward distinguishing it from other tip cells in the sprout having the maximum VEGFA level compared to any other cell. As the stalk and tip cells migrate through the ECM following up the chemotactic (moving up VEGFA gradients) and haptotactic cues (moving preferably along ECM fibers if in a scenario with non-uniform ECM), they define the morphology of the outgrowing sprout, with tip cells leading the sprout polarisation. Tip cells contact other tip cells (anastomosis) to add new vessel circuits to the existing network, a result which is also dynamically captured in our model.

Briefly, the no gradient scenarios (1 and 2) resulted in a mass of elongated but undirected cells, which evenly fill the space with a checkerboard-like pattern of stalk and tip cells (see Figure 5.10). However, the scenarios (3 and 4) with static gradients resulted in big swollen sprouts. Our aim was to reproduce the sprout formation as depicted in Figure 5.1. That was achieved with the last two scenarios (5 and 6) with the macrophage. In particular, there was narrower sprout formation in non-uniform ECM (scenario 6) compared to the uniform ECM (scenario 5). The latter case resulted in slightly swollen sprouts since cells have the same attachment preference to the ECM everywhere in the domain.

By considering the above results, we may conclude that narrow sprout formation (as in Figure 5.1) can be closely approximated under the scenario 6 with heterogeneous VEGF (with macrophage) and heterogeneous (non-uniform) ECM in $\sim$18 hrs. However, at later time points cells start surrounding the fixed macrophage without being able to produce a longer sprout formation (see Figure 5.10). To tackle this problem, we extended our model by incorporating macrophage motility (moving away from the blood vessel), so that the sprout can prolong further. Interesting questions which arise at this point concern the time that the macrophage should start moving, and its speed. To begin with, we simply allowed the macrophage to start moving from the beginning of a simulation. Regarding its speed, since it is difficult to achieve equality between the speeds of the sprout and the macrophage, we assessed various speeds of the macrophage. We found that low or medium macrophage speeds could result in sprout formation of a limited length because of sprout splitting. On the other hand,

high speed resulted in no sprouting because the macrophage moves too fast and VEGF gradients do not allow for tip cell activation. Therefore, all of the cells in the blood vessel remained as stalks. In order to alleviate the problems with the speed of the macrophage and the sprout splitting, we presented an alternative way of macrophage motility. That is, the macrophage can move only when it comes in contact with the sprout implying that there exists some form of feedback mechanism between the sprout and the macrophage. In that way, we achieved a better balance between the speeds of the sprout and the macrophage, resulting in a straight and long sprout along the whole numerical domain without splitting (see Figure 5.19). However, in an attempt to get multiple sprouts or network development we further extended the model by introducing two moving macrophages. In that case, the splitting problem was once again evident, since cell proliferation was not able to sustain two long sprouts. By increasing cell proliferation rate, we found that this could partially solve the problem, but not always. Therefore, the problem with sprout splitting remains as an open question for future work.

Sensitivity analysis was performed for key parameters, such as the VEGF decay rate (δ), the strength of chemotaxis (λ_{chem}), and the strength of the attachment to the ECM (λ_{ECM}). In particular, in basal decay rates there is directed sprouting and polarised proliferation. However, in small δ the sprout eventually splits, whereas in large δ there is no tip cell activation and, therefore, no sprout formation. Regarding λ_{chem}, if it is small, the sprout is not able to reach the macrophage, whereas in large λ_{chem} the sprout splits. It was also shown that the value of λ_{ECM} affects the speed of the sprout. As might be expected, if λ_{ECM} is large the speed of the sprout falls below the available experimental measurements since cells strongly adhere to the ECM.

Overall, our model has reproduced many experimentally observed aspects of sprout formation including tip cell selection and a realistic sprout formation. A nice feature of this model is its ability to form sprouts as a result of natural dynamics from the VEGFA-Delta-Notch signalling and tip cell competition without emerging from predefined probabilistic rules (e.g. [41, 191]). Various studies [157, 220] hypothesized that autocrine regulation of the chemoattractant VEGF (playing the role of ECM) is responsible for the formation of vascular networks *in vitro*. However, *in vivo* this might not be true. Therefore, we explicitly incorporated the role of ECM instead of using a short diffusive (and unrealistic) VEGF secreted from cells. In reality, active tip cells produce matrix metalloproteinases (MMPs) which allow them to invade the ECM. However, in this study MMP secretion and proteolysis were not considered.

In conclusion, although there are limitations in the current model, we believe that it in-

corporates several biological assumptions allowing them to emerge dynamically leading to realistic sprouting morphology and extension speed.

CHAPTER 6

Conclusions & Future work

The corpus luteum (CL) is a tissue which develops in the ovary, in the wound space created by follicular ovulation, and produces the progesterone needed for pregnancy. The CL consists of several vascular (e.g. endothelial cells (ECs), pericytes (PCs)), and avascular (e.g. luteal cells (LCs), immune cells) cell types. LCs are the main cell type responsible for the progesterone production. The rapid growth of the CL has been compared with the most malignant vascular tumours [197]. It requires angiogenesis, the creation of new blood vessels from pre-existing ones, a process which is regulated by several growth factors, e.g. fibroblast growth factor 2 (FGF2). Inadequate vascularisation is likely to result in poor CL function, which is linked to infertility in cows [146].

Motivated by the importance of angiogenesis on CL growth and its possible impact on fertility, our focus throughout has been placed upon the interplay among the different scale levels to tackle such a biological problem, e.g. tissue, cellular, subcellular, and exracellular level.

Firstly, in Chapter 2, we started with a coarse-grained level (the tissue) with the development of a time-dependent ordinary differential equation (ODE) model for the CL growth. The four model variables are the volumes of the ECs, LCs, and stromal cells (such as PCs), and the concentration of FGF2. We assumed that the CL volume is a continuum of the volumes of the three cell types. The ECs (which represent the vascular density in the CL) enhance the proliferation rate of the other two cell types, and the FGF2 (produced by ECs and LCs) enhances the EC proliferation rate. We postulated that if the CL volume exceeds a threshold value, then cell growth is inhibited. We defined the *discontinuity boundary* (Σ) to be the surface at which the volume threshold is attained. This threshold separates the model into different cases: above, below, or on Σ. Therefore, the model was analysed as a Filippov (piece-wise smooth) system. We

applied stability analysis and bifurcation theory for the standard (when the CL volume is above or below the threshold value), and *sliding* (when the CL volume is on the discontinuity) solutions. To investigate the importance of angiogenesis on CL growth we determined how the system dynamics change as ρ_5, the maximal EC proliferation rate, is varied. In a weak angiogenic environment (low ρ_5), the CL volume remains constant (sliding on the discontinuity boundary), and the system evolves to one of two solutions. If the growth rate of LCs exceeds that of the stromal cells, then the LCs grow at the expense of the stromal cells with the latter eventually not being able to survive. In that case, LCs produce high amounts of progesterone acquired for embryo development. However, low ρ_5, implies few blood vessel (ECs) development, which is probably not adequate for progesterone transportation to the uterus. Alternatively, if the stromal cells are more proliferative, they dominate the CL, and progesterone production ceases (since LCs vanish). In both cases, low progesterone compromises pregnancy. In a high angiogenic environment (high ρ_5), the system leaves the discontinuity boundary and evolves to a steady state for which the CL contains only blood vessels, which is biologically implausible. For intermediate values of ρ_5, a healthy growth of the CL (with all its cellular components being present) is maintained, which is necessary to sustain a healthy pregnancy.

Motivated by *in vitro* CL (morphological and quantitative) data provided in Chapter 3, an important question arises about the role of cell communication in cell aggregation and sprout formation. In particular, in Chapter 3 we summarised published results [11, 34, 201, 202], including novel ones from Robinson's Lab focusing on the endothelial and pericyte temporal growth and cluster formation. Interesting observations emerged from preliminary results. Notably, some EC clusters vanish during the multi-cell type (incorporating all the CL cell types) system, probably due to reduced survivability of ECs or some apoptotic cells within a cluster attract immune cells which in turn digest the whole cluster. Another notable observation is the cross-talk between individual PCs and endothelial clusters. Double localisation (cell staining) of ECs and PCs showed that PCs are possibly attracted by EC clusters, and also revealed that they may form an integral part of them (see Figure 3.7). Immunocytochemistry techniques, however, proved to be difficult at the early time points (e.g. 6hrs, 12 hrs) and image analysis and quantification of results was not possible. In addition, the experimental systems in Robinson's Lab use all the CL cell types in the same *in vitro* culture providing a closer approximation to the *in vivo* environment compared to other *in vitro* cultures which use only a single cell type (mainly ECs). However, this complicates matters in terms of distinguishing cell behaviours and factors which contribute to the overall cell dynamics. Therefore, in the next Chapter which deals with cell aggregation we used

data from literature, mainly from Orlidge and D'Amore [173].

In Chapter 4, we looked at the next finer scale (the cell level) in order to model the EC-PC interactions. While the ECs are the better characterised of the two, PCs are now coming into focus as important regulators of angiogenesis and blood vessel function. In an attempt to understand the main angiogenic processes, several experimental systems to date have been developed *in vitro* by incorporating homogeneous EC populations. Very few of them, however, have studied heterogeneous co-cultures with both cell types. Orlidge and D'Amore published some intriguing results in their study [173]. They found that the presence of PCs could totally inhibit the EC growth, by suggesting that this could be a result of the transforming growth factor-β (TGF-β), activated once the two cell types come into contact. Contact inhibition plays a significant role in developmental angiogenesis and tissue/tumour growth, and so our aim was to investigate the possible mechanisms which can lead to total inhibition of the EC growth. Contact between cells implies that contact area (therefore, cell shape) and cell-cell contact energies (forces) would be important variables. As a consequence, we decided to use a cellular potts model (CPM) within which these variables can be explicitly incorporated. The main assumptions in our model were adopted from [173]. In particular, ECs and growth arrested PCs were cultured in a 1:1 ratio, with no addition of any external growth factor in the culture. In [173], the low and sparse initial seeding cell density imply little to no contact between the cells. For that reason, in our model we used random (since cells are unbiased from any growth factor) cell motility in order to allow for cell-cell interaction, with both cell types being able to move randomly in the numerical domain. The motility of cells was governed by the speed (r), and the persistence time (t_{per}; time of movement without change of direction). EC division was also considered in our CPM and that was implemented via a phase cell cycle. Mechanical contact between cells and diffusive TGF-β secreted from both ECs and PCs at their contact area are two factors which contributed to delayed EC cell cycle. This implies that ECs in an aggregate (especially in the presence of PCs) have a more delayed cell cycle compared to individual ECs (which are not contact inhibited). The parameters used for motility and division were estimated as those giving the best fit to the experimental growth data in [173]. Data on cell motility are not provided in [173], so we began our simulations with single EC experiments in order to estimate r (by fixing t_{per} as in [131]) which resulted in a cell speed similar to that found in [131]. In doing this, we proceeded with pure EC populations in order to assess clustering in different motility scenarios (low, medium, and high speed). Results showed that in low speed, there was no clustering in contrast to medium speed where the number of clusters increased. In higher speed, clustering decreased and that was a result of the detachment of clustered

cells due to their high motility. Further *in silico* experiments showed that by increasing cell density the growth of the EC population becomes more linear compared to the step-like behaviour in lower density. This is a result of the increased contact between cells in higher cell density, which implies that few cells remain as individuals and, therefore, the whole cell population becomes less synchronised (cells divide at different time points). By varying cell density concurrently with cell motility, we found that there is increased EC proliferation in a lower density and higher motility environment. Furthermore, results from co-culture (EC-PC) *in silico* experiments showed that medium and high speed scenarios are more likely to result in total inhibition of the EC growth. Interestingly, in such cases, results suggest that the effective range of the diffusive TGF-β is a crucial determinant of the degree of EC growth inhibition. Motivated by studies in [173], we also investigated the effect of different initial seeding EC:PC ratios on the inhibition of the EC growth. Altered ratios have been observed in several diseases (e.g. multiple sclerosis [35], brain tumour [268], diabetic retinopathy [83]). Experimental results from [173], and our *in silico* results showed that a decreased PC to EC ratio is able to disrupt the total inhibition of the EC growth.

In Chapter 5, we developed a CPM to study the evolution of the sprout formation. Both vascular cell types (ECs and PCs) have a distinct role in this process, but we chose to focus on one cell type, the ECs, and particularly, on its two phenotypes: stalk and tip cells. We are mainly interested on how a sprout develops initiated from a parent blood vessel towards a pro-angiogenic growth factor (e.g. VEGFA). There are two signalling pathways which are regarded as the main controllers of this process: Delta-Notch (D-N), which is responsible for cell phenotype (e.g. stalk, tip) decisions, and VEGFA. In our model we explore six different scenarios regarding the VEGF and extracellular matrix (ECM) profiles, by considering either homogeneous (no gradients) or heterogeneous (with static gradients or gradients produced by a fixed macrophage) VEGFA, and uniform or non-uniform ECM environment.

The macrophage-mediated VEGFA generates gradients in the domain, and D-N signalling controls the tip cell activation. A stalk cell becomes a tip cell if its Delta levels (which are upregulated from the macrophage-mediated VEGFA) exceed a threshold value. After the tip cell activation, the D-N signalling regulates the stalk-tip distribution along the parent blood vessel and the new sprout, the so called 'salt and pepper' (checkerboard) pattern which prohibits tip cells being next to each other. Stalk cells adjacent to tip cells were allowed to grow and divide based on a cell cycle time estimated from available retina experimental data [Courtesy of Dr. Luisa-Iruela Arispe]. Those stalk cells and the tip cells were able to elongate. Non-uniform ECM was also

incorporated in our model and was represented by randomly distributed ECM fibers. ECM and chemotaxis (towards up VEGFA gradients) can greatly impact the sprout polarisation. It has been suggested that the macrophage acts as a 'bridge' cell which can bring two tip cells (from two different sprouts) together [56]. This is called sprout anastomosis (or fusion). Our model reproduces phenomena in sprouting angiogenesis, including sprout morphology and tip competition, and explains and predicts perturbation experiments on the D-N signalling pathway. Sprout formation was the interest of several *in silico* models to date, each one focussing on a particular topic. However, our model is the first that incorporates all of the aforementioned mechanisms (e.g. D-N and VEGF signalling, cell cycle model for stalk cell division, non-uniform ECM) together.

Briefly, considering macrophage-mediated VEGFA along with the non-uniform ECM resulted in a close approximation to the sprout formation as depicted in the schematic in Figure 5.1. However, although the fixed macrophage allowed for a narrow sprout, after a certain period of time cells started to surround the macrophage resulting in a mass of cells. In an attempt to produce a longer sprout we extended our model to allow for macrophage motility. By considering the difficulty to achieve a good match between sprout and macrophage speed, we started with the macrophage moving from the beginning of a simulation in various cell motilities. Low and medium speeds resulted in sprout formation of a limited length (sprout splitting before reaching the end of the domain). Interestingly, an alternative way of macrophage motility, that is, the macrophage moves only when it is in contact with the sprout, resulted in a long, and straight sprout without splitting. However, the splitting problem was again evident when we incorporated two moving macrophages in an attempt to produce multiple sprouts and, ultimately, network formation. We observed that increased cell proliferation could alleviate the problem, but not always. Therefore, the splitting problem along with the macrophage speed remain as the main focus of future work.

6.1 Future work

The models presented in this thesis consistently point to the importance of cell-cell interactions in angiogenic processes (e.g. cell aggregation, sprout formation) and CL/tissue growth. ECs and PCs are the main vascular cell types. Despite their great importance in regulating several angiogenic processes, PCs have not yet received the attention they deserve.

In Chapter 2, the results from the ODE model were based on parameter estimates which were chosen as reasonably as possible from independent data. However, future work

may involve a more systematic parameter sensitivity analysis to assess the robustness of the results (steady states that the system evolves to). PCs are perivascular cells that are typically associated with ECs in microvessels. Experiments performed by Redmer *et al.* in [195] suggest that PCs represent a large proportion of the proliferating cells during the early stage of the CL development. In the same study, PCs appeared to be among the first cells (along with ECs) to migrate into the hypoxic granulosa region after ovulation. It has been suggested that PCs are capable of guiding sprouting processes by migrating ahead of ECs and expressing VEGF, a potent mitogenic factor that can induce the ECs to proliferate subsequent to migration [195]. Therefore, it is possible to amend the model by incorporating more angiogenic factors (e.g. VEGF), and also more explicitly define the role of PCs in the CL growth and development along with ECs. In that case, a CL with no stromal cells/PCs ($R = 0$) could imply a poorly functioning vasculature *in vivo*. Given also that PCs provide stability to the vasculature, the model could further suggest that loss of PCs might be a strong candidate for poor embryo development since a leaky and not stable vasculature (without PCs) is not able to provide an embryo with the appropriate amounts of nutrients. Perivascular cells, play a critical role in angiogenesis and PC regulation may provide a novel mechanism for regulating CL growth and tissue growth in general. Finally, the ODE model could also be extended in a spatial model by using a cellular potts model (CPM) since cell-cell contacts and cell area (important variables in a tissue growth model) are explicitly incorporated in the CPM framework.

In Chapter 3, preliminary results from *in vitro* CL studies have shed light on possible cross-talk between ECs and PCs. Our aim is to pursue this direction by doing more experiments which can allow for further morphological and quantitative data. We are particularly interested in the number of ECs and PCs in order to evaluate the growth of the two cell types, the covered area of the two cell types in the culture domain, the ratio of ECs-PCs within clusters which could provide a measure of the PC recruitment towards EC clusters, and also the number of PCs being in close proximity with EC clusters.

In Chapter 4, the interaction of cells with the ECM is regarded as a crucial aspect of cell aggregation mechanisms. ECs are anchorage-dependent and their growth is contact-inhibited. In addition, ECs and PCs synthesise matrix components [36], which could markedly influence EC proliferation.
Several *in vitro* and *in vivo* studies [42, 99, 188] indicate that not only physical interactions (by contact), but also a variety of external factors may impact the growth of vascular ECs. These signals appear to be mediated by both soluble and ECM-bounded

compounds. The diffusive factors may emanate from the EC themselves or the PCs. A question is whether and how PCs might inhibit EC growth in a different way to that suggested by our model (regarding the role of TGF-β). Except from TGF-β, the secretion of TIMP3 and Ang1 from PCs might be another important signalling pathway to consider in the context of the stabilisation of EC growth. In addition, it is unclear whether long-range contact inhibition, possibly mediated by long cellular processes (via filopodia extensions; see Figure 4.13) is active and necessary to explain contact inhibition. Therefore, a possible extension of the model to incorporate the role of filopodia would be informative. Our model assumptions were mainly based on the experimental system of Orlidge and D'Amore [173], where PCs were growth arrested. It would be interesting to assess the role of PC proliferation on the inhibition of the EC growth.

In Chapter 5, PCs could also be incorporated in the sprouting model as the cells which can provide stabilisation and maturation to the new sprout. It has recently been suggested (personal communication with Dr. Luisa-Iruela Arispe) that both PCs and astrocytes (since they secrete VEGFA) enhance sprout polarisation and it would be an interesting direction to explore. Regarding mitosis, stalk cell division could be enhanced by VEGFA concentration as was the case in Qutub and Popel [191]. In addition, some of our model parameters were chosen despite a lack of evidence concerning their plausible values, and therefore, a quantitative validation of the model is difficult at some points. In order to make it more realistic, we could for instance use realistic values for Delta threshold for tip cell activation, and ECM density. If we would have more quantitative data from experimental observations we could use this information to further calibrate our model. Finally, in the case where the macrophage is allowed to move, the problem with sprout splitting and the choice of the macrophage speed remain as another direction for further investigation.

In conclusion, we believe that the EC-PC interactions along with the ECM environment will be the focus of future research in angiogenesis and tissue growth and this will be the direction of our future work.

We would like to close this Chapter by providing some simulation results (see Figure 6.1), where we were attempting to obtain sprouting and network formation starting from endothelial cell (stalk) clusters integrated in initially uniform VEGFA concentration which enhances the D-N signalling. This could be thought of as a unification of work described in Chapters 4 and 5. Stalk and tip cells take up VEGFA, which results in lower VEGFA at the centre of a cluster, and as we observe at early time points (e.g. 12-18 hrs) we can get a checkerboard-like pattern formation of a cluster with tip cells

integrated within the whole cluster. However, as time progresses, Delta at the centre of the cluster drops and, therefore, the tip cells are converted back into stalk cells. As a result, tip cells only form around the perimeter of the cluster, where the VEGFA is higher.

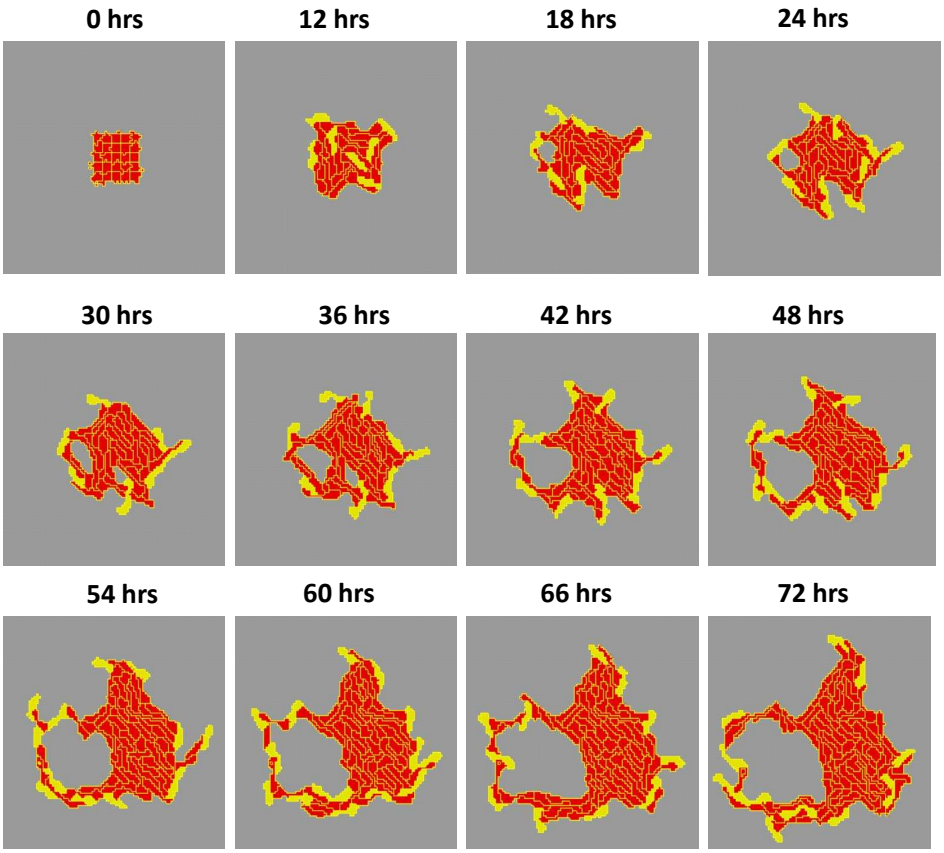

Figure 6.1: Representative snapshots at different time points (up to 3 days) in an attempt to get network formation from a cluster of cells in an initially uniform VEGFA field taken up by stalk and tip cells. Parameters: VEGFA= 1. Key: stalk cells (red), tip cells (yellow).

Glossary

During the literature search, I have tried to compose this list of commonly used biological vocabulary found in many of the research papers.

- **angiogenesis:** is the formation of new blood vessels from pre-existing ones.
- **chemotaxis:** is the characteristic movement or orientation of an organism or cell along a chemical concentration gradient either toward or away from the chemical stimulus.
- **corpus luteum:** is the tissue that emerges from an ovulated follicle during the oestrous cycle, and it is responsible for the progesterone production needed for pregnancy.
- **endothelium:** is the thin layer of cells that lines the interior surface of blood vessels
- **extracellular:** is the outside the plasma membrane. The functional barrier between the inside and outside of a cell.
- **extracellular matrix (ECM):** is the extracellular part of animal tissue that provides structural support to the animal cells and regulates the cell's dynamic behaviour.
- **growth factor (GF):** is an extracellular signaling molecule. There are two types of GFs related to angiogenesis. The pro-angiogenic, which stimulate a cell to grow or proliferate (e.g. vascular endothelial growth factor (VEGF), fibroblast growth factor (FGF), Ang1), and the anti-angiogenic, which fight angiogenesis (e.g. angiostatin, endostating, MMPs, Ang2).
- **haptokinesis:** is the sensitivity of cells to absolute concentrations of ECM components.
- **haptotaxis:** is the directional migration of cells up ECM gradients.

- **in vitro:** the recreation of biological processes in an artificial laboratory environment.
- **in vivo:** biological processes that take place within a living organism or cell.
- **macrophages:** (Greek: big eaters) are cells produced by the differentiation of monocytes in tissues. Their role is to phagocytose and then digest, cellular debris and pathogens. An additional role, with a great impact on angiogenesis is the secretion of GFs (e.g. VEGFA), which can enhance the angiogenic network development via the endothelial proliferation and migration.
- **matrix metalloproteinase (MMPs):** proteolytic enzymes that degrade extracellular matrix. They are inhibited by tissue inhibitors of matrix metalloproteinases (TIMPs).
- **Notch signalling:** is an important signalling pathway for cell-cell communication, regulation of cell-fate decision (e.g. interchange between the two endothelial cell phenotypes, stalk and tip cells), and many other processes such as neural function and development, cardiovascular development etc.
- **pericytes:** are cells that surround the endothelium. They have several roles in angiogenesis (e.g. provide stability to the angiogenic network), and particularly on the endothelial cells (e.g. inhibit their growth).
- **stalk cells:** are specialised endothelial cells present in the stalk (lumen) region of vascular sprouts (behind the tip cell), which strongly proliferate to allow for sprout extension.
- **tip cells:** are specialised endothelial cells. They are lumenless cells characterised by long filipodia extension. These cells are present at the leading edge of vascular sprouts that integrate directional cues from their environment. This defines the direction in which the new sprouts grow. Commonly, tip cells do not proliferate.

References

[1] E. Adashi. The potential relevance of cytokines to ovarian physiology. *J. Steroid Biochem. and Molec. Biol.*, 43:439–444, 1992.

[2] M. Aikawa and P. Libby. The vulnerable atherosclerotic plaque: pathogenesis and therapeutic approach. *Cardiov. Pathol.*, 13:125–138, 2004.

[3] N. Akhtar, E.B. Dickerson, and R. Auerbach. The sponge/matrigel angiogenesis assay. *Angiogenesis*, 5:75–80, 2002.

[4] L. Alberi, S. Liu, Y. Wang, R. Badie, C. Smith-Hicks, J. Wu, T.J. Pierfelice, B. Abazyan, M.P. Mattson, D. Kuhl, M. Pletnikov, P.F. Worley, and N. Gaiano. Activity-induced notch signaling in neurons requires arc/arg3.1 and is essential for synaptic plasticity in hippocampal networks. *Neuron*, 69:437–444, 2011.

[5] W.L. Amselgruber, M. Schafer, and F. Sinowatz. Angiogenesis in the bovine corpus luteum: an immunocytochemical and ultrastructural study. *Anat. Histol. Embryol.*, 28:157–166, 1999.

[6] A.R. Anderson and M.A.J. Chaplain. Continuous and discrete mathematical models of tumor induced angiogenesis. *Bull. Math. Biol.*, 60(5):857–899, 1998.

[7] B. Appel, L.A. Givan, and J.S. Eisen. Delta-notch signaling and lateral inhibition in zebrafish spinal cord development. *BMC Dev. Biol.*, 1:13, 2001.

[8] A. Armulik, C. Betsholtz, and A. Abramsson. Endothelial/Pericyte interactions. *Circ. Res.*, 97:512–523, 2005.

[9] R. Auerbach, R. Lewis, B. Shinners, L. Kubai, and N. Akhtar. Angiogenesis assays: a critical overview. *Clin. Chem.*, 49:32–40, 2003.

[10] D.H. Ausprunk and J. Folkman. Migration and proliferation of endothelial cells in preformed and newly formed blood vessels during tumor angiogenesis. *Microvasc. Res.*, 14:53–65, 1977.

[11] P. Bagavandoss and J. Wilks. Isolation and characterization of microvascular endothelial cells from developing corpus luteum. *Biol. Reprod.*, 44:1132–1139, 1991.

[12] D. Balding and D.L.S. McElwain. Mathematical modelling of tumour-induced capillary growth. *J. Theor. Biol.*, 114:53–73, 1985.

[13] A.J. Bardin, R. Le Borgne, and F. Schweisguth. Asymmetric localization and function of cell-fate determinants: a fly's view. *Curr. Opin. Neurobiol.*, 14:6–14, 2004.

[14] A.L. Bauer, Y. Jiang, and T.L. Jackson. A cell-based model exhibiting branching and anastomosis during tumor-induced angiogenesis. *Bioph. J.*, 92:3105–3121, 2007.

[15] A. Beenken and M. Mohammadi. The FGF family: biology, pathophysiology and therapy. *Nature Rev.*, 8:235–253, 2009.

[16] K. Bentley, H. Gerhardt, and P.A. Bates. Agent-based simulation of notch-mediated tip cell selection in angiogenic sprout initialisation. *J. Theor. Biol.*, 250:25–36, 2008.

[17] K. Bentley, G. Mariggi, H. Gerhardt, and P.A. Bates. Tipping the balance: robustness of tip cell selection, migration and fusion in angiogenesis. *PLoS Comput. Biol.*, 5:e1000549, 2009.

[18] G. Bergers and S. Song. The role of pericytes in blood-vessel formation and maintenance. *Neuro-Oncology*, 7:452–464, 2005.

[19] B. Berisha, D. Schams, M. Kosmann, W. Amselgruber, and R. Einspanier. Expression and tissue concentration of VEGF, its receptors and localization in the bovine corpus luteum during estrous cycle and pregnancy. *Biol. Reprod.*, 63:1106–1114, 2000.

[20] M. Bernardo, C. Budd, A.R. Champneys, and P. Kowalczyk. Piecewise-smooth dynamical systems: theory and applications. *Springer*, 2008.

[21] M. Bernardo, A. Nordmark, and G. Olivar. Discontinuity-induced bifurcations of equilibria in piecewise-smooth and impacting dynamical systems. *Physica D*, 237:119–136, 2008.

[22] D.A. Beysens, G. Forgacs, and J.A. Glazier. Cell sorting is analogous to phase ordering in fluids. *PNAS*, 97:9467–9471, 2000.

[23] S. Bray. Notch signalling: a simple pathway becomes complex. *Nat. Rev. Mol. Cell Biol.*, 7:678–689, 2011.

[24] H.M. Byrne and M.A.J. Chaplain. Mathematical models for tumour angiogenesis: numerical simulations and nonlinear wave solutions. *Bull. Math. Biol.*, 57(3):461–486, 1995.

[25] Y. Cao, A. Hong, H. Schulten, and M.J. Post. Update on therapeutic neovascularization. *Cardiov. Res.*, 65:639–648, 2005.

[26] P. Carmeliet. Mechanisms of angiogenesis and arteriogenesis. *Nat. Med.*, 6:389–395, 2000.

[27] P. Carmeliet. Angiogenesis in life, disease and medicine. *Nature*, 438:932–936, 2005.

[28] P. Carmeliet and R.K. Jain. Angiogenesis in cancer and other diseases. *Nature*, 407:249–257, 2000.

[29] M.A.J. Chaplain. The mathematical modelling of tumour angiogenesis and invasion. *ActaBiotheor*, 43:387–402, 1995.

[30] M.A.J. Chaplain. Mathematical modeling of angiogenesis. *J. Neurooncol.*, 50:37–51, 2000.

[31] M.A.J. Chaplain and M.E. Orme. A mathematical model of vascular tumour growth and invasion. *Math. Comp. Modelling*, 23(10):43–60, 1996.

[32] M.A.J. Chaplain and A.M. Stuart. A model mechanism for the chemotactic response of endothelial cells to tumour angiogenesis factor. *IMA J. Math. Appl. Med. Biol.*, 10:149–168, 1993.

[33] Y.C. Cheng, M. Amoyel, X. Qiu, Y.J. Jiang, Q. Xu, and D.G. Wilkinson. Notch activation regulates the segregation and differentiation of rhombomere boundary cells in the zebrafish hindbrain. *Dev. Cell*, 6:539–550, 2004.

[34] L. Christenson and R. Stouffer. Isolation and culture of microvascular endothelial cells from the primate corpus luteum. *Biol. Reprod.*, 55:1397–1404, 1996.

[35] L. Claudio and C.F. Brosnan. Effects of prazosin on the blood-brain barrier during experimental autoimmune encephalomyelitis. *Brain Res.*, 594:233–243, 1992.

[36] M.P. Cohen, R.N. Frank, and A.A. Khalifa. Collagen production by cultured retinal capillary pericytes. *Invest. Ophthalmol. Vis. Sci.*, 19:90–94, 1980.

[37] J.R. Collier, N.A. Monk, P.K. Maini, and J.H. Lewis. Pattern formation by lateral inhibition with feedback: a mathematical model of delta-notch intercellular signalling. *J. Theor. Biol.*, 183:429–446, 1996.

[38] A. Colombo. A bifurcation analysis of discontinuous systems: theory and applications. *PhD thesis, Politecnico di Milano, Italy*, 2009.

[39] P.A. D'Amore. Mechanisms of endothelial growth control. *Am. J. Respir. Cell Mol. Biol.*, 6:1–8, 1992.

[40] P.A. D'Amore and S.R. Smith. Growth factor effects on cells of the vascular wall: a survey. *Growth Factors*, 8:61–75, 1993.

[41] A. Das, D. Lauffenburger, H. Asada, and R.D. Kamm. A hybrid continuum-discrete modelling approach to predict and control angiogenesis: analysis of combinatorial growth factor and matrix effects on vessel-sprouting morphology. *Philos. Trans. A*, 368:2937–2960, 2010.

[42] G.E. Davis and D.R. Senger. Endothelial extracellular matrix: biosynthesis, remodeling, and functions during vascular morphogenesis and neovessel stabilization. *Circ. Res.*, 97:1093–1097, 2005.

[43] J. de Celis and A. Garcia-Bellido. Roles of the notch gene in drosophila wing morphogenesis. *Mech. Dev.*, 46:109–122, 1994.

[44] F. De Smet, I. Segura, K. De Bock, P.J. Hohensinner, and P. Carmeliet. Mechanisms of vessel branching: filopodia on endothelial tip cells lead the way. *Arteriosc. Thromb. Vasc. Biol.*, 29:639–649, 2009.

[45] E. Dejana. Endothelial cell-cell junctions: happy together. *Nature*, 5:261–270, 2004.

[46] R. del Toro, C. Prahst, T. Mathivet, G. Siegfried, J.S. Kaminker, B. Larrivee, C. Breant, A. Duarte, N. Takakura, A. Fukamizu, J. Penninger, and A. Eichmann. Identification and functional analysis of endothelial tip cell-enriched genes. *Blood*, 116:4025–4033, 2010.

[47] C.J. Dente, C.P. Steffes, C. Speyer, and J.G. Tyburski. Pericytes augment the capillary barrier in in vitro cocultures. *J. Surg. Res.*, 97:85–91, 2001.

[48] M.L. Dequeant and O. Pourquie. Segmental patterning of the vertebrate embryonic axis. *Nat. Rev. Genet.*, 9:370–382, 2008.

[49] P.A. DiMilla, J.A. Stone, J.A. Quinn, S.M. Albelda, and D.A. Lauffenburger. Maximal migration of human smooth muscle cells on fibronectin and type IV collagen occurs at an intermediate attachment strength. *J. Cell Biol.*, 122:729–737, 1993.

[50] P. Dore-Duffy. Isolation and characterization of cerebral microvascular pericytes. *Methods Mol. Med.*, 89:375–382, 2003.

[51] S. Dormann and A. Deutsch. Modelling of self-organised avascular tumour growth with a hybrid cellular automaton. *In Silico Biology*, 2:393–406, 2002.

[52] M.I. Dorrell, E. Aguilar, and M. Friedlander. Retinal vascular development is mediated by endothelial filopodia, a preexisting astrocytic template and specific R-cadherin adhesion. *Invest. Ophthalmol. Vis. Sci.*, 43:3500–3510, 2002.

[53] J.K. Dow and R.W. deVere White. Fibroblast growth factor 2: its structure and property, paracrine function, tumor angiogenesis, and prostate-related mitogenic and oncogenic functions. *Urology*, 55:800–806, 2000.

[54] D. Drasdo and M. Loeffler. Individual-based models to growth and folding in one-layered tissues: intestinal crypts and early development. *Nonlinear Anal.*, 47:245–256, 2001.

[55] A.J. Duleba, R.Z. Spaczynski, A. Arici, R. Carbone, and H.R. Behrman. Proliferation and differentiation of rat theca-interstitial cells: comparison of effects induced by platelet-derived growth factor and insulin-like growth factor-1. *Biol. Reprod.*, 60:546–550, 1999.

[56] A. Fantin, J.M. Vieira, G. Gestri, L. Denti, Q. Schwarz, S. Prykhozhij, F. Peri, S.W. Wilson, and C. Ruhrberg. Tissue macrophages act as cellular chaperones for vascular anastomosis downstream of VEGF-mediated endothelial tip cell induction. *Blood*, 116:829–840, 2010.

[57] N. Ferrara and W.J. Henzel. Pituitary follicular cells secrete a novel heparin-binding growth factor specific for vascular endothelial cells. *Biochem. Biophys. Res. Commun.*, 161:851–858, 1989.

[58] A.F. Filippov. Differential equations with discontinuous righthand sides. *Kluwer Academic Publishers, Dordrecht, The Netherlands*, 1988.

[59] J. Folkman. Tumour angiogenesis: therapeutic implications. *New Engl. J. Medic.*, 285:1182–1186, 1971.

[60] J. Folkman. Tumor angiogenesis: a possible control point in tumor growth. *Ann. Intern. Med.*, 82:96–100, 1975.

[61] J. Folkman and P.A. D'Amore. Blood vessel formation: what is its molecular basis? *Cell*, 87:1153–1155, 1996.

[62] J. Folkman and M. Klagsbrun. Angiogenic factors. *Science*, 235:113–130, 1987.

[63] J.V. Forrester, A. Chapman, C. Kerr, J. Roberts, W.R. Lee, and J.M. Lackie. Bovine retinal explants cultured in collagen gels. a model system for the study of proliferative retinopathy. *Arch. Ophthalmol.*, 108:415–420, 1990.

[64] R.N. Frank, T.J. Turczyn, and A. Das. Pericyte coverage of retinal and cerebral capillaries. *Invest. Ophthalmol. Vis. Sci.*, 31:999–1007, 1990.

[65] H.M. Fraser and S.F. Lunn. Regulation and manipulation of angiogenesis in the primate corpus luteum. *Reproduction*, 121:355–362, 2001.

[66] H.M. Fraser and C. Wulff. Angiogenesis in the corpus luteum. *Reprod. Biol. Endocr.*, 1:88, 2003.

[67] N.W. Gale, M.G. Dominguez, I. Noguera, L. Pan, V. Hughes, D.M. Valenzuela, A.J. Murphy, N.C. Adams, H.C. Lin, J. Holash, G. Thurston, and G.D. Yancopoulos. Haploinsufficiency of delta-like 4 ligand results in embryonic lethality due to major defects in arterial and vascular development. *PNAS*, 101:15949–15954, 2004.

[68] J. Galle, M. Loeffler, and D. Drasdo. Modeling the effect of deregulated proliferation and apoptosis on the growth dynamics of epithelial cell populations in vitro. *Bioph. J.*, 88:62–75, 2005.

[69] R.F. Gariano and T.W. Gardner. Retinal angiogenesis in development and disease. *Nature*, 438:960–966, 2005.

[70] H. Gerhard and C. Betsholtz. Endothelial-pericyte interactions in angiogenesis. *Cell Tissue Res.*, 314:15–23, 2003.

[71] H. Gerhardt. VEGF and endothelial guidance in angiogenic sprouting. *Organogenesis*, 4:241–246, 2008.

[72] H. Gerhardt, M. Golding, M. Fruttiger, C. Ruhrberg, A. Lundkvist, A. Abramsson, M. Jeltsch, C. Mitchell, K. Alitalo, D. Shima, and C. Betsholtz. VEGF guides angiogenic sprouting utilizing endothelial tip cell filopodia. *J. Cell Biol.*, 161:1163–1177, 2003.

[73] H. Gerhardt, C. Ruhrberg, A. Abramsson, H. Fujisawa, D. Shima, and C. Betsholtz. Neuropilin-1 is required for endothelial tip cell guidance in the developing central nervous system. *Dev. Dyn.*, 231:503–509, 2004.

[74] P. Gerlee and A. Anderson. A hybrid cellular automaton model of clonal evolution in cancer: The emergence of the glycolytic phenotype. *J. Theor. Biol.*, 250:705–722, 2008.

[75] I. Geudens and H. Gerhardt. Coordinating cell behaviour during blood vessel formation. *Development*, 138:4569–4583, 2011.

[76] M.A. Gimbrone, R.S. Cotran, and J. Folkman. Endothelial regeneration: studies with human endothelial cells in culture. *Ser. Haematol.*, 4:453–455, 1973.

[77] E. Girsh, Y. Greber, and R. Meidan. Luteotrophic and luteolytic interactions between bovine small and large luteal-like cells and endothelial cells. *Biol. Reprod.*, 52:954–962, 1995.

[78] JA. Glazier and F. Graner. Simulation of the differential adhesion driven rearrangement of biological cells. *Phys. Rev. E*, 47(3):2128–2154, 1993.

[79] R. Goodyear and G. Richardson. Pattern formation in the basilar papilla: evidence for cell rearrangement. *J. Neurosci.*, 17:6289–6301, 1997.

[80] BM. Gumbiner. Cell adhesion: the molecular basis of tissue architecture and morphogenesis. *Cell*, 84:345–357, 1996.

[81] M. Gyllenberg and G.F. Webb. Quiescence as an explanation of gompertzian tumour growth. *Growth Dev. Aging*, 53:25–33, 1989.

[82] P. Hahnfeldt, D. Panigraphy, J. Folkman, and L. Hlatky. Tumor development under angiogenic signaling: a dynamical theory of tumor growth, treatment response and postvascular dormancy. *Cancer Res.*, 59:4770–4775, 1999.

[83] H.P. Hammes, J. Lin, O. Renner, M. Shani, A. Lundqvist, C. Betsholtz, M. Brownlee, and U. Deutsch. Pericytes and the pathogenesis of diabetic retinopathy. *Diabetes*, 51:3107–3112, 2002.

[84] P. Heitzler and P. Simpson. The choice of cell fate in the epidermis of drosophila. *Cell*, 64:1083–1092, 1991.

[85] M. Hellstrom, M. Kalen, P. Lindhal, A. Abramsson, and C. Betsholtz. Role of PDGF-B and PDGFR-beta in recruitment of vascular smooth muscle cells and

pericytes during embryonic blood vessel formation in the mouse. *Development*, 126:3047–3055, 1999.

[86] M. Hellstrom, L.K. Phng, J.J. Hofmann, E. Wallgard, L. Coultas, P. Lindblom, J. Alva, A.K. Nilsson, L. Karlsson, N. Gaiano, K. Yoon, J. Rossant, M.L. Iruela-Arispe, M. Kalen, H. Gerhardt, and C. Betsholtz. Dll4 signalling through Notch1 regulates formation of tip cells during angiogenesis. *Nature*, 445:776–780, 2007.

[87] P. Helmbold, R.C. Nayak, W.C. Marsch, and I.M. Herman. Isolation and in vitro characterization of human dermal microvascular pericytes. *Microvasc. Res.*, 61:160–165, 2001.

[88] K.K Hirschi and P.A. D'Amore. Pericytes in the microvasculature. *Cardiov. Res.*, 32(4):687–698, 1996.

[89] K.K. Hirschi and P.A. DAmore. Control of angiogenesis by the pericyte: molecular mechanisms and significance. *EXS*, 79:419–428, 1997.

[90] S. Hoehme and D. Drasdo. A cell-based simulation software for multi-cellular systems. *Bioinformatics*, 26:2641–2642, 2010.

[91] J.J. Hofmann and M.L. Iruela-Arispe. Notch signaling in blood vessels: who is talking to whom about what? *Circ. Res.*, 100:1556–1568, 2007.

[92] M. Holcombe, S. Coakley, and R. Smallwood. A general framework for agent-based modelling of complex systems. *Proceedings of the 2006 European Conference on Complex Systems*, 2006.

[93] TE. Holy, M. Dogterom, B. Yurke, and S. Leibler. Assembly and positioning of microtubule asters in microfabricated chambers. *PNAS*, 94:6228–6231, 1997.

[94] H. Honda, M. Tanemura, and T. Nagai. A three-dimensional vertex dynamics cell model of space-filling polyhedra simulating cell behavior in a cell aggregate. *J. Theor. Biol.*, 226:439–453, 2004.

[95] H. Hunigen, P. Bisplinghoff, J. Plendl, and M. Bahramsoltani. Vascular dynamics in relation to immunolocalisation of VEGF-A, VEGFR-2 and Ang-2 in the bovine corpus luteum. *Acta Histoch.*, 110:462–472, 2008.

[96] R.H.F. Hunter. Physiology of the graafian follicle and ovulation. *Cambridge University press*, 2003.

[97] Muskavitch M Huppert S, Jacobsen T. Feedback regulation is central to deltanotch signalling required for drosophila wing vein morphogenesis. *Development*, 124:3283–3291, 1997.

[98] M.L. Iruela-Arispe and G.E. Davis. Cellular and molecular mechanisms of vascular lumen formation. *Dev. Cell*, 16:222–231, 2009.

[99] M.L. Iruela-Arispe, C.A. Diglio, and E.H. Sage. Modulation of extracellular matrix proteins by endothelial cells undergoing angiogenesis in vitro. *Arterioscler. Thromb.*, 11:805–815, 1991.

[100] T. Iso, L. Kedes, and Y. Hamamori. HES and HERP families: multiple effectors of the Notch signaling pathway. *J. Cell Physiol.*, 194:237–255, 2003.

[101] S. Isogai, N.D. Lawson, S. Torrealday, M. Horiguchi, and B.M. Weinstein. Angiogenic network formation in the developing vertebrate trunk. *Development*, 130:5281–5290, 2003.

[102] E.A. Jaffe, R.L. Nachman, C.G. Becker, and C. Richard Minick. Culture of human endothelial cells derived from umbilical veins. *J. Clin. Inv.*, 11:2745–2756, 1973.

[103] L. Jakobsson, C.A. Franco, K. Bentley, R.T. Collins, B. Ponsioen, I.M. Aspalter, I. Rosewell, M. Busse, G. Thurston, A. Medvinsky, S. Schulte-Merker, and H. Gerhardt. Endothelial cells dynamically compete for the tip cell position during angiogenic sprouting. *Nat. Cell Biol.*, 12:943–953, 2010.

[104] I. Ji, R. Slaughter, J. Ellis, T. Ji, and W. Murdoch. Analyses of ovine corpora lutea for tumor necrosis factor mRNA and bioactivity during prostaglandin-induced luteolysis. *Molec. Cell. Endocrin.*, 81:77–80, 1991.

[105] Y. Jiang, H. Levine, and J.A. Glazier. Possible cooperation of differential adhesion and chemotaxis in mound formation of dictyostelium. *Bioph. J.*, 75:2615–2625, 1998.

[106] Y. Jiang, J. Pjesivac-Grbovic, C. Cantrell, and J.P. Freyer. A multiscale model for avascular tumor growth. *Bioph. J.*, 89:3884–3894, 2005.

[107] N. Jo, C. Mailhos, and M. et al. Ju. Inhibition of platelet-derived growth factor B signaling enhances the efficacy of anti-vascular endothelial growth factor therapy in multiple models of ocular neovascularization. *Am. J. Pathol.*, 168(6):2036–2053, 2006.

[108] J.L. Juengel and G.D. Niswender. Molecular regulation of luteal progesterone synthesis in domestic ruminants. *J. Reprod. Fert. Suppl.*, 54:193–205, 1999.

[109] S. Kaessmeyer and J. Plendl. Angiogenesis and vasculogenesis in the corpus luteum in vitro. *Clin. Hemorh. Microc.*, 41:83–101, 2009.

[110] M. Kamouchi, T. Ago, and T. Kitazono. Brain pericytes: emerging concepts and functional roles in brain homeostasis. *Cell Mol. Neurobiol.*, 2010.

[111] A.F. Karamysheva. Mechanisms of angiogenesis. *Biochemistry*, 73:751–762, 2008.

[112] K. Kawasaki, T. Nagai, and K. Nakashima. Vertex models for two-dimensional grain growth. *Phil. Mag.*, B60:399–421, 1989.

[113] J.B. Kearney, N.C. Kappas, C. Ellerstrom, F.W. DiPaola, and V.L. Bautch. The VEGF receptor flt-1 (VEGFR-1) is a positive modulator of vascular sprout formation and branching morphogenesis. *Blood*, 103:4527–4535, 2004.

[114] B.M. Kenyon, E.E. Voest, C.C. Chen, E. Flynn, J. Folkman, and R.J. D'Amato. A model of angiogenesis in the mouse cornea. *Invest. Ophthalmol. Vis. Sci.*, 37:1625–1632, 1996.

[115] Jin-Hong Kim, K. Kushiro, N. Graham, and A. Asthagiri. Tunable interplay between epidermal growth factor and cell-cell contact governs the spatial dynamics of epithelial growth. *PNAS*, 106:11149–11153, 2009.

[116] M.A. Klagsbrun and P.A. D'Amore. Regulators of angiogenesis. *Ann. Rev. Phys.*, 53:217–239, 1991.

[117] A.E. Koch. Angiogenesis as a target in rheumatoid arthritis. *Ann. of Rheum. Dis.*, 62 Suppl 2:60–67, 2003.

[118] T. Kondo, K. Hosoya, S. Hori, M. Tomi, S. Ohtsuki, H. Takanaga, E. Nakashima, H. Iizasa, T. Asashima, M. Ueda, M. Obinata, and T. Terasaki. Establishment of conditionally immortalized rat retinal pericyte cell lines (TR-rPCT) and their application in a co-culture system using retinal capillary endothelial cell line (TR-iBRB2). *Cell Struct. Funct.*, 28:145–153, 2003.

[119] T. Kondo, K. Hosoya, S. Hori, S. Tomi, M. Ohtsuki, and T. Terasaki. PKC/MAPK signaling suppression by retinal pericyte conditioned medium prevents retinal endothelial cell proliferation. *J. Cell. Phys.*, 203:378–386, 2005.

[120] F. Kozusko and Z. Bajzer. Combining gompertzian growth and cell population dynamics. *Math. Biosci.*, 185:153–167, 2003.

[121] L.T. Krebs, J.R. Shutter, K. Tanigaki, T. Honjo, K.L. Stark, and T. Gridley. Haploinsufficient lethality and formation of arteriovenous malformations in Notch pathway mutants. *Genes Dev.*, 18:2469–2473, 2004.

[122] M.E. Kutcher and I.M. Herman. The pericyte: cellular regulator of microvascular blood flow. *Microv. Res.*, 77:235–246, 2009.

[123] V.A. Kuznetsov, I.A. Makalkin, M.A. Taylor, and A.S. Perelson. Nonlinear dynamics of immunogenic tumors: parameter estimation and global bifurcation analysis. *Bull. Math. Biol.*, 56:295–321, 1994.

[124] Y.A. Kuznetsov, S. Rinaldi, and A. Gragnani. One-parameter bifurcations in planar Filippov systems. *Intern. J. Bif. Chaos*, 13:2157–2188, 2003.

[125] A.K. Laird. Dynamics of tumour growth. *Br. J. Cancer*, 18:490–502, 1964.

[126] A.K. Laird. Dynamics of tumour growth: comparison of growth rates and extrapolation of growth curve to one cell. *Br. J. Cancer*, 19:278–291, 1964.

[127] M. Laird. Angiogenesis during luteal development in the cow. *PhD thesis, University of Nottingham, UK*, 2010.

[128] L. Lamalice, F. Le Boeuf, and J. Huot. Endothelial cell migration during angiogenesis. *Circ. Res.*, 100:782–794, 2007.

[129] L.A. Lardon, B.V. Merkey, S. Martins, A. Doetsch, C. Picioreanu, J.U. Kreft, and B.F. Smets. iDynoMiCS: next-generation individual-based modelling of biofilms. *Environmental Microbiology*, 13:2416–2434, 2011.

[130] Y. Lee, S. Kouvroukoglou, L.V. McIntire, and K. Zygourakis. A cellular automaton model for the proliferation of migrating contact-inhibited cells. *Bioph. J.*, 69:1284–1298, 1995.

[131] Y. Lee, L.V. McIntire, and K. Zygourakis. Analysis of endothelial cell locomotion: differential effects of motility and contact inhibition. *Biotech. Bioeng.*, 43:622–634, 1994.

[132] J.D. Leslie, L. Ariza-McNaughton, A.L. Bermange, R. McAdow, S.L. Johnson, and J. Lewis. Endothelial signalling by the Notch ligand Delta-like 4 restricts angiogenesis. *Development*, 134:839–844, 2007.

[133] H.A. Levine, S. Pamuk, B.D. Sleeman, and M. Nilsen-Hamilton. A mathematical model of capillary formation and development in tumour angiogenesis: penetration into the stroma. *Bull. Math. Biol.*, 63:801–863, 2001.

[134] S. Li, J.L. Guan, and S. Chien. Biochemistry and biomechanics of cell motility. *Ann. Rev. Biomed. Eng.*, 7:105–150, 2005.

[135] L. Liang, S.F. Norrelykke, and E.C. Cox. Persistent cell motion in the absence of external signals: a search strategy for eukaryotic cells. *PLoS ONE*, 3(5):e2093, 2008.

[136] T. Lieber, S. Kidd, and G. Struhl. DSL-notch signaling in the drosophila brain in response to olfactory stimulation. *Neuron*, 69:468–481, 2004.

[137] D.W. Lincoln, R.G. Whitney, and J.R. Smith. In vitro proliferation and lifespan of bovine aorta endothelial cells: response to conditioned media. *J. Cell Sci.*, 56:281–292, 1982.

[138] P. Lindahl, B.R. Johansson, P. Leveen, and C. Betsholtz. Pericyte loss and microaneurysm formation in PDGF-B-deficient mice. *Science*, 277:242–245, 1997.

[139] Z.J. Liu, T. Shirakawa, Y. Li, A. Soma, M. Oka, G.P. Dotto, R.M. Fairman, O.C. Velazquez, and M. Herlyn. Regulation of Notch1 and Dll4 by vascular endothelial growth factor in arterial endothelial cells: implications for modulating arteriogenesis and angiogenesis. *Molec. and Cell. Biol.*, 23:14–25, 2003.

[140] B. Lobel and E. Levy. Formation, development and involution of corpora lutea. *Acta Endocr.*, 132:35–51, 1968.

[141] I.B. Lobov, S. Rao, T.J. Carroll, J.E. Vallance, M. Ito, J.K. Ondr, S. Kurup, D.A. Glass, M.S. Patel, W. Shu, E.E. Morrisey, A.P. McMahon, G. Karsenty, and R.A. Lang. WNT7b mediates macrophage-induced programmed cell death in patterning of the vasculature. *Nature*, 15:417–421, 2005.

[142] I.B. Lobov, R.A. Renard, N. Papadopoulos, N.W. Gale, G. Thurston, G.D. Yancopoulos, and S.J. Wiegand. Delta-like ligand 4 (Dll4) is induced by VEGF as a negative regulator of angiogenic sprouting. *PNAS*, 104:3219–3224, 2007.

[143] C.L. Maier, B.R. Shepherd, T. Yi, and J.S. Pober. Explant outgrowth, propagation and characterization of human pericytes. *Microcirc.*, 17:367–380, 2010.

[144] D.G. Mallet and L.G. De Pillis. A cellular automata model of tumor-immune system interactions. *J. Theor. Biol.*, 239:334–350, 2006.

[145] G.E. Mann. Corpus luteum size and plasma progesterone concentration in cows. *Anim. Reprod. Sci.*, 115:296–299, 2009.

[146] G.E. Mann, G.E. Lamming, R.S. Robinson, and D.C. Wathes. The regulation of interferon-tau production and uterine hormone receptors during early pregnancy. *J. Reprod. Fertil. Suppl.*, 54:317–328, 1999.

[147] D. Manoussaki. A mechanochemical model of angiogenesis and vasculogenesis. *ESAIM-Math. Model. and Num. Anal.*, 37:581–599, 2000.

[148] D. Manoussaki, S.L. Lubkin, R.B. Vernon, and J.D. Murray. A mechanical model for the formation of vascular networks *in vitro*. *ActaBiotheor*, 44:271–282, 1996.

[149] N.V. Mantzaris, S. Webb, and H.G. Othmer. Mathematical modeling of tumor-induced angiogenesis. *J. Math. Biol.*, 49(2):111–187, 2004.

[150] A. Martin, M.R. Komada, and D.C. Sane. Abnormal angiogenesis in diabetes mellitus. *Medic. Res. Rev.*, 23:117–145, 2003.

[151] J.V. May, A.J. Bridge, E.D. Gotcher, and B.K. Gangrade. The regulation of porcine theca cell proliferation in vitro: synergistic actions of epidermal growth factor and platelet-derived growth factor. *Endocrinology*, 131:689–697, 1992.

[152] M. Mazzone, D. Dettori, R. Leite de Oliveira, S. Loges, T. Schmidt, B. Jonckx, Y.M. Tian, A.A. Lanahan, P. Pollard, C. Ruiz de Almodovar, F. De Smet, S. Vinckier, J. Aragons, K. Debackere, A. Luttun, S. Wyns, B Jordan, A. Pisacane, B. Gallez, M.G. Lampugnani, E. Dejana, M. Simons, P. Ratcliffe, P. Maxwell, and P. Carmeliet. Heterozygous deficiency of PHD2 restores tumor oxygenation and inhibits metastasis via endothelial normalization. *Cell*, 136:839–851, 2009.

[153] S.R. McDougall, M.G. Watson, A.H. Devlin, C.A. Mitchell, and M.A.J. Chaplain. A hybrid discrete-continuum mathematical model of pattern prediction in the developing retinal vasculature. *Bull. Math. Biol.*, (in press), 2012.

[154] H.M. McGettrick, K. Hunter, P.A. Moss, C.D. Buckley, G.E. Rainger, and G.B. Nash. Direct observations of the kinetics of migrating T cells suggest active retention by endothelial cells with continual bidirectional migration. *J. Leukoc. Biol.*, 85(1):98–107, 2009.

[155] R.M.H. Merks, S. Brodsky, M. Goligorksy, S. Newman, and J.A Glazier. Cell elongation is key to in silico replication of in vitro vasculogenesis and subsequent remodeling. *Devel. Biol.*, 289:44–54, 2006.

[156] R.M.H. Merks, M. Guravage, D. Inze, and G.T.S. Beemster. VirtualLeaf: an open-source framework for cell-based modeling of plant tissue growth and development. *Plant Physiology*, 155(2):656–666, 2011.

[157] R.M.H. Merks, E.D. Perryn, A. Shirinifard, and J.A. Glazier. Contact-inhibited chemotaxis in de novo and sprouting blood-vessel growth. *PLoS Comput. Biol.*, 4:e1000163, 2008.

[158] F. Milde, M. Bergdorf, and P. Koumoutsakos. A hybrid model of three-dimensional simulations of sprouting angiogenesis. *Bioph. J.*, 95:3146–3160, 2008.

[159] T. Minakawa, J. Bready, J. Berliner, M. Fisher, and P.A. Cancilla. In vitro interaction of astrocytes and pericytes with capillary-like structures of brain microvessel endothelium. *Lab. Invest.*, 65:32–40, 1991.

[160] C.A. Mitchell, C.S. Rutland, M. Walker, M. Nasir, A.J. Foss, C. Stewart, H. Gerhardt, M.A. Konerding, W. Risau, and H.C. Drexler. Unique vascular phenotypes following over-expression of individual VEGFA isoforms from the developing lens. *Angiogenesis*, 9(4):209–224, 2006.

[161] J.C.M. Mombach and J.A. Glazier. Single cell motion in aggregates of embryonic cells. *Phys. Rev.*, 76:3032–3035, 1996.

[162] J.D. Murray. On the mechanochemical theory of biological pattern formation with applications to vasculogenesis. *C.R.Biologies*, 326:239–252, 2003.

[163] J.D. Murray, G.F. Oster, and A.K. Harris. A mechanical model for mesenchymal morphogenesis. *J. Math. Biol.*, 17(1):125–129, 1983.

[164] L. Muthukrishnan, E. Warder, and P.L. McNeil. Basic fibroblast growth factor is efficiently released from a cytosolic storage site through plasma membrane disruptions of endothelial cells. *J. Cell Physiol.*, 148:1–16, 1991.

[165] T. Nagai, S. Ohta, K. Kawasaki, and T. Okuzono. Computer simulation of cellular pattern growth in two and three dimensions. *Phase Transitions*, 28:177–211, 1990.

[166] T.J. Newman. Modeling multi-cellular systems using sub-cellular elements. *Math. Biosci. Eng.*, 2:611–622, 2005.

[167] L.T. Nicklin. Functional development of the bovine corpus luteum. *PhD Thesis, University of Nottingham, UK*, January 2005.

[168] G. Niswender, T. Reimers, M. Diekman, and T. Nett. Blood flow: a mediator of ovarian function. *Biol. Reprod.*, 14:64–81, 1976.

[169] I. Noguera-Troise, C. Daly, N.J. Papadopoulos, S. Coetzee, P. Boland, N.W. Gale, H.C. Lin, G.D. Yancopoulos, and G. Thurston. Blockade of Dll4 inhibits tumour growth by promoting non-productive angiogenesis. *Nature*, 444:1032–1037, 2006.

[170] M.J. O'Dowd and E.E. Philipp. The history of obstetrics and gynaecology. *The Parthenon publishing group*, 1994.

[171] L. Olsen, J.A. Sherratt, P.K. Maini, and F. Arnold. A mathematical model for the capillary endothelial cell-extracellular matrix interactions in wound healing angiogenesis. *IMA J. Math. Appl. Med. Biol.*, 14:261–281, 1997.

[172] B. Olszewska-Pazdrak, T.W. Hein, P. Olszewska, and D.H. Carney. Chronic hypoxia attenuates VEGF signaling and angiogenic responses by downregulation of KDR in human endothelial cells. *Am. J. Physiol. Cell Physiol.*, 296:1162–1170, 2009.

[173] A. Orlidge and P.A. D'Amore. Inhibition of capillary endothelial cell growth by pericytes and smooth muscle cells. *J. Cell Biol.*, 105:1455–1462, 1987.

[174] M.E. Orme and M.A.J. Chaplain. A mathematical model of the first steps of tumour-related angiogenesis: capillary sprout formation and secondary branching. *IMA J. Math. Appl. Med. Biol.*, 13:73–98, 1996.

[175] M.E. Orme and M.A.J. Chaplain. Two-dimensional models of tumour angiogenesis and anti-angiogenesis strategies. *IMA J. Math. Appl. Med. Biol.*, 14:189–205, 1997.

[176] J.D. O'Shea, R.J. Rodgers, and M.J. D'Occhio. Cellular composition of the cyclic corpus luteum of the cow. *J. Reprod. Fert.*, 85:483–487, 1989.

[177] G.F. Oster, J.D. Murray, and A.K. Harris. Mechanical aspects of mesenchymal morphogenesis. *J. Embryol. Exp. Morph.*, 78:83–125, 1983.

[178] H.G. Othmer and A. Stevens. Aggregation, blowup and collapse: The ABC's of taxis in reinforced random walks. *SIAM J. Applied Math.*, 57:1044–1081, 1997.

[179] M.R. Owen and J.A. Sherratt. Modelling the macrophage invasion of tumours: effects on growth and composition. *IMA J. Mathem. Appl. Med. Biol.*, 15:165–185, 1998.

[180] M.R. Owen, J. Stamper, M. Muthana, G.W. Richardson, J. Dobson, C.E. Lewis, and H.M. Byrne. Mathematical modeling predicts synergistic antitumor effects of combining a macrophage-based, hypoxia-targeted gene therapy with chemotherapy. *Cancer Res.*, 71:2826–2837, 2011.

[181] L. Paavola. The corpus luteum of the guinea pig IV. Fine structure of macrophages during pregnancy and postpartum luteolysis and the phagocytosis of luteal cells. *Am. J. Anat.*, 154:337–364, 1979.

[182] N. Paweletz and M. Knierim. Tumor-related angiogenesis. *Crit. Rev. Oncol. Hematol.*, 9:197–242, 1989.

[183] M.S. Pepper, S.J. Mandriota, M. Jeltsch, V. Kumar, and K. Alitalo. VEGF-C synergizes with bFGF and VEGF in the induction of angiogenesis in vitro and alters endothelial cell extracellular proteolytic activity. *J. Cell Physiol.*, 177:439–452, 1998.

[184] L.K. Phng, M. Potente, J.D. Leslie, J. Babbage, D. Nyqvist, I. Lobov, J.K. Ondr, S. Rao, R.A. Lang, G. Thurston, and H. Gerhardt. Nrarp coordinates endothelial Notch and Wnt signaling to control vessel density in angiogenesis. *Dev. Cell*, 16:70–82, 2009.

[185] P.T. Piiroinen and Y.A. Kuznetsov. An event-driven method to simulate filippov systems with accurate computing of sliding motions. *ACM Trans. Math. Softw.*, 34, Article 13, 2008.

[186] J. Pitt-Francis, P. Pathmanathan, M.O. Bernabeu, R. Bordas, J. Cooper, A.G. Fletcher, G.R. Mirams, P. Murray, J.M. Osbourne, A. Walter, S.J. Chapman, A. Garny, I.M.M. van Leeuwen, P.K. Maini, B. Rodriguez, S.L. Waters, J.P. Whiteley, H.M. Byrne, and D.J. Gavaghan. Chaste: a test-driven approach to software development for biological modelling. *Comput. Phys. Comm.*, 180(12):2452–2471, 2009.

[187] M.J. Plank. Cell-based models of tumour angiogenesis. *PhD Thesis, University of Leeds, UK*, 2003.

[188] Z. Poltorak, T. Cohen, R. Sivan, Y. Kandelis, G. Spira, I. Vlodavsky, E. Keshet, and G. Neufeld. VEGF145, a secreted vascular endothelial growth factor isoform that binds to extracellular matrix. *J. Biol. Chem.*, 272:7151–7158, 1997.

[189] P.J. Polverini. Angiogenesis in health and disease: Insights into basic mechanisms and therapeutic opportunities. *J. Dent. Educ.*, 66(8):962–975, 2002.

[190] M. Presta, J.A.M. Maier, M. Rusnati, and G. Ragnotti. Basic fibroblast growth factor: production, mitogenic response, and post-receptor signal transduction in cultured normal and transformed fetal bovine aortic endothelial cells. *J. Cell. Physiol.*, 141:517–526, 1989.

[191] A.A. Qutub and A.S. Popel. Elongation, proliferation and migration differentiate endothelial cell phenotypes and determine capillary sprouting. *BMC Syst. Biol.*, 26:3–13, 2009.

[192] M. Ramsauer, R. Dermietzel, D.C. Spray, and M. Nedergaard. Pericytes and their contribution to the blood-brain barrier, in blood-brain barriers: from ontogeny to artificial interfaces. *Wiley-VCH Verlag GmbH and Co. KGaA, Weinheim, Germany*, 1, 2007.

[193] M. Ramsauer, D. Krause, and R. Dermietzel. Angiogenesis of the blood-brain barrier in vitro and the function of cerebral pericytes. *FASEB J.*, 2002.

[194] A. Raza, M.J. Franklin, and A.Z. Dudek. Pericytes and vessel maturation during tumor angiogenesis and metastasis. *Am. J. Hematol.*, 85:593–598, 2010.

[195] D.A. Redmer, V. Doraiswamy, B.J. Bortnem, K. Fisher, A. Joblonka-Shariff, A.T. Grazul-Bilska, and L.P. Reynolds. Evidence for a role of capillary pericytes in vascular growth of the developing ovine corpus luteum. *Biol. Reprod.*, 65:879–889, 2001.

[196] L.P. Reynolds, S.D. Killilea, A.T. Bilska, and D.A. Redmer. Mitogenic factors of corpora lutea. *Progress in Growth Factor Res.*, 5:159–175, 1994.

[197] L.P. Reynolds and D.A. Redmer. Angiogenesis in the ovary. *Reprod. Fert.*, 1:182–192, 1996.

[198] L.P. Reynolds and D.A. Redmer. Expression of the angiogenic factors, bFGF and VEGF, in the ovary. *Anim. Sci.*, 76:1671–1681, 1998.

[199] L.P. Reynolds and D.A. Redmer. Growth and development of the corpus luteum. *Reprod. Fert.*, 54:181–191, 1999.

[200] J. Ridgway, G. Zhang, Y. Wu, S. Stawicki, W.C. Liang, Y. Chanthery, J. Kowalski, R.J. Watts, C. Callahan, I. Kasman, M. Singh, M. Chien, C. Tan, J.A. Hongo, F. de Sauvage, G. Plowman, and M. Yan. Inhibition of Dll4 signalling inhibits tumour growth by deregulating angiogenesis. *Nature*, 444:1083–1087, 2006.

[201] R.S. Robinson, A.J. Hammond, M.G. Hunter, and G.E. Mann. A novel physiological culture system that mimics luteal angiogenesis. *Reprod. Fert.*, 135(3):405–413, 2008.

[202] R.S. Robinson, A.J. Hammond, M.G. Hunter, G.E. Mann, K.J. Woad, and M. Laird. Angiogenesis and vascular function in the ovary. *Reprod. Fert.*, 138:869–881, 2009.

[203] R.S. Robinson, L. Nicklin, A. Hammond, D. Schams, M. Hunter, and G.E. Mann. Fibroblast growth factor 2 is more dynamic than vascular endothelial growth

factor A during the follicle-luteal transition in the cow. *Biol. Reprod.*, 77:28–36, 2007.

[204] R.S. Robinson, L.T. Nicklin, A.J. Hammond, D. Schams, M.G. Hunter, , and G.E. Mann. Fibroblast growth factor 2 is more dynamic than vascular endothelial growth factor a during the follicle-luteal transition in the cow. *Biol. Reprod.*, 77:28–36, 2007.

[205] F. Roegiers and Y.N. Jan. Asymmetric cell division. *Curr. Opin. Cell Biol.*, 16:195–205, 2004.

[206] S.F. Rymo, H. Gerhardt, S. Wolfhagen, F., R. Lang, A. Uv, and C. Betsholtz. A two-way communication between microglial cells and angiogenic sprouts regulates angiogenesis in aortic ring cultures. *PLoS ONE*, 6:e15846, 2011.

[207] R.C. Sainson, J. Aoto, M.N. Nakatsu, M. Holderfield, E. Conn, E. Koller, and C.C. Hughes. Cell-autonomous notch signaling regulates endothelial cell branching and proliferation during vascular tubulogenesis. *FASEB J.*, 19:1027–1029, 2005.

[208] Y. Sato, R. Hamanaka, J. Ono, M. Kuwano, D.B. Rifkin, and R. Takaki. The stimulatory effect of PDGF on vascular smooth muscle cell migration is mediated by the induction of endogenous basic fgf. *Biochem. Bioph. Res. Commun.*, 174:1260–1266, 1991.

[209] Y. Sato and D.B. Rifkin. Inhibition of endothelial cell movement by pericytes and smooth muscle cells: Activation of a latent transforming growth factor-beta 1-like molecule by plasmin during co-culture. *J. Cell Biol.*, 109:309–315, 1989.

[210] N.J. Savill and P. Hogeweg. Modelling morphogenesis: From single cells to crawling slugs. *J. Theor. Biol.*, 184:229–235, 1997.

[211] J.C. Schaff, B.M. Slepchenko, and L.M. Loew. Physiological modeling with the virtual cell framework. *Methods Enzymol.*, 321:1–23, 2000.

[212] G. Schaller and M. Meyer-Hermann. Multicellular tumor spheroid in an off-lattice Voronoi-Delaunay cell model. *Phys. Rev.*, 71:051910, 2005.

[213] D. Schams and B. Berisha. Angiogenic factors (VEGF, FGF and IGF) in the bovine corpus luteum. *Reprod. and Devel.*, 48:233–242, 2002.

[214] D. Schams and B. Berisha. Regulation of corpus luteum function in cattle-an overview. *Reprod. Dom. Anim.*, 39:241–251, 2004.

[215] D. Schams, B. Berisha, M. Steffl, and W. Amselgruber. Changes in FGF2 and its receptors in bovine follicles before and after GnRH application and after ovulation. *Reproduction*, 131:319–329, 2006.

[216] T. Schmidt and P. Carmeliet. Blood-vessel formation: bridges that guide and unite. *Nature*, 465:697–699, 2010.

[217] R. Schuster and H. Schuster. Reconstruction models for the ehrlich ascites tumor of the mouse. *Math. Popul. Dyn.*, 2:335–348, 1995.

[218] L. Schweigerer, G. Neufeld, J. Friedman, J.A. Abraham, J.C. Fiddes, and D. Gospodarowicz. Capillary endothelial cells express basic fibroblast growth factor, a mitogen that promotes their own growth. *Nature*, 325:257–259, 1987.

[219] D.R. Senger, C.A. Perruzzi, M. Streit, V.E. Koteliansky, A.R. de Fougerolles, and M. Detmar. The alpha(1)beta(1) and alpha(2)beta(1) integrins provide critical support for vascular endothelial growth factor signaling, endothelial cell migration, and tumor angiogenesis. *Am. J. Pathol.*, 160:195–204, 2002.

[220] G. Serini, D. Ambrosi, E. Giraudo, A. Gamba, L. Preziosi, and F. Bussolino. Modeling the early stages of vascular network assembly. *EMBO J.*, 22(8):1771–1779, 2003.

[221] L. Seugnet, P. Simpson, and M. Haenlin. Transcriptional regulation of notch and delta: requirement for neuroblast segregation in drosophila. *Development*, 124:2015–2025, 1997.

[222] G. Seydoux and I. Greenwald. Cell autonomy of lin-12 function in a cell fate decision in c. elegans. *Cell*, 57:1237–1245, 1989.

[223] D. Shaw and J. Britt. Concentrations of tumor necrosis factor α and progesterone within the bovine corpus luteum sampled by continuous-flow microdialysis during luteolysis *in vivo*. *Biol. Reprod.*, 53:847–854, 1995.

[224] O. Shaya and D. Sprinzak. From Notch signaling to fine-grained patterning: modeling meets experiments. *Curr. Opin. Genet. Dev.*, 21:1–8, 2011.

[225] Y. Shi and T. Duke. Cooperative model of bacteria sensing. *Phys. Rev. E*, 58:6399–6406, 1998.

[226] K. Shirasuna, A. Nitta, J. Sineenard, T. Shimizu, H. Bollwein, and A. Miyamoto. Vascular and immune regulation of corpus luteum development, maintenance, and regression in the cow. *Domest. Anim. Endocrinol.*, 43(2):198–211, 2012.

[227] A. Shirinifard, JS. Gens, BL. Zaitlen, NJ. Poplawski, M. Swat, and J. Glazier. 3D Multi-cell simulation of tumor growth and angiogenesis. *PLoS ONE*, 4:e7190, 2009.

[228] A. Sica, P. Larghi, A. Mancino, L. Rubino, C. Porta, M.G. Totaro, M. Rimoldi, S.K. Biswas, P. Allavena, and A. Mantovani. Macrophage polarization in tumour progression. *Semin. Cancer. Biol.*, 18:349–355, 2008.

[229] A.F. Siekmann and N.D. Lawson. Notch signalling limits angiogenic cell behaviour in developing zebrafish arteries. *Nature*, 445:781–784, 2007.

[230] D.E. Sims. Recent advances in pericyte biology - implications for health and disease. *Can. J. Cardiol.*, 7:431–443, 1991.

[231] L.S. Sleer and CC. Taylor. Cell-type localization of platelet-derived growth factors and receptors in the postnatal rat ovary and follicle. *Biol. Reprod.*, 76:379–390, 2007.

[232] J.T. Smith, J.T. Elkin, and W.M. Reichert. Directed cell migration on fibronectin gradients: effect of gradient slope. *Exp. Cell Res.*, 312:2424–2432, 2006.

[233] M.F. Smith, E.W. McIntush, and G.W. Smith. Mechanisms associated with corpus luteum development. *J. Anim. Sci.*, 72:1857–1872, 1994.

[234] P. Speiser, A.M. Gittelsohn, and A. Patz. Studies on diabetic retinopathy. 3.influence of diabetes on intramural pericytes. *Arch. Ophthalmol.*, 80:332–337, 1968.

[235] D. Sprinzak, A. Lakhanpal, L. Lebon, L.A. Santat, M.E. Fontes, G.A. Anderson, J. Garcia-Ojalvo, and M.B. Elowitz. Cis-interactions between notch and delta generate mutually exclusive signalling states. *Nature*, 465:86–95, 2010.

[236] M.S. Steinberg. On the mechanism of tissue reconstruction by dissociated cells: I. population kinetics, differential adhesiveness, and the absence of directed migration. *PNAS*, 48:1577–1582, 1962.

[237] M.S. Steinberg. Reconstruction of tissues by dissociated cells. some morphogenetic tissue movements and the sorting out of embryonic cells may have a common explanation. *Science*, 141:401–408, 1963.

[238] D. Stekel, J. Rashbass, and E.D. Williams. A computer graphic simulation of squamous epithelium. *J. Theor. Biol.*, 175:283–293, 1995.

[239] C.L. Stokes and D.A. Lauffenburger. Analysis of the roles of microvessel endothelial cell random motility and chemotaxis in angiogenesis. *J. Theor. Biol.*, 152:377–403, 1991.

[240] S. Suchting, C. Freitas, F. le Noble, R. Benedito, C. Breant, A. Duarte, and A. Eichmann. The Notch ligand Delta-like 4 negatively regulates endothelial tip cell formation and vessel branching. *PNAS*, 104:3225–3230, 2007.

[241] A. Szabo, E. Mehes, E. Kosa, and A. Czirok. Multicellular sprouting in vitro. *Bioph. J.*, 95:2702–2710, 2008.

[242] A. Szabo, R. Unnep, E. Mehes, W.O. Twal, W.S. Argraves, Y. Cao, and A. Czirok. Collective cell motion in endothelial monolayers. *Phys. Biol.*, 7:046007, 2010.

[243] A. Szabo, K. Varga, T. Garay, B. Hegedus, and A. Czirok. Invasion from a cell aggregate - the roles of active cell motion and mechanical equilibrium. *Phys. Biol.*, 9:016010, 2012.

[244] G.M. Szpak, E. Lewandowska, T. Wierzba-Bobrowicz, E. Bertrand, E. Pasennik, T. Mendel, T. Stepien, A. Leszczynska, and J. Rafalowska. Small cerebral vessel disease in familial amyloid and non-amyloid angiopathies: FAD-PS-1 (P117L) mutation and CADASIL. *Immunohist. ultrastr. studies. Folia Neuropathol*, 45:192–204, 2007.

[245] Y. Takai, J. Miyoshi, W. Ikeda, and H. Ogita. Nectins and nectin-like molecules: roles in contact inhibition of cell movement and proliferation. *Nat. Rev. Molec. Cell Biol.*, 9:603–615, 2008.

[246] C.C. Taylor. Platelet-derived growth factor activates porcine thecal cell phosphatidylinositol-3-kinase-Akt/PKB and ras-extracellular signal-regulated kinase-1/2 kinase signaling pathways via the platelet-derived growth factor-beta receptor. *Endocrinology*, 141:1545–1553, 2000.

[247] R. Thommen, R. Humar, G. Misevic, M.S. Pepper, AWA. Han, M. John, and E.J. Battegay. PDGF-BB increases endothelial migration and cord movements during angiogenesis in vitro. *J. Cell Biochem.*, 64:403–413, 1997.

[248] S.S. Tolsma, S.M. Stack, and N. Bouck. Lumen formation and other angiogenic activities of cultured capillary endothelial cells are inhibited by thrombospondin-1. *Microv. Res.*, 54:13–26, 1997.

[249] P.C. Tsang, J.P. Poff, E.P. Boulton, and W.A. Condon. Four-day-old bovine corpus luteum: Progesterone production and identification of matrix metalloproteinase activity in vitro. *Biol. Reprod.*, 53:1160–1168, 1995.

[250] S. Turner and J.A. Sherratt. Intercellular adhesion and cancer invasion: a discrete simulation using the extended potts model. *J. Theor. Biol.*, 216:85–100, 2002.

[251] J.J. Tyson and B. Novak. Regulation of the eukaryotic cell cycle: molecular antagonism, hysteresis, and irreversible transitions. *J. Theor. Biol.*, 210:249–263, 2001.

[252] P. van Heyningen, A.R. Calver, and W.R. Richardson. Control of progenitor cell number by mitogen supply and demand. *Curr. Biol.*, 11:232–241, 2001.

[253] P. Vitorino and T. Meyer. Modular control of endothelial sheet migration. *Genes Dev.*, 22:3268–3281, 2008.

[254] D. von Tell, A. Armulik, and C. Betsholtz. Pericytes and vascular stability. *Exp. Cell Res.*, 312:623–629, 2006.

[255] M.A. Vorontchikhina, R.C. Zimmermann, C.J. Shawber, H. Tang, and J. Kitajewski. Unique patterns of Notch1, Notch4 and Jagged1 expression in ovarian vessels during folliculogenesis and corpus luteum formation. *Gene Expr. Patterns*, 5:701–709, 2005.

[256] D.C. Walker, J.S. Southgate, G. Hill, M. Holcombe, D.R. Hose, S.M. Wood, S. MacNeil, and R.H. Smallwood. The Epitheliome: modelling the social behaviour of cells. *BioSystems*, 76:89–100, 2004.

[257] Y. Wallez, I. Vilgrain, and P. Huber. Angiogenesis: the VE-cadherin switch. *Trends Cardiov. Med.*, 16:55–59, 2006.

[258] M.F. Ware, A. Wells, and D.A. Lauffenburger. Epidermal growth factor alters fibroblast migration speed and directional persistence reciprocally and in a matrix-dependent manner. *J. Cell Sci.*, 111:2423–2432, 1998.

[259] M. Weliky, S. Minsuk, R. Keller, and G.F. Oster. Notochord morphogenesis in xenopus laevis: simulation of cell behaviour underlying tissue convergence and extension. *Development*, 113:1231–1244, 1991.

[260] H. West, W.D. Richardson, and M. Fruttiger. Stabilization of the retinal vascular network by reciprocal feedback between blood vessels and astrocytes. *Development*, 132(8):1855–1862, 2005.

[261] D. Weygand, Y. Brchet, and J. Lpinoux. A vertex dynamics simulation of grain growth in two dimensions. *Phil. Mag.*, B78:329–352, 1989.

[262] V.B. Wigglesworth. Local and general factors in the development of 'pattern' in rhodnius prolixus (hemiptera). *J. Exp. Biol.*, 17:180–201, 1940.

[263] M. Wiltbank. Cell types and hormonal mechanisms associated with mid-cycle corpus luteum function. *J. Anim. Sci.*, 72:1873–1883, 1994.

[264] S. Yamagishi and T. Imaizumi. Pericyte biology and diseases. *Int. J. Tissue React.*, 27:125–135, 2005.

[265] G.D. Yancopoulos, S. Davis, N.W. Gale, J.S. Rudge, S.J. Wiegand, and J. Holash. Vascular-specific growth factors and blood vessel formation. *Nature*, 14:242–248, 2000.

[266] J. Zheng, D.A. Redmer, and L.P. Reynolds. Vascular development and heparin-binding growth factors in the bovine corpus luteum at several stages of the estrous cycle. *Biol. Reprod.*, 49:1177–1189, 1993.

[267] X. Zheng, G.Y. Koh, and T. Jackson. A continuous model of angiogenesis: initiation, extension, and maturation of new blood vessels modulated by vascular endothelial growth factor, angiopoietins, platelet-derived growth factor-B, and pericytes. *AIMS, Discr. and Cont. Dyn. Systems - Series B*, (in press).

[268] B.V. Zlokovic. The blood-brain barrier in health and chronic neurodegenerative disorders. *Neuron*, 57:178–201, 2008.